PLASMONIC NANOCAVITIES AND THEIR INTERACTION WITH QUANTUM EMITTERS

BY

KALUN BEDINGFIELD

A THESIS SUBMITTED TO THE UNIVERSITY OF BIRMINGHAM FOR THE DEGREE OF

DOCTOR OF PHILOSOPHY

METAMATERIALS RESEARCH GROUP
SCHOOL OF PHYSICS AND ASTRONOMY
UNIVERSITY OF BIRMINGHAM
AUGUST 2022

ABSTRACT

When a photonic environment hosts an emitter, it heavily influences its spontaneous emission. For an emitter placed within a photonic environment that supports extreme field enhancements, their light-matter interactions are also significantly altered. One such example of an extreme photonic environment is that of a plasmonic nanocavity, which is a plasmonic gap of just 1-2 nm formed between two metallic nanostructures. The nanoparticle-on-mirror geometry—formed of a metallic nanoparticle assembled on a flat metallic substrate, separated by a dielectric spacer—is a plasmonic nanocavity that has become particularly prolific in experimental literature, recently used to realise the room temperature light-matter strong coupling between a plasmonic mode and a single molecule. Emitters placed within such plasmonic nanocavities experience sub-wavelength field confinements and extreme light enhancements, due to the intense hybridisation of localised plasmons that are evanescently bound to the metallic surfaces. This thesis explores the optical properties of plasmonic nanocavities and their complex light-matter interactions with emitters hosted within them, aiding in the future potential to facilitate strongly coupled quantum devices that operate in ambient conditions.

The emission and excitation properties of plasmonic nanoantennas are explored initially, addressing the misconception that energy can be coupled into all plasmonic systems just as efficiently as it is out-coupled. Using a Green's function formalism to decompose the modal plasmonic response, the dominant out-coupling of certain plasmonic nanocavities is unveiled through a mode selectivity of the excitational properties—

accentuated by non–quasi-static metallic elements of the system. Custom designs of plasmonic systems are then considered to tailor relative in- and out-coupling rates, capable of supporting both enhanced and retarded excitation regimes.

The near-field resonances and complex eigenfrequencies are then obtained for a series of realistic polyhedral nanocavity geometries. Although most theoretical studies of plasmonic nanocavities have focused on spherical nanoparticles, in reality they acquire a polyhedral shape during fabrication due to the crystalline nature of gold. Each polyhedron supports multiple unique facet assemblies whose exact morphology dramatically controls the supported modes, their spectral arrangement and their degeneracies. Projecting the modal response to the far-field, we reveal the paramountcy of the facet shape, neighbouring facets and polyhedral symmetry on their ability to radiate from the system: showing the extraordinarily strong dependence on the position and frequency of the emitter within the nanocavity, as well as the morphology of the system. This work paves the way in identifying the shape and symmetry of nanocavity geometries, as well as in determining the exact position of an emitter placed within a realistic plasmonic nanocavity.

Finally, we consider the quantum nature of emitters to model their cyclic energy exchange with plasmonic nanocavities (i.e. Rabi oscillations). We develop a quantum mechanical description via a mode quantisation scheme for the plasmonic modes that, unlike most methods currently proposed in the literature, is fully consistent in returning the classical limit. The Rabi oscillations are explored for multi-emitter systems—through the dependencies of emitter positioning and arrangement within the cavity—in addition to Rabi splitting and anti-crossing dynamics, when operating in a laser driven excitation regime. Excited emitter longevity is explored through exotic state preparations, uncovering massive lifetime enhancements for emitter initialised systems, where semi-persistent states may be long lived even in these extreme yet lossy nanoantennas systems—capable of aiding in the room temperature strong coupling of quantum plasmonic devices.

ACKNOWLEDGMENTS

TO MY FAMILY AND FRIENDS

FOR YOUR UNWAVERING LOVE AND SUPPORT

TO ANGELA

FOR THE INCREDIBLE OPPORTUNITY YOU HAVE GIVEN ME

AND FOR HELPING ME BECOME WHO I AM TODAY

CONTENTS

LIST OF FIGURES

LIST OF PUBLICATIONS

The following publications constitute the main works that are presented in this thesis, for which I have been the main contributor:

- Kalun Bedingfield and Angela Demetriadou. On the excitation and radiative decay rates of plasmonic nanoantennas. *Nanophotonics*, vol. 11, no. 10, 2022, pp. 2271-2281.

- Kalun Bedingfield, Eoin Elliott, Nuttawut Kongsuwan, Jeremy J. Baumberg and Angela Demetriadou. Morphology Dependence of NanoParticle-on-Mirror Geometries: A Quasinormal Mode analysis. *EPJ Appl. Metamat.*, vol. 9, no. 3, 2022.

- Kalun Bedingfield, Eoin Elliott, Arsenios Gisdakis, Nuttawut Kongsuwan, Jeremy J Baumberg and Angela Demetriadou. Plasmonic Modes of Polyhedral Nanocavities. *Under Preparation*.

- Kalun Bedingfield, Benjamin Yuen and Angela Demetriadou. Entanglement of Quantum Emitters Strongly Coupled with Plasmonic Nanocavities. *Under Preparation*.

Additional publications in the duration of my PhD include:

- Eoin Elliott, Kalun Bedingfield, Junyang Huang, Shu Hu, Bart de Nijs, Angela Demetriadou and Jeremy J. Baumberg. Fingerprinting the Hidden Facets of Plasmonic Nanocavities. *Accepted: ACS Photonics*, 2022.
- Angelo Angelini, Kalun Bedingfield and Angela Demetriadou. Modeling Steady State Photothermal Properties of Gold-Based Nano-Systems. *Under Preparation*.

A selection of these works were presented at the following international conferences:

- Kalun Bedingfield and Angela Demetriadou. On the Radiative Emission and Excitation Rate of Quantum Emitters in Plasmonic Nanostructures. *2020 Fourteenth International Congress on Artificial Materials for Novel Wave Phenomena (Metamaterials)* 2020, pp. 433-435. (Oral Presentation)
- Kalun Bedingfield, Eoin Elliott, Nuttawut Kongsuwan, Jeremy J. Baumberg and Angela Demetriadou. Quasinormal Mode Analysis of Polygon-on-Mirror Geometries. *2021 Fifteenth International Congress on Artificial Materials for Novel Wave Phenomena (Metamaterials)* 2021, pp. 038-040. (Poster Presentation)

1 INTRODUCTION

The interaction between light and matter—such as a molecule—has the ability to alter the emissive capabilities of the matter. If they exchange energy fast enough—faster than energy is lost from the system—they hybridise and become intrinsically linked. Once the optical environment supports a coupling that is sufficiently strong, they can no longer act independently and instead form hybridised states. This strong coupling between light and matter was first achieved in an optical environment in 1983, and required the collective interaction of many atoms [1]; the strong coupling of a single molecule was later achieved in 1992 using a high finesse cavity [2], however, both of these experiments could only be realised at cryogenic temperatures. It wasn't until very recently that the cryogenic limitation of light-matter strong coupling was overcome, and was achieved through the introduction of plasmonic nanocavities [3]. As such, the field of nanoplasmonics has since developed rapidly, progressing from emitter-ensembles toward single molecule room temperature strong coupling [4].

In this thesis, light-matter interactions are explored in the context of quantum emitters (QEs) coupled to plasmonic nanocavities, from both classical and quantum perspec-

tives, using numerical and theoretical techniques. These works reveal many of the intricacies of how plasmonic nanocavities emit and receive energy, the manner in which the morphology of a system dictates its optical response, and the entanglement of emitter-ensembles within a nanocavity. This supports the experimental identification of emitter positioning within plasmonic systems, unveils tailored fabrication designs which can greatly increase Raman emissions, and offers massive emitter lifetime enhancements through the formation of semi-persistent states. Together these works drive toward the facilitation of strongly coupled quantum devices that operate at room temperature.

This chapter gives an overview of plasmonic nanocavities, how they host and facilitate QEs, where they fit in the wider literature, and the tools with which their interactions may be theoretically modelled. Section 1.1 discusses the field of plasmonics and how this has lead to the formation of plasmonic nanocavities. This is followed by Section 1.2, which introduces the relevant theoretical framework required to describe plasmonic light-matter interactions from a quantum perspective—as well as the numerical modelling techniques. Lastly, Section 1.3 summarises the content for the remainder of the thesis.

1.1 INTRODUCTION TO PLASMONICS

Initially proposed in 1952 by Pines and Bohm [5], plasmons are the quasiparticles of plasma oscillations arising from the collective motion of delocalised electron clouds. The field of plasmonics considers the confinement of light—electromagnetic (EM) fields—

to metal-dielectric interfaces, where external light drives the collective oscillation of the metal's conduction electrons. These conduction electron oscillations are also known as surface plasmons (SPs), as they form at—and are bound to—the metal-dielectric interface, and decay exponentially away from the interface (i.e. evanescently) into the dielectric.

For such evanescent waves to be bound to an interface, the electric permittivities of the two materials (ε_1 and ε_2) must follow $\varepsilon_1 + \varepsilon_2 < 0$, and hence the real part of one of the electric permittivities must be negative. A specific combination of materials are therefore required for the interface to satisfy this condition; at optical frequencies this is achieved using metallic and dielectric media. Due to the complex refractive indices of metals, SPs are evanescently confined to the interface and exponentially decay away from the metallic surface. It is this extremely localised nature of SPs that enables the confinement of incident EM fields to regions well below the diffraction limit [6–8]. Of these eigenstates bound to the interface, two types of SPs exist and are discussed below.

1.1.1 PROPAGATING SURFACE PLASMON POLARITONS

The first type of SPs considered here sees the collective electron oscillations propagating along—and bound to—the flat metallic surface of a metal-dielectric interface (as shown in Figure 1.1A). They arise through the coupling with photons, forming a polaritonic state—a coupled light-matter wave—known as propagating surface plasmon polaritons (SPPs). As they exist outside of the light cone—see Figure 1.1B—they are evanescently confined to

the surface and therefore cannot be directly coupled to by incident light. In the absence of inhomogeneities, SPPs are prevented from radiating energy from the system and propagate until their energy is lost through Ohmic heating of the metal [9]. They also cannot be excited from the dielectric side of the interface, due to the mismatch in the EM wave's momentum.

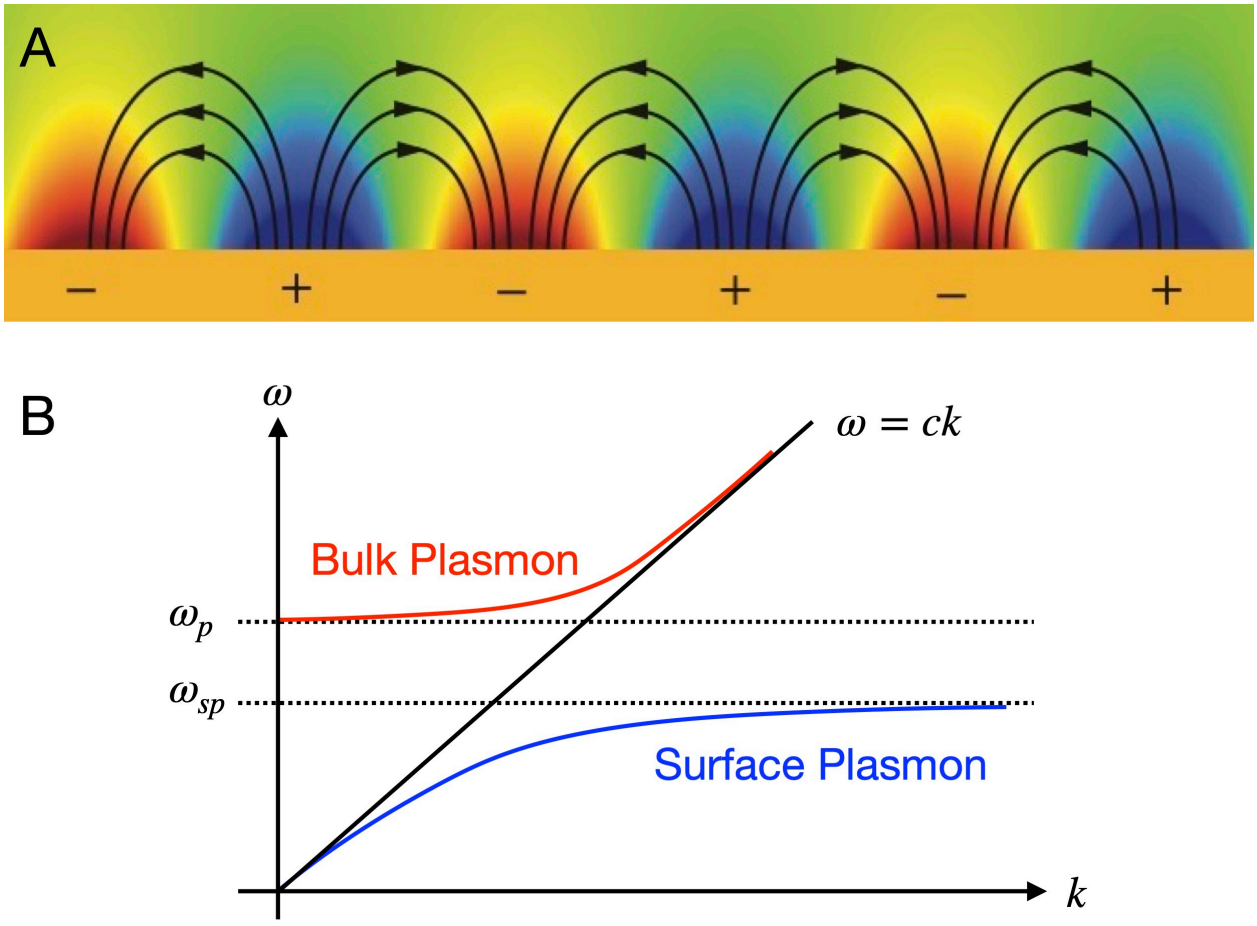

Figure 1.1: A. The electric field associated to a propagating SPP evanescently bound to the interface between a metal and a dielectric. Oscillating charges form along the metal, and the SPPs exponentially decay with distance away from the metal's surface [9]. B. Plasmon dispersion diagram (without losses), showing the bulk and surface plasmons as a function of frequency (ω) and wavevector (k).

1.1.2 LOCALISED SURFACE PLASMON RESONANCES

The second type of SPs emerge for certain nanostructures surrounded by dielectric media, such as an isolated spherical nanoparticle (NP), where the evanescent eigenstates are bound to the metal-dielectric interface and do not propagate. When driven by an external EM field, the collective electron oscillations are localised within the nanostructure—as shown in Figure 1.2—and therefore termed localised surface plasmon resonances (LSPRs). These evanescent fields yield strong enhancements in the immediate vicinity of the nanostructure, which exponentially decay away from the metallic surface; in comparison to the wavelength of the incident EM fields, this leads to the confinement of the

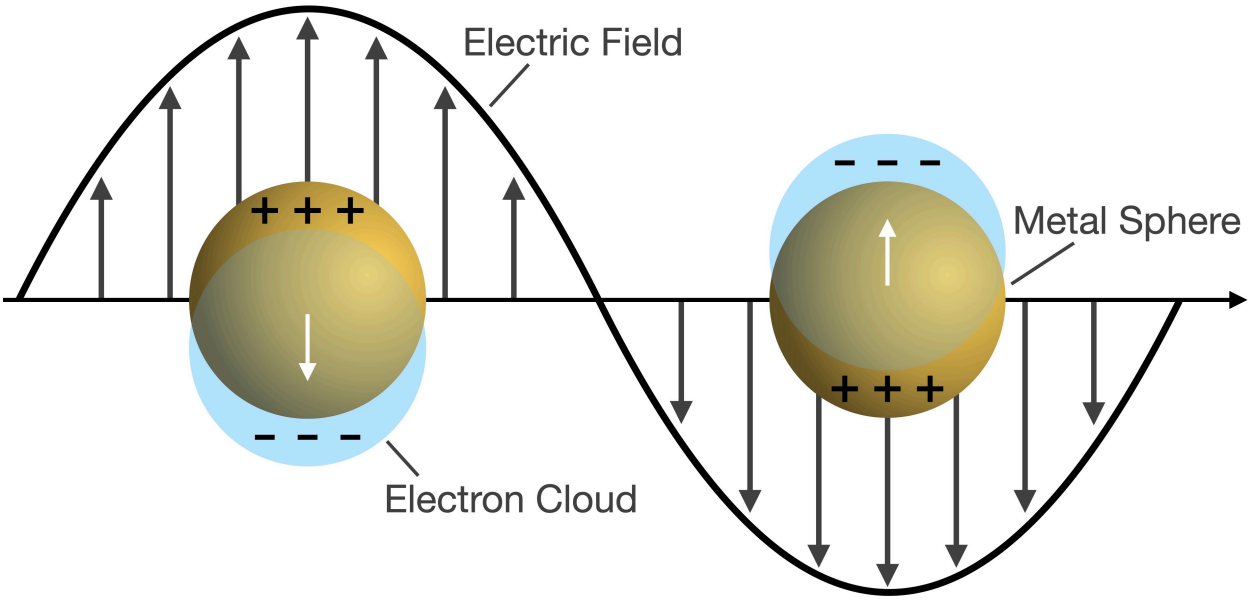

Figure 1.2: The formation of LSPRs due to the collective electron oscillations induced in a metallic nanostructure by an external EM driving field. The positive charges within the metal give rise to the oscillatory nature of the electrons through the restoring force they apply to confine the electron cloud.

fields to sub-wavelength volumes. The natural resonances with which the collective electron cloud oscillates are referred to as plasmonic modes, which are frequently used in characterising the properties of plasmonic systems and are the main type of SPs considered throughout this thesis. These plasmonic nanostructures often offer strong radiative capabilities, and efficiently emit energy to the far-field.

1.1.3 PLASMONIC NANOANTENNAS

By tightly coupling two or more plasmonic nanostructures, one can form a plasmonic nanoantenna that supports a gap of just a few nanometres. Within this gap—also known as a nanocavity—the plasmonic modes of each structure hybridise, yielding an extreme field confinement and a massively increased light enhancement [6–8, 10]. Various plasmonic nanoantenna designs exist which make use of the extreme plasmonic environments, each with unique properties tailored for specific applications throughout the fields of nanoplasmonics and nanophotonics.

One such design is that of the Bow-Tie antenna, which consists of two triangular prisms oriented such that a nanocavity is formed between two of the triangular corners—as shown in Figure 1.3A. The curved edges act as a series of dipole antennas with various widths and gap sizes—each of which support a separate resonance—leading to a very broadband antenna that provides huge design flexibility [11, 12]. Another design is that of the Yagi-Uda nanoantenna, as shown in Figure 1.3B, which takes the form of an antenna design seen in the aerials for TV and radio communications, but constructed

at the nanoscale [13]. It consists of a series of parallel dipole antennas whose lengths are chosen to efficiently transmit and direct EM fields [14]. For more information, there are several good reviews that outline many of the nanoantenna designs currently being explored throughout the literature [15–17].

Of these countless nanoantennas, in recent years one design in particular has become a popular structure throughout experimental literature: that of the nanoparticle-

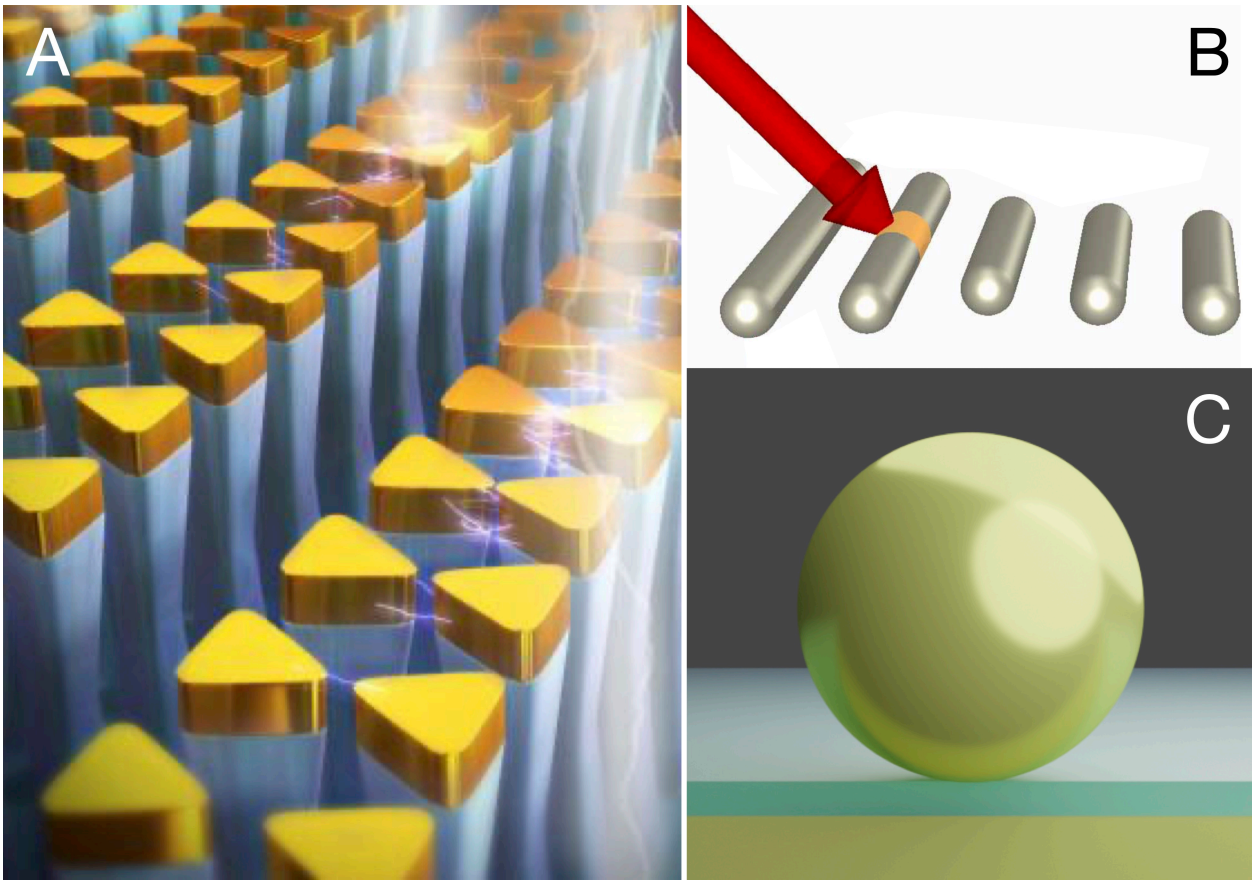

Figure 1.3: A. An array of Bow-Tie antennas, each consisting of two triangular metallic nano-prisms that form a nanocavity between two of the corners [12]. B. The Yagi-Uda antenna, consisting of a series of dipole antennas with differing lengths, arranged in parallel [13, 14]. C. The NPoM geometry, for a spherical NP assembled on a flat metallic substrate, separated by a dielectric spacer.

on-mirror (NPoM) geometry. It consists of a metallic NP assembled on a flat metallic substrate, separated by a dielectric spacer—such as molecules, polymers, perovskites or inorganic layers [7]—and forms a nanocavity between the two metallic structures (as shown in Figure 1.3C), with the ability to forms gaps as small as 0.3 nm. The NPoM geometry has drawn significant attention due to the suitability of its environment for studying the interactions between light (plasmons) and matter (molecules), as the extremely small nanocavities required for strong coupling can be achieved relatively easily [4]. Recent developments in nanofabrication techniques [18–22] have allowed for the creation of very robust cavities, offering angstrom-level gap accuracy by specifically choosing the molecular monolayer in the gap [19, 23, 24]. Such structures manage to enhance the field intensity by more than three orders of magnitude [25–28], and have been shown to facilitate light-matter strong coupling at room temperature [4]—where the cyclic exchange of energy occurs between light and matter (i.e. Rabi oscillations). The ambient condition strong coupling has further heightened the profile of the NPoM geometry, for its potential to facilitate quantum devices without cryogenic treatment.

By placing QEs—such as J-aggregates [29], quantum dots [30] or any molecule that has the ability to absorb and emit photons (fluoresce) [4]—near a plasmonic nanoantenna, they couple to the plasmonic modes and exchange energy. Their interaction with the strong field confinement of the plasmonic environment means the emitters will also experience an enhanced emission rate (increased relative to the emission rate of emitters in free-space). However, plasmonic nanostructures also support a series of higher order plasmonic modes that are more closely bound to the metallic surface, and lack efficient

energy radiation. They posses many decay channels through which energy may be non-radiatively lost from the system, via processes such as Ohmic losses in the metal—which lead to the heating of the nanostructure—and the launching of propagating SPPs (if they are supported by the system). Emitters placed in the close vicinity (within 10 nm) of isolated plasmonic nanostructures are therefore quenched due to these non-radiative decay channels, whereby the plasmonic enhancement is largely diminished and all enhanced radiative capabilities are lost. However, the 1-2 nm nanocavities supported by plasmonic nanoantennas are able to overcome this quenching of QEs [25–28]. The plasmonic 'hot-spots' supported by these nanocavities alter the dark nature of higher order modes (their low radiative capabilities), and therefore increase the efficiency with which energy is radiated to the far-field. This has been demonstrated experimentally and theoretically through DNA-origami techniques that control the placement of emitters within nanocavities [10].

Note that it is worth distinguishing these plasmonic nanocavities from those explored in optics literature. Unlike the low losses and relatively long interaction times of traditional high finesse optical cavities, plasmonic environments posses significant loss channels; in spite of this, the extreme field enhancements and nanoscale mode volumes of plasmonic nanocavities facilitate room temperature strong coupling through light-matter interactions on ultrafast timescales.

1.1.4 APPLICATIONS OF NANOANTENNAS

Since the appearance of nanoantennas, the field of plasmonics has rapidly evolved with various developments present in spectroscopy [31], solar cells [32, 33], and medical treatments [34] due to their extreme localisation and emission properties. Specifically, plasmonic nanoantennas see application in modern cancer therapy techniques [35]. Plasmonic photo-thermal therapy takes advantage of the rapid growth of cancerous sites by functionalising gold NPs, allowing them to path through the body to these regions of high metabolic activity, thus accumulating and binding to the cancerous cells. Through a near–infra-red laser excitation, LSPRs are induced in the NPs to enable the local heating and killing of the cancerous cells [36]. The unique characteristics of plasmonic nanoantennas are also employed in: molecule sensing applications [37], real-time sensing of chemical processes [38], and hot electron generation [39]—amongst many others.

The extreme plasmonic environments created by plasmonic nanocavities, however, have also enabled a plethora of extraordinary realisations [29], such as the imaging of single molecules placed inside a nanocavity [40, 41], the single molecule strong coupling and ultrafast single photon emission at room temperature [4, 30], and the interrogation of targeted chemical bonds within a single molecule via the formation of a pico-cavity [18, 42]. Plasmonic nanocavities also see applications in non-linear pumping of vibrational states [43], enhanced exciton photo-luminescence [44] and mid-infrared upconversion detectors [45, 46] to name but a few.

The ability of plasmonic nanocavities to amplify the radiative capabilities of emitters in the cavity also increases their Raman signals, where the chemical bonds of a molecule are excited via laser stimulation, then later relax to a molecular vibrational state and emit a photon; the phenomenon of surface-enhanced Raman spectroscopy (SERS) is now a very common far-field technique for analysing how emitters are altered by the plasmonic environment of a nanocavity [47]. Conversely to the enhanced emission rate, nanocavities also play a crucial role in how emitters are excited from the far-field.

1.2 PROPERTIES OF LIGHT-MATTER INTERACTIONS

In order to study the interactions between emitters and plasmonic environments, one must be familiar with the theoretical quantities and models that regularly see use throughout the field, as well as the software and numerical techniques available.

1.2.1 LOCAL DENSITY OF STATES – FERMI'S GOLDEN RULE

Plasmonic light-matter interactions investigated from a quantum perspective (otherwise known as quantum plasmonics) often see the QEs represented as two-level systems [17], with various parameters used in characterising their interactions. One such quantity—which is particularly crucial for describing the interactions of a QE with the local environment supported by a plasmonic nanocavity—is that of the local density of states (LDoS), $\rho(\omega)$. The LDoS quantifies the photonic decay channels available for a QE to couple to

when placed within a specific environment—such as the extreme field enhancement and confinement offered by a plasmonic nanocavity.

Fermi's golden rule describes the rate at which a free-space QE in its excited state decays to its ground state, which follows:

$$\gamma_{free} = \frac{2\pi}{\hbar^2} \left| \langle f | \hat{\mu} \cdot \hat{\mathbf{E}}_{vac} | i \rangle \right|^2 \rho(\omega) \ , \tag{1.1}$$

where $\hat{\mathbf{E}}_{vac}$ is the vacuum-field operator. Free-space spontaneous emission is analogous to stimulated emission, where the stimulation arises from vacuum field perturbations [48]—as shown in Figure 1.4A.

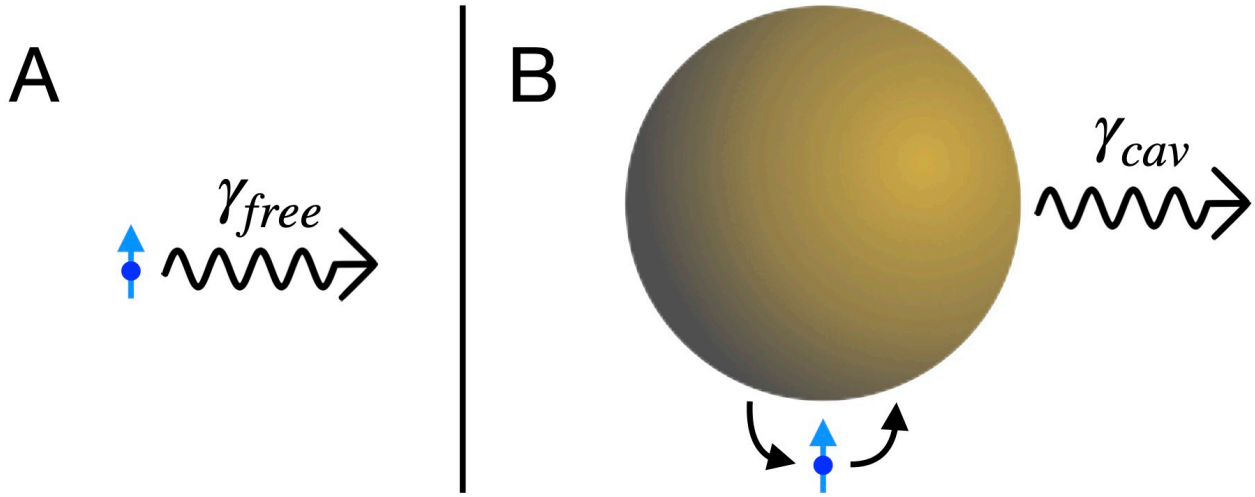

Figure 1.4: A. Free-space spontaneous emission of a QE (blue dot, with the arrow depicting its polarisation) due to random perturbations from the vacuum-field. B. Enhanced emitter decay rate due to the energy exchange with the plasmonic environment and the increased LDoS it offers.

By placing the QE within the cavity of a plasmonic nanoantenna, its spontaneous emission rate is drastically altered through the LDoS and the abundance of available decay channels. Inline with the Green's function approach presented in Chapter 2, the frequency dependent LDoS may be expressed in terms of the dyadic Green's function ($\overleftrightarrow{\mathbf{G}}$), that essentially represents the local field at position $\mathbf{r}'$:

$$\rho(\omega) = \frac{6\omega}{\pi c^2}\left[\hat{\mu}\cdot \mathrm{Im}\{\overleftrightarrow{\mathbf{G}}(\mathbf{r}',\mathbf{r}')\}\cdot\hat{\mu}\right] , \tag{1.2}$$

where $\hat{\mu}$ is the dipole moment operator of the emitter.

If the emitter is placed at the hot-spot of the cavity—where the largest field enhancement is focused—the LDoS resonates with the dominant LSPRs; for a cavity that supports a singular resonance (ω_{pl}), the LDoS can effectively be described with a single Lorentzian. From this Lorentzian, one can identify the quality factor (or Q-factor) as $Q = \frac{\omega_{pl}}{\Delta\omega}$, where ω_{pl} and $\Delta\omega$ are respectively the peak frequency and full-width half-maximum of the singular resonance—the latter of which describes the non-radiative contribution of the particular plasmonic resonance [48].

On resonance the LDoS reduces to $\rho(\omega_{pl}) = \frac{2Q}{\pi\omega_{pl}}$, and leads to the following simple expression for the emitter's decay rate when placed at the cavity extrema:

$$\gamma_{cav} = \frac{2}{\hbar\varepsilon_0}\mu^2\frac{Q}{V} , \tag{1.3}$$

where the middle component describes the contribution from the emitter (with a dipole

moment μ), and the last fraction describes the photonic environment. Here V is the mode volume, which measures the spatial confinement of the LSPR via the region of space it occupies.

By comparing the decay rates of the emitter when placed within a nanocavity relative to the emitter in free space, one may identify the Purcell factor as $F_p = \frac{\gamma_{cav}}{\gamma_{free}}$; this describes how the spontaneous emission rate of the emitter is modified by the presence of the photonic environment, with contributions directly originating from both the emitter itself, as well as the specific field enhancement and confinement supplied by the cavity. On resonance, the Purcell factor becomes:

$$F_p = \frac{3}{4\pi^2}\left(\frac{\lambda}{n}\right)^3 \frac{Q}{V} \,, \tag{1.4}$$

where n is the refractive index of the material where the emitter is placed [49]. Whether the Purcell factor is greater or less than unity directly correlates to the nanocavity respectively enhancing or inhibiting the spontaneous decay of the emitter.

Despite the significant loss channels and thus low quality factors—on the scale of $Q \approx 10$—supported by plasmonic systems, the extreme light confinement leads to nanoscale mode volumes that result in very strong overall field enhancements. This yields Purcell factors on the scale of $F_p \approx 10^6$, whereby the field strength in the cavity is enhanced relative to the strength in free-space. The faster decay rate within these nanocavities directly increases the fluorescence rate of QEs, and thus facilitates strong coupling through ultrafast light-matter interactions.

1.2.2 GOLD AT OPTICAL FREQUENCIES

The material for every metallic nanostructure considered throughout this thesis is chosen to be gold. Although many other metals (such as silver) support plasmonic resonances, gold is chemically inert, which is hugely beneficial for hosting a wide array of molecules; gold is widely used in fabricating plasmonic nanostructures, and often used to perform surface chemistry. In describing the material properties of nanostructures, one must consider the electric permittivity—for gold this is dispersive (frequency dependent), $\varepsilon(\omega)$.

The electric permittivity can generally be described by the Drude model: $\varepsilon(\omega) = 1 - \omega_p^2/(\omega^2 + i\omega\gamma)$, which treats the conduction electrons as a nearly-free plasma that move and rebound off static positive charges. This offers a reasonable description at optical frequencies but deviates at ultra-violet frequencies due to intra- and inter-band electronic transitions. These valence electrons are bound to the positive ions, and are better described by a Lorentz model: $\varepsilon(\omega) = 1 - \omega_p^2/(\omega^2 - \omega_0^2 + i\omega\gamma)$. This treats the valence electrons as a damped harmonic oscillator, and resonates close to their electronic transition frequency (ω_0).

For an electric permittivity that accurately describes both the bound and delocalised electrons, one must consider a Drude-Lorentz model. This can be written generally for N Drude-Lorentz poles:

$$\varepsilon(\omega) = \varepsilon_\infty \left(1 + \sum_{k=1}^{N} \frac{\omega_{p,k}^2}{\omega_{0,k}^2 - \omega^2 - i\gamma_k\omega} \right) , \tag{1.5}$$

where ω is the angular frequency; ε_∞ is a constant relative electric permittivity; $\omega_{0,k}$ and $\omega_{p,k}$ are the respective plasma frequencies of the k-th Drude and Lorentz terms; and γ_k is the k-th Lorentz viscous damping coefficient.

Here we consider an $N = 2$ pole Drude-Lorentz electric permittivity for gold, which reduces the general expression of equation 1.5 to:

$$\varepsilon(\omega) = \varepsilon_\infty \left(1 + \frac{\omega_{p,1}^2}{\omega_{0,1}^2 - \omega^2 - i\gamma_1\omega} + \frac{\omega_{p,2}^2}{\omega_{0,2}^2 - \omega^2 - i\gamma_2\omega}\right) , \tag{1.6}$$

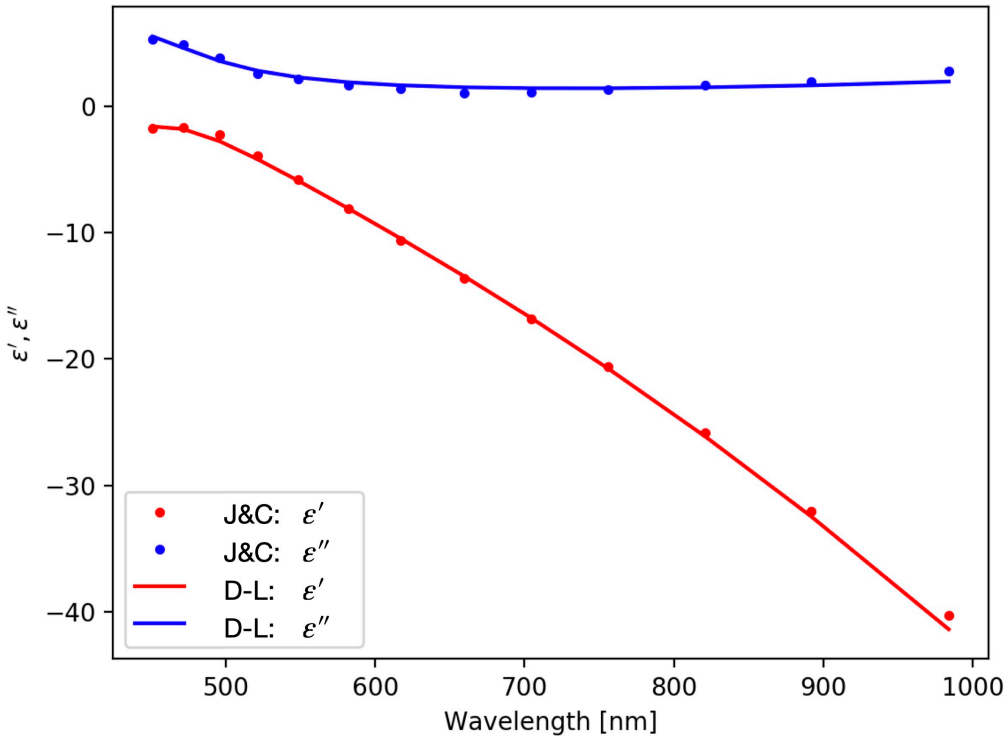

Figure 1.5: The real (ε', red) and imaginary (ε'', blue) components of the electric permittivity of Gold over a wavelength range of $450 - 950$ nm. Comparison of Johnson and Cristyś experimental data (points) with the fit following the Drude-Lorentz model (curve) of equation 1.5.

where $\varepsilon_\infty = 6\varepsilon_0$, $\omega_{p,1} = 5.37 \times 10^{15}$ rad/s, $\omega_{0,1} = 0$ rad/s, $\gamma_1 = 6.216 \times 10^{13}$ rad/s, $\omega_{p,2} = 2.2636 \times 10^{15}$ rad/s, $\omega_{0,2} = 4.572 \times 10^{15}$ rad/s, and $\gamma_2 = 1.332 \times 10^{15}$ rad/s. These values are obtained by fitting the 2-pole Drude-Lorentz model to the experimental electric permittivity data from Johnson and Christy [50]. These are compared in Figure 1.5, revealing the strong agreement in both the real and imaginary components across the extended optical–ultra-violet range.

1.2.3 NUMERICAL METHODS

For the plasmonic nanocavities presented throughout this thesis, their optical properties are obtained by solving Maxwell's equations using two primary methods: the finite-difference time-domain (FDTD) method [51] in Lumerical's FDTD software, and the finite-element method (FEM) [52] in COMSOL Multiphysics 5.6. These are both very popular softwares within the nanophotonics community as they can be applied to arbitrary media and for any geometry. They offer different advantages and disadvantages, and are in many ways complementary methods. Although these two methods present different spatial discretisation processes, both methods can represent an infinite space within a finite simulation space. This is achieved by surrounding the plasmonic systems with perfectly matched layers (PMLs) that efficiently absorb incident EM fields and minimise reflections back into the system.

Due to the very small size of the nanometre gap compared to the metallic nanostructures forming the gap in the plasmonic nanocavities, a uniform meshing scheme would

be too computationally expensive—but also largely unnecessary to enable converged solutions. Throughout the geometries considered in this thesis, adaptive meshing regimes are employed to efficiently discretise the space—such that sub-nanometre meshing may be achieved locally to the cavity, whilst the NP maintains a computationally less intensive $1\text{-}5$ nm meshing.

FINITE DIFFERENCE METHOD

FDTD uses Yee's method [53], where the spatial domain is discretised into a grid and forms a series of Yee cells; this numerical technique uses rectangular (2D) and cuboidal (3D) meshing regimes. The electric and magnetic fields are stored at separate locations within each Yee cell, such that each component of the electric field is halfway between each component of the magnetic field—and vice versa. A central-difference approximation is then utilised in order to solve the time-dependent partial differential form of Maxwell's equations in the time-domain. The simulations are then computed using Yee's leapfrog method, whereby the electric and magnetic fields are calculated on alternating staggered time steps. The solutions are obtained by repeating this process until the simulations are converged—where the EM behaviour reaches the steady-state.

Although the FDTD method is mostly limited to the time-domain, it provides very robust computations and can be applied to both active and non-linear systems. However, even when using adaptive meshing techniques, FDTD's rectangular based meshing can lead to rather inefficient meshing localisation and thus require increased levels of computational demand.

FINITE ELEMENT METHOD

On the other hand, the FEM method in COMSOL can be applied to both frequency and time-domain calculations, and implements a meshing regime that forms connected elements through a matrix of basis functions. Algorithms are run in order to minimise and optimise the matrix system, leading to computations that are—in general—much more efficient than their FDTD counterparts. These basis functions can be implemented to discretise the spatial domain using a variety (and combination) of mesh element shapes.

In addition to the rectangular/cuboidal meshing of FDTD, FEM in COMSOL commonly implements triangular (2D) and tetrahedral (3D) discretisation regimes. These are greatly advantageous in modelling curved or complex geometrical structures with minimal meshing error, as well as better handling dispersive media and efficiently solving highly-resonant systems. The triangular-based meshing regimes offer greatly improved meshing localisations, considerably improving computational efficiencies. For large and intricate systems, however, the meshing can become computationally complex to initialise and may require higher memory capabilities.

1.3 SUMMARY OF CONTENTS

This thesis explores the light-matter interactions of plasmonic nanocavities coupled to fluorescent emitters, and is structured into five chapters (inclusive of this introductory chapter). Chapter 2 identifies the origin of unequal radiative and excitational rates in plasmonic

nanoantenna and nanocavity geometries, using a Green's function approach to decompose the modal nature of the plasmonic response. Chapter 3 explores the near-field and far-field behaviours of realistic polyhedral NPoM geometries, through a quasi-normal mode methodology. Chapter 4 utilises the QNM approach to describe the NPoM from a quantum perspective, investigating the entanglement and exotic state preparations of multiple emitters arranged within a plasmonic nanocavity. The thesis is finally summarised in Chapter 5, with an outlook to future work.

2 EXCITATION AND RADIATIVE DECAY RATES OF PLASMONIC NANOANTENNAS

2.1 INTRODUCTION

To date the analysis of the NPoM and other nanoantenna geometries have predominantly focused on the scattering and absorption responses. These methods are then required to infer the properties of the near-field from the far-field emissions, missing out on a plethora of intricacies of the interactions within the nanocavity. In all the analyses and methodologies discussed in Subsection 1.1.4, the fluorescent molecule is excited by an external plane wave and is detected from its far-field emission—both of these processes happen via the same set of plasmonic modes supported by the nanoantenna. The manner in which energy is coupled into and out of the system is an element of these studies that is often overlooked or misunderstood.

It is often thought that energy from the far-field couples into plasmonic nanostructures (in-coupling) just as efficiently as a fluorescent molecule within the nanocavity radiates energy to the far-field (out-coupling)—as both processes occur via the same set of plasmonic modes. In this chapter, we show that in some plasmonic nanoantennas systems the above statement does not always hold, and through a Green's function based Mie theory multipolar decomposition we identify the origin of this behaviour.

No matter whether the interest is in the interaction between emitters, the translation of near-field resonances to far-field spectra, or the efficiency of emission in SERS experiments, a better understanding of how plasmonic systems in- and out-couple energy is greatly beneficial. This chapter therefore explores the excitational and emissive properties of plasmonic nanoantennas, with the aim to aid in designing future plasmonic systems with tailored characteristics.

A COMMENT ON RECIPROCITY

Reciprocity dictates the identical manner in which EM systems receive and radiate energy [54]. By definition, in a reciprocal system, if the locations of a source and detector are to be interchanged, the received signal remains unchanged [55]. Using a Green's function notation, the nature of reciprocity is expressed mathematically as: $\mathbf{G}(\mathbf{r}, \mathbf{r}') = \mathbf{G}(\mathbf{r}', \mathbf{r})$, where the first and second arguments refer to the source and detector locations, respectively [48]. This argument is universally found throughout all fields of EMs, including plasmonics. Therefore one would expect to observe equal rates at which energy is coupled into and out of a plasmonic system.

2.1.1 EXCITATION AND EMISSION OF QUANTUM EMITTERS

To explore how QEs interact with the intense environments supported by plasmonic systems, it is imperative to work with parameters that are most pertinent to current experimental methodologies. A pair of such parameters are the excitation (γ_{exc}) and radiative decay (γ_{rad}) rates, which are readily accessible in experimental procedures. These complementary processes describe the manner in which energy is coupled into and out of QEs when interacting with EM fields—both in free space and within plasmonic nanocavities.

The γ_{exc} measures the enhancement to the rate at which an external source is able to excite a QE when it is placed in the vicinity of a nanoantenna—as shown in Figure 2.1A. Relative to a free space QE excited by an external source, a QE placed within a nanoantenna experiences an increased γ_{exc} due to the enhancement of the plasmonic system.

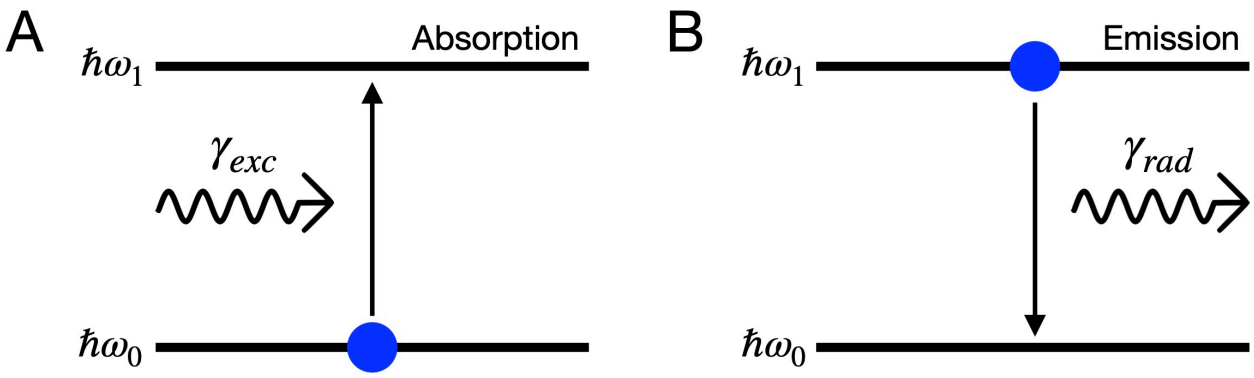

Figure 2.1: Absorption (A) and emission (B) processes of a two-level system representation of a QE, respectively accepting and emitting energy at rates enhanced by γ_{exc} and γ_{rad}.

This enhancement follows:

$$\gamma_{exc} = \frac{|\hat{\mu} \cdot \mathbf{E}(\mathbf{r}')|^2}{|\hat{\mu} \cdot \mathbf{E}_0(\mathbf{r}')|^2} \ , \tag{2.1}$$

where $\mathbf{r}'$ is the position of the QE, $\hat{\mu}$ is the QE's dipole moment unit vector, $\mathbf{E}(\mathbf{r}')$ and $\mathbf{E}_0(\mathbf{r}')$ are the total electric field vectors—at the location of the QE—respectively with and without the plasmonic environment present [21, 48].

Conversely, the γ_{rad} governs the radiative capabilities of a QE enhanced by a plasmonic environment, relative to the emission in free space—see Figure 2.1B. Specifically, the γ_{rad} measures the enhancement to the efficiency of a QE in emitting energy to the far-field, when placed at a position $\mathbf{r}'$ near a plasmonic system. For the perfectly spherical NP considered later, the γ_{rad} takes the form of equation (2.86). It is usually calculated by integrating the total energy emitted from the combined QE-nanoantenna system on a putative spherical surface enclosing the whole system, and normalised to the radiated energy of the QE in free space [56].

The radiative emission of a QE via the plasmonic environment is one mechanism through which it can relax from an excited state. Another mechanism, which can be significant in plasmonic systems, measures the rate at which energy is coupled into the non-radiative decay channels of the system—with a corresponding non-radiative decay rate (γ_{nrad}). Depending on the system and its supported channels, the γ_{nrad} encompasses the contributions from the launching of evanescent SPPs and the heating within the metal due to Ohmic losses; this quantity is of less significance for the analysis of the in- and out-coupling rates, but will later offer a few important intricacies. Together these decay

channels form the total decay rate of a QE: $\gamma = \gamma_{rad} + \gamma_{nrad}$, and therefore allows the radiative efficiency (quantum yield) to be defined as: $\eta = \gamma_{rad}/\gamma$.

Through the γ_{exc} and γ_{rad}, one may additionally explore how the placement of a QE in a plasmonic environment alters its spontaneous emission rate (γ_{em}). The enhanced rate at which a QE will fluoresce due to the presence of a nanoantenna is proportional to both the increased rate of photon capture (excitation) and the efficiency with which the QE relaxation leads to radiative emission: $\gamma_{em} = \gamma_{exc}\eta$.

NUMERICAL ANALYSIS

Before moving on, it is worth introducing the techniques used to obtain the numerical results presented throughout this chapter. For the γ_{exc}, a plane wave source is considered to find the component of the electric field that is aligned with the emitter's dipole moment ($\hat{\mu}$), at its position $\mathbf{r}_0$. Inline with the analytics presented in Section 2.2, an x-polarised and z-propagating plane wave is considered. This is schematically shown in Figure 2.2, where the plane wave is injected on the red box surrounding the plasmonic system and is detected at the position shown by the blue circle. The x-component of the electric field is then normalised to the same electric field component when the plasmonic structure is not present, according to equation 2.1.

For the γ_{rad}, a classical dipole source with orientation along $\hat{\mu}$ is implemented at the position $\mathbf{r_0}$—in the same location where the fields are detected when calculating the γ_{exc}. This is numerically implemented using an x-polarised dipole source at the same location

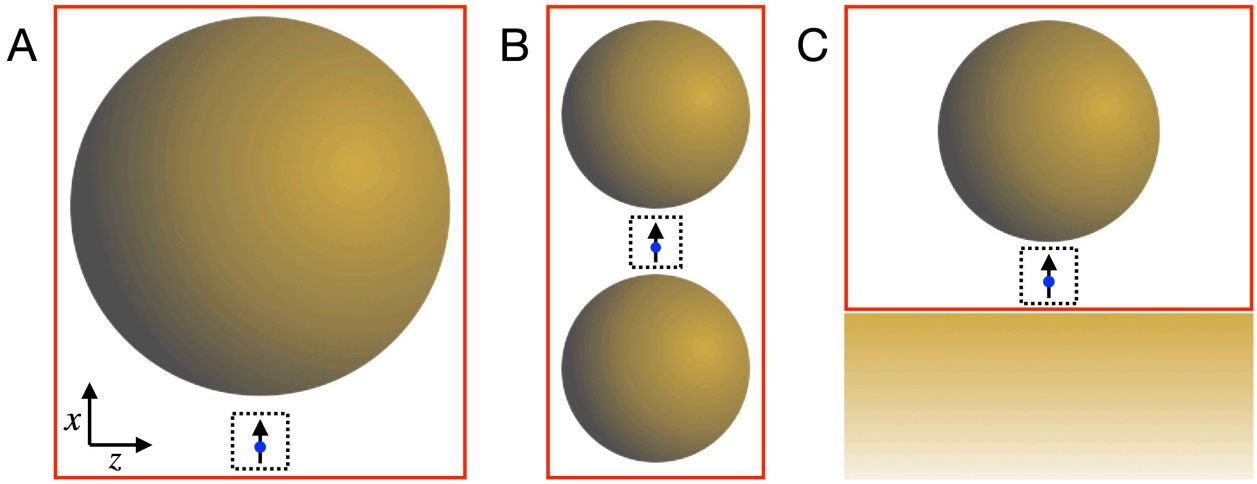

Figure 2.2: Schematics for the numerical implementation of the γ_{exc} and γ_{rad}, for: (A) an isolated spherical NP, (B) a symmetric dimer antenna, and (C) the NPoM geometry.

of the blue circle. The fields may then be directly integrated on the surface of the red box that surrounds the structure, obtaining the rate at which energy passes through it. By measuring γ from the fields directly emitted from the dipole source (the small black dashed box), the γ_{nrad} can also be found from the difference between the total and radiative energy contributions.

2.1.2 REPRESENTATIVE NANOANTENNAS

To motivate the work presented in this chapter on the differing ability of plasmonic systems to facilitate the coupling of energy into and out of nearby emitters, the γ_{exc} and γ_{rad} are considered for three representative plasmonic nanoantennas. These consist of: an isolated NP; a symmetric dimer antenna, consisting of two identical NPs separated by a gap of $d = 1$ nm; and the NPoM geometry, formed of a NP assembled $d = 1$ nm above a flat gold substrate. In each case, the NP's considered are spherical, made of gold, and

have a diameter of 60 nm—with the geometries shown in the insets of Figure 2.3. For consistency, unless otherwise explicitly stated, throughout this chapter the emitter is chosen to be x-polarised—such that the dipole moment is oriented across the cavity—and placed 0.5 nm away from the NP surface, along the positive x-axis: $\{r_p + 0.5 \text{ nm}, 0, 0\}$. Additionally, whenever an external source is present we considered an x-polarised plane wave propagating along the positive z-axis.

The isolated NP in Figure 2.3A demonstrates the expected equal in- and out-coupling rates ($\gamma_{exc} = \gamma_{rad}$)—which are calculated numerically using a FDTD methodol-

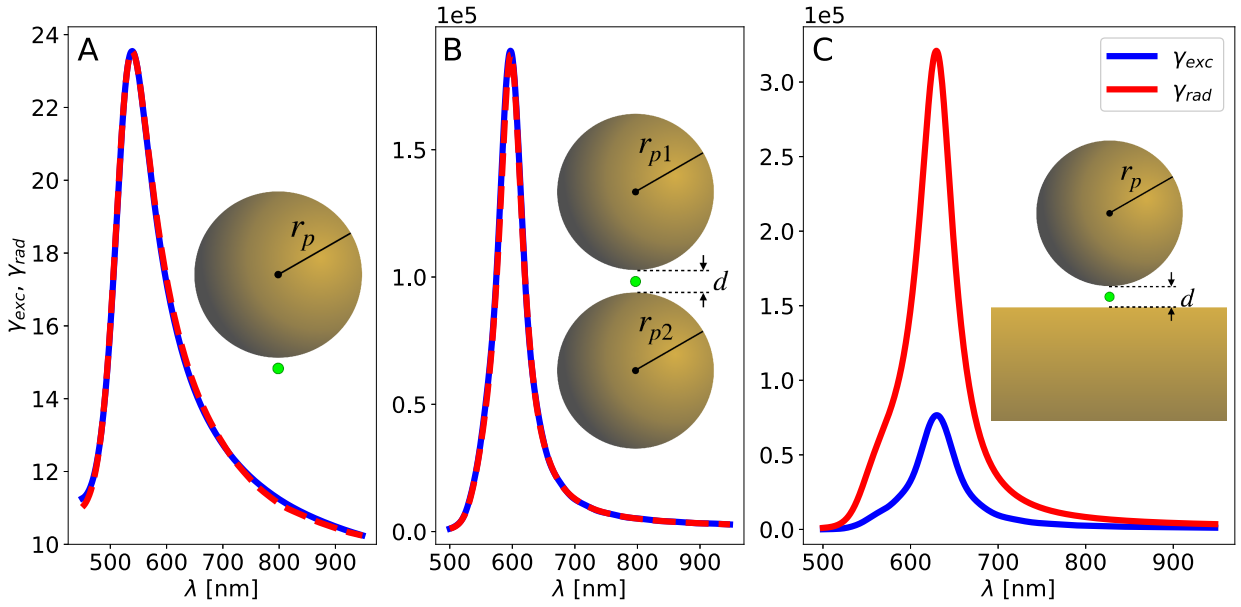

Figure 2.3: The γ_{exc} (blue) and γ_{rad} (red) obtained from FDTD calculations for different nanoplasmonic systems: (A) isolated $2r_p = 60$ nm NP; (B) dimer antenna of $2r_{p1} = 2r_{p2} = 60$ nm NPs with a $d = 1$ nm separation; and (C) NPoM geometry of a $2r_p = 60$ nm NP assembled $d = 1$ nm above a flat gold substrate. The green dot indicates the position of the molecule which: is excited in the γ_{exc} calculation, and is the source when determining the γ_{rad}.

ogy [51]. The symmetric dimer antenna of two such NPs forms a tightly coupled nanocavity, leading to: extreme field enhancements, the hybridisation of the modes from each NP, and a significant red-shifting of the system's plasmonic response. Despite all this, this system retains the equal γ_{exc} and γ_{rad}—as shown in Figure 2.3B.

In comparison to this symmetric dimer antenna, the very similar system of the NPoM geometry—where the lower NP of the dimer is replaced with an infinite substrate—exhibits a completely different behaviour of $\gamma_{exc} \neq \gamma_{rad}$ (see Figure 2.3C). This is surprising as the NPoM is often considered a near-identical system to the symmetric dimer, due to the image charges forming in the metallic substrate. With the γ_{rad} an order of magnitude larger than the γ_{exc}, an emitter in the cavity is therefore able to radiate energy from the system much more efficiently than an external source can couple energy into the emitter. This result is of significant interest in part because of the many similarities the NPoM shares with the symmetric dimer, but largely due to the current popularity of the NPoM configuration throughout the fields of plasmonics and nanophotonics—it is therefore a great motivation to understand where these seemingly non-reciprocal results originate.

Recent literature [10] has revealed how nanoantennas are able to suppress the quenching of emitters placed close to plasmonic structures: the extreme enhancement and confinement in the cavity alters the radiative capabilities of the higher order dark modes. Changing their nature from dark to bright increases their radiative efficiency (γ_{rad}), as evidenced by the 10^4 increase in the γ_{exc} and γ_{rad} of the dimer and NPoM geometries relative to the isolated NP. In comparison, the γ_{nrad} for these systems are shown in Fig-

ure 2.4, in each case revealing a prominent peak at $\lambda = 500$ nm due to the collective response of the higher order modes that are predominantly dark. Additional non-radiative peaks also coincide with the resonances of the in- and out-couple rates. Although the γ_{exc} and γ_{rad} for all these systems increase, they remain lower than the non-radiative contributions; the presence of the nanocavity, however, does increase them relative to the γ_{nrad}, due to the better spatial confinement of the higher order modes within the cavity. The

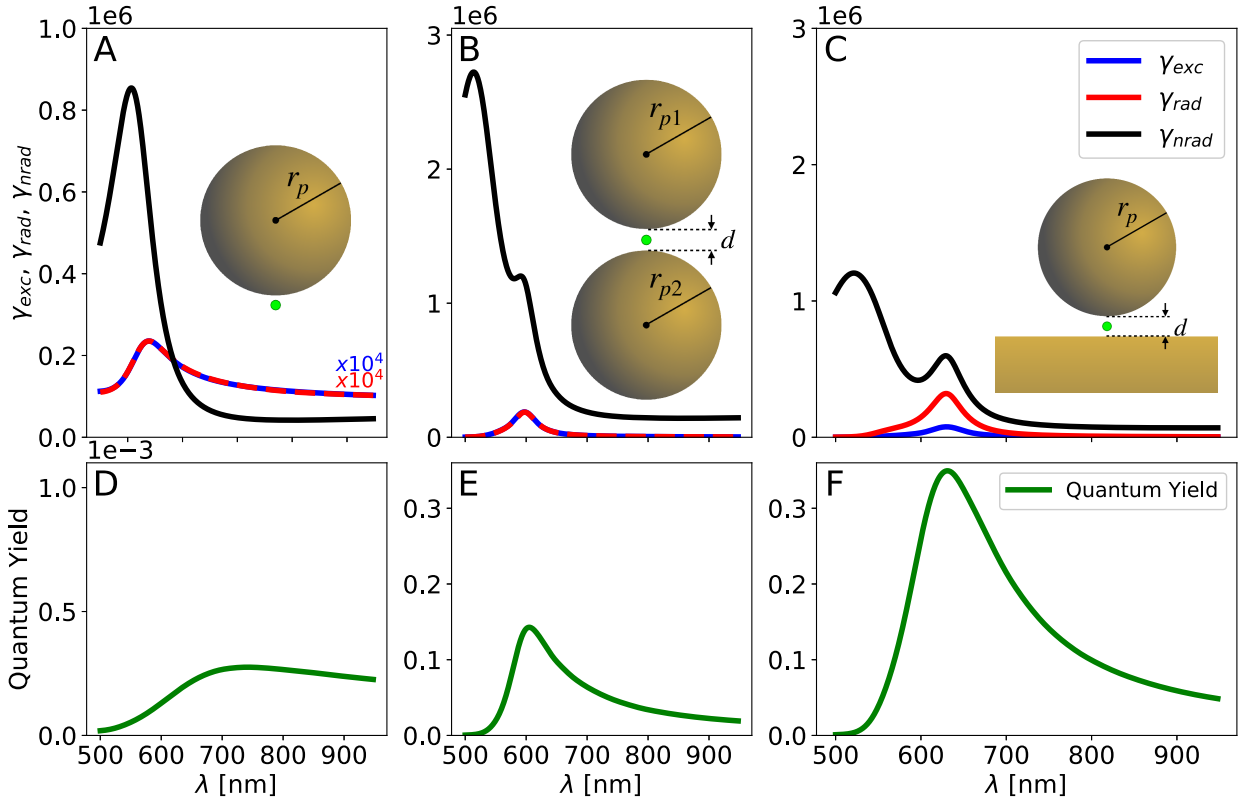

Figure 2.4: Numerical comparison of the γ_{exc} (blue) and γ_{rad} (red) with the γ_{nrad} (black) in different nanoplasmonic systems: (A) isolated 60 nm NP; (B) Dimer of $2r_{p1} = 2r_{p2} = 60$ nm NPs with a $d = 1$ nm separation; and (C) NPoM geometry for a 60 nm NP and a $d = 1$ nm separation. The green dot indicates the position of the molecule which: is excited in the γ_{exc} calculation, and is the source when determining the γ_{rad} and γ_{nrad}. (D)-(F) compare the corresponding quantum yield for the systems in (A)-(C).

increase of the radiative emission rate compared to the total decay rate therefore leads to an increase in the quantum yield, as shown in Figure 2.4D-F.

The differing rates at which energy can be in- and out-coupled from the NPoM geometry has significant ramifications, for example: the realisation of room temperature single molecule strong coupling [4], the applications of SERS in mapping of nanocavity hot-spots [57], and the suppression of quenching [10]. The remainder of this chapter is dedicated to understanding the origin of the NPoM geometry's unequal in- and out-coupling rates, and utilising this to form unique plasmonic nanoantennas with tailored excitational and emissive properties.

2.2 MODE DECOMPOSITION FOR THE EXCITATION AND RADIATIVE DECAY RATES

To gain insight on how the γ_{exc} and γ_{rad} emerge in nanoantenna systems, we employ a Green's function approach to identify the modes supported by isolated metallic NPs—which makes use of a Mie theory based analytical methodology. This is an incredibly powerful tool for describing how homogeneous and isotropic spherical particles scatter EM waves. Mie theory describes spherical NPs made of any general material properties, such as the metallic particles necessary for plasmonics [58]. It is able to reveal the rich multi-modal response of particles through finding exact solutions, and can do so for particles of any size [59]. This methodology offers the invaluable tool of decomposing the

plasmonic response of the system into a set of discrete eigenmodes, and can even do so for more complicated systems where the quasi-static limit is insufficient. Using this model, we derive expressions for the EM fields and obtain analytical descriptions for the γ_{exc} and γ_{rad}; this allows us to—separately for each mode—consider how the plasmonic environment interacts with a molecule, and how the energy is emitted to the far-field.

To obtain the analytical expressions for the γ_{exc} and γ_{rad} of an isolated spherical metallic NP interacting with a molecule, we start by obtaining the inhomogeneous scalar Helmholtz equations (subsection 2.2.1) in order to perform a multipolar decomposition for a dipole source in free space (subsection 2.2.2). We then introduce a spherical NP into the model (subsection 2.2.3) before integrating the radiative energy to obtain the γ_{rad} (subsection 2.2.4), and finally we move the dipole source into the far-field to analytically generate the plane wave source required to obtain the γ_{exc} (subsection 2.2.5).

2.2.1 ELECTROMAGNETIC MODE ANALYSIS

As plasmons originate on metallic structures under the influence of EM fields, Maxwell's equations are the obvious starting point when formulating their description. They will therefore be introduced here, along with the vector and scalar Helmholtz equations, to describe the plasmonic modes of any such system. Our Mie theory based analytical model starts by considering Maxwell's equations [48, 56, 60–70]:

$$\nabla \times \mathbf{E}(\mathbf{r}, t) = -\frac{\partial \mathbf{B}(\mathbf{r}, t)}{\partial t} \tag{2.2}$$

$$\nabla \times \mathbf{H}(\mathbf{r},t) = \mathbf{J}(\mathbf{r},t) + \frac{\partial \mathbf{D}(\mathbf{r},t)}{\partial t} \tag{2.3}$$

$$\nabla \cdot \mathbf{D}(\mathbf{r},t) = \rho \tag{2.4}$$

$$\nabla \cdot \mathbf{B}(\mathbf{r},t) = 0 \ , \tag{2.5}$$

for a source current $\mathbf{J}(\mathbf{r},t)$ and charge density $\rho(\mathbf{r},t)$. By applying the Lorentz gauge: $\nabla \cdot \mathbf{A} + \frac{1}{c_0^2}\frac{d\phi}{dt} = 0$, for a time-harmonic vector potential $\mathbf{A}(\mathbf{r},t)$ and a scalar potential $\phi(\mathbf{r},t)$ in an infinite and homogeneous space, the electric and magnetic fields are respectively given by:

$$\mathbf{E} = -\nabla\phi - \frac{\partial \mathbf{A}}{\partial t} \tag{2.6}$$

$$\mathbf{H} = \frac{1}{\mu_0\mu}\nabla \times \mathbf{A} \ . \tag{2.7}$$

Taking the divergence allows Maxwell's equations to be rewritten in terms of these vector and scalar potentials,

$$\nabla^2\phi - \frac{1}{c_0^2}\frac{\partial^2\phi}{\partial t^2} = -\frac{\rho}{\varepsilon_0\varepsilon} \tag{2.8}$$

$$\nabla^2\mathbf{A} - \frac{1}{c_0^2}\frac{\partial^2\mathbf{A}}{\partial t^2} = -\mu_0\mu\mathbf{J} \ , \tag{2.9}$$

which reduces Maxwell's equations to a set of four scalar differential equations—as the three orthogonal scalar components of the vector potential and source current each satisfy their own respective scalar equation.

For EM waves that follow a time-harmonic oscillation of the form $e^{-i\omega t}$, these scalar

differential equations become:

$$[\nabla^2 + k^2]\phi = -\frac{\rho}{\varepsilon_0 \varepsilon} \tag{2.10}$$

$$[\nabla^2 + k^2]A_i = -\mu_0 \mu J_i \ , \tag{2.11}$$

which all therefore take the same general form of the inhomogeneous scalar Helmholtz equation:

$$[\nabla^2 + k^2]\psi(\mathbf{r}) = -f(\mathbf{r}) \ . \tag{2.12}$$

For the specific case in which no source current is present, both $\mathbf{J}$ and ρ are zero, and equations 2.10 and 2.11 instead take the general form of the homogeneous scalar Helmholtz equation:

$$[\nabla^2 + k^2]\psi(\mathbf{r}) = 0 \ . \tag{2.13}$$

This can be solved by considering a separation of variables into functions that depend solely on r, θ and ϕ [58]:

$$\psi(\mathbf{r}) = R(r)\Theta(\theta)\Phi(\phi) \ . \tag{2.14}$$

By first finding their independent solutions, the full solution to the homogeneous scalar

Helmholtz equation—as outlined in Appendix A1—becomes:

$$\psi(\mathbf{r}) = \sum_{l=0}^{\infty} \sum_{m=-l}^{l} A_{l,m} z_l(kr) Y_l^m(\Omega_r) \ , \tag{2.15}$$

with a summation over both the angular, l, and magnetic, m, quantum numbers—where l is a positive integer, and m takes integer values in the range $-l \leq m \leq l$. Here $A_{l,m}$ is a scalar constant to be determined for the system in question; $z_l(kr)$ are the spherical Bessel functions of either the first (j_l) or second (y_l) kind, or a linear combination of the two (spherical Hankel function); and $Y_l^m(\Omega_r)$ are the spherical Harmonics at the angular position of $\Omega_r = \{\theta_r, \phi_r\}$, given by

$$Y_l^m(\Omega_r) = \sum_{e,o} \sqrt{(2l+1)\frac{(l-m)!}{(l+m)!}}\ P_l^m(\cos\theta_r) \begin{cases} \cos m\phi \\ \\ \sin m\phi \end{cases} \ , \tag{2.16}$$

where $P_l^m(\cos\theta)$ is the associated Legendre polynomial, and the summation accounts for both the even and odd ϕ-responses of the system.

A NOTE ON SPHERICAL BESSEL FUNCTIONS

The spherical Bessel function of the first kind, $j_l(x)$, provides a sinusoidal oscillation with position, x. This has a gradually decreasing peak amplitude with each oscillation, and describes in-going waves. Conversely, the spherical Bessel function of the second kind, $y_l(x)$, describes sinusoidal oscillations that diverge to large negative values close to the origin ($x = 0$).

Finally, the spherical Bessel function of the third kind (spherical Hankel function) is the linear combination of the first and second kinds into a complex function: $h_l^{(1)}(x) = j_l(x) + iy_l(x)$. This complex function retains the sinusoidal oscillations but, depending on the sign, can describe out-going waves. For the modes supported by plasmonic NPs, the spherical Bessel functions supply the radial oscillatory nature.

A NOTE ON SPHERICAL HARMONICS

The spherical harmonics are special functions that excel in solving partial differential equations. They exist on the surface of a sphere and form a complete set of orthogonal functions, capable of expanding any general function on the sphere. For a spherical metallic NP in a uniform background, these spherical harmonics outline the complete multipolar set of orthogonal plasmonic modes [71]. The (l, m)-labelling assigned to each mode describes the number of nodes across the sphere (l), and the number of anti-node pairs along each axis (m) [72]—as shown in Figure 2.5.

VECTOR SPHERICAL HARMONICS

For systems with elements of spherical symmetry, it is instructive to expand the model in terms of vector spherical harmonics (VSHs). For a consistent model with previous analyses, here the general formulation of Mie theory outlined in Bohren [58] and Tai [73] is followed—where the explicit dependence of the scalar functions are retained in the VSHs. The VSHs are constructed from a scalar function (ψ) and an arbitrary constant vector ($\mathbf{r}$):

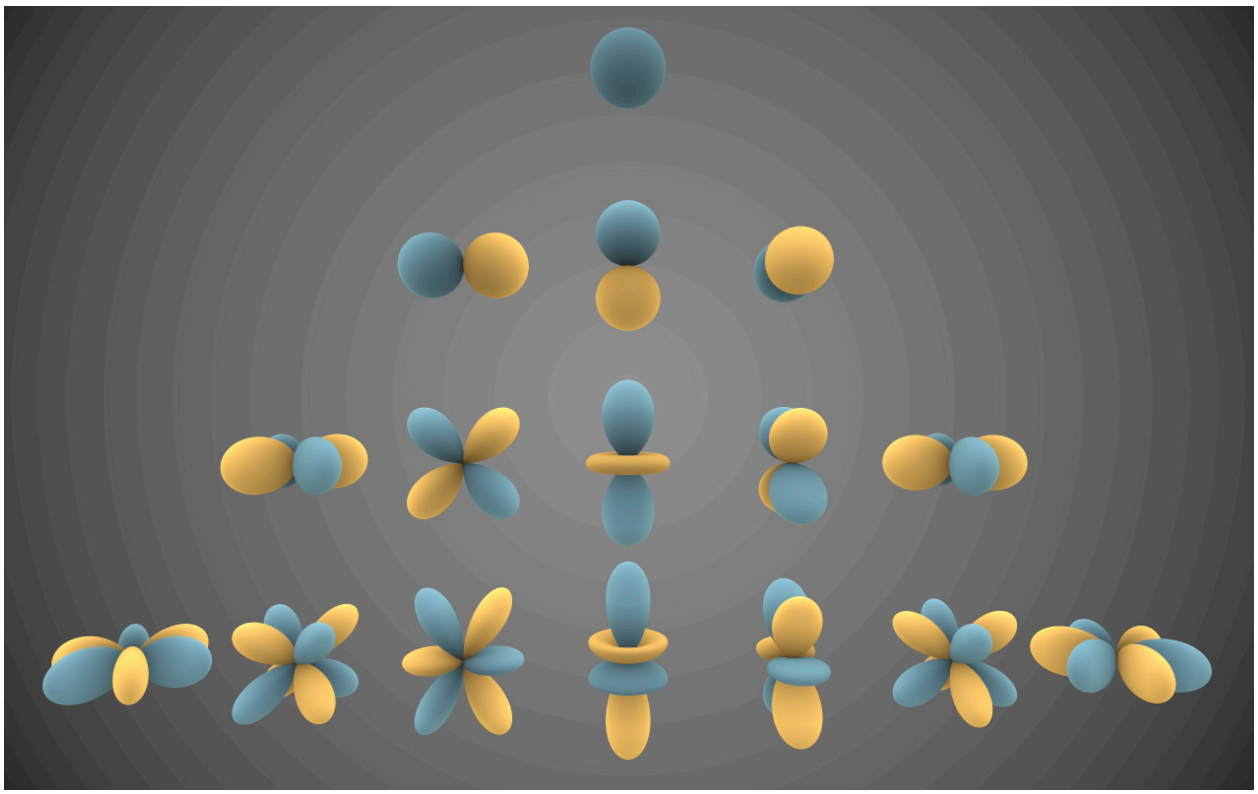

Figure 2.5: Spherical harmonics on the surface of a sphere, for a series of modes describing the number of nodes across the sphere and anti-node pairs along each axis [74].

$$\mathbf{M}_{l,m}(k\mathbf{r}) = \nabla \times (\mathbf{r}\psi) \tag{2.17}$$

$$\mathbf{N}_{l,m}(k\mathbf{r}) = \frac{\nabla \times \mathbf{M}_{l,m}(k\mathbf{r})}{k} \tag{2.18}$$

$$\mathbf{X}_{l,m}(k\mathbf{r}) = \nabla\psi \ . \tag{2.19}$$

Note that for the remainder of the analysis the longitudinal VSH—$\mathbf{X}_{l,m}(k\mathbf{r})$, that generally describes source fields—is ignored. As indicative of all EM fields, these VSHs definitions reveals that they are divergence free, their curls are proportional to each other ($\nabla \times \mathbf{N} = k\mathbf{M}$), and they satisfy the vector Helmholtz equation. Therefore, the scalar function

ψ must satisfy the homogeneous scalar Helmholtz equation: $[\nabla^2 + k^2]\psi = 0$, with the same solution of equation 2.15. Using this solution, the components of the VSHs can be expressed explicitly in terms of their even and odd ϕ-dependence:

$$\mathbf{M}_{l,m}^{e,o}(k\mathbf{r}) = \begin{pmatrix} 0 \\ \frac{m}{\sin\theta} z_l(kr) P_l^m(\cos\theta) \begin{cases} -\sin m\phi \\ \cos m\phi \end{cases} \\ -z_l(kr)\partial_\theta P_l^m(\cos\theta) \begin{cases} \cos m\phi \\ \sin m\phi \end{cases} \end{pmatrix} \tag{2.20}$$

$$\mathbf{N}_{l,m}^{e,o}(k\mathbf{r}) = \frac{1}{kr} \begin{pmatrix} l(l+1) z_l(kr) P_l^m(\cos\theta) \begin{cases} \cos m\phi \\ \sin m\phi \end{cases} \\ [krz_l(kr)]'\partial_\theta P_l^m(\cos\theta) \begin{cases} \cos m\phi \\ \sin m\phi \end{cases} \\ \frac{m}{\sin\theta}[krz_l(kr)]' P_l^m(\cos\theta) \begin{cases} -\sin m\phi \\ \cos m\phi \end{cases} \end{pmatrix}, \tag{2.21}$$

where the partial derivatives are written in the form $\partial_x = \frac{\partial}{\partial x}$, and the prime in the $[krz_l(kr)]'$ terms refer to the differential with respect to the argument of the function—in this case kr.

2.2.2 DIPOLE SOURCE IN FREE SPACE

Following the general formalisms of Low [60], Bohren [58] and Tai [73], the EM fields from a dipole source in free space appear naturally from the solutions of the inhomogeneous scalar Helmholtz equation. A useful alternative formulation to equation 2.12 sees the inhomogeneous scalar Helmholtz equation expressed in terms of Green's functions, for a current source $\mathbf{J}$ at position $\mathbf{r}'$:

$$[\nabla^2 + k^2]G(\mathbf{r}, \mathbf{r}') = -\delta(\mathbf{r} - \mathbf{r}') \ , \tag{2.22}$$

where $\delta(\mathbf{r} - \mathbf{r}')$ is the Dirac delta function at the position of the source current. This gives the solution for the electric vector potential ($\mathbf{A}$) as:

$$A_i(\mathbf{r}) = -\mu_0 \int G(\mathbf{r}, \mathbf{r}')J_i(\mathbf{r}')d\mathbf{r}' \ . \tag{2.23}$$

By applying the Lorentz gauge: $\nabla \cdot \mathbf{A} + \frac{1}{c_0^2}\frac{d\phi}{dt} = 0$, the electric field's dependence on the scalar potential (ϕ) is removed, and it can be expressed solely in terms of the vector potential, as:

$$\mathbf{E}(\mathbf{r}) = i\omega\Big(1 + \frac{1}{k^2}\nabla\nabla\cdot\Big)\mathbf{A}(\mathbf{r}) \ . \tag{2.24}$$

The substitution of the vector potential into the electric field definition allows the Green's function components to be expressed as:

$$\mathbf{G}_i(\mathbf{r},\mathbf{r}') = \Big(1 + \frac{1}{k^2}\nabla\nabla\cdot\Big)G_0(\mathbf{r},\mathbf{r}')\hat{\mathbf{e}}_i \ , \tag{2.25}$$

which—when using the vector identity: $\nabla\cdot\left[G_0(\mathbf{r},\mathbf{r}')\overleftrightarrow{\mathbf{I}}\right] = \nabla G_0(\mathbf{r},\mathbf{r}')$, where $\overleftrightarrow{\mathbf{I}}$ is unit dyadic tensor—defines all Green's function components in one dyadic Green's function tensor:

$$\overleftrightarrow{\mathbf{G}}(\mathbf{r},\mathbf{r}') = \Big[\overleftrightarrow{\mathbf{I}} + \frac{1}{k^2}\nabla\nabla\cdot\Big]G_0(\mathbf{r},\mathbf{r}') \ . \tag{2.26}$$

For a singular dipole with a source current of $\mathbf{J}(\mathbf{r}') = -i\omega\mathbf{p}(\mathbf{r}')\delta(\mathbf{r}-\mathbf{r}')$ placed at $\mathbf{r}'$—where the dipole moment is given by $\mathbf{p}(\mathbf{r}') = qr'\hat{\mathbf{e}}_i$, for a dipole charge q—the electric and magnetic fields are expressed in terms of the dyadic Green's function tensor:

$$\mathbf{E} = \omega^2\mu_0\overleftrightarrow{\mathbf{G}}(\mathbf{r},\mathbf{r}')\cdot\mathbf{p}(\mathbf{r}') \tag{2.27}$$

$$\mathbf{H} = -i\omega\Big[\nabla\times\overleftrightarrow{\mathbf{G}}(\mathbf{r},\mathbf{r}')\Big]\cdot\mathbf{p}(\mathbf{r}') \ . \tag{2.28}$$

Note that for a multi-emitter system of N-dipoles, the source current can easily be generalised by introducing the relevant summation: $\mathbf{J}(\mathbf{r}') = -i\omega\sum_n \mathbf{p}_n(\mathbf{r}')\delta(\mathbf{r}-\mathbf{r}'_n)$.

Through the use of the Ohm-Rayleigh method [73], the dyadic Green's function tensor of equation 2.26 can be expressed in terms of the VSHs $\mathbf{M}_{l,m}$ and $\mathbf{N}_{l,m}$. From the matrix form of the wave equation:

$$\nabla \times \nabla \times \overleftrightarrow{G}(\mathbf{r}, \mathbf{r}') - k^2 \overleftrightarrow{G}(\mathbf{r}, \mathbf{r}') = \overleftrightarrow{I}\delta(\mathbf{r} - \mathbf{r}') \ , \tag{2.29}$$

along with the unit dyadic tensor identity—for constants $A_{l,m}$ and $B_{l,m}$:

$$\nabla \times \left[\overleftrightarrow{I}\delta(\mathbf{r} - \mathbf{r}')\right] = \int_0^\infty d\kappa \sum_{l,m} \left[\mathbf{N}^{e,o}_{l,m}(\kappa) \otimes \mathbf{A}^{e,o}_{l,m} + \mathbf{M}^{e,o}_{l,m}(\kappa) \otimes \mathbf{B}^{e,o}_{l,m}\right] \tag{2.30}$$

$$= \int_0^\infty d\kappa \sum_{l,m} \left[A_{l,m}\mathbf{N}^{e,o}_{l,m}(\kappa) \otimes \mathbf{M}^{e,o}_{l,m}(\kappa') + B_{l,m}\mathbf{M}^{e,o}_{l,m}(\kappa) \otimes \mathbf{N}^{e,o}_{l,m}(\kappa')\right] \ , \tag{2.31}$$

the Green's Dyadic tensor becomes:

$$\overleftrightarrow{\mathbf{G}}(\mathbf{r}, \mathbf{r}') = C_{l,m} \begin{cases} \mathbf{M}^{e,o\ (3)}_{l,m}(k\mathbf{r}) \otimes \mathbf{M}^{e,o\ (1)}_{l,m}(k\mathbf{r}') + \mathbf{N}^{e,o\ (3)}_{l,m}(k\mathbf{r}) \otimes \mathbf{N}^{e,o\ (1)}_{l,m}(k\mathbf{r}') & r > r' \\ \mathbf{M}^{e,o\ (1)}_{l,m}(k\mathbf{r}) \otimes \mathbf{M}^{e,o\ (3)}_{l,m}(k\mathbf{r}') + \mathbf{N}^{e,o\ (1)}_{l,m}(k\mathbf{r}) \otimes \mathbf{N}^{e,o\ (3)}_{l,m}(k\mathbf{r}') & r < r' \end{cases} \ , \tag{2.32}$$

where $C_{l,m} = \frac{ik}{4\pi}(2 - \delta_0)\frac{2l+1}{l(l+1)}\frac{(l-m)!}{(l+m)!}$. See Appendix A2 where we used the Ohm-Rayleigh methodology and orthogonality conditions to find $C_{l,m}$.

Note that the $\mathbf{r}'$-dependence of the dipole moment means the dot product only applies to the VSHs that share this dependence. These terms result in scalar quantities, which can be tidied away via the introduction of the following notation:

$$s_{l,m}^{e,o\ (i)} = \left(\mathbf{M}_{l,m}^{e,o\ (i)}(k\mathbf{r}') \cdot \mathbf{p}(\mathbf{r}')\right) \tag{2.33}$$

$$t_{l,m}^{e,o\ (i)} = \left(\mathbf{N}_{l,m}^{e,o\ (i)}(k\mathbf{r}') \cdot \mathbf{p}(\mathbf{r}')\right) \ . \tag{2.34}$$

So, the electric and magnetic fields at position $\mathbf{r}$ due to a dipole source in free space at $\mathbf{r}'$ are decomposed into a set of modes, and expressed in terms of the VSHs as:

$$\mathbf{E}(\mathbf{r}) = \omega^2 \mu_0 C_{l,m} \sum_{e,o} \begin{cases} s_{l,m}^{e,o\ (1)} \mathbf{M}_{l,m}^{e,o\ (3)}(k\mathbf{r}) + t_{l,m}^{e,o\ (1)} \mathbf{N}_{l,m}^{e,o\ (3)}(k\mathbf{r}) & r > r' \\ s_{l,m}^{e,o\ (3)} \mathbf{M}_{l,m}^{e,o\ (1)}(k\mathbf{r}) + t_{l,m}^{e,o\ (3)} \mathbf{N}_{l,m}^{e,o\ (1)}(k\mathbf{r}) & r < r' \end{cases} \tag{2.35}$$

$$\mathbf{H}(\mathbf{r}) = -i\omega k C_{l,m} \sum_{e,o} \begin{cases} s_{l,m}^{e,o\ (1)} \mathbf{N}_{l,m}^{e,o\ (3)}(k\mathbf{r}) + t_{l,m}^{e,o\ (1)} \mathbf{M}_{l,m}^{e,o\ (3)}(k\mathbf{r}) & r > r' \\ s_{l,m}^{e,o\ (3)} \mathbf{N}_{l,m}^{e,o\ (1)}(k\mathbf{r}) + t_{l,m}^{e,o\ (3)} \mathbf{M}_{l,m}^{e,o\ (1)}(k\mathbf{r}) & r < r' \end{cases} \ . \tag{2.36}$$

Here the first and second terms represent the magnetic (TM) and electric (TE) modes, respectively. As the multipolar nature of the methodology emerges from the solutions of the Helmholtz equation, it applies throughout the description of the EM fields, and propagates through to the expressions for the γ_{exc} and γ_{rad}.

2.2.3 SPHERICAL ISOLATED NANOPARTICLE

To extend the above formulation to describe a free-space dipole source placed in the vicinity of a spherical metallic NP, the incident, internal and scattered components of the

EM fields are expressed in a similar formalism as equations 2.35 and 2.36. The boundary conditions are then applied, which define the field continuities at the surface of the NP.

The permeabilities (which enter through the electric field) and refractive indices (which directly modify the VSHs) are first generalised for the homogeneous medium surrounding the NP $\{\mu_1, n_1\}$ and the NP itself $\{\mu_2, n_2\}$, respectively—where the refractive index of the NP is introduced relative to the index of the background medium, as $N = n_2/n_1$.

The dyadic Green's function solution for a free space dipole source (of equation 2.32) now becomes the incident component of the total dyadic, with the internal and scattered components taking the same general form—with a set of l-dependent coefficients: $a_l,\ b_l,\ c_l$ and d_l, that are defined by the boundary conditions. As both parts of the Green's dyadic piecewise function have the same dependence on the VSHs, the incident, scattered and internal dyadic Green's function components are considered—without loss of generality—in the region of $r < r'$ only:

$$\overleftrightarrow{\mathbf{G}}_{inc}(\mathbf{r}, \mathbf{r}') = C_{lm}\left[\mathbf{M}^{(1)}_{l,m}(k\mathbf{r}) \otimes \mathbf{M}^{(3)}_{l,m}(k\mathbf{r}') + \mathbf{N}^{(1)}_{l,m}(k\mathbf{r}) \otimes \mathbf{N}^{(3)}_{l,m}(k\mathbf{r}')\right] \tag{2.37}$$

$$\overleftrightarrow{\mathbf{G}}_{scat}(\mathbf{r}, \mathbf{r}') = C_{lm}\left[a_l\mathbf{M}^{(3)}_{l,m}(k\mathbf{r}) \otimes \mathbf{M}^{(3)}_{l,m}(k\mathbf{r}') + b_l\mathbf{N}^{(3)}_{l,m}(k\mathbf{r}) \otimes \mathbf{N}^{(3)}_{l,m}(k\mathbf{r}')\right] \tag{2.38}$$

$$\overleftrightarrow{\mathbf{G}}_{int}(\mathbf{r}, \mathbf{r}') = C_{lm}\left[c_l\mathbf{M}^{(1)}_{l,m}(Nk\mathbf{r}) \otimes \mathbf{M}^{(3)}_{l,m}(k\mathbf{r}') + d_l\mathbf{N}^{(1)}_{l,m}(Nk\mathbf{r}) \otimes \mathbf{N}^{(3)}_{l,m}(k\mathbf{r}')\right]. \tag{2.39}$$

The internal component retains the radial dependence of the incident component—the spherical Bessel function, due to its in-going nature—but adopts the wavevector associated with the NP's material with respect to the surrounding material: replacing k with Nk. A pair of l-dependent absorption coefficients (c_l and d_l) are introduced, one for each

term. Conversely, the scattered component retains the same wavevector (k), but adopts a spherical Hankel function radial dependence of the radiative fields due to the out-going nature—as indicated by the superscript $^{(3)}$. Here the scattering coefficients (a_l and b_l) are introduced. Note that these changes only affect the VSHs with the radial dependence $\mathbf{r}$, and those that are instead functions of $\mathbf{r}'$ are unchanged as the dipole location is always outside of the NP.

Due to the non-vacuum surroundings, the relation between the electric field and the dyadic Green's function (see equation 2.27) must be generalised to account for the material permeability:

$$\mathbf{E} = \omega^2 \mu_0 \mu \overleftrightarrow{\mathbf{G}}(\mathbf{r}, \mathbf{r}') \cdot \mathbf{p}(\mathbf{r}') \ . \tag{2.40}$$

Therefore, the incident, scattered and internal components of the multipolar electric field are given by:

$$\mathbf{E}_{inc} = \omega^2 \mu_0 \mu_1 C_{lm} \Big[s_{l,m}^{(3)} \mathbf{M}_{l,m}^{(1)}(k\mathbf{r}) + t_{l,m}^{(3)} \mathbf{N}_{l,m}^{(1)}(k\mathbf{r}) \Big] \tag{2.41}$$

$$\mathbf{E}_{scat} = \omega^2 \mu_0 \mu_1 C_{lm} \Big[a_l s_{l,m}^{(3)} \mathbf{M}_{l,m}^{(3)}(k\mathbf{r}) + b_l t_{l,m}^{(3)} \mathbf{N}_{l,m}^{(3)}(k\mathbf{r}) \Big] \tag{2.42}$$

$$\mathbf{E}_{int} = \omega^2 \mu_0 \mu_2 C_{lm} \Big[c_l s_{l,m}^{(3)} \mathbf{M}_{l,m}^{(1)}(Nk\mathbf{r}) + d_l t_{l,m}^{(3)} \mathbf{N}_{l,m}^{(1)}(Nk\mathbf{r}) \Big] \ , \tag{2.43}$$

with similar relations for the magnetic field originating from $\mathbf{H} = -i\omega \Big[\nabla \times \overleftrightarrow{\mathbf{G}}(\mathbf{r}, \mathbf{r}') \Big] \cdot \mathbf{p}(\mathbf{r}')$.

To complete these equations, the four l-dependent coefficients ($a_l,\ b_l,\ c_l$ and d_l) must be identified. This requires solving for the boundary conditions to enforce a continu-

ity of the tangential field components across the surface of the NP—where $r = r_p$—which are given by:

$$(\mathbf{E}_{inc} + \mathbf{E}_{scat} - \mathbf{E}_{int})\,|_{r=r_p} \times \hat{\mathbf{e}}_r = 0 \tag{2.44}$$

$$(\mathbf{H}_{inc} + \mathbf{H}_{scat} - \mathbf{H}_{int})\,|_{r=r_p} \times \hat{\mathbf{e}}_r = 0\ . \tag{2.45}$$

By separately considering the θ and ϕ components of the electric and magnetic boundary conditions, they lead to a set of four unique simultaneous equations:

$$\mu_1 j_l(kr_p) + \mu_1 a_l h_l^{(1)}(kr_p) = \mu_2 c_l j_l(Nkr_p) \tag{2.46}$$

$$\mu_1 N[kr_p j_l(kr_p)]' + \mu_1 b_l N[kr_p h_l^{(1)}(kr_p)]' = \mu_2 d_l[Nkr_p j_l(Nkr_p)]' \tag{2.47}$$

$$[kr_p j_l(kr_p)]' + a_l[kr_p h_l^{(1)}(kr_p)]' = c_l[Nkr_p j_l(Nkr_p)]' \tag{2.48}$$

$$j_l(kr_p) + b_l h_l^{(1)}(kr_p) = d_l N j_l(Nkr_p)\ . \tag{2.49}$$

Solving the above system of equations, the four coefficients are obtained:

$$a_l = \frac{\mu_2 j_l(Nkr_p)[kr_p j_l(kr_p)]' - \mu_1 j_l(kr_p)[Nkr_p j_l(Nkr_p)]'}{\mu_1 h_l^{(1)}(kr_p)[Nkr_p j_l(Nkr_p)]' - \mu_2 j_l(Nkr_p)[kr_p h_l^{(1)}(kr_p)]'} \tag{2.50}$$

$$b_l = \frac{\mu_1 N^2 j_l(Nkr_p)[kr_p j_l(kr_p)]' - \mu_2 j_l(kr_p)[Nkr_p j_l(Nkr_p)]'}{\mu_2 h_l^{(1)}(kr_p)[Nkr_p j_l(Nkr_p)]' - \mu_1 N^2 j_l(Nkr_p)[kr_p h_l^{(1)}(kr_p)]'} \tag{2.51}$$

$$c_l = \frac{\mu_1 j_l(kr_p)[kr_p h_l^{(1)}(kr_p)]' - \mu_1 h_l^{(1)}(kr_p)[kr_p j_l(kr_p)]'}{\mu_2 j_l(Nkr_p)[kr_p h_l^{(1)}(kr_p)]' - \mu_1 h_l^{(1)}(kr_p)[Nkr_p j_l(Nkr_p)]'} \tag{2.52}$$

$$d_l = \frac{\mu_1 N j_l(kr_p)[kr_p h_l^{(1)}(kr_p)]' - \mu_1 N h_l^{(1)}(kr_p)[kr_p j_l(kr_p)]'}{\mu_1 N^2 j_l(Nkr_p)[kr_p h_l^{(1)}(kr_p)]' - \mu_2 h_l^{(1)}(kr_p)[Nkr_p j_l(Nkr_p)]'}\ . \tag{2.53}$$

With these coefficients, the analytical model decomposes the modal plasmonic response of an isolated NP due to a classical dipole source excitation. For a more detailed explanation of the origin of these expressions, please refer to Appendix A3.

2.2.4 RADIATIVE DECAY RATE

With the modal expansion for the electric and magnetic fields in and around an isolated NP, the interaction with a dipole source excitation has been detailed. This model is now used to determine the rate at which energy is radiated from the system to the far-field (γ_{rad}), for a emitter placed at $\mathbf{r}'$. This is achieved by considering the rate at which energy crosses a putative sphere of radius $R = 1$m (such that $R \gg r'$) that surrounds the structure (isolated spherical NP), and is expressed by [75]:

$$W_{total} = \int \mathbf{S}_{total}(\mathbf{r}) \cdot \hat{\mathbf{n}} dA \ , \tag{2.54}$$

where $\mathbf{S}_{total}(\mathbf{r}) = \frac{1}{2}\text{Re}\left[\mathbf{E}_{total}(\mathbf{r}) \times \mathbf{H}^*_{total}(\mathbf{r})\right]$ is the Poynting vector at location $\mathbf{r}$, and $\hat{\mathbf{n}}$ is the unit vector normal to the surface of the putative sphere enclosed by dA. Since only the normal component of the Poynting vector reaches the far field, we are left with $\mathbf{S}_{total}(\mathbf{r}) \cdot \hat{\mathbf{n}} = \frac{1}{2}\text{Re}\left[E^{\theta}_{total} H^{\phi *}_{total} - E^{\phi}_{total} H^{\theta *}_{total}\right]$. The total fields are the summation of the incident and scattered fields (for a dipole source), as both lead to the emission of radiation away from the system: $\mathbf{E}_{total} = \mathbf{E}_{inc} + \mathbf{E}_{scat}$.

By grouping the relevant terms, this can be separated into three separate Poynting

vector components:

$$\mathbf{S}_{total}(\mathbf{r}) \cdot \hat{\mathbf{n}} = \mathbf{S}_{inc}(\mathbf{r}) \cdot \hat{\mathbf{n}} + \mathbf{S}_{scat}(\mathbf{r}) \cdot \hat{\mathbf{n}} + \mathbf{S}_{ext}(\mathbf{r}) \cdot \hat{\mathbf{n}} \ , \tag{2.55}$$

which respectively correspond to the incident, scattered and extinction contributions:

$$\mathbf{S}_{inc}(\mathbf{r}) \cdot \hat{\mathbf{n}} = \frac{1}{2}\mathrm{Re}\left[\mathbf{E}_{inc}(\mathbf{r}) \times \mathbf{H}^*_{inc}(\mathbf{r})\right] \cdot \hat{\mathbf{n}} \tag{2.56}$$

$$\mathbf{S}_{scat}(\mathbf{r}) \cdot \hat{\mathbf{n}} = \frac{1}{2}\mathrm{Re}\left[\mathbf{E}_{scat}(\mathbf{r}) \times \mathbf{H}^*_{scat}(\mathbf{r})\right] \cdot \hat{\mathbf{n}} \tag{2.57}$$

$$\mathbf{S}_{ext}(\mathbf{r}) \cdot \hat{\mathbf{n}} = \frac{1}{2}\mathrm{Re}\left[\mathbf{E}_{inc}(\mathbf{r}) \times \mathbf{H}^*_{scat}(\mathbf{r}) + \mathbf{E}_{scat}(\mathbf{r}) \times \mathbf{H}^*_{inc}(\mathbf{r})\right] \cdot \hat{\mathbf{n}} \ . \tag{2.58}$$

The total rate at which energy passes through the putative sphere can therefore also be divided into three terms:

$$W_{total} = W_{inc} + W_{scat} - W_{ext} \ , \tag{2.59}$$

where:

$$W_{inc} = \int \mathbf{S}_{inc}(\mathbf{r}) \cdot \hat{\mathbf{n}} dA \tag{2.60}$$

$$W_{scat} = \int \mathbf{S}_{scat}(\mathbf{r}) \cdot \hat{\mathbf{n}} dA \tag{2.61}$$

$$W_{ext} = -\int \mathbf{S}_{ext}(\mathbf{r}) \cdot \hat{\mathbf{n}} dA \ , \tag{2.62}$$

and each term discussed in detail below. Note the that minus sign in front of W_{ext} appears purely due to convention.

INCIDENT ENERGY

The incident field contribution to the total energy decay rate is considered first:

$$W_{inc} = \int \mathbf{S}_{inc}(\mathbf{r}) \cdot \hat{\mathbf{n}} dA \ , \tag{2.63}$$

where $\mathbf{S}_{inc}(\mathbf{r})$ is the incident Poynting vector, given by

$$\mathbf{S}_{inc}(\mathbf{r}) \cdot \hat{\mathbf{n}} = \frac{1}{2}\text{Re}\left[\mathbf{E}_{inc}(\mathbf{r}) \times \mathbf{H}^*_{inc}(\mathbf{r})\right] \cdot \hat{\mathbf{n}} \tag{2.64}$$

$$= \frac{1}{2}\text{Re}\left[E^{\theta}_{inc} H^{\phi *}_{inc} - E^{\phi}_{inc} H^{\theta *}_{inc}\right] \ . \tag{2.65}$$

As this only considers the incident field which leads to direct emission to the far field—reaching the putative sphere at $R = 1$m—only the $r > r'$ piece of the field equations are required, which gives the following reduced field components from equations 2.35 and 2.36:

$$E^{\theta}_{inc} = C_{lm} \sum_{e,o} \left[s^{e,o\ (1)}_{l,m} \mathbf{M}^{e,o\ (3)}_{l,m\ \theta}(k\mathbf{r}) + t^{e,o\ (1)}_{l,m} \mathbf{N}^{e,o\ (3)}_{l,m\ \theta}(k\mathbf{r}) \right] \tag{2.66}$$

$$E^{\phi}_{inc} = C_{lm} \sum_{e,o} \left[s^{e,o\ (1)}_{l,m} \mathbf{M}^{e,o\ (3)}_{l,m\ \phi}(k\mathbf{r}) + t^{e,o\ (1)}_{l,m} \mathbf{N}^{e,o\ (3)}_{l,m\ \phi}(k\mathbf{r}) \right] \tag{2.67}$$

$$H^{\theta *}_{inc} = \frac{k}{i\omega\mu_1\mu_0} C^*_{lm} \sum_{e,o} \left[s^{e,o\ (1)*}_{l,m} \mathbf{N}^{e,o\ (3)*}_{l,m\ \theta}(k\mathbf{r}) + t^{e,o\ (1)*}_{l,m} \mathbf{M}^{e,o\ (3)*}_{l,m\ \theta}(k\mathbf{r}) \right] \tag{2.68}$$

$$H^{\phi *}_{inc} = \frac{k}{i\omega\mu_1\mu_0} C^*_{lm} \sum_{e,o} \left[s^{e,o\ (1)*}_{l,m} \mathbf{N}^{e,o\ (3)*}_{l,m\ \phi}(k\mathbf{r}) + t^{e,o\ (1)*}_{l,m} \mathbf{M}^{e,o\ (3)*}_{l,m\ \phi}(k\mathbf{r}) \right] . \tag{2.69}$$

After a fair amount of algebra in expanding out the VSHs and the even/odd components of the spherical harmonics—see Appendix A4 for more details, and to highlight some of the intricacies here—the term $(\mathbf{E}_{inc}(\mathbf{r}) \times \mathbf{H}^*_{inc}(\mathbf{r})) \cdot \hat{\mathbf{n}}$ simplifies to:

$$E^{\theta}_{inc}H^{\phi *}_{inc} - E^{\phi}_{inc}H^{\theta *}_{inc} = \frac{1}{ir\omega\mu_1\mu_0}|C_{l,m}|^2 \left[\left(\frac{mP^m_l(\cos\theta)}{\sin\theta}\right)^2 + (\partial_\theta P^m_l(\cos\theta))^2\right] \tag{2.70}$$
$$\times \sum_{e,o}\left[|s^{e,o\ (1)}_{l,m}|^2 h^{(1)}_l(kr)[krh^{(1)*}_l(kr)]' - |t^{e,o\ (1)}_{l,m}|^2 h^{(1)*}_l(kr)[krh^{(1)}_l(kr)]'\right] .$$

Then, the incident energy decay rate can be obtained by integrating over the putative sphere enclosing the system:

$$W_{inc} = \frac{1}{2}\mathrm{Re}\left[\int_0^{2\pi}\int_0^{\pi}\left(E^{\theta}_{inc}H^{\phi *}_{inc} - E^{\phi}_{inc}H^{\theta *}_{inc}\right) r^2\sin\theta d\theta d\phi\right] . \tag{2.71}$$

The above double integral simplified since several standard integrals of the associated Legendre polynomials emerge [59]. A similar simplification of the spherical Bessel function terms is required, and with the use of the Wronskian: $j_l(x)y'_l(x) - j'_l(x)y_l(x) = -\frac{1}{x^2}$, the incident energy from a source at $\mathbf{r}'$ crossing a putative sphere enclosing the system is given by:

$$W_{inc} = \frac{k}{16\pi\omega\mu_1\mu_0}(2-\delta_0)^2\frac{2l+1}{l(l+1)}\frac{(l-m)!}{(l+m)!}\sum_{e,o}\left[|s^{e,o\ (1)}_{l,m}|^2 + |t^{e,o\ (1)}_{l,m}|^2\right] , \tag{2.72}$$

where $\delta_0 = 1$ when $m = 0$, and zero otherwise. Conversely, if the dipole source is outside the putative sphere (in the regime $r < r'$), the incident contribution to the decay rate is zero.

SCATTERED ENERGY

While the analytics above finds the energy reaching the putative sphere directly from the source, one must also account for the energy scattered by the NP, which is given by:

$$W_{scat} = \int \mathbf{S}_{scat}(\mathbf{r}) \cdot \hat{\mathbf{n}} dA \ , \tag{2.73}$$

where $\hat{\mathbf{n}}$ is the unit vector normal to the sphere, and $\mathbf{S}_{scat}(\mathbf{r})$ is the scattered Poynting vector—given by:

$$\mathbf{S}_{scat}(\mathbf{r}) \cdot \hat{\mathbf{n}} = \frac{1}{2}\text{Re}\left[\mathbf{E}_{scat}(\mathbf{r}) \times \mathbf{H}^*_{scat}(\mathbf{r})\right] \cdot \hat{\mathbf{n}} \tag{2.74}$$

$$= \frac{1}{2}\text{Re}\left[E^{\theta}_{scat} H^{\phi *}_{scat} - E^{\phi}_{scat} H^{\theta *}_{scat}\right] \ . \tag{2.75}$$

Conversely to the case of the incident energy decay rate, the scattered field contributions only require the $r < r'$ portion of the EM field equations. Due to the symmetry of the dyadic Green's function about r', the scattered Poynting vector shares an identical form as for the incident fields, with the singular exchange of:

$$s^{e,o\ (1)}_{l,m} \longrightarrow u^{e,o\ (3)}_{l,m} = a_l \left(\mathbf{M}^{e,o\ (3)}_{l,m}(k\mathbf{r}') \cdot \mathbf{p}(\mathbf{r}')\right) \tag{2.76}$$

$$t^{e,o\ (1)}_{l,m} \longrightarrow v^{e,o\ (3)}_{l,m} = b_l \left(\mathbf{N}^{e,o\ (3)}_{l,m}(k\mathbf{r}') \cdot \mathbf{p}(\mathbf{r}')\right) \ , \tag{2.77}$$

also noting the change of the radial dependence to the spherical Hankel function.

By inspection, the scattered energy contribution to the total decay rate is given by:

$$W_{scat} = \frac{k}{16\pi\omega\mu_1\mu_0}(2-\delta_0)^2\frac{2l+1}{l(l+1)}\frac{(l-m)!}{(l+m)!}\sum_{e,o}\left[|u_{l,m}^{e,o\ (3)}|^2 + |v_{l,m}^{e,o\ (3)}|^2\right] . \tag{2.78}$$

EXTINCTION ENERGY

The remaining cross-terms between the incident and scattered field in the Poynting vector are grouped together and coined as the extinction contribution to the total radiative decay rate. As before, the same procedure is roughly followed, but now for the more complicated case of the extinction contribution to the decay rate—which considers:

$$W_{ext} = -\int \mathbf{S}_{ext}(\mathbf{r})\cdot\hat{\mathbf{n}}dA\ , \tag{2.79}$$

where $\mathbf{S}_{ext}(\mathbf{r})$ is the extinction Poynting vector, given by:

$$\mathbf{S}_{ext}(\mathbf{r})\cdot\hat{\mathbf{n}} = \frac{1}{2}\mathsf{Re}\left[\mathbf{E}_{inc}(\mathbf{r})\times\mathbf{H}^*_{scat}(\mathbf{r}) + \mathbf{E}_{scat}(\mathbf{r})\times\mathbf{H}^*_{inc}(\mathbf{r})\right]\cdot\hat{\mathbf{n}} \tag{2.80}$$

$$= \frac{1}{2}\mathsf{Re}\left[E^{\theta}_{inc}H^{\phi *}_{scat} - E^{\phi}_{inc}H^{\theta *}_{scat} + E^{\theta}_{scat}H^{\phi *}_{inc} - E^{\phi}_{scat}H^{\theta *}_{inc}\right] . \tag{2.81}$$

After substituting in the VSHs components, and explicitly considering the even and odd components of the spherical harmonics, equation 2.81 simplifies to:

$$\mathbf{S}_{ext}(\mathbf{r})\cdot\hat{\mathbf{n}} = \frac{1}{2}\mathsf{Re}\left[\frac{1}{ir\omega\mu_1\mu_0}|C_{l,m}|^2\left\{\left(\frac{mP_l^m(\cos\theta)}{\sin\theta}\right)^2 + \left(\partial_\theta P_l^m(\cos\theta)\right)^2\right\}\right.$$
$$\times\sum_{e,o}\left\{\left[s_{l,m}^{e,o\ (1)}u_{l,m}^{e,o\ (3)*} + u_{l,m}^{e,o\ (3)}s_{l,m}^{e,o\ (1)*}\right]h_l^{(1)}(kr)[krh_l^{(1)*}(kr)]'\right. \tag{2.82}$$
$$\left.\left. - \left[t_{l,m}^{e,o\ (1)}v_{l,m}^{e,o\ (3)*} + v_{l,m}^{e,o\ (3)}t_{l,m}^{e,o\ (1)*}\right]h_l^{(1)*}(kr)[krh_l^{(1)}(kr)]'\right\}\right] .$$

Via the application of the same standard integrals for the associated Legendre polynomial, and of the Wronskian on the spherical Bessel functions, the extinction energy contribution to the total decay rate is given by:

$$W_{ext} = -\frac{k}{16\pi\omega\mu_1\mu_0}(2-\delta_0)^2\frac{2l+1}{l(l+1)}\frac{(l-m)!}{(l+m)!} \tag{2.83}$$
$$\times\sum_{e,o}\left[s_{l,m}^{e,o\ (1)}u_{l,m}^{e,o\ (3)*} + u_{l,m}^{e,o\ (3)}s_{l,m}^{e,o\ (1)*} + t_{l,m}^{e,o\ (1)}v_{l,m}^{e,o\ (3)*} + v_{l,m}^{e,o\ (3)}t_{l,m}^{e,o\ (1)*}\right] ,$$

with more details on the deviation given in Appendix A5.

TOTAL ENERGY

Recall that the total rate at which energy crosses through the putative sphere is given by:

$$W_{total} = W_{inc} + W_{scat} - W_{ext} . \tag{2.84}$$

The summation of these terms gives the final expression for the total energy passing through the putative sphere:

$$W_{total} = \frac{k}{16\pi\omega\mu_1\mu_0}(2-\delta_0)^2\frac{2l+1}{l(l+1)}\frac{(l-m)!}{(l+m)!}\sum_{e,o}\left[|s_{l,m}^{e,o\ (1)} + u_{l,m}^{e,o\ (3)}|^2 + |t_{l,m}^{e,o\ (1)} + v_{l,m}^{e,o\ (3)}|^2\right] . \tag{2.85}$$

Finally, to obtain the radiative decay rate for an isolated NP excited by a dipole source, the total energy passing through the putative sphere is normalised with the energy when no NP is present (i.e. W_{inc}):

$$\gamma_{rad} = \frac{W_{total}}{W_{inc}} = \frac{\sum_{l,m}(2-\delta_0)^2\frac{2l+1}{l(l+1)}\frac{(l-m)!}{(l+m)!}\sum_{e,o}\left[|s_{l,m}^{e,o\ (1)} + a_l s_{l,m}^{e,o\ (3)}|^2 + |t_{l,m}^{e,o\ (1)} + b_l t_{l,m}^{e,o\ (3)}|^2\right]}{\sum_{l,m}(2-\delta_0)^2\frac{2l+1}{l(l+1)}\frac{(l-m)!}{(l+m)!}\sum_{e,o}\left[|s_{l,m}^{e,o\ (1)}|^2 + |t_{l,m}^{e,o\ (1)}|^2\right]} . \tag{2.86}$$

It is therefore apparent that the scalar coefficients $s_{l,m}^{e,o\ (1)}$ and $t_{l,m}^{e,o\ (1)}$ respectively describe the TE and TM contributions of how a dipole source at $\mathbf{r}'$ couples energy into free-space modes; $s_{l,m}^{e,o\ (3)}$ and $t_{l,m}^{e,o\ (3)}$ similarly describe how the dipole source couples energy into the photonic modes of TE and TM polarisations, respectively. It is also evident that in the absence of the NP—where the scattering coefficients a_l and b_l are zero—the radiative decay rate returns to unity, and the molecule experiences no plasmonic enhancement to its free-space decay.

MODAL DECOMPOSITION FOR THE NON-RADIATIVE DECAY RATE

As more of a side note, the non-radiative decay rate can be determined using a similar method as above. The energy from a dipole source that is not radiated to the far-field is dissipated through Ohmic losses in the metal, and leads to the heating of the NP. The power dissipated within the lossy medium is given by:

$$P_{abs}(r) = \frac{1}{2}\mathsf{Re}\left[\mathbf{E}_{int} \cdot \mathbf{J}^*\right] \ , \tag{2.87}$$

and the total energy absorbed by the NP is found by integrating the fields over the volume of the lossy medium:

$$W_{abs} = \int_0^{r_p}\int_0^{\pi}\int_0^{2\pi} P_{abs}(r)\ r^2 \sin\theta dr d\theta d\phi \ . \tag{2.88}$$

Following the procedure outlined in Appendix A6, the absorption energy is given by:

$$W_{abs} = \frac{\omega k^2}{16\pi}\frac{2l+1}{l(l+1)}\frac{(l-m)!}{(l+m)!}(2-\delta_0)^2 \mathsf{Im}\left[\varepsilon_{Au}(\omega)\right] \sum_{e,o}\Bigg[|n_{l,m}^{e,o}|^2 \int_0^{r_p} r^2 |j_l(Nkr)|^2 dr + |w_{l,m}^{e,o}|^2 \frac{1}{N^2k^2}\int_0^{r_p}\left(l(l+1)|j_l(Nkr)|^2 + |[Nkrj_l(Nkr)]'|^2\right)dr\Bigg] \ . \tag{2.89}$$

The total non-radiative decay rate is then given by normalising this absorption energy by the incident energy from the dipole:

$$\gamma_{nrad} = \frac{W_{abs}}{W_{inc}} \ . \tag{2.90}$$

2.2.5 EXCITATION RATE

With the mode decomposition of the γ_{rad} established for the isolated spherical NP system, our attention now turns to performing a similar mode decomposition for the γ_{exc}. This first entails obtaining an expression for an EM plane wave that will be used as the source in exciting the emitter. By considering the limit where $r' \to \infty$, the wavefront from the dipole source reaching the NP has negligible variation across it, and can therefore be considered a plane wave.

FROM A DIPOLE SOURCE TO A PLANE WAVE EXCITATION

The methodology described above is general, and therefore capable of describing dipole sources at any position r'. To expand this to a plane wave excitation, one only needs to take the approximation of $r' \to \infty$. To aid in the numerical efficiency of solving this plane wave source, this subsection is dedicated to simplifying the analytical expressions in this regime.

Recalling the definition of the dyadic Green's function in equation 2.32:

$$\overleftrightarrow{\mathbf{G}}(\mathbf{r},\mathbf{r}') = C_{l,m}\begin{cases} \mathbf{M}_{l,m}^{e,o\ (3)}(k\mathbf{r}) \otimes \mathbf{M}_{l,m}^{e,o\ (1)}(k\mathbf{r}') + \mathbf{N}_{l,m}^{e,o\ (3)}(k\mathbf{r}) \otimes \mathbf{N}_{l,m}^{e,o\ (1)}(k\mathbf{r}') & r > r' \\ \mathbf{M}_{l,m}^{e,o\ (1)}(k\mathbf{r}) \otimes \mathbf{M}_{l,m}^{e,o\ (3)}(k\mathbf{r}') + \mathbf{N}_{l,m}^{e,o\ (1)}(k\mathbf{r}) \otimes \mathbf{N}_{l,m}^{e,o\ (3)}(k\mathbf{r}') & r < r' \end{cases} . \tag{2.91}$$

For the plane wave source, where $r' \to \infty$, only the $r < r'$ regime is required. The electric

field for this plane wave is therefore:

$$\mathbf{E} = \omega^2 \mu_0 \mu_1 C_{lm} \left[s_{lm}^{e,o\ (3)} \mathbf{M}_{l,m}^{e,o\ (1)}(k\mathbf{r}) + t_{lm}^{e,o\ (3)} \mathbf{N}_{l,m}^{e,o\ (1)}(k\mathbf{r}) \right] , \tag{2.92}$$

where $s_{lm}^{e,o(3)} = \mathbf{M}_{l,m}^{e,o\ (3)}(k\mathbf{r}') \cdot \mathbf{p}(\mathbf{r}')$ and $t_{lm}^{e,o(3)} = \mathbf{N}_{l,m}^{e,o\ (3)}(k\mathbf{r}') \cdot \mathbf{p}(\mathbf{r}')$. To reduce these expressions, consider specifically the placement of an x-polarised dipole at $z' = -\infty$ (where $\mathbf{r}' \rightarrow [r' = \infty, \theta' = \pi, \phi' = 0]$) which corresponds to a z-propagating, x-polarised plane wave. This positioning leads to the reduction of the dipole moment, which in spherical coordinates becomes: $\mathbf{p}(\mathbf{r}') = p_0 \hat{\mathbf{e}}_x = -p_0 \hat{\mathbf{e}}_\theta$. The dot product with the VSHs then reduces the coefficients: $s_{lm}^{e\ (3)}$ and $t_{lm}^{o\ (3)}$ disappear, whereas the other two components become:

$$s_{lm}^{o\ (3)} = -p_0 h_l^{(1)}(kr') \frac{m}{\sin\theta'} P_l^m(\cos\theta') \tag{2.93}$$

$$t_{lm}^{e\ (3)} = -p_0 \frac{1}{kr'} [kr' h_l^{(1)}(kr')]' \ \frac{\partial P_l^m(\cos\theta')}{\partial \theta'} . \tag{2.94}$$

In the asymptotic limit, where $kr' \gg l^2$, these two spherical Hankel functions reduce to their asymptotic forms:

$$h_l^{(1)} \sim \frac{(-i)^l e^{ikr'}}{ikr'} \tag{2.95}$$

$$\left[kr' h_l^{(1)}(kr') \right]' \sim \frac{(-i)^l e^{ikr'}}{ikr'} (1 + ikr') , \tag{2.96}$$

recalling that the prime in the $[xz_l(x)]'$ terms refers to the differential with respect to the argument of the function, x. For $\theta' = \pi$, the first associated Legendre polynomial expression is only non-zero when $m = \pm 1$. Choosing the solution of $m = 1$, these two expressions

become:

$$\frac{m}{\sin\theta'}P_l^m(\cos\theta')\Big|_{\theta'=\pi,\ m=1} = -\frac{1}{2}l(l+1)(-1)^{l-1} \tag{2.97}$$

$$\frac{\partial P_l^m(\cos\theta')}{\partial\theta'}\Big|_{\theta'=\pi,\ m=1} = -\frac{1}{2}l(l+1)(-1)^{l}\ . \tag{2.98}$$

Therefore, the two remaining coefficients reduce to: $s_{l,1}^{o\ (3)} = -t_{l,1}^{e\ (3)} = -p_0\frac{1}{2}l(l+1)\frac{i^l e^{ikr'}}{ikr'}$, and the plane wave electric field generated by an x-polarised dipole source place at $z = -\infty$ is given by:

$$\mathbf{E} = -\omega^2\mu_0 i^l\frac{(2l+1)}{l(l+1)}\frac{p_0 e^{ikr'}}{4\pi r'}\left[\mathbf{M}_{l,1}^{o\ (1)}(k\mathbf{r}) - i\mathbf{N}_{l,1}^{e\ (1)}(k\mathbf{r})\right]\ . \tag{2.99}$$

This equation is in agreement with the multipolar expansion of plane waves obtained with a different method [58].

EXCITATION RATE

To finally obtain an expression for the γ_{exc} of a QE place at r' in the vicinity of a NP, the total intensity is needed (incident plus scattered) and normalised to the incident intensity. Similarly to the incident fields, one can apply the approximation of $r' \to \infty$ for the scattered fields of equation 2.42 to obtain more simplified equations for an external plane wave source. Writing the incident and scattered components together gives [58]:

$$\begin{pmatrix}\mathbf{E}_{PW}^{inc}(\mathbf{r})\\ \\ \mathbf{E}_{PW}^{scat}(\mathbf{r})\end{pmatrix} = E_0\sum_l i^l\frac{2l+1}{l(l+1)}\left[\begin{pmatrix}\mathbf{M}_{l,1}^{o\ (1)}\\ \\ a_l\mathbf{M}_{l,1}^{o\ (3)}\end{pmatrix} - i\begin{pmatrix}\mathbf{N}_{l,1}^{e\ (1)}\\ \\ b_l\mathbf{N}_{l,1}^{e\ (3)}\end{pmatrix}\right]\ , \tag{2.100}$$

where a_l and b_l are the Mie scattering coefficients derived earlier, $E_0 = \omega^2 \mu_0 \frac{p_0}{4\pi r'} e^{ikr'}$, and the dipole source amplitude for this polarisation becomes: $\mathbf{p}(\mathbf{r}') = p_0 \delta(r - r') \hat{\mathbf{e}}_x$.

With these equations now simplified for the specific plane wave polarisation and propagation direction considered here, the rate at which the plane wave couples energy into a molecule at position $\mathbf{r} = \mathbf{r}_0$ can be identified. This is proportional to the total electric field (incident plus scattered) relative to the field without the plasmonic system present (incident field):

$$\gamma_{exc} = \frac{\left| \hat{\mu} \cdot [\mathbf{E}_{PW}^{inc}(\mathbf{r}_0) + \mathbf{E}_{PW}^{scat}(\mathbf{r}_0)] \right|^2}{\left| \hat{\mu} \cdot \mathbf{E}_{PW}^{inc}(\mathbf{r}_0) \right|^2} , \tag{2.101}$$

where the molecule at $\mathbf{r}_0$ that is being excited has a dipole moment directed along the unit vector $\hat{\mu}$.

2.3 ISOLATED METALLIC NANOPARTICLES

With analytical expressions for both the γ_{exc} and γ_{rad}, this section utilises the mode formalism to understand the origin of the coupling differences. Although the analytics here are limited to isolated spherical NPs, the multipolar decomposition offers a deep understanding into the rich modal nature of the plasmonic response, as well as their interactions with the exact emitter positioning.

Recalling the motivation behind this analysis: Figure 2.3 reveals the identical manner in which an isolated spherical NP (and symmetric spherical dimer antenna) is able

to equally emit and receive energy (i.e. $\gamma_{rad} = \gamma_{exc}$). In contrast, the NPoM geometry radiates energy much more efficiently than it can be in-coupled (i.e. $\gamma_{rad} > \gamma_{exc}$). Utilising the formulation derived in Section 2.2, Figure 2.6A compares the analytical form of the γ_{exc} and γ_{rad} (solid lines) with the numerical FDTD calculations (dashed lines)—for the same structure as in Figure 2.3A, with an emitter placed 0.5 nm away from the surface of an isolated spherical NP of diameter $2r_p = 60$ nm. It is immediately obvious that all these lines are in strong agreement and describe the same singular resonance around 525 nm, with the modal decomposition revealing that only the first order mode ($l = 1$) contributes to this resonance. The energy therefore couples out of the system via the $l = 1$ mode in

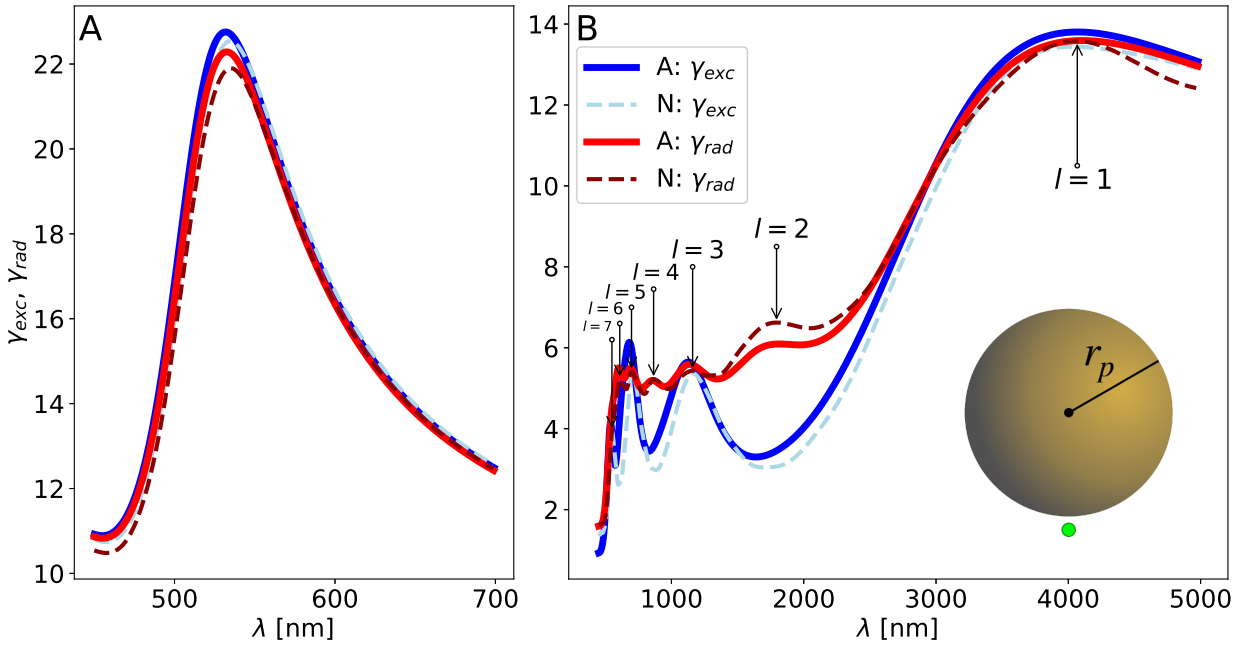

Figure 2.6: The γ_{exc} (blue) and γ_{rad} (red) for isolated spherical NPs of diameters (A) 60 nm and (B) 1 μm. The analytical modal decompositions (full lines) and numerical FDTD calculations (dashed lines) are plotted together for comparison. In (B), the series of resonances are labelled by their corresponding angular momentum quantum number, l, which emerges from the modal decomposition.

the same manner in which energy is in-coupled—and so: $\gamma_{exc} = \gamma_{rad}$.

Despite the qualitative agreement, there are small differences between the analytical and numerical results which must be noted and addressed. The slight variations are an outcome of numerical limitations: due to the extreme closeness of the molecule to the surface of the NP and the greatly sub-nanometer meshing this requires—any additional demand would be too computationally expensive. The γ_{rad} is much more sensitive to the meshing due to the position of the molecule and majority of the energy being confined to the area of extreme meshing, and it is therefore much more significantly affected by the computational limitations. In light of this, the γ_{exc} is calculated for the 60 nm NP in Appendix Figure A1 using three different methods. This compares the analytical model to numerical results found using FDTD and COMSOL—highlighting the variation with the mesh type, numerical precision, and the electric permittivity fitting required for dispersive optical parameters in time domain calculations.

The NP considered in Figure 2.6A is well within the quasi-static limit ($2r_p = 60$ nm $\ll 500$ nm), as are the NPs used in the construction of the symmetric dimer and NPoM geometries of Figure 2.3B and C. However, the overall system of the NPoM geometry is very much non–quasi-static due to the semi-infinite mirror, which one can approximate as a very large spherical NP. Using the analytic model that is valid for spherical NPs of any size, the numerical and analytical in- and out-coupling rates are compared in Figure 2.6B for a non–quasi-static spherical gold NP of diameter $2r_p = 1$ μm. This reveals a series of higher order modes, and a significant red-shifting of the $l = 1$ mode from 525 nm

to ~ 4 μm. More importantly are the differences that arise between the γ_{exc} and γ_{rad}, where—depending on the wavelength—they are not always equal.

To shed some light on what is happening here, Figure 2.7 decomposes the γ_{exc} and

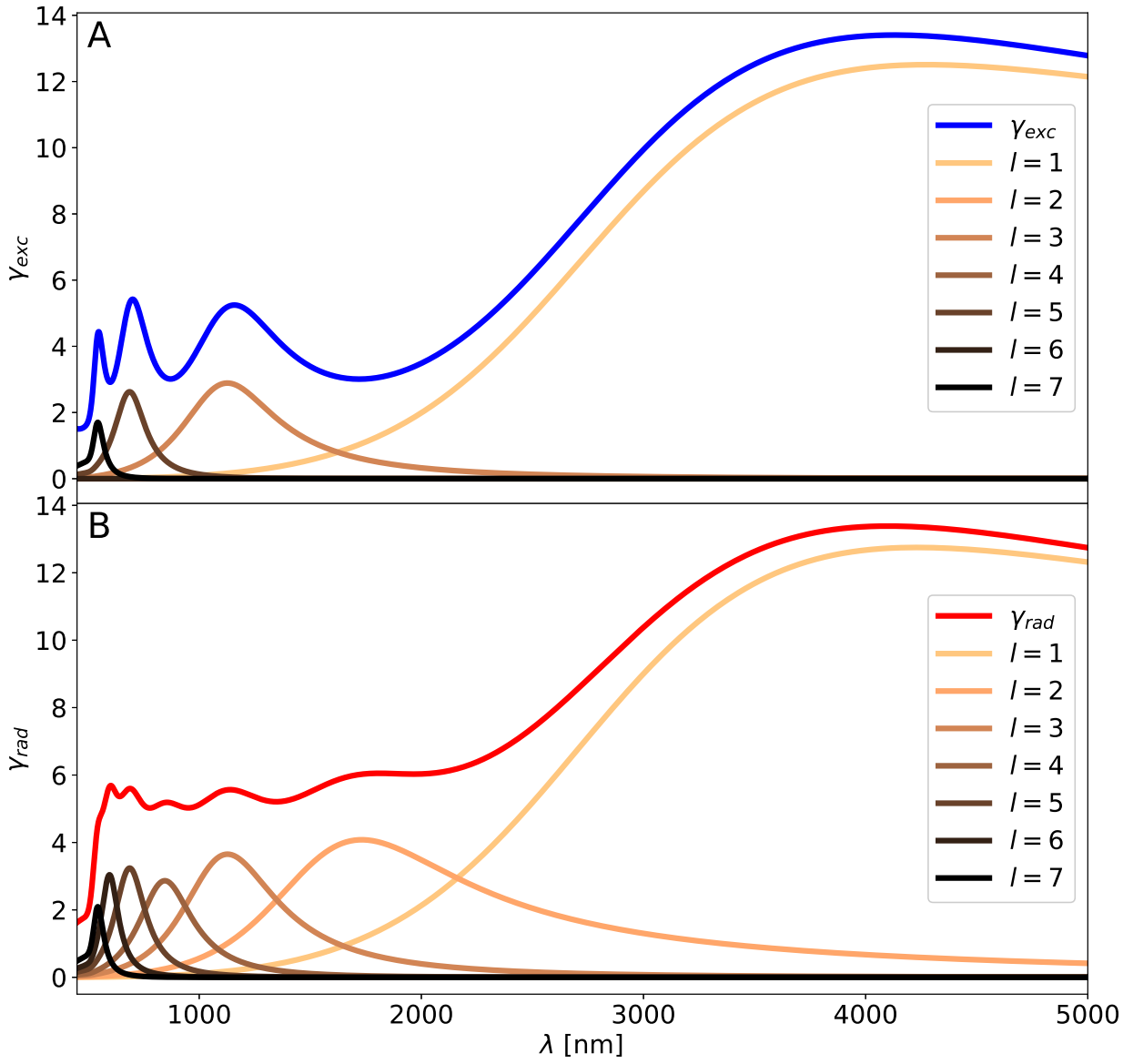

Figure 2.7: The analytical (A) γ_{exc} and (B) γ_{rad} for a 1 μm diameter isolated NP, for an x-polarised molecule placed 0.5 nm above the NP in the x-axis. The decomposition reveals the modal response for each quantity.

γ_{rad} into the contributions from each mode. This reveals seven dominant resonances that form the radiative response of this system, and in contrast only four resonant excitational modes. More specifically, the γ_{exc} only consists of odd-l modes, with significant minima where the even-l radiative peaks occur. Finally, it is worth drawing attention to the breadth and tails of the modal lines, and the significant overlap between neighbouring modes. The differing efficiency with which the in- and out-coupling rates couple to these modes is explored in the next subsection.

2.3.1 PLANE WAVE SELECTIVITY

The γ_{rad} has been shown to support modes of every l—regardless of whether it is even or odd—due to the close proximity of the molecule to the surface of the NP. To understand this, recall the multipolar nature supplied by the spherical harmonics: each l mode has $(2l+1)$ m-configurations of the same mode with different orientations about the NP. As a molecule emits with wavevectors pointing in all direction, there is always an m-configuration of the incident wavevectors available for efficient coupling to—as demonstrated for the first four modes in Figure 2.8A-D. Note that all $(2l+1)$ configurations contribute to the total γ_{rad}, and a molecule in the close vicinity of the NP is therefore able to efficiently couple to plasmonic modes of every l.

In contrast, a plane wave source of a specific polarisation breaks the $(2l+1)$ symmetry of the plasmonic modes and defines the available m-configuration(s) before it even reaches the NP. Referring back to Subsection 2.2.5—where we took the approximation

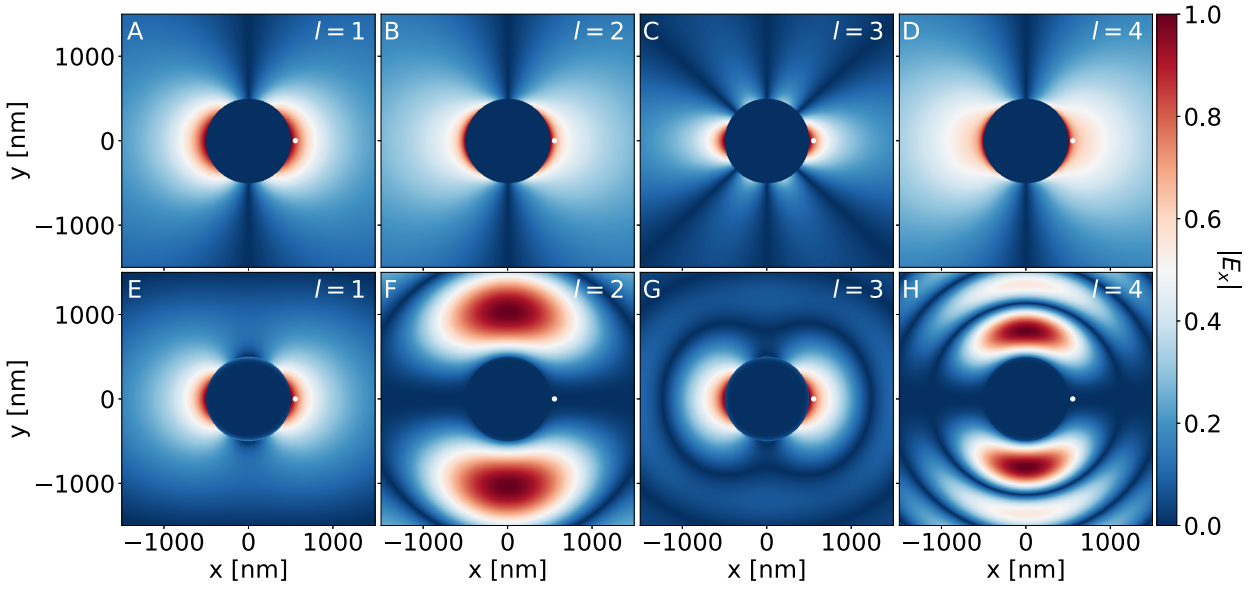

Figure 2.8: The total $|E_x|$ fields of a 1 μm diameter NP excited by: a close proximity dipole source (A-D); and an x-polarised plane wave (E-H). These are obtained from the analytical modal decomposition for modes: (A,E) $l = 1$, (B,F) $l = 2$, (C,G) $l = 3$, (D,H) $l = 4$. The white dot indicates the position of the molecule which: is excited in the γ_{exc} calculation, and is the source when determining the γ_{rad}.

that $r' \to \infty$—we had to define the x-polarised and z-propagating plane wave considered here, which limits the excitation to the $m = 1$-configuration. This $m = 1$ restriction leads to $\pi/2$-rotations between consecutive l-modes [76]. This is demonstrated in Figure 2.8E-H for the modal $|E_x|$ fields around the NP, where the extrema rotates around the NP by $90°$ with each l-mode. The $|E_y|$ and $|E_z|$ field components are respectively shown in Appendix Figures A2 and A3. With the white dot marking the location of the x-polarised molecule, it becomes clear that a plane wave is only able to efficiently excite the molecule for odd-l modes, and therefore only odd-l modes contribute to the γ_{exc}.

With the understanding of why these in- and out-coupling rates differ for the non–

quasi-static NP, it is worth momentarily returning to the quasi-static NP in Figure 2.6A. As this system is only able to efficiently support the $l = 1$ mode for both the dipole source excitation (in the vicinity of the NP) and the plane wave excitation, it therefore exhibits equal in- and out-coupling rates with $\gamma_{rad} = \gamma_{exc}$.

2.3.2 SIZE DEPENDENCE

From the understanding of the equal coupling rates of the quasi-static NP and the unequal coupling of the non–quasi-static NP, this section more closely analyses the regime where the differences start to emerge. To do this, the in- and out-coupling rates are explored as a function of both wavelength and NP radius—as shown in Figure 2.9. This reveals how the modes red-shift as the size of the NP is increased, with additional higher order modes appearing once each previous mode has sufficiently shifted [77]. By following the maxima lines of each mode (black dashed lines), the lack of even-l modes in the γ_{exc} compared to the γ_{rad} is clearly apparent. The size dependence of deviating coupling rates only becomes significant beyond the quasi-static limits (around $2r_p > 150$ nm), where the phase propagation of the plane wave across the NP can no longer be ignored—resulting in the more efficient coupling into the $l = 2$ mode, once the $l = 1$ has adequately red-shifted. Note again that this differing behaviour is unrelated to the reciprocity of the system, which has been shown to remain reciprocal, but instead originates from the plane wave polarisation that induces mode selectivity. Mathematically, this originates from the following reduction: $\{ s_{l,m}^{e\,(3)},\ s_{l,m}^{o\,(3)},\ t_{l,m}^{e\,(3)}, t_{l,m}^{o\,(3)}\} \longrightarrow \{ s_{l,1}^{o\,(3)}, t_{l,1}^{e\,(3)}\}$.

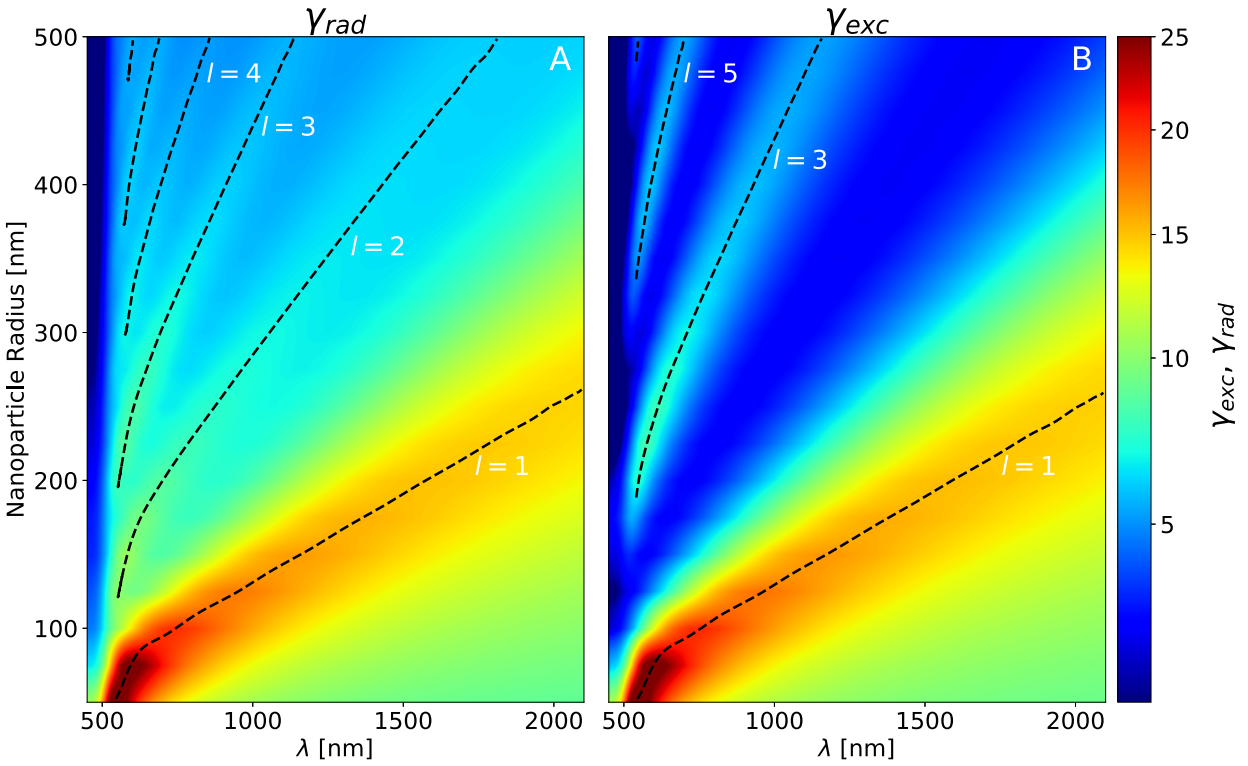

Figure 2.9: The (A) γ_{rad} and (B) γ_{exc} for isolated NPs obtained analytically from the model—as a function of wavelength (λ) and the NP radius (r_p). The black dashed lines highlight the maxima curves for each l-labelled resonance.

To elaborate on what is meant by a NP efficiently supporting the in- or out-coupling of a certain mode, Figure 2.10 shows how the first three modes couple for three different sized NPs—when excited by a plane wave source—with the white dot indicating the molecule position where γ_{exc} is measured. Here the NP radii are 30 nm, 100 nm and 500 nm, with the normalised $|E_z|$ fields presented on resonance for each mode. This confirms the ability of each of the NP sizes to couple into the $l = 1$ mode, whereas the smallest NP shows no coupling into the $l = 2$ mode—highlighting the quasi-static effect. With the $l = 3$ mode, only the largest of the three NPs is able to efficiently couple to it.

Similarly, Appendix Figure A4 reveals the mode coupling for the same three NP radii when excited by a dipole source placed in close proximity to the NP surface.

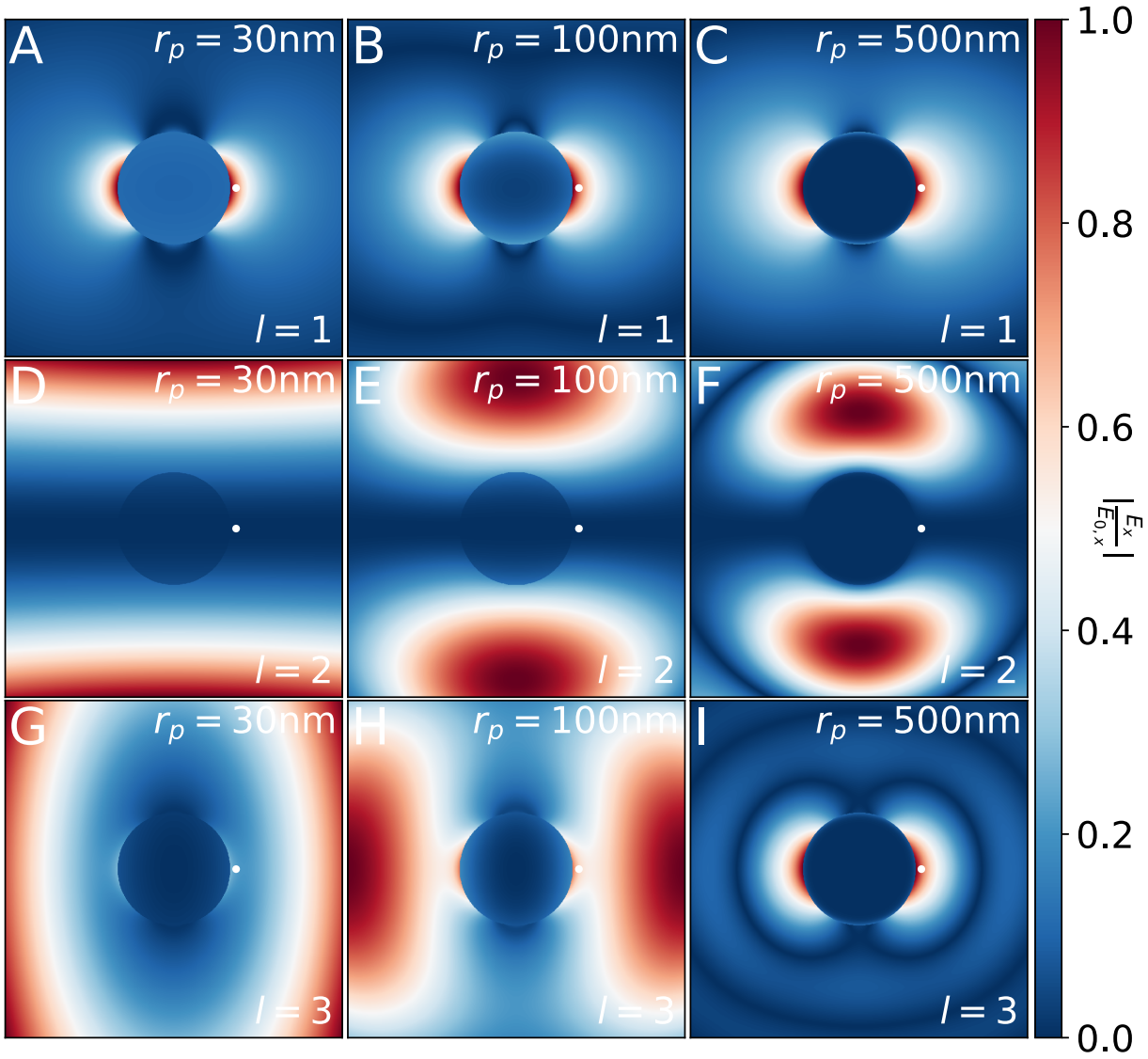

Figure 2.10: The modal contribution to the normalised electric field intensity around an isolated NP due to an x-polarised plane wave excitation. (A-C) $l = 1$ mode. (D-F) $l = 2$ mode. (G-I) $l = 3$ mode. (A,D,G) $r_p = 30$ nm. (B,E,H) $r_p = 100$ nm. (C,F,I) $r_p = 500$ nm. The white dot indicates the position of the molecule which is excited in the γ_{exc} calculation.

2.4 PLASMONIC NANOANTENNAS

With a strong understanding of how the in- and out-coupling differences arise in isolated NP systems, our attention now returns to the more complicated geometries of nanoantennas—namely the symmetric dimer and NPoM geometry introduced at the start of this chapter (recall Figure 2.3). In aid of simplicity, note that the source/detector is always considered at the centre of the cavity for each of the nanoantenna systems considered here.

The behaviour of the symmetric dimer antenna—consisting of two $2r_{p,1} = 2r_{p,2} = 60$ nm NPs with the molecule placed at the centre of a 1 nm gap—naturally follows from the analysis of the isolated NP of the same size. As this resides within the quasi-static limit, the hybridisation that occurs in the cavity simply comprises of the $l = 1$ mode of each NP. Although this hybridisation leads to an extreme enhancement of the fields within the cavity and an overall red-shift of the resulting resonance, it reveals that quasi-static nanoantennas have the ability to maintain equal γ_{exc} and γ_{rad}—as shown in Figure 2.3B.

Recalling the comparison to the γ_{nrad} for this system in Figure 2.4B, this hybridisation was shown to have increased the quantum yield and therefore suppress the quenching of emitters in the vicinity—in agreement with Kongsuwan [10]. In addition to the mechanism they identified for the suppression of the quenching—the radiative alteration of higher order modes—another is revealed here. The modal decomposition shows that the contribution to the hybridisation for all but the lowest order mode from each NP is

negligible, and that the observed increased quantum yield and suppressed quenching originate solely from the hybridisation process—not the radiative alteration of any higher order modes.

2.4.1 NANOANTENNA FORMATION

For more complicated nanoantenna geometries—such as asymmetric dimers, or dimers where one or both of the components lie outside of the quasi-static regime—the analysis must be handled more carefully due to the series of modes supported by the system (recall Figure 2.9).

We first consider an asymmetric dimer consisting of a quasi-static NP of 60 nm diameter assembled a distance d above a non–quasi-static NP of diameter 1 μm. From the detailed understanding gained in the previous section for the isolated components of this dimer antenna, Figure 2.11 numerically simulates the formation of the nanoantenna—noting that the wavelength range here is truncated to the regime around the resonance of the 60 nm NP. Initially for a large separation ($d = 50$ nm), the response of the system is dominated by the 1 μm NP and is almost identical to the isolated 1 μm NP of Figure 2.6B—as the NPs have negligible coupling for such large d. The nanoantenna is then gradually formed by reducing the separation of the NPs, from $d = 50$ nm to $d = 1$ nm, which sees the progressive coupling between the $l = 1$ mode of the 60 nm NP with the series of modes of the 1 μm NP that occupy the same wavelength range. The grey dashed line marks the dominant interaction wavelength between these modes. The hybridisation that occurs

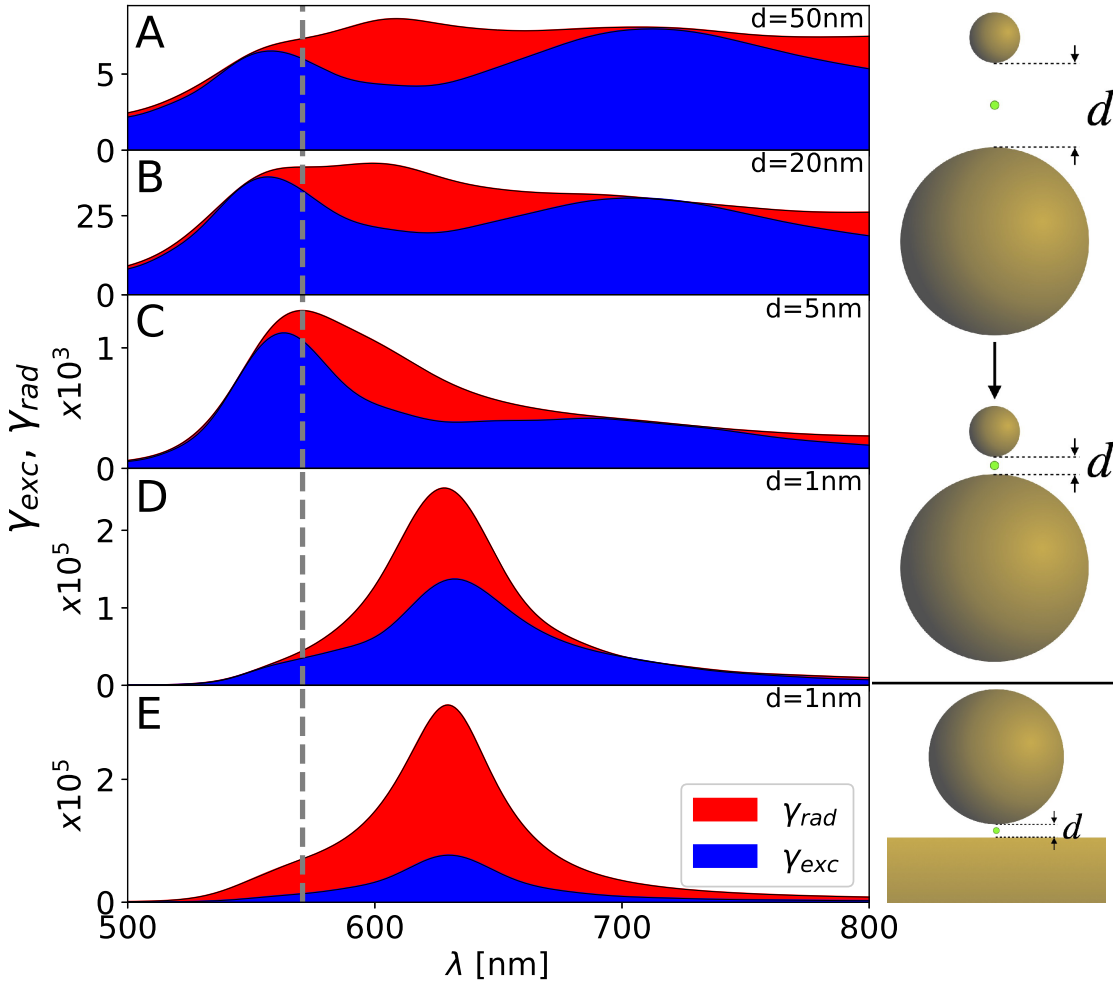

Figure 2.11: The γ_{exc} (blue) and γ_{rad} (red) calculated numerically for: (A-D) asymmetric dimer antennas of diameters of 60 nm and 1 μm; and (E) the NPoM configuration with a NP of diameter 60 nm. These have gap sizes of: (A) 50 nm, (B) 20 nm, (C) 5 nm, and (D-E) 1 nm. The grey dashed line marks the dominant interaction wavelength between these modes of the dimer. The schematics on the right illustrate the closure of the gap, with the green dot indicating the position of the molecule that: is excited in the γ_{exc} calculation, and is the source when determining the γ_{rad}.

between the modes leads to an increase in both the in- and out-coupling rates by orders of magnitude. Despite this enhancement, the hybridisation accentuates any underlying differences between the γ_{exc} and γ_{rad} for any of the nanoantenna's components. For a

$d = 5$ nm separation, the overall resonance is inline with that of the 60 nm NP, with only a small relative increase in the coupling rate differences.

However, once the cavity is reduced further (down to $d = 1$ nm), the modes couple significantly more tightly; this causes a dramatic red-shifting of the hybridised response for such a relatively small separation change. This shifting leads to the primary overlap and hybridisation of the 60 nm NP's $l = 1$ mode with the $l = 6$ mode of the 1 μm NP. Due to the missing γ_{exc} resonance at the $l = 6$ mode, the hybridisation of this $d = 1$ nm cavity leads to the emergence of vastly different in- and out-coupling rates—in comparison to the response of the nanoantenna for a $d = 5$ nm cavity where the 60 nm NP primarily couples to the $l = 7$ mode of the 1 μm NP. This separation dependence analysis of the asymmetric dimer antennas supplies an invaluable demonstration of how the response of nanoantennas directly originates from the plasmonic responses of its isolated components; for unequal coupling rates, this specifically points to non–quasi-static elements.

The conclusion that the unequal coupling rates observed in plasmonic nanoantennas originate from the selective coupling of their constituent plasmonic components, is fully consistent with EM reciprocity arguments. As we have seen from the Green's function notation for the analytical description of the γ_{exc} and γ_{rad}, the response of these constituent components are indeed consistent with $\mathbf{G}(\mathbf{r}, \mathbf{r}') = \mathbf{G}(\mathbf{r}', \mathbf{r})$—where the system remains unchanged under the interchange of the source ($\mathbf{r}$) and detector ($\mathbf{r}'$). The observations for the differing γ_{exc} and γ_{rad} seen in these plasmonic nanoantennas is therefore unrelated to the reciprocity of the system.

In comparison to this asymmetric dimer antenna, Figure 2.11E shows the qualitative equivalency of the NPoM geometry when both antennas consider a $d = 1$ nm cavity and a top NP of 60 nm diameter. Due to the size ratio of the 60 nm and 1 μm NPs, in many respects this dimer antenna very much resembles the NPoM geometry; relative to the 60 nm NP, the 1 μm NP effectively appears as a semi-infinite metallic mirror. Unlike the 1 μm NP, the mirror does not support a discrete set of modes; instead, it offers a continuum of evanescent eigenmodes (SPPs) that are still able to hybridise with the $l = 1$ mode of the 60 nm NP. The NPoM exhibits a larger difference in the in- and out-coupling rates, and this is due to the mode continuum contributing a greater number of even l-modes. It is therefore reasonable to consider the NPoM as an extreme form of asymmetric dimmer antenna, and an even better comparison could be made by increasing the size of the non–quasi-static NP; as this becomes closer to a semi-infinite mirror, it will support a greater number of even-l modes within the frequency bandwidth of the 60 nm NP's $l = 1$ mode and appear ever closer to the NPoM response.

It must be noted that the incident plane wave here is parallel to the mirror, which may not be feasible experimentally due to the infinitely large size of the substrate. If any oblique angled excitation were to be used instead, the response would be a superposition of the normal and in-place incidences—relative to the substrate. The normal incidence response, however, does not contribute in the same frequency range—as shown in Appendix Figure A5. Another point to note is that throughout the analysis presented here, the source/detector is always considered at the centre of nanoantenna cavities, however, the same conclusions about the origin of differing coupling rates still arise when considering

other positions within the cavities. The effect of the position within the cavity is explored in Appendix Figure A6 and A7, where it becomes clear that the same relationship between the γ_{exc} and γ_{rad} is obtained—independently of the emitter's position within the cavity.

2.4.2 TAILORED OPTICAL PROPERTIES OF NANOANTENNAS

This final subsection aims to draw all the elements of this chapter together to design nanoantennas with tailored, relative coupling efficiencies. This uses the understanding of how the size of the NP governs which modes are efficiently supported, and how these properties are altered via the formation of the cavity in nanoantenna geometries. To be consistent with geometries presented throughout this chapter, only spherical dimer antennas are presented here—although, it is true that other non-spherical based plasmonic nanoantennas would offer additional design flexibility [77, 78], as discussed in Chapter 3.

In order to form a plasmonic nanoantenna with one or more non–quasi-static elements that is also capable of exhibiting a hybridised response with equal γ_{exc} and γ_{rad}, our attention must return to Figure 2.9. By consulting the dependence of the number of supported modes and their spectral-positioning on the size of the NP, it is possible to select NPs such that the formation of a dimer antenna would result in the desired equal coupling rates. To do this, the NPs are required such that they offer odd-l modes that are well-separated from neighbouring even-l modes, and that the spectral positions of these modes are complementary to each other—once the red-shifting that occurs during the nanocavity formation is taken into account.

The NPs chosen to form this asymmetric dimer antenna have diameters of $2r_{p,1} = 60$ nm and $2r_{p,2} = 500$ nm, with Figure 2.12A showing the overlap between the 60 nm NP's $l = 1$ mode at 525 nm and the $l = 3$ mode of the 500 nm NP at ~ 600 nm. Although the spectral separation of the 500 nm NP's $l = 3$ mode from its $l = 2$ and $l = 4$ modes is relatively small, the bandwidth of the 60 nm NP's singular mode is much narrower and focuses the coupling primarily to 500 nm NP's $l = 3$—once the hybridisation supplies a red-shift of ~ 100 nm to the overall resonance of the dimer. The full hybridised response of this

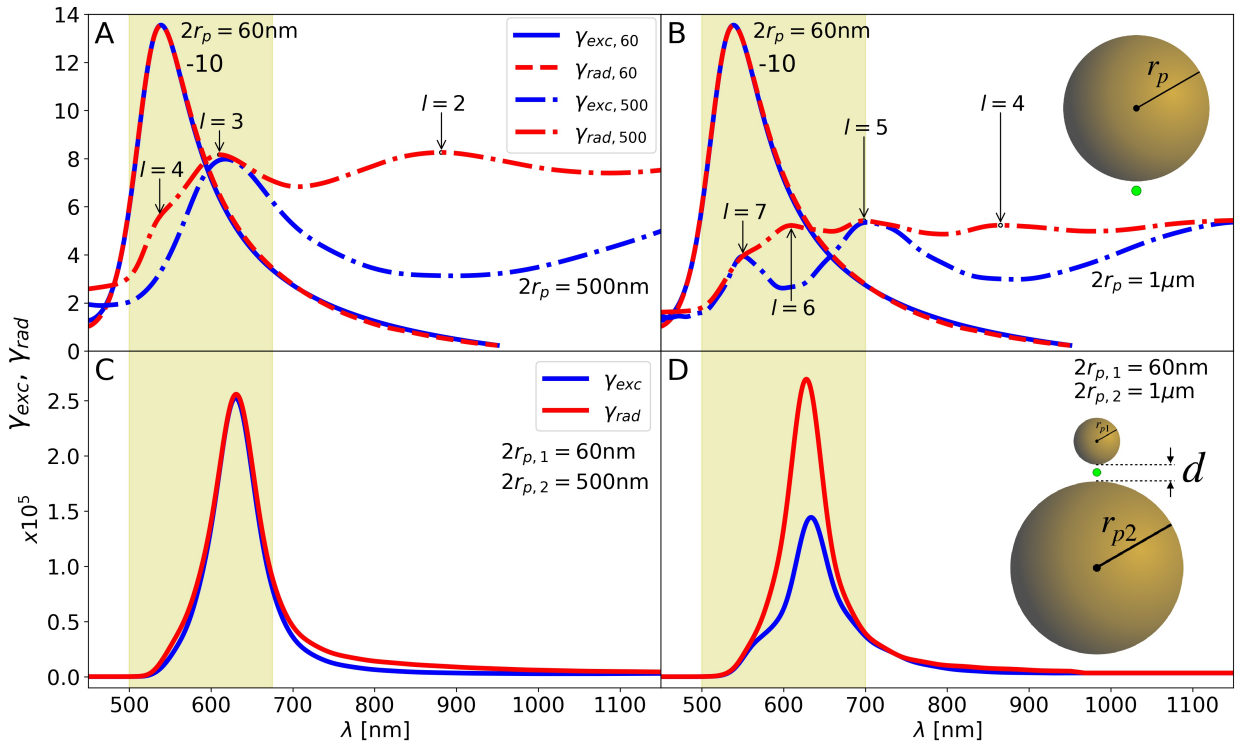

Figure 2.12: The γ_{exc} (blue) and γ_{rad} (red) for isolated NPs of diameters: (A) 60 nm (full/dashed lines) and 500 nm (dot-dashed lines); and (B) 60 nm (full/dashed lines) and 1 μm (dot-dashed lines). Similarly for asymmetric dimer antennas with gaps of $d = 1$ nm and diameters: (C) $2r_{p,1} = 60$ nm and $2r_{p,2} = 500$ nm; and (D) $2r_{p,1} = 60$ nm and $2r_{p,2} = 1$ μm. The green dot in each inset indicates the position of the molecule which: is excited in the γ_{exc} calculation, and is the source when determining the γ_{rad}.

asymmetric dimer antenna—where the 60 nm NP is assembled $d = 1$ nm above the 500 nm NP—is shown in Figure 2.12C. The overall plasmonic response clearly demonstrates that $\gamma_{exc} = \gamma_{rad}$ is possible, despite a component of the system being well outside of the quasi-static regime—supporting multiple modes that the γ_{exc} cannot efficiently couple to.

Note that small deviations to the equal in- and out-coupling rates arise on both sides of the main resonance. These are due to the tails of the $l = 2$ and $l = 4$ modes of the 500 nm NP, respectively overlapping with the $l = 1$ mode of the 60 nm NP in the regions of $\lambda = 540$-575 nm and $\lambda = 700$-1000 nm. In summary, the equality of the γ_{exc} and γ_{rad} in non–quasi-static systems requires: the primary coupling of one or more odd-l modes from each component; a significant spectral overlap between these modes, once the red-shifting of the cavity hybridisation is considered; and the ensurance of sufficiently narrow bandwidth modes and/or modes that are well spectrally separated from neighbouring even l-modes.

In contrast, for certain applications it may be desirable for a system to maintain a high radiative efficiency whilst instead limiting the excitation efficiency. For a system which offers this relative excitation retardance, consider an asymmetric dimer antenna consisting of a $2r_{p,1} = 60$ nm NP assembled $d = 1$ nm above a $2r_{p,2} = 1$ μm NP. The γ_{exc} and γ_{rad} for these isolated components are shown in Figure 2.12B, which—after considering the red-shift supplied by the hybridising cavity—leads to the primary overlap and coupling of the 60 nm NP's $l = 1$ mode with the $l = 6$ mode of the 1 μm NP. The plasmonic response of this nanoantenna is shown in Figure 2.12D, revealing that the γ_{rad} is

significantly larger than the γ_{exc} (approximately twice as large). Contrary to the previous system, the tails of the 1 μm NP's neighbouring $l = 5$ and $l = 7$ modes overlap with the 60 nm NP's $l = 1$ mode, producing regions of equal in- and out-coupling rates at $\lambda = 675$-800 nm and $\lambda = 540$-575 nm, respectively.

The significance of our findings presented throughout this chapter are highlighted here in appropriate contexts. The γ_{exc} and γ_{rad} observed for these nanoantenna geometries reveals a great deal about the interactions of the plasmonic modes with molecules in the vicinity of metallic systems. The relative coupling rates for different systems is of specific interest where the near-to-far-field relationship is of great significance [79–81]. For example, in SERS—where a laser-stimulated excitation of a molecule's chemical bonds later emits a photon as it relaxes to a molecular vibrational state—it is the radiative far-field emission that leads to the detection of Raman signals [47]. The extreme confinement and field enhancement of plasmonic nanoantennas greatly increased the intensity of the Raman signals. However, they are also highly dependent on the laser's ability to excite the molecule and the system's ability to release this energy to the far-field where it is detected [18]—both processes occur via the same set of plasmonic modes. It is therefore apparent how the work outlined here encourages the design of plasmonic nanoantennas which take an active role in optimising the efficiency of how the system both in- and out-couples energy.

Recent works which demonstrate the room temperature strong coupling of a single molecule are a similar story; here the fluorescent molecule receives a plane wave excita-

tion via the plasmonic modes, and the hybrid states are observed in the far-field through the radiative emission [4, 82]. In addition, future applications of plasmonic nanoantennas in the engineering of room temperature quantum states would need to consider this fine balance between the excitation and radiative properties. It is therefore vital to discern how the γ_{exc} and γ_{rad} originate in plasmonic systems, with the ability to design and fabricate plasmonic environments with specific properties.

2.5 CONCLUSIONS

The coupling of QEs (such as fluorescent molecules, single atoms, quantum dots) to plasmonic environments has, in recent years, lead to the realisation of room temperature quantum effects of light-matter interactions. Along with dimer antennas, these works have primarily focused on the NPoM geometry for its fantastic photonic platform where, until now, it was believed that energy could be coupled into the system just as efficiently as it is out-coupled. Here a methodology based on Mie theory is adopted to describe and decompose the modal response of metallic isolated spherical NPs. Through the observations of in- and out-coupling rates for non–quasi-static systems, it becomes apparent that only the γ_{rad} is able to efficiently couple to modes of every l, whereas the γ_{exc} is limited to odd-l modes. This arises due to the polarisation of the plane wave excitation, which limits the modes available for it to efficiently couple to; in contrast, a close proximity dipole source emits with wavevectors in all directions, and can therefore always efficiently cou-

ple to one of the $2l + 1$ configurations. This persists to nanoantenna geometries, where in forming the nanocavity the hybridisation of the modes from each component leads to selective enhancement region(s). Depending on the modal distribution about these region(s), this can produce nanoantennas with a plasmonic response that accentuates the differences between the γ_{exc} and γ_{rad}—compared to the isolated components.

In general, plasmonic systems consisting of one or more non–quasi-static elements release energy to the far-field much more efficiently than energy can be coupled into the system—which has been shown here to be unrelated to the reciprocity of the system, as $\mathbf{G}(\mathbf{r}, \mathbf{r}') = \mathbf{G}(\mathbf{r}', \mathbf{r})$. Lastly, the custom design of plasmonic antennas was considered in light of the above revelations; here systems with tailored relative in- and out-coupling rates were explored. The works presented in this chapter unveil a deeper understanding of how plasmonic systems facilitate and control the interactions between light and matter, with specific applications when the near-to-far-field relationship is of significant importance—such as: single molecule strong coupling [4], SERS [18], and quantum computing with DNA-origami controlled qubits [57] to name but a few.

3 PLASMONIC MODES OF POLYHEDRAL NANOCAVITIES

3.1 INTRODUCTION

Plasmonic nanocavities to date have been primarily explored experimentally [8, 28, 83], with their optical behaviours observed and measured in the far-field—mainly via scattering methods and dark-field microscopy [57, 84, 85]; this can lead to inconsistencies coming from the selective coupling of incident excitations [86]—as discussed in Chapter 2—as well as the interference of spectrally close cavity resonances [87]. Few studies have explored the near-field plasmonic modes within nanocavities [72], with the majority of theoretical studies focusing on the near-field resonances for particular incident field excitations [84, 87, 88]. This alone provides a very limited view of the radiative and non-radiative decay channels of the modes, as well as the manner in which energy may be out-coupled from the system [72]. In order to address this—and to obtain the modes of a system independently of the incident excitation—one must perform an EM modal

decomposition of the hybridised plasmonic response.

Recently, it was shown in [72] that the EM modal decomposition of two NPoM geometries can reveal all the plasmonic modes of the system—specifically for a sphere-on-mirror (SoM) and a truncated-sphere-on-mirror (TSoM)—as well as their respective near- and far-field behaviours. However, systems such as these are lossy and open—possessing dissipative pathways and emission channels out of the system—and can therefore only be effectively described using a quasi-normal mode (QNM) analysis [61, 89–91]. This decomposes the plasmonic response into a set of modes with complex eigenfrequencies—where the real part gives the resonant frequency of the system, and the imaginary part corresponds to the lossy nature of the mode [92]. We made use of the efficient QNM solver 'QNMEig'—developed by the Lalanne group and found here—which utilises an auxiliary-field approach to obtain the modal eigenvalues and near-field charge distributions supported by a plasmonic nanoantenna [61, 89, 93, 94]. This analysis reveals the importance of the NP's facet on the supported near-field charge distributions and—through a near-to-far-field-transformation (NFFT)—the corresponding far-field profiles, with nanometre-scale changes to the facet morphology drastically impacting both the near- and far-fields. This is crucial for understanding how the positioning of emitters within plasmonic environments affects their interactions with the near-field, as well as the significant impact this has on how the energy is coupled out to reach the far-field [4, 78].

Even though almost all theoretical studies focus on spherical or truncated-spherical NPoM configurations, in reality NPs do not have such an ideal shape (as in Figure 3.1A).

During fabrication, gold NPs most commonly acquire a polyhedral shape due to the crystalline nature of the metal [77]. Recent experimental work [77] has revealed that NPs commonly adopt one of three polyhedral shapes: (i) cuboctahedron, (ii) rhombicuboctahedron and (iii) decahedron—as respectively shown in Figure 3.1B-D, together with scanning electron microscopy images. When such NPs are assembled on a mirror, much more complex nanocavities are formed whose EM responses (both in the near- and far-fields) are not yet well understood. This is hindering current efforts to interpret experimental results, most severely in the mapping of emitter positions within realistic nanocavities.

In this chapter, we perform a QNM analysis on commonly occurring polyhedra-on-mirror nanoantennas. We reveal that the shape and symmetry of both the NP and the nanocavity it forms dominate the overall optical response of the system. Each unique

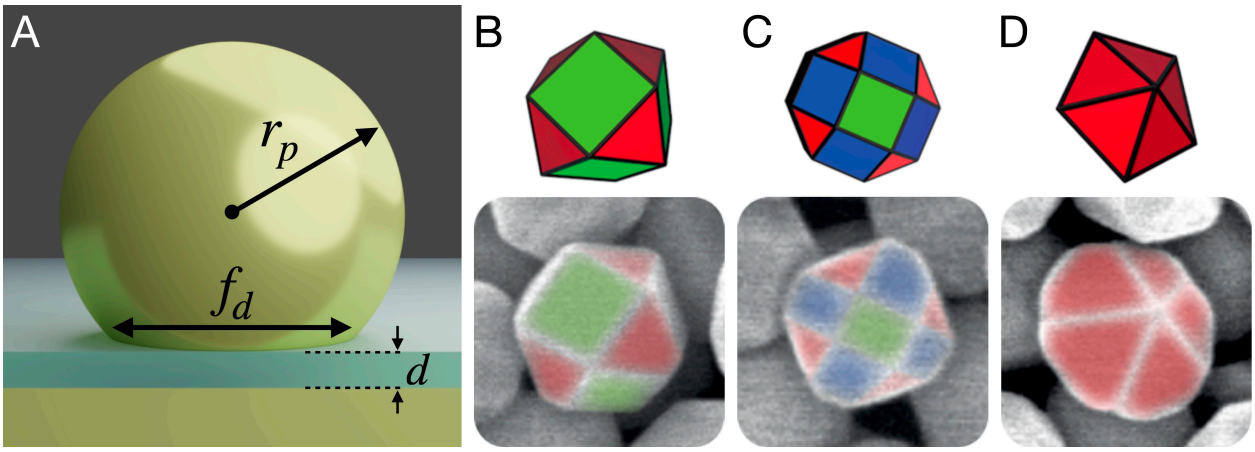

Figure 3.1: A. TSoM schematic for a gold NP of radius r_p with a circular facet of diameter f_d a distance d above a gold substrate, separated by a spacer of refractive index n. Polyhedral NP structures above their scanning electron microscopy images: (B) cuboctahedron, (C) rhombicuboctahedron and (D) decahedron [77]. The green, red and blue facets refer to planes of gold atom crystallisation $\{100\}$, $\{110\}$ and $\{111\}$, respectively.

facet assembly supports a distinct set of QNMs, and we detail how nanometre intricacies of each facet morphology and NP symmetry dramatically affect the resonant frequencies of the modes and their optical response—both in terms of the near-field charge distributions within the nanocavity and, through a NFFT, the ability of each mode to out-couple energy to the far-field. It should be noted that same shape NPs give very different results when assembled on the mirror with a different facet: in certain scenarios this is true even when the facet shape and size are identical. We show that the original nomenclature for SoM and TSoM configurations developed in [72] still holds, despite the lack of spherical symmetry in the polyhedral systems. Through a recombination technique, the modal far-field responses can be utilised to obtain the total far-field emission profile of a geometry for the placement of an emitter at a specific position within the nanocavity. This work paves the way towards building and utilising realistic plasmonic nanocavities, with the ability to determine the NP shape and its specific configuration with respect to the mirror via its far-field emission and resonant frequencies—and even to determine the position of an emitter within the nanocavity.

3.2 QUASI-NORMAL MODE ANALYSIS OF PLASMONIC NANOCAVITIES

Plasmonic nanoantennas are open systems with efficient radiative emission capabilities that also possess dissipative elements—due to the Ohmic losses in the metal. They are

therefore non-Hermitian systems—as energy is not conserved during EM oscillations—and cannot be described with the natural method of normal modes [93]; instead, a QNM description is required which yields complex eigenfrequecies, whose resonances are intrinsic to the arbitrary shaped system and independent of the excitation field [71]. Due to the complex nature of these eigenfrequencies, QNMs diverge at large distances and only form a complete set within the cavity—the normalisation of QNMs has therefore proven mathematically difficult. This has been evaded in literature for some time by considering the energy dissipation as a perturbation to a Hermitian system [95]. Although this may be sufficient in high finesse cavities (such as those considered in optical environments), this phenomenological approach is insufficient to adequately describe systems with lower quality factors—such as the plasmonic nanocavities considered here [93]. Current numerical techniques can remedy this normalisation problem, however, by surrounding the system with perfectly matched layers (PMLs) that absorbed all the energy that is emitted to the far-field; this causes the eigenstates to exponentially decay within the PMLs, and thus counteracts the divergence of the QNMs [61]. The QNMs therefore become square-integrable and normalisable—as well as forming a complete set over the entire mapped space, rather than just within the cavity. Different methods exist on obtaining the energy emitted to the far-field and used in normalising the QNMs, with a recent review outlining the current methodologies seen in literature [90].

In recent years, there have been significant advancements in the development of quasi-normal analyses for such open and dissipative nanophotonic environments, with some notable examples being: the auxiliary-field eigenvalue method [61, 71, 93], the

time-domain method [96, 97], and the pole-search method [89, 98, 99]. In this thesis, we use the QNM methodology developed by Lalanne et al. [61, 71, 93], where the auxiliary-fields are used to account for the dispersive behaviour of the metals and to linearise the eigenvalue problem [71, 100–106]. This returns each QNM's eigenvector (i.e. EM near-field vectors) and their corresponding complex eigenfrequencies (i.e. eigenvalues): $\tilde{\omega}_i = \omega_i - i\kappa_i$, where the real part ($\omega_i$) is the spectral resonant frequency of the QNM, and the imaginary part (κ_i) is the modal linewidth that describes the total losses attributed to both the radiative and dissipative decay channels of each mode. This method is briefly outlined here and discussed in detail in [61, 71, 72, 93].

In general, the QNMs of a plasmonic system can be found by solving the source-free Maxwell's equations:

$$\begin{pmatrix} 0 & i\varepsilon(\mathbf{r},\tilde{\omega}_i)^{-1}\nabla\times \\ -i\mu(\mathbf{r},\tilde{\omega}_i)^{-1}\nabla\times & 0 \end{pmatrix} \begin{pmatrix} \tilde{\mathbf{E}}_i(\mathbf{r}) \\ \tilde{\mathbf{H}}_i(\mathbf{r}) \end{pmatrix} = \tilde{\omega}_i \begin{pmatrix} \tilde{\mathbf{E}}_i(\mathbf{r}) \\ \tilde{\mathbf{H}}_i(\mathbf{r}) \end{pmatrix} , \tag{3.1}$$

for the modal electric $\tilde{\mathbf{E}}_i(\mathbf{r})$ and magnetic $\tilde{\mathbf{H}}_i(\mathbf{r})$ field vectors—which must satisfy the Sommerfeld radiation condition for outgoing waves to ensure energy leaks away from the system—where $\varepsilon(\mathbf{r},\tilde{\omega}_i)$ and $\mu(\mathbf{r},\tilde{\omega}_i)$ are the position and frequency dependent permittivity and permeability. Here, we consider metallic structures (that have no magnetic optical response) with the electric permittivity described by the N-pole Drude-Lorentz model of equation 1.5:

$$\varepsilon(\omega) = \varepsilon_\infty \left(1 + \sum_{k=1}^{N} \frac{\omega_{p,k}^2}{\omega_{0,k}^2 - \omega^2 - i\gamma_k\omega} \right) , \tag{3.2}$$

where $\omega_{p,k}$, $\omega_{0,k}$ and γ_k are the plasma frequency, resonant frequency and decay rate of the k-th Drude-Lorentz pole, respectively, and ε_∞ is the asymptotic permittivity. This introduces a non-linearity into the eigenvalue problem, due to the dependence of the metal's optical response on the resonant frequency. However, the Hamiltonian of the system can be linearised through the introduction of a pair of auxiliary fields [61]:

$$\tilde{\mathbf{P}}_{i,k}(\mathbf{r}) = \frac{\varepsilon_\infty \omega_{p,k}^2}{\omega_{0,k}^2 - \tilde{\omega}_i^2 - i\gamma_k \tilde{\omega}_i} \tilde{\mathbf{E}}_i(\mathbf{r}) \tag{3.3}$$

$$\tilde{\mathbf{J}}_{i,k}(\mathbf{r}) = -i\tilde{\omega}_i \tilde{\mathbf{P}}_{i,k}(\mathbf{r}) \ , \tag{3.4}$$

where $\tilde{\mathbf{P}}_{i,k}$ and $\tilde{\mathbf{J}}_{i,k}$ are respectively the auxiliary polarisation and current vectors of the i^{th} QNM and k^{th} Drude-Lorentz pole of the metal. For a two-pole ($N = 2$) Drude-Lorentz model, the linearised system to be solved is given by:

$$\begin{pmatrix} 0 & -i\mu_0^{-1}\nabla\times & 0 & 0 & 0 & 0 \\ i\varepsilon_0^{-1}\nabla\times & 0 & 0 & -i\varepsilon_\infty^{-1} & 0 & -i\varepsilon_\infty^{-1} \\ 0 & 0 & 0 & i & 0 & 0 \\ 0 & i\omega_{p,1}^2\varepsilon_\infty & -i\omega_{0,1}^2 & -i\gamma_1 & 0 & 0 \\ 0 & 0 & 0 & 0 & 0 & i \\ 0 & i\omega_{p,2}^2\varepsilon_\infty & 0 & 0 & -i\omega_{0,2}^2 & -i\gamma_2 \end{pmatrix} \begin{pmatrix} \tilde{\mathbf{H}} \\ \tilde{\mathbf{E}} \\ \tilde{\mathbf{P}}_1 \\ \tilde{\mathbf{J}}_1 \\ \tilde{\mathbf{P}}_2 \\ \tilde{\mathbf{J}}_2 \end{pmatrix} = \tilde{\omega}_i \begin{pmatrix} \tilde{\mathbf{H}} \\ \tilde{\mathbf{E}} \\ \tilde{\mathbf{P}}_1 \\ \tilde{\mathbf{J}}_1 \\ \tilde{\mathbf{P}}_2 \\ \tilde{\mathbf{J}}_2 \end{pmatrix} , \tag{3.5}$$

where a full description can be found in [61]. This methodology can be employed using the QNM solver 'QNMEig' [94], which is an open-source code utilising COMSOL Multi-physics [52].

In order to implement the above methodology into the COMSOL Multiphysics environment, equation 3.5 is first transformed into a quadratic eigenvalue problem for which stable and efficient algorithms exist:

$$\hat{\mathbf{K}} \begin{pmatrix} \tilde{\mathbf{E}}_m \\ \tilde{\mathbf{P}}_m \end{pmatrix} + \tilde{\omega}_m \hat{\mathbf{C}} \begin{pmatrix} \tilde{\mathbf{E}}_m \\ \tilde{\mathbf{P}}_m \end{pmatrix} + \omega_m^2 \hat{\mathbf{M}} \begin{pmatrix} \tilde{\mathbf{E}}_m \\ \tilde{\mathbf{P}}_m \end{pmatrix} = 0 \ , \tag{3.6}$$

where $\hat{\mathbf{K}} = \begin{pmatrix} \nabla \times \mu_0^{-1} \nabla \times & 0 \\ \varepsilon_\infty & \omega_m^2 \end{pmatrix}$ is the stiffness matrix, $\hat{\mathbf{C}} = \begin{pmatrix} 0 & 0 \\ 0 & i\gamma \end{pmatrix}$ is the damping matrix, and $\hat{\mathbf{M}} = \begin{pmatrix} -\varepsilon_\infty & -1 \\ 0 & 1 \end{pmatrix}$ is the mass matrix. The coupled partial differential equations are first converted into their equivalent weak formulations which, for a system of multiple Lorentz-poles, has the form [61]:

$$\int_V \nabla \times \mathbf{F}(\mathbf{r}) \cdot \mu^{-1} \nabla \times \tilde{\mathbf{E}}_m(\mathbf{r}) - \tilde{\omega}_m^2 \varepsilon_\infty \mathbf{F}(\mathbf{r}) \cdot \tilde{\mathbf{E}}_m(\mathbf{r}) - \omega_m^2 \mathbf{F}(\mathbf{r}) \cdot \sum_i \tilde{\mathbf{P}}_{m,i}(\mathbf{r}) d^3\mathbf{r} = 0 \tag{3.7}$$

$$\int_V \varepsilon_\infty \omega_p^2 \mathbf{F}(\mathbf{r}) \cdot \tilde{\mathbf{E}}_m(\mathbf{r}) - \omega_0^2 \mathbf{F}(\mathbf{r}) \cdot \tilde{\mathbf{P}}_{m,i}(\mathbf{r}) + i\tilde{\omega}_m \gamma_i \mathbf{F}(\mathbf{r}) \cdot \tilde{\mathbf{P}}_{m,i}(\mathbf{r}) + \tilde{\omega}_m^2 \mathbf{F}(\mathbf{r}) \cdot \tilde{\mathbf{P}}_{m,i}(\mathbf{r}) d^3\mathbf{r} = 0 \ , \tag{3.8}$$

where $\mathbf{F}(\mathbf{r})$ is an arbitrary smooth function, usually referred to as the test function. This may then be directly entered into COMSOL to perform a finite-element numerical eigensolution, and obtain the eigenvalues (complex resonant frequencies) and eigenvectors (near-field EM vectors) of the above linearised system [93]. Note that the scattering cross-sections may be obtained from this methodology, through a reconstruction process of the

QNMs—as discussed in our collaborative work that can be found in [107]—without the need to run additional COMSOL calculations.

3.3 POLYHEDRON-ON-MIRROR NANOCAVITIES

During the fabrication of NPs, the crystalline nature of gold leads to the formation of polyhedral shapes: each of which exhibit multiple facets with various shapes and, when assembled on a mirror, tend to do so with one facet parallel to the mirror. To date, we have theoretically modelled faceted NPoM geometries by truncating a perfectly spherical NP to form the TSoM geometry [72, 84], which assembles on the mirror with its circular facet—as shown in Figure 3.1A. To allow comparison of the TSoM geometry with the polyhedral NPoM assemblies and to introduce the nomenclature used, here we initially perform a QNM analysis on the TSoM geometry with: a NP of radius $r_p = 40$ nm, a circular facet of diameter $f_d = 20$ nm, and a spacer of thickness $d = 1$ nm with refractive index $n = 1.45$.

3.3.1 TSoM NANOCAVITY

Figure 3.2 (top row) shows the first six normalised electric field distributions on a plane through the centre of the TSoM nanocavity (parallel to the mirror) in order of increasing energy, highlighting the clear confinement within the bounds of the circular facet. The spherical harmonic nomenclature developed in [72] for identifying and labelling the set of supported QNMs is used here, with each QNM labelled according to (l, m)—for a set

of positive integers l and $-l \leq m \leq l$. The nomenclature shows that all modes with $m = 0$ have an anti-node at the centre of the nanocavity, and all $m \neq 0$ modes have a central node. More specifically, the $(1, 0)$ mode exhibits a large anti-node, whereas the

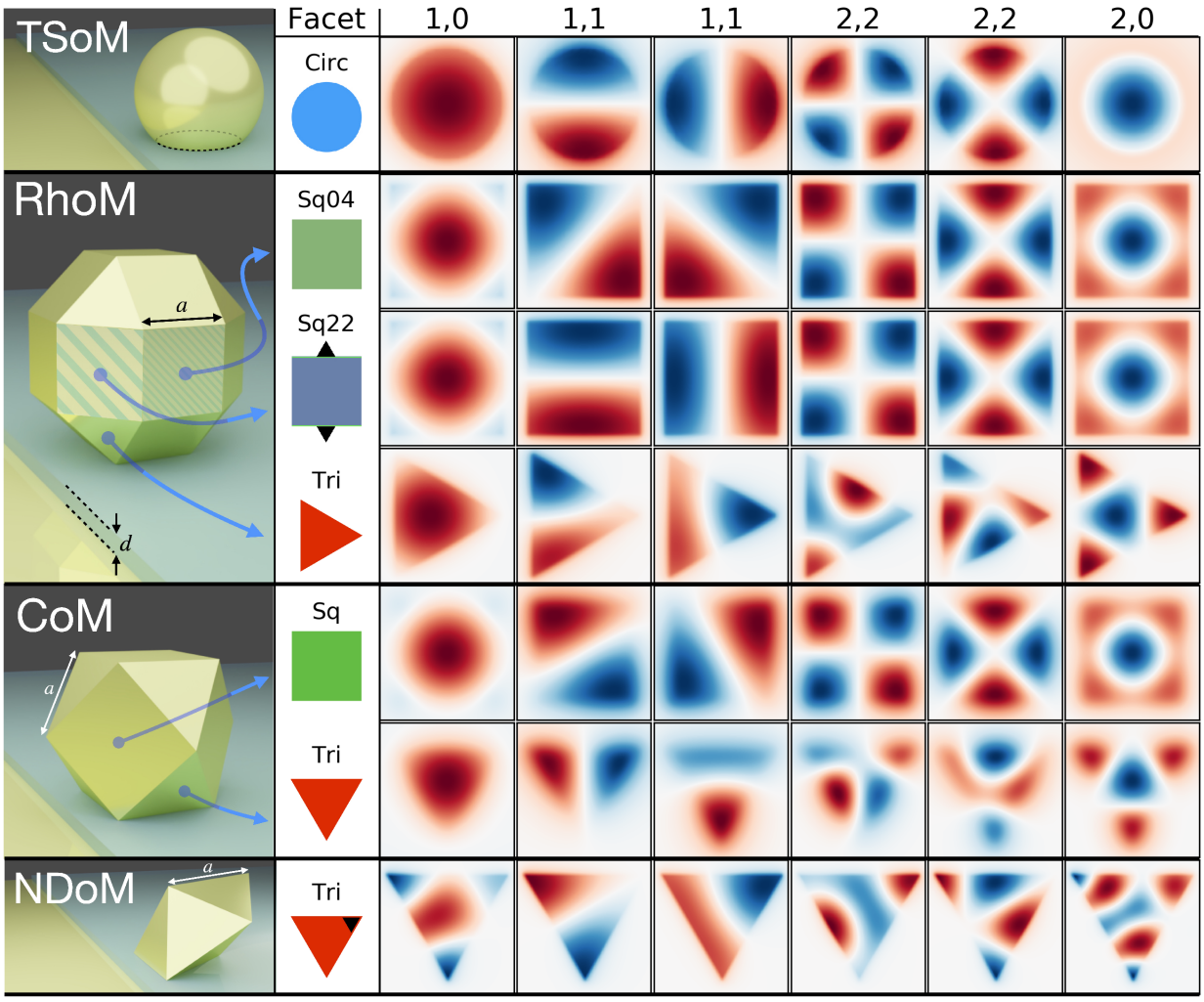

Figure 3.2: QNMs of the different NPoM structures, for a characteristic edge length a and spacer thickness d. The geometries from top to bottom are the: circular facet of the TSoM; two square and one triangular facets of the RhoM; singular square and triangular facets of the CoM; and the triangular facet of the NDoM. The modes from left to right are: $(1, 0)$, $(1, 1)$, $(1, 1)$, $(2, 2)$, $(2, 2)$, $(2, 0)$, where the colour corresponds to the normalised QNM electric fields (Re[$E_{z,lm}$]) on the xy-plane through the centre of their respective cavities.

pair of $(1,1)$ modes display $2m$-lobed field distributions. Higher order m-modes extend this nature, such as the 4-lobes of the $(2,2)$ modes. Whereas higher order l-modes see a concentric confinement of the mode within the facet—as shown by the $(2,0)$ mode, which has an additional anti-node ring surrounding the central extrema in comparison to the $(1,0)$ mode. Note that the cylindrical symmetry of the facet means that $(l,|m|)$-mode pairs are energetically degenerate and their numerically identified orientation angle is arbitrary, with the only restriction being that the modes in each pair are orthogonal to each other.

To aid the visualisation of the modes' energetic ordering and degeneracies, we show the spectral behaviour of the TSoM modes (top row) in Figure 3.3. Each QNM's complex eigenfrequency ($\tilde{\omega}_i = \omega_i - i\kappa_i$)—obtained from the numerical QNM calculations—is fitted to a Lorentzian:

$$L(\omega) = \frac{(\kappa_i/2)^2}{(\kappa_i/2)^2 + (\omega - \omega_i)^2} \,, \tag{3.9}$$

such that its resonant frequency and linewidth are respectively described by Re$\{\tilde{\omega}\}$ and Im$\{\tilde{\omega}\}$. Note that dashed lines are used to represent degenerate modes.

Here we consider the three most common NP shapes that occur during fabrication due to the crystalline nature of gold: (a) rhombicuboctahedron, (b) cuboctahedron, and (c) decahedron—as shown in Figure 3.1. Note that for each of the polyhedron shapes, every edge is equal in length. Therefore, instead of a NP radius, these geometries can be parameterised by their characteristic edge length, which here are taken to be $a_{\text{RhoM}} = 30$ nm, $a_{\text{CoM}} = 8$ nm, and $a_{\text{NDoM}} = 47$ nm, respectively for the rhombicuboctahedron, cuboctahedron and decahedron NPs. These values were chosen such that their respective $(1,0)$

modes have the same resonant frequency (Re$\{\tilde{\omega}\}$), which helps highlight the spectral positioning of all other modes relative to the $(1, 0)$ mode.

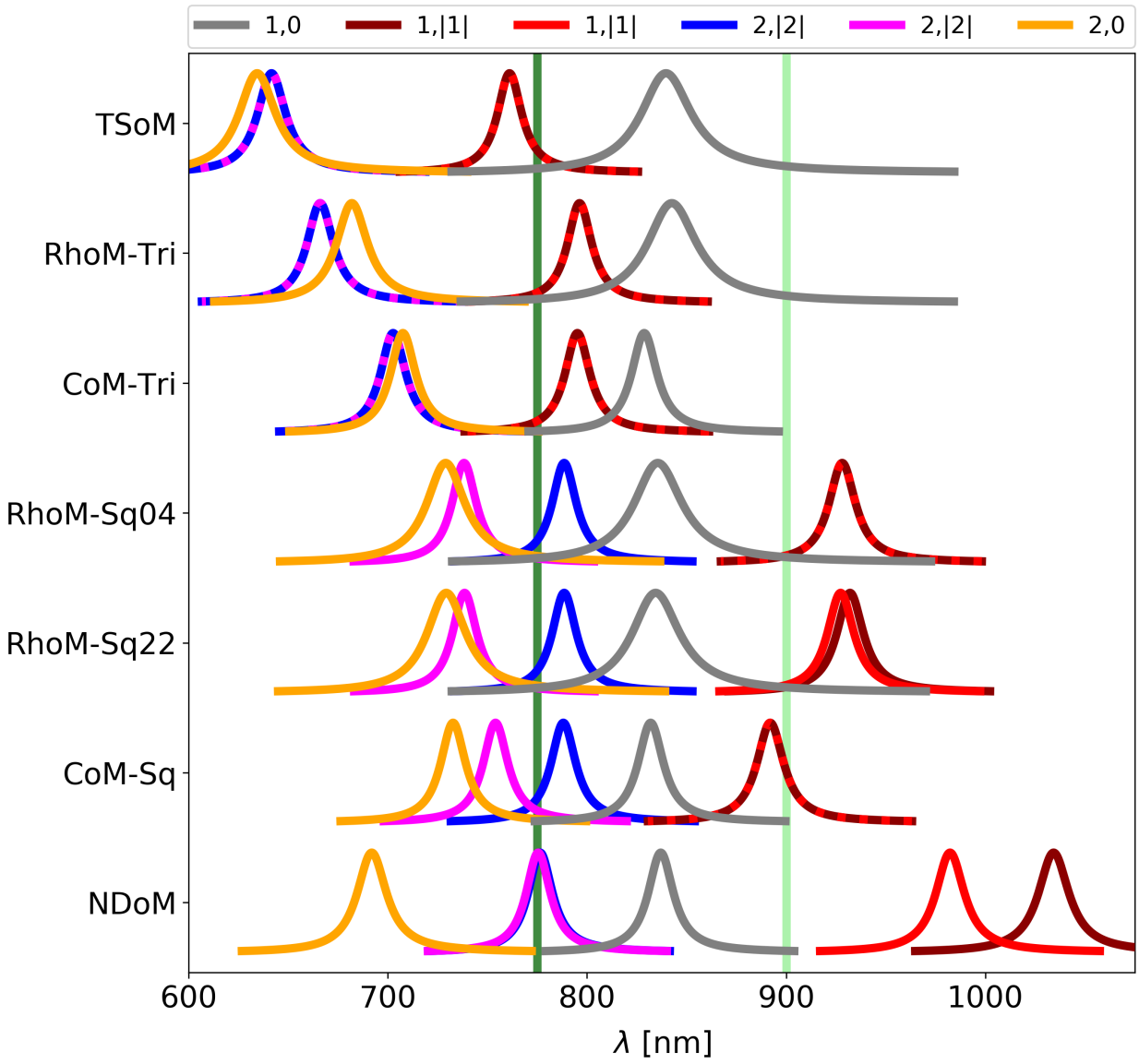

Figure 3.3: Complex QNM eigenfrequencies fitted to Lorentzians, showing their spectral arrangement and energetic ordering for the: circular facet of the TSoM; two square and one triangular facets of the RhoM; singular square and triangular facets of the CoM; and the triangular facet of the NDoM. Dashed lines represent degenerate QNMs. Vertical lines mark the wavelengths of (dark green) 775nm and (light green) 900nm.

When these polyhedral NPs are assembled on a mirror, they yield unique nanocavity systems due to the multiple distinct facets of each NP that can be assembled onto the mirror (see Figure 3.2) [107]. More specifically, the rhombicuboctahedron-on-mirror (RhoM) system has three unique arrangements on the mirror: two square facets, one with four square neighbouring facets (Sq04) and one with two square and two triangular neighbours (Sq22); and one triangular facet [78] (see Figure 3.2). The cuboctahedron-on-mirror (CoM) system has two unique arrangements on the mirror—one square and one triangular facet—whereas the decahedron NP has ten identical triangular facets, and therefore only offers a singular unique facet with which the nanodecahedron-on-mirror (NDoM) can be assembled [1].

For each of these structures a background material of air is considered, along with the same spacer of thickness $d = 1$ nm and refractive index $n = 1.45$. To ensure that our calculations represent realistic systems, we have rounded the edges of the polyhedral NPs with a curvature of $\rho = 1$ nm—as shown in Figure 3.4—which means that approximately three gold atoms are forming each edge.

3.3.2 RhoM NANOCAVITY

The first polyhedral structure considered here is the RhoM geometry assembled on its Sq04 facet, whose QNMs are shown in the second row of Figure 3.2 beneath the corresponding (l, m) mode of the TSoM—to aid in their comparison. Although the RhoM-Sq04

[1] Examples of CoM and NDoM geometries were built in COMSOL by Eoin Elliott, University of Cambridge. All calculations were performed by Kalun Bedingfield, University of Birmingham.

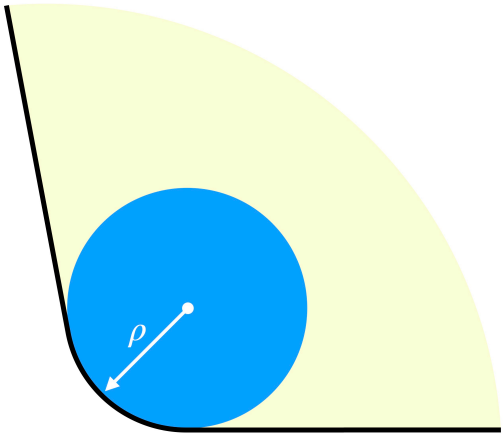

Figure 3.4: Schematic showing the edge rounding, ρ, to each polyhedral geometry.

nanocavity does not have a cylindrical symmetry (as the TSoM does), it is apparent that the same spherical harmonic nomenclature can still be adopted here to adequately identify and describe these modes. Here the $(1,0)$ mode is distorted to the square shape of the facet, but retains the same spatial characteristic with a circular central anti-node, as for the TSoM. Unlike the cylindrical symmetry of the TSoM and the arbitrary orientation of its modes, the $(1,1)$ modes of the RhoM-Sq04 preferentially orientate towards the facet corners, due to the greater charge concentration there. Due to the four-fold symmetry of the RhoM when assembled on this facet, the $(1,1)$ modes remain orthogonal and energetically degenerate (similarly to the TSoM's $(1,1)$ modes). Figure 3.3 also shows the redshifting of the $(1,1)$ modes and the unusual observation of higher order modes being more energetically favourable than the $(1,0)$ mode. This same symmetry, however, causes the two $(2,2)$ modes to lose their degeneracy (see Figure 3.3), since one of the $(2,2)$ modes has its anti-nodes in the corners of the facet—where the charges are more favourably concentrated—while the second $(2,2)$ mode is orthogonally arranged with its anti-nodes at the less-confined facet edges, forcing them to lose their degeneracy. The

RhoM-Sq04 $(2, 0)$ mode has two concentric anti-nodes that are more clearly confined to the bounds of the square facet.

The Sq22 facet of the rhombicuboctahedron NP has the same size and shape as its Sq04 facet, and therefore forms a geometrically identical nanocavity when assembled on the mirror (RhoM-Sq22). One can therefore easily assume that the QNMs in the gap of the RhoM-Sq22 system would be identical to those of the RhoM-Sq04 nanocavity. However, the RhoM-Sq22 system carries a two-fold symmetry (instead of the four-fold symmetry of the RhoM-Sq04) due to the pair of triangular facets neighbouring the Sq22 facet—as indicated by the small black triangles in the RhoM-Sq22 inset of Figure 3.2. These triangular facets lie at an angle slightly closer to the mirror compared to the neighbouring square facets, which increases the field confinement along the edges adjacent to them. This creates an effectively elongated facet for the EM fields due to an unequal charge confinement supplied by the neighbouring square and triangular facets. Although the $m = 0$ modes are largely unchanged compared to the RhoM-Sq04 modes, the broken geometrical symmetry of the RhoM-Sq22 nanocavity has a significant impact on the rest of the modes. The pair of $(1, 1)$ modes reorientate to instead align with the sides of the facet rather than the corners—preserving their orthogonality. However, the unequal charge confinement across the facet breaks the degeneracy of the $(1, 1)$ modes (see Figure 3.3), with the mode directed between the neighbouring two triangular facets being more energetically favourable. Interestingly, the $(2, 2)$ modes retain their orientations compared to their RhoM-Sq04 counterparts, but due to the unequal charge confinement across the Sq22 facet, the second $(2, 2)$ mode loses its central node—with significant consequences

to the far-field emission, as discussed later. Note that for a larger edge rounding, the elongated confinement across this facet is much more profound, with a visible stretching of the $(2,0)$ mode and more pronounced loss of the second $(2,2)$ mode's central node; Appendix Figure A8 compares the near-field modes of the RhoM-Sq22 with 1 nm and 5 nm rounding.

The final unique orientation of the RhoM geometry sees the assembly of the NP on its triangular facet (RhoM-Tri). Although the morphology of this facet is significantly different to both the circular and square facets seen so far, the same spherical harmonic nomenclature applies for its QNMs. The $(1,0)$ mode is clearly identifiable, with the single central anti-node confined to the bounds of the triangular facet. Due to the mismatch between the two lobes of the $(1,1)$ modes and the three-fold symmetry of the triangular facet, the $(1,1)$ modes are less energetically favourable than the $(1,0)$ mode; however, they remain orthogonal to each other and are energetically degenerate (see Figure 3.3). Similarly, the $(2,2)$ modes remain degenerate, but the three-fold symmetry of the geometry alters the charge distributions such that the nodal lines do not cross. The $(2,0)$ mode now exhibits stronger fields concentrations in the three corners of the facet, but otherwise remains unchanged. Even though we have so far discussed the nanocavities formed by just one polyhedral NP shape (the rhombicuboctahedron), the formation of three distinct nanocavities have been identified—each exhibiting a different optical response.

3.3.3 CoM NANOCAVITY

We next consider the CoM geometry, which can create nanocavities with either a square or triangular facet. When assembled on its square facet (CoM-Sq), it has the same facet shape and four-fold symmetry as the RhoM-Sq04, and supports an almost identical set of QNMs—with energetically degenerate $(1,1)$ modes and spectrally split $(2,2)$ modes. When instead assembled on the mirror with its triangular facet (CoM-Tri), the facet shape and three-fold symmetry of the CoM-Tri geometry lead to a very similar set of QNMs as those supported by the RhoM-Tri. Note that the edge length of the cuboctahedron NP considered here is $a_{CoM} = 8$ nm, which is much smaller than the edge length of the rhombicuboctahedron NP ($a_{RhoM} = 30$ nm). The edge length dictates the frequency regime in which the modes appear, and were chosen such that each system's $(1,0)$ mode has the same resonant frequency (see Figure 3.3). However, since the rounding was kept the same for each structure—at $\rho = 1$ nm—there is softer charge confinement at the edges of the CoM facets. The smaller facet areas and proportionally larger rounding (with respect to the edge length) of the CoM leads to much less pronounced QNM field confinements. For further discussion see Appendix A11, where the CoM geometry for edge lengths of $a_{CoM} = 8$ nm and $a_{CoM} = 20$ nm are compared.

3.3.4 NDoM NANOCAVITY

Finally, we consider the NDoM geometry that has ten identical triangular facets, allowing for a single unique facet assembly on the mirror (see Figure 3.2). The slanting of the decahedron NP leads to a strong asymmetry in the field confinement across the facet, with the black triangle in the inset of Figure 3.2 (bottom row) indicating the corner of the facet that sits underneath the NP and receives the weakest confinement. This unequal field confinement leads to an 'effective' facet centre that lies slightly closer to the corner under the NP, instead of the equilateral triangular facet's centre. This distorts the set of QNMs supported by the NDoM nanocavity, compared to those observed for the RhoM-Tri and CoM-Tri geometries. The $(1,0)$ mode is most affected by this asymmetry and 'effective' facet centre, which appears to push the charge distributions towards the corner under the NP—so much so that additional concentric anti-nodes appear. A similar behaviour is observed for higher order $m = 0$ modes, with the $(2,0)$ mode changing profile significantly. Although the $(1,1)$ modes appear similar to those of the RhoM-Tri and CoM-Tri, the unequal confinement across the facet leads to the loss of their degeneracy and a large spectral separation (see Figure 3.3). Due to the form of the $(2,2)$ modes, however, they are negligibly affected by this weakly confined corner underneath the NP and just about lose their degeneracy. Note that the NDoM exhibits a wide spectral range due to the large size of the structure, in comparison to the narrow spectral breadths of the much smaller CoM assemblies.

3.4 MODAL FAR-FIELD EMISSION PROFILES

Having obtained the QNMs and complex eigenfrequencies of these polyhedral NPoM geometries—observing the effects of NP symmetry and nanoscale changes of the facet morphology—it is now prudent to explore how the geometrical differences affect their out-coupling of energy to the far-field. We perform a near-to-far-field-transformation (NFFT) for the QNM near-fields shown in Figure 3.2, in order to obtain the far-field Poynting flux. We use the software RETOP [108, 109]—developed by the Lalanne group and can be found here—which is designed to implement NFFTs for stratified media with dispersive elements [72, 110–112]—such as the nanocavities discussed here. The QNM electric $\tilde{\mathbf{E}}_{lm}(\mathbf{r})$ and magnetic $\tilde{\mathbf{H}}_{lm}(\mathbf{r})$ fields of each (l, m) mode are considered on a region enclosing the NP, ensuring that it intersects all material layers of the system: in our case this is the mirror, spacer and air domains—see the red box in Figure 3.5A. These near-fields $(\tilde{\mathbf{E}}_{lm}(\mathbf{r}), \tilde{\mathbf{H}}_{lm}(\mathbf{r}))$ are projected to the far-field $(\tilde{\mathbf{E}}^{ff}_{lm}, \tilde{\mathbf{H}}^{ff}_{lm})e^{i\omega_{em}R/c}$ on a hemispherical dome of radius $R = 1$m above the NPoM geometry, at a frequency ω_{em}—see the red dome in Figure 3.5B. From these far-fields, the time-average Poynting flux $\langle S_{lm}\rangle = \text{Re}[\tilde{\mathbf{E}}^{ff\,*}_{lm} \times \tilde{\mathbf{H}}^{ff}_{lm}]/2$ is calculated for each (l, m) mode as a function of the polar (θ) and azimuthal (ϕ) angles of the dome, where the polar angle is zero at the top.

The far-field emission patterns are shown in Figure 3.6, where the time-averaged Poynting fluxes $\langle S_{lm}\rangle$ are plotted for each of the structures discussed above—with each mode corresponding to their near-field counterpart in Figure 3.2. We initially introduce

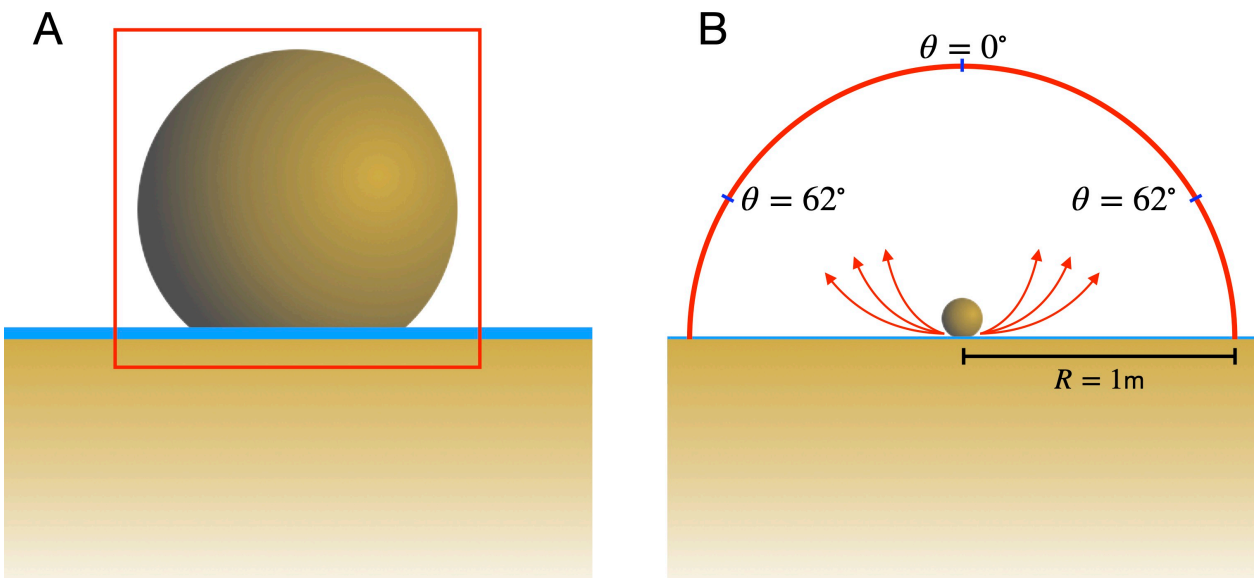

Figure 3.5: A. Schematic showing how RETOP calculates the far-field emission of inhomogeneities in stratified media. The electric and magnetic field components are collected on the surface of a box that surrounds the NP and intersects all material layers. B. The dome over the NP on which the far-field electric and magnetic field components are calculated, at a distance of 1 m away from the NP. The polar angle across this hemisphere is centered on the NP, reaching $90°$ at the mirror.

the far-field emission patterns for the TSoM geometry—with its cylindrically symmetric circular facet—that have previously been discussed in [72]. All $m = 0$ modes emit in a conical shape—with the maximum energy occurring at $\theta = 62°$ [7, 113, 114]—whereas the pair of $(1, 1)$ modes largely emit normally away from the mirror, with smaller contributions following their near-field lobes (as shown by the white dashed lines) [78]. All other $m > 1$ modes exhibit $2m$-lobes of equal intensity, emitted conically away from the mirror at the same angle of $\theta = 62°$. Each pair of $m \neq 0$ modes retain their orthogonality in the far-field, as well as the directionality of their near-field counterparts.

It should be noted that the NFFT used to obtain the far-field emissions in Figure 3.6 is extremely sensitive to the EM fields obtained from the numerical QNM calculations,

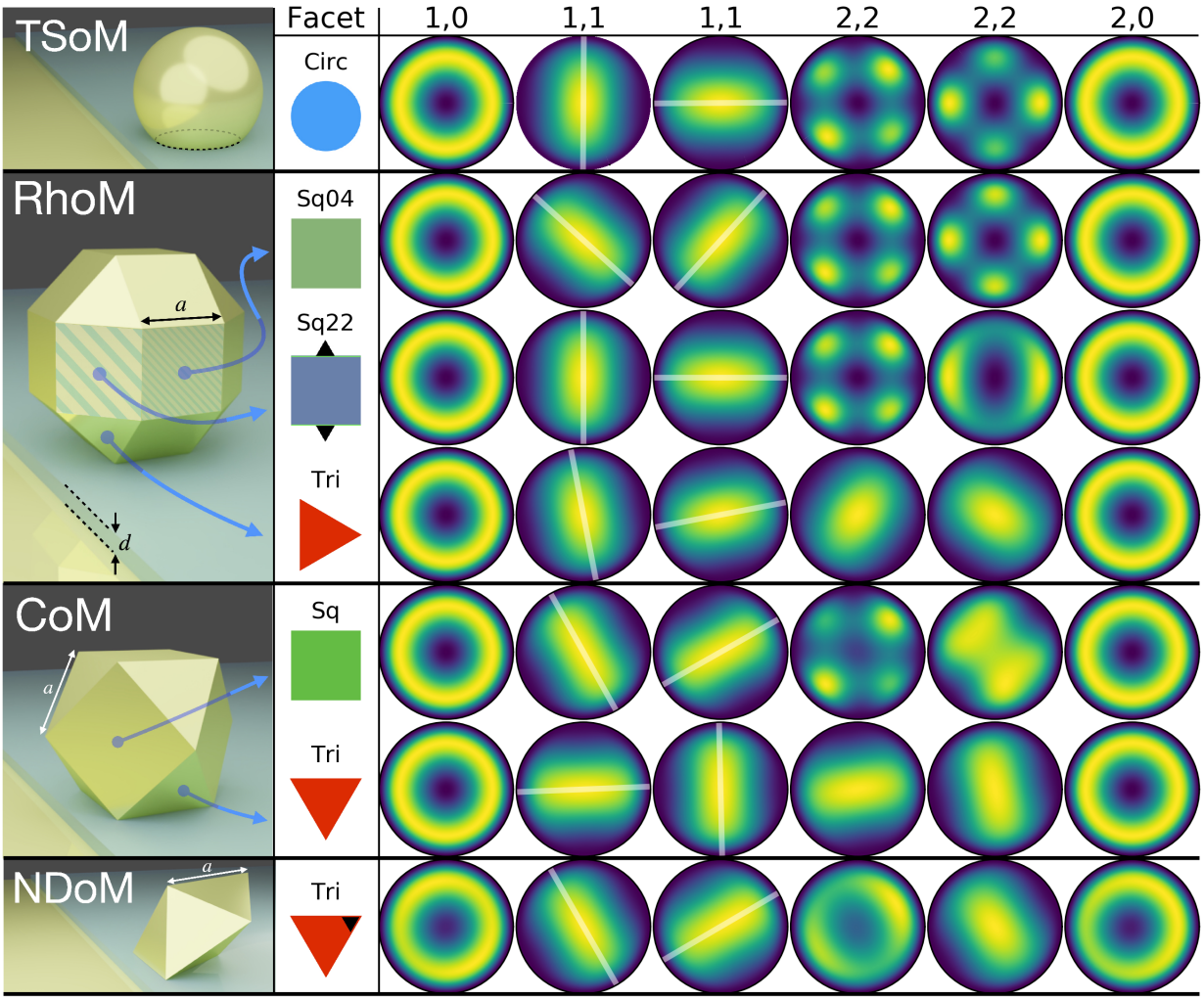

Figure 3.6: Far-field emission for the QNMs of the different NPoM structures, for a characteristic side length a and spacer thickness d. The geometries from top to bottom: circular facet of the TSoM; two square and one triangular facets of the RhoM; singular square and triangular facets of the CoM; and the triangular facet of the NDoM. The modes from left to right: $(1,0)$, $(1,1)$, $(1,1)$, $(2,2)$, $(2,2)$, $(2,0)$, where the colour corresponds to the normalised time averaged Poynting flux $\langle S_{lm} \rangle$. Thin white lines are added over the $(1,1)$ modes to highlight the correspondence of their direction and orthogonality with their near-field counterparts.

for which a lot of attention was paid and extensive optimisation was performed—with increasingly finer meshing required for higher order modes. This introduces some small numerical errors that lead to the intensity variations seen for some far-field lobes. In fact, with our current computational capabilities it is too expensive to distinguish the far-field lobes for modes of $m > 3$.

Returning to the polyhedron-on-mirror nanocavities discussed above, the far-field emission patterns are shown in Figure 3.6 for which we explore the effects of morphological facet intricacies and geometrical symmetries—as observed in each mode's near-field charge distribution. All $m = 0$ modes emit with a conical shape and have the same maximum emission angle of $\theta = 62°$, regardless of the nanocavity's morphology [78]. The $(1, 1)$ modes are similarly consistent across all nanocavities, emitting largely normally to the mirror but also with smaller contributions that align with the near-field lobes of each mode—therefore preserving the orthogonality between each mode pair; the only difference between the $(1, 1)$ modes of each nanocavity system is the azimuthal orientation of their far-field emissions. Similarly, the $(2, 2)$ modes mostly retain their four-lobed emission patterns for nanocavities formed with a square facet (i.e. RhoM-Sq04, RhoM-Sq22, CoM-Sq), and again closely follow their near-field distributions.

A notable exception is the second $(2, 2)$ mode of the RhoM-Sq22 nanocavity, whose near-field appears elongated due to the more shallow inclination of the neighbouring triangular facets—compared to the neighbouring square facets—which breaks the four-fold symmetry of the facet. As discussed earlier, this 'effective' elongation of the facet destroys

the node at the centre of the second $(2,2)$ mode, which now experiences a non-zero E_z-field. This has the remarkable ability to completely dominate the emissive response of the system, which instead acquires a more conical far-field emission—with the peak intensity at the same $\theta = 62°$. By increasing the edge rounding from $\rho = 1$ nm to $\rho = 5$ nm, the far-field profile becomes almost identical to an $m = 0$ mode—as shown in Appendix Figure A8 for a $\rho = 5$ nm rounding. Additionally, the second $(2,2)$ mode of the CoM-Sq nanocavity appears to be an exception to the general four-lobed emission of most $(2,2)$ modes. However, the unconventional far-field emission of this mode is due to the small size of the NP ($a_{CoM} = 8$ nm), which leads to a relatively large rounding of the edges and a non-ideal confinement of the fields within the nanocavity. If one increases the edge length of the cuboctahedron NP to $a_{CoM} = 20$ nm, this mode regains its four-lobe far-field emission—see Appendix Figure A9.

Although the $m = 0$ and $(1,1)$ modes of nanocavities formed with triangular facets retain the same far-field emissions as the TSoM nanocavity, the $(2,2)$ modes lose their four-lobed emission. Interestingly, they instead emit normally away from the mirror and very similarly to the extended single anti-node of $(1,1)$ modes—with almost identical far-field patterns observed for both the RhoM-Tri and CoM-Tri nanocavities. This is due to the four-fold symmetry of the TSoM's $(2,2)$ modes 'squeezed' within a triangular facet (see Figure 3.2), which destroys its four-fold symmetry. Instead, the 'overall' far-field response is dominated by the dipoles that form between the anti-nodes of the near-field charge distributions which posses opposite signs; this results in far-field emissions that are very similar to $(1,1)$ modes, whose directionality is dictated by these anti-node dipoles (see

Figure 3.2)—remarkably still retaining their mode orthogonalities.

Furthermore, the NDoM geometry—that only creates triangular nanocavities—also exhibits different far-field emissions for the $(2, 2)$ modes. The decahedron NP assembled on the mirror creates an asymmetric geometry that causes unequal confinement across the triangular facet; this effectively shifts the centre of the facet closer to the corner of the facet that sits underneath the NP (indicated with a black triangle in Figure 3.6) and adds an 'effective' elongation to the near-fields of both the $(2, 2)$ modes. This causes the near-fields of the second $(2, 2)$ mode to resemble the first $(1, 1)$ mode, and therefore emit to the far-field in a similar manner—normally away from the mirror. The first $(2, 2)$ mode behaves similarly, but additionally loses its central lobe in the near-field; its far-field emission is therefore a superposition of a conical emission (similar to $m = 0$ modes) and a normal emission (similar to a $(1, 1)$ mode). Finally, this 'effective' elongation of the facet impacts the far-field emission of the $(2, 0)$ mode which, although still conical, is now asymmetric—with higher intensity along the azimuthal angle that aligns with the 'effective' centre of the triangular facet.

3.5 TOTAL FAR-FIELD EMISSION PROFILES

Even though some modes appear unaffected by the large geometrical differences between these nanocavities, the far-field profiles of other modes show an extraordinarily strong dependence on the exact morphology of the facet and the symmetry of the overall

system. Although the far-field emissions of these polyhedral NPoM geometries are crucial for understanding how each mode couples energy out of the cavity to reach the far-field, one cannot excite QNMs individually. For example, an emitter in the cavity couples to many modes, forming an overall optical response that is dependent on both the spatial and spectral properties of each mode and the emitter. Therefore, to calculate the total optical response of a system—and its overall far-field emission—the collective response of all the QNMs must be considered. To do this, a set of coupling coefficients are required that quantify how well each QNM couples to the emitter—at position $\mathbf{r}_{em}$ with transition frequency ω_{em}—and therefore contributes to the total EM fields [72, 93]:

$$\{\tilde{\mathbf{E}}(\mathbf{r}), \tilde{\mathbf{H}}(\mathbf{r})\} = \sum_{lm} \alpha_{lm}(\mathbf{r}_{em}, \omega_{em}) \{\tilde{\mathbf{E}}_{lm}(\mathbf{r}), \tilde{\mathbf{H}}_{lm}(\mathbf{r})\} \ , \tag{3.10}$$

where $\{\tilde{\mathbf{E}}_{lm}(\mathbf{r}), \tilde{\mathbf{H}}_{lm}(\mathbf{r})\}$ are the EM near-fields of mode (l, m), $\{\tilde{\mathbf{E}}(\mathbf{r}), \tilde{\mathbf{H}}(\mathbf{r})\}$ are the total fields and $\alpha_{lm}(\mathbf{r}_{em}, \omega_{em})$ is the excitation coefficient of mode (l, m). In order to find these α-coefficients, an expression for the Lorentz reciprocity theorem must first be obtained.

Consider the time harmonic Maxwell's equations from equation 3.1:

$$\nabla \times \mathbf{E} = i\omega\mu_0 \mathbf{H} \tag{3.11}$$

$$\nabla \times \mathbf{H} = -i\omega\varepsilon(\mathbf{r}, \omega)\mathbf{E} + \mathbf{J}_{ext} \ , \tag{3.12}$$

for which two unique solutions exist: $\{\mathbf{H}_1, \mathbf{E}_1, \omega_1, \mathbf{J}_1\}$ and $\{\mathbf{H}_2, \mathbf{E}_2, \omega_2, \mathbf{J}_2\}$. Through the application of the divergence theorem, $\nabla \cdot (\mathbf{A} \times \mathbf{B}) = (\nabla \times \mathbf{A}) \cdot \mathbf{B} - \mathbf{A} \cdot (\nabla \times \mathbf{B})$, on the

vector $\mathbf{E}_2 \times \mathbf{H}_1 - \mathbf{E}_1 \times \mathbf{H}_2$, the Lorentz reciprocity theorem is given by:

$$\begin{aligned}\iint_S (\mathbf{E}_2 \times \mathbf{H}_1 - \mathbf{E}_1 \times \mathbf{H}_2)\, d^2\mathbf{r} = i \iiint_V \mathbf{E}_1 \cdot [\omega_1 \varepsilon(\mathbf{r}, \omega_1) - \omega_2 \varepsilon(\mathbf{r}, \omega_2)]\, \mathbf{E}_2 \; d^3\mathbf{r} \\ -i \iiint_V \mu_0 \mathbf{H}_1 \cdot (\omega_1 - \omega_2)\, \mathbf{H}_2 \; d^3\mathbf{r} \\ - \iiint_V (\mathbf{J}_1 \cdot \mathbf{E}_2 - \mathbf{J}_2 \cdot \mathbf{E}_1) \; d^3\mathbf{r} \; ,\end{aligned} \tag{3.13}$$

for a surface S enclosing a volume V. An expression for the α-coefficients may be found by inputting the fields of the emitter $\{\mathbf{H}_1 = \mathbf{H}, \mathbf{E}_1 = \mathbf{E}, \omega_1 = \omega_{em}, \mathbf{J}_1 = -i\omega\mu\delta(\mathbf{r} - \mathbf{r}_{em})\}$—where μ is the dipole moment—and the i^{th} QNM $\{\mathbf{H}_2 = \tilde{\mathbf{H}}_i, \mathbf{E}_2 = \tilde{\mathbf{E}}_i, \omega_2 = \tilde{\omega}_i, \mathbf{J}_2 = 0\}$ into the Lorentz reciprocity theorem of equation 3.13 to give:

$$\sum_i B_{i,j}(\omega_{em}) \alpha_j(\mathbf{r}_{em}, \omega_{em}) = -\mu \cdot \tilde{\mathbf{E}}_i(\mathbf{r}_{em}) \; , \tag{3.14}$$

where the matrix $B_{i,j}(\omega)$ is the dipole coupling operator and is given by [72, 93]:

$$B_{i,j}(\omega_{em}) = \iiint_V \tilde{\mathbf{E}}_j \cdot [\omega_{em} \varepsilon(\mathbf{r}, \omega_{em}) - \tilde{\omega} \varepsilon(\mathbf{r}, \tilde{\omega})]\, \tilde{\mathbf{E}}_i - \mu_0 \tilde{\mathbf{H}}_j \cdot (\omega_{em} - \tilde{\omega}_i)\, \tilde{\mathbf{H}}_i \; d\mathbf{r}^3 \; . \tag{3.15}$$

Through the inversion of equation 3.14, the α-coefficients are given by [93]:

$$\alpha_i(\mathbf{r}_{em}, \omega_{em}) = -\omega_{em} \sum_j B^{-1}_{i,j}(\omega_{em}) \mu \cdot \tilde{\mathbf{E}}_j(\mathbf{r}_{em}) \; . \tag{3.16}$$

Here i and j separately sum over the collection of QNMs, which for each of the systems considered here includes twenty modes.

The total far-field emission of each structure is related to its modal components using the same set of α-coefficients, as [72, 93]:

$$\{\tilde{\mathbf{E}}^{ff}(\mathbf{r}), \tilde{\mathbf{H}}^{ff}(\mathbf{r})\} = \sum_{lm} \alpha_{lm}(\mathbf{r}_{em}, \omega_{em})\{\tilde{\mathbf{E}}^{ff}_{lm}(\mathbf{r}), \tilde{\mathbf{H}}^{ff}_{lm}(\mathbf{r})\} \ . \tag{3.17}$$

The total time-average Poynting flux in the far-field is therefore given by $\langle S_{tot} \rangle = \text{Re}[\tilde{\mathbf{E}}^{ff\,*} \times \tilde{\mathbf{H}}^{ff}]/2$, and is dependent on both the transition frequency ω_{em} of the emitter, and its position within the nanocavity $\mathbf{r}_{em}$ [72]. By determining the α-coefficients, the total far-field emission pattern for each polyhedral structure excited by a dipole source within the nanocavity can therefore be identified through the recomposition of each modal emission profile. The resonant frequency of the emitter ω_{em} determines which of the nanocavity's modes will be excited. By consulting the spectral arrangement and localisation of each structure's modes (as shown in Figure 3.3), we identify two frequencies for the dipole emitter—one either side of the $(1, 0)$ mode resonance—at $\lambda_{em} = 775$ nm and $\lambda_{em} = 900$ nm, respectively shown as dark and light green vertical dashed lines. These dipole frequencies were chosen to highlight how the α-coefficients and far-field emissions change as different modes are excited in the system, as well as how the position of the emitter changes.

We start with the nanocavities formed of triangular facets (i.e. CoM-Tri, RhoM-Tri, NDoM-Tri), and plot the α-coefficients for a series of emitter positions P along the height h of the equilateral triangular facet—as shown atop Figure 3.7 Column A, and specifically for each nanocavity in the insets of Figure 3.8—on a plane halfway between the NP facet and

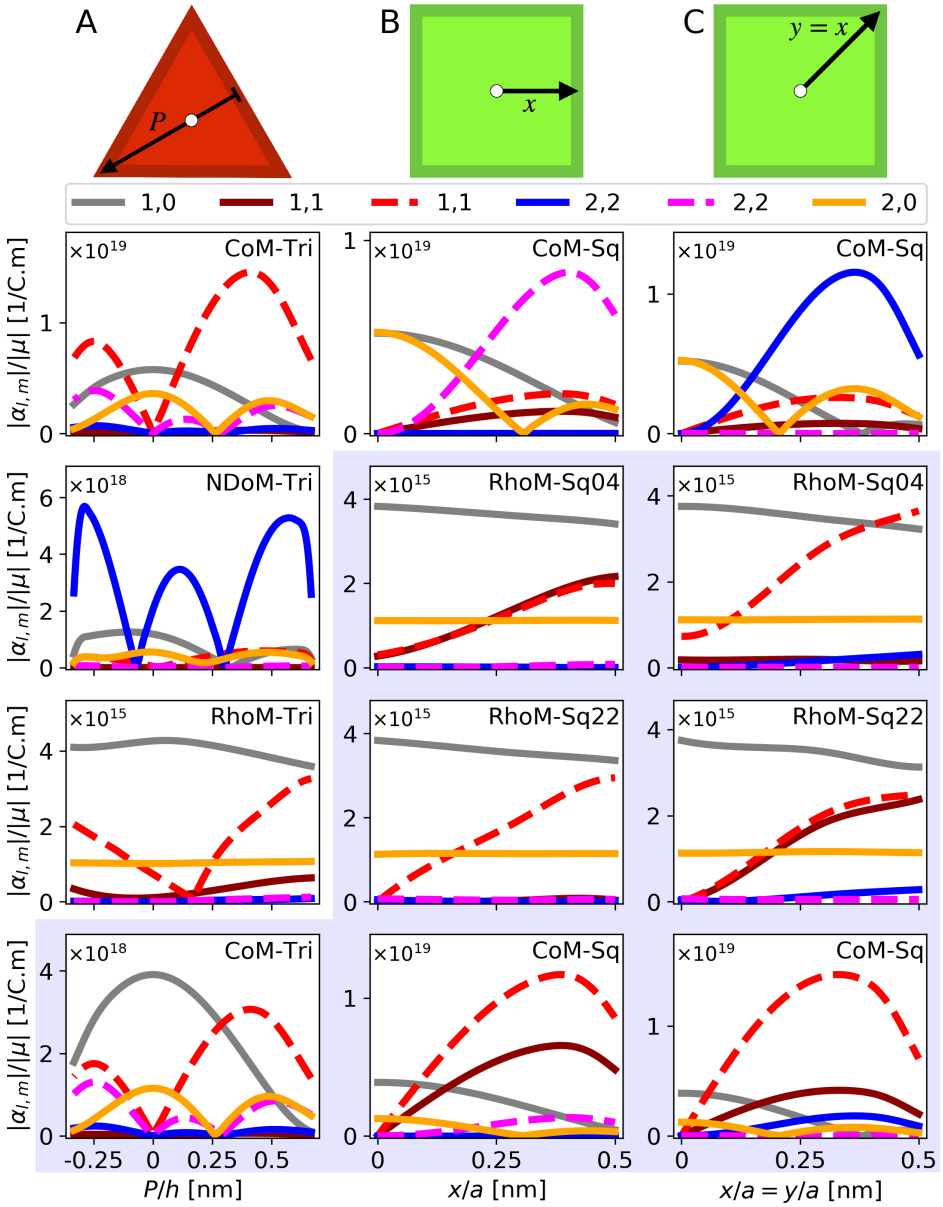

Figure 3.7: α-coefficients of the polyhedral NPoM geometries, for a series of emitter positions within the nanocavities. Column A - The triangular facets of the polyhedral systems, following a path from the facet edge to the opposing corner, through the centre of the facet—normalised to the height of the triangular facet ($h = \sqrt{3}a/2$). Column B - The square facets of the polyhedral systems, following a path along the x-axis from the centre of the facet. Column C - The square facets of the polyhedral systems, following a path along the diagonal from the centre of the facet. White and blue backgrounds respectively correspond to emitter transition wavelengths of $\lambda_{em} = 775$ nm and $\lambda_{em} = 900$ nm.

the mirror. To ensure consistency between our results for each system, the orientation of the path is chosen to follow the nodal line of the first $(1, 1)$ mode's near-field. Note that P is measured relative to the centre of the equilateral triangular facet, and that figures with white (blue) backgrounds show the α-coefficients for a dipole emitter resonant at $\lambda_{em} = 775$ nm ($\lambda_{em} = 900$ nm). More results are shown in Appendix Figure A10.

For the CoM-Tri nanocavity at $\lambda_{em} = 775$ nm, an emitter at the centre of the facet coincides with the anti-nodes of $m = 0$ modes—where $m \neq 0$ modes have no fields—which therefore dominate the α-coefficients. In the negative region of the path $P/h < 0$ (i.e. towards the facet edge), the α-coefficients of the second $(1, 1)$ and $(2, 2)$ modes increase, since this is the region where their near-field anti-nodes exist. Similarly, when the emitter is placed in the positive region of the path ($P/h > 0$), the second $(1, 1)$ mode further dominates due to its stronger near-fields. These values of the α-coefficients dominate the overall far-field emission profile of the CoM-Tri nanocavity, which is shown in Figure 3.8 (top row) for the different positions of the dipole emitter. For $P/h < 0$ the $m = 0$ modes emit relatively efficiently, in addition to the second $(1, 1)$ and $(2, 2)$ modes; together these produce a conical far-field emission with an asymmetry due to the primary coupling on one side of the second $(1, 1)$ and $(2, 2)$ modes. Similarly for an emitter moving towards the positive $P/h > 0$ direction, but gradually the second $(1, 1)$ and $(2, 2)$ modes dominate, producing a far-field emission focused towards a specific solid angle.

For an emitter of $\lambda_{em} = 900$ nm instead, the α-coefficients of the $(1, 0)$ mode completely dominate the rest of the modes (see Figure 3.7) and therefore the far-field emis-

sion too (Figure 3.8, bottom row)—with the $(1,1)$ mode only interfering with the $(1,0)$ mode once the emitter reaches the corner of the triangular facet. This is similarly true for the RhoM-Tri nanocavity, where the $(1,0)$ mode dominates for an emitter with $\lambda_{em} = 775$ nm—evident from the α-coefficient values (see Figure 3.7) and the far-field emissions (Figure 3.8 - third row). Again the second $(1,1)$ mode interferes with the emission of the $(1,0)$ mode only when the emitter is placed at the corner of the triangular facet.

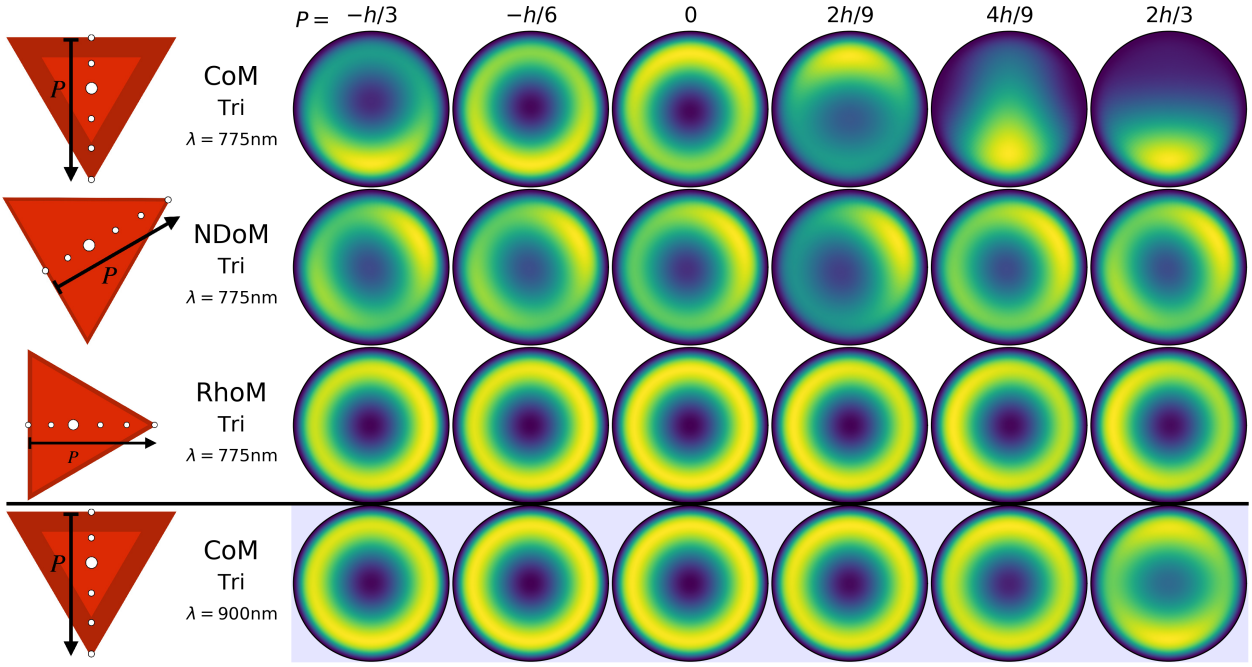

Figure 3.8: Reconstructed total far-field emission of the different particle-on-mirror structures, for a series of emitter positions within the nanocavities. The geometries are the CoM, NDoM and RhoM structures assembled on their triangular facets, with the colour corresponding to the normalised time averaged total Poynting flux $\langle S_{tot} \rangle$. The emitter positions follow a path P, from the facet edge to the opposing corner, through the centre of the facet—and is shown normalised to the height of the triangular facet ($h = \sqrt{3}a/2$). White and blue backgrounds respectively correspond to emitter transition wavelengths of $\lambda_{em} = 775$ nm and $\lambda_{em} = 900$ nm.

In contrast to CoM-Tri and RhoM-Tri nanocavities, the NDoM (that only forms triangular nanocavities) shows a very intriguing behaviour. The α-coefficients show some contribution from the $m = 0$ modes and a negligibly small contribution from the $(1, 1)$ modes—across the entire path of the emitter—and is instead dominated by the first $(2, 2)$ mode (see Appendix Figure 3.7). This is also reflected in the far-field emission patterns (see Figure 3.8, second row), where the first $(2, 2)$ mode primarily contributes. When the emitter is positioned at $P = 2h/9$, the α-coefficient of the first $(2, 2)$ mode becomes comparable in value with the second $(1, 1)$ mode as well as the $m = 0$ modes, which increases the asymmetry in the otherwise conical far-field emission. However, the first $(2, 2)$ mode dominates most of the far-field emission, regardless of the emitter's position, and always exhibiting a 'horse-shoe' emission pattern—as observed experimentally (see Appendix Figure A11). It should be noted that the asymmetry of the decahedron NP induces an 'effective' facet centre that is different to the geometrical centre ($P/h = 0$) of the triangular facet (as discussed earlier), which is clearly evident from the α-coefficient of the $(1, 0)$ mode that peaks at $P/h \sim 0.12$.

We perform a similar study for nanocavities formed with square facets (i.e. CoM-Sq, RhoM-Sq04, RhoM-Sq22). Due to the differing arrangements of the modes' near-fields within these square nanocavities, two paths for the emitter positions are taken for each facet assembly. Both start at the centre of the facet, with one path tracing horizontally towards the facet edge (i.e. along the x-axis)—see Figure 3.7, Column B—and the other diagonally to the facet corner (see Figure 3.7, Column C).

We start with the CoM-Sq nanocavity for an emitter of wavelength $\lambda_{em} = 775$ nm. In Figure 3.7 we see that the $m = 0$ modes are dominant for an emitter at the centre of the facet—as expected from their near-field profiles—but as we move towards the facet edge (corner), we see that the second (first) $(2, 2)$ mode dominates. This is also evident from the far-field emissions shown in Figure 3.9 (first and second rows). When the emitter is at the centre of the facet, a conical emission is observed (coming from the $m = 0$ modes), but as the emitter approaches the facet edge or corner, the respective $(2, 2)$ modes dominate the far-field emission. Note that the stronger excitation of the $(2, 0)$ mode at the corners of the square facet leads to a more conical far-field emission when the emitter is placed closer to the facet corners. If we now consider an emitter resonant at $\lambda_{em} = 900$ nm moving along the same paths within the CoM-Sq nanocavity, we observe a very different behaviour. At this wavelength, an emitter very efficiently couples into the $(1, 1)$ modes and somewhat efficiently into the $(1, 0)$ mode—as the α-coefficients show in Figure 3.7. The $(1, 1)$ modes dominate the far-field emission of the system as the emitter moves away from the facet centre—as shown in Figure 3.9, bottom two rows. The unequal amplitudes of the two $(1, 1)$ modes is due to the orientation of each mode's near-fields, which do not fully align with the corners (or the edges) of the square facet. This is primarily due to the small size of the NP and relatively large curvature (i.e. the field confinement in the gap is not optimal).

Finally, we consider the RhoM-Sq04 nanocavity for an emitter of $\lambda_{em} = 900$ nm, again moving from the centre of the square facet along either horizontal or diagonal paths. The α-coefficients (see Figure 3.7) show that the $(1, 0)$ mode dominates, with both $(1, 1)$

modes increasing as the emitter moves horizontally, and only the second $(1, 1)$ mode increasing as the emitter moves diagonally towards the facet corner. This behaviour is

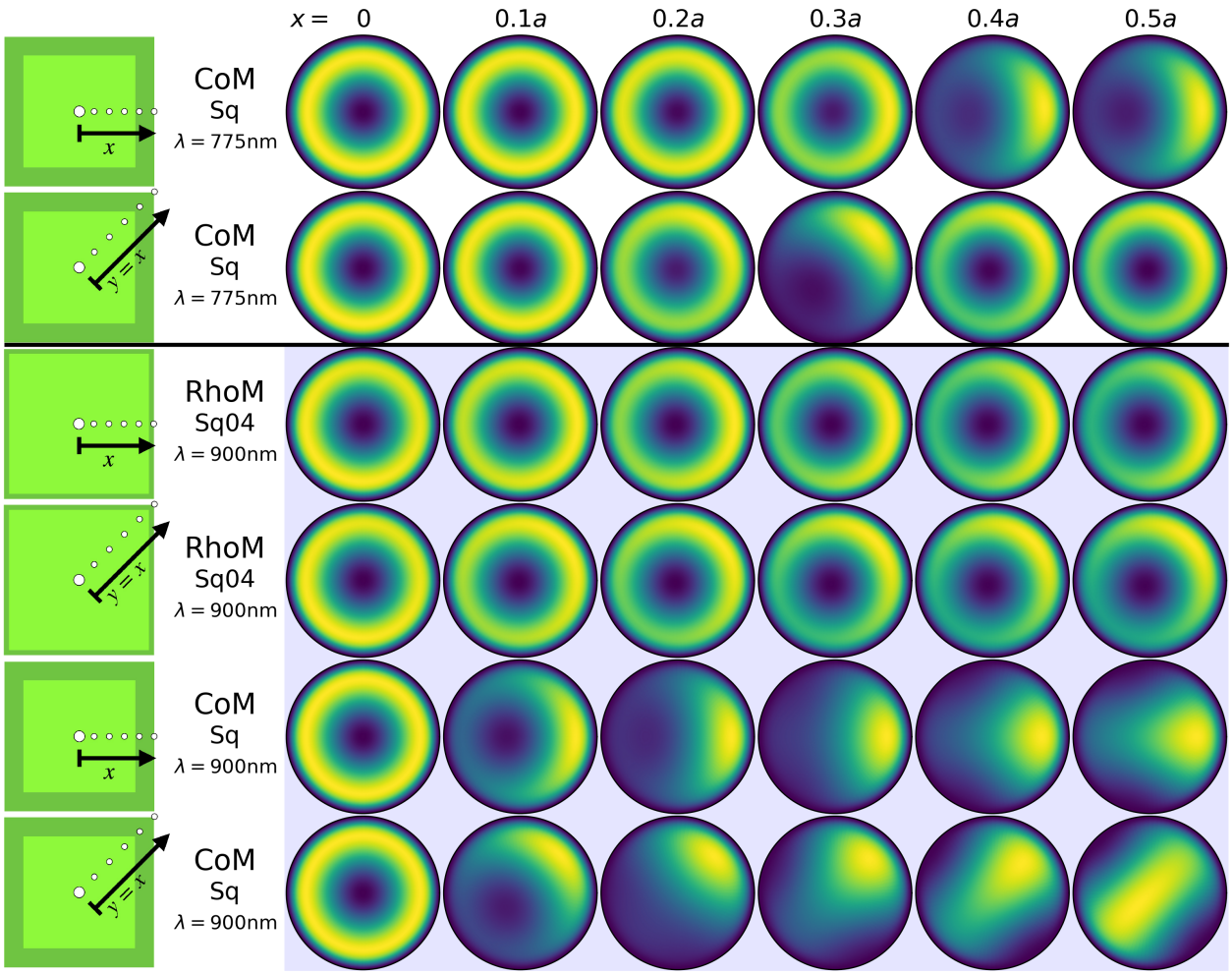

Figure 3.9: Reconstructed total far-field emission of the different particle-on-mirror structures, for a series of emitter positions within the nanocavities. The geometries are the CoM and RhoM structures assembled on their square facets, with the colour corresponding to the normalised time averaged total Poynting flux $\langle S_{tot} \rangle$. For each structure, two emitter paths are considered: one from the centre of the facet to the edge, along the x-axis; and the other from the centre of the facet to the corner, along the diagonal. White and blue backgrounds respectively correspond to emitter transition wavelengths of $\lambda_{em} = 775$ nm and $\lambda_{em} = 900$ nm.

also reflected in the far-field emission patterns shown in Figure 3.9 (third and fourth rows), where an emitter at the centre of the square facet produces a perfect conical emission, but an asymmetric emission emerges as the emitter moves away from the centre. Note that the direction of the far-field emission asymmetry follows the position of the emitter within the nanocavity. The RhoM-Sq22 geometry shares strong similarities in facet shape and spectral arrangements with the RhoM-Sq04 nanocavity, and therefore has a nearly identical set of α-coefficients (see Figure 3.7) and far-field emission patterns. The only distinct difference is that the $(1,1)$ modes of RhoM-Sq22 align with the edges of the square facet instead of the corners (as it does for the RhoM-Sq04 nanocavity), and therefore the α-coefficient values for the horizontal and diagonal paths of the emitter are switched compared to those of the RhoM-Sq04 nanocavity.

Hence, the α-coefficients and far-field emission patterns of these polyhedral NPoM nanocavities reveal a rich and intricate optical response that is highly dependent on the modes' near-field and spectral properties, as well as the emitter's frequency and position within each nanocavity. In general, the α-coefficients follow the intensities of the corresponding near-fields of each mode: the only exception being the $(2,0)$ mode for the RhoM assemblies, which does not strongly respond to the emitter's positioning within the nanocavity—for the emitter transition wavelengths chosen here. Note that for each nanocavity and emitter path, the edge rounding leads to a reduction in the α-coefficient values, but of varying degree depending on the confinement and localisation of each mode to the facet edge/corner, and the rounding size relative to each NP's edge length. These alpha-coefficients have additionally allowed for the reconstruction of the total far-

field response of these systems, revealing the strong morphology dependence on both the facet shape and NP symmetry—as well as producing a series of unique emission profiles that aid in identifying the NP's shape and facet configuration from its far-field emission. The results are essential for identifying which modes are significant during the interactions of emitters placed within realistic plasmonic nanocavities. It also paves the way towards determining the exact position of an emitter within a nanocavity by simply recording the system's far-field emission pattern.

SERS is a very powerful tool for sensing analyte molecules, and is one such process that could greatly benefit from the results presented here. SERS relies on strong Raman signals emitted from the nanostructure to the far-field, however, these heavily depend of the near-field charges and are only found in a few sites due to variational effects of nanostructure morphology [47]. Aiding in selecting only the most promising of sites is the extremely fast process of dark-field spectroscopy; the screening capabilities this offers requires a clear understanding between the near-field resonances and the far-field scattering properties [79–81]. Through the use of combined near-field QNM analysis and NFFT techniques considered here, the effects of the facet morphology in these polyhedral NPoM geometries directly aids in the application of dark-field spectroscopy for the selection of promising SERS sites.

3.6 CONCLUSIONS

Gold NPs acquire various polyhedral shapes during their fabrication, due to the crystalline nature of gold. Here we perform a QNM analysis on the three most commonly occurring polyhedral NPs (i.e. cuboctahedron, rhombicuboctahedron, decahedron) when assembled on a flat gold mirror—revealing the rich multi-modal nature of their optical responses. Through the QNM analysis of several polyhedron-on-mirror nanoantennas—and the variety of unique facet assemblies they form—the dominance of the nanogap morphology on the plasmonic response is identified. More specifically, we uncover the paramountcy of the facet shape—in addition to the impact of polyhedral symmetry and neighbouring facets—on the near-field charge distributions supported by each nanocavity, as well as the effect this has on the spectral arrangements and modal degeneracies. Pairing this with a NFFT technique to obtain the far-field Poynting flux of each mode, a plethora of morphological-dependent intricacies reveal the manner with which each mode is able to out-couple energy from these systems, and how nanoscale alterations of the facet can fundamentally alter the emission patterns.

Through the determination of modal α-coefficients, the total far-field response of each polyhedral NPoM geometry is reconstructed for specific emitter frequencies and placements within the cavities—highlighting the availability of each mode to couple with the emitter, and just how extraordinarily strongly the polyhedral symmetry and emitter frequency control the nanocavities' radiative emission profiles. This enables the direct com-

parison with experimental measurements, therefore significantly aiding in the intuition and interpretation of how emitters placed in these realistic nanocavities interact with the extreme plasmonic environment, as well as the manner in which these systems facilitate the out-coupling of energy to the far-field. Hence, this work paves the way in understanding and deciphering the shape and facet assembly of the NPs via their far-field emissions, as well as determining the exact positioning of an emitter within such nanocavities.

4 ENTANGLEMENT OF QUANTUM EMITTERS STRONGLY COUPLED TO PLASMONIC NANOCAVITIES

4.1 INTRODUCTION

To date, the light-matter interactions of QEs with nanoplasmonic devices have predominantly been studied experimentally, via far-field measurements of the combined system [4, 7, 8, 28–30, 115, 116]. To reveal the quantum dynamics of the system, one needs to employ theoretical descriptions. However, significant difficulties emerge when realistically describing the photonic modes of the plasmonic nanocavity and when obtaining the quantum dynamics of the combined system—due to both the dispersive optical response of the metal and the open and lossy nature of plasmonic environment. The dispersive nature of metal creates difficulties in obtaining the eigen-solutions of Maxwell's equations, and therefore in decomposing the plasmonic modes of a nanocavity. Several

techniques have emerged in the past few years which try to solve this classical problem [61, 71, 89, 93, 96–99]. The QNMs obtained often yield complex eigenfrequencies, with on-going discussions on the best way to normalise them and obtain their mode volumes [117, 118]. In addition, the open and dissipative nature of a plasmonic environment creates a non-Hermitian system and leads to QNM solutions—since energy is not conserved during the EM oscillations. The non-Hermitian nature of the system further complicates theoretical quantum mechanical descriptions of the overall combined system (plasmons and QEs). Nevertheless, several different methods have been proposed recently which try to address this issue [118–128]. Some go as far as describing the optomechanical behaviour of the molecules [129, 130], but they tend to focus on quantum scattering processes and spontaneous emission (i.e. Purcell factor); in general, they also do not offer the quantum dynamics of the system, which hinders our attempts to design and build quantum devices with nanoplasmonic elements that operate at room temperature.

In this chapter, we propose a theoretical description based on an open quantum system for multiple QEs placed in a plasmonic nanocavity—specifically the cavity of the SoM geometry—and reveal a semi-persistent entanglement between the QEs that is twelve times longer lived than the plasmonic excitation. We use a QNM analysis method [61, 71, 89, 93] to decompose and quantise the plasmonic modes of the nanocavity, describe external sources as driving fields, model the losses in the system with external reservoirs, and obtain the system's full range of quantum electrodynamics (QED).

We demonstrate that our description also directly links the quantum variables to experimentally measurable quantities—such as the extinction cross-section—enabling the study of quantum light-matter interactions in plasmonic devices in a way that is fully consistent in returning the classical limit. Most importantly, using this description we find semi-persistent entanglement emerging when multiple QEs are placed in a plasmonic nanocavity. This entanglement is present even for just two QEs, and its existence seems to be independent of the QEs location—as long as each QE is strongly coupled to the plasmon mode. This work provides us with the full quantum dynamics of QEs in plasmonic environments, and paves the way towards building quantum devices operating at ambient condition.

4.2 QUANTUM DESCRIPTION OF OPEN AND LOSSY PLASMONIC NANOCAVITIES

Quantum plasmonics has received considerable interest in the past seven years due to experimental demonstrations of quantum processes, such as light-matter strong-coupling, at room temperature [4, 29, 30]. The open and lossy nature of plasmonic environments, however, creates a non-Hermitian system and places significant theoretical impediments on using common cavity QED descriptions—which are usually developed for high-finesse cavities. Recently, several quantum descriptions have been proposed with the aim of overcoming the non-Hermitian nature of the problem [119, 125, 131]. Even though each

method is a significant breakthrough, they often focus on quantum scattering processes and the spontaneous emission [132–134]—by presenting the modification to the Purcell factor as a result of the QE's interaction with the plasmons—with no explicit quantum dynamics provided [118, 121, 123, 125, 127]. An exception is the Weisskopf-Wigner theory that was recently employed to obtain the quantum dynamics, but one cannot easily generalise this method to describe multiple QEs or entangled states. It also leads to surprisingly fast Rabi-oscillations [120, 122, 124, 126, 128]. Alternatively, one can use the semi-classical Maxwell-Bloch description [4, 10, 135, 136] but it only describes the problem within the first-quantisation, and therefore cannot describe spontaneous emission, entanglement or any non-classical light emerging from nanoplasmonic devices. Hence, to describe entanglement or correlations between multiple emitters within a plasmonic nanocavity, one needs to introduce new theoretical descriptions.

Here we introduce an open quantum system formalism that allows us to obtain the quantum dynamics of multiple QEs placed in a plasmonic nanocavity, their entangled dynamics, and also derive experimentally measurable quantities. The Hamiltonian ($\mathcal{H}$) of the system contains the description for the plasmonic modes derived from classical QNM calculations, multiple QEs, the interaction between the plasmonic modes and the QEs, a driving (pump) field, and reservoirs representing the loss channels. We start by decomposing the photonic response of the plasmonic system into QNMs, using the 'QNMEig' methodology described in Chapter 3 and in [61, 71, 89, 93]. This method provides the near-fields of each plasmonic mode and complex eigenfrequency [92] $\tilde{\omega}_{cav} = \omega_{cav} - i\kappa_{out}$, where ω_{cav} is the resonant frequency of the cavity and κ_{out} the total decay rate

of the plasmonic nanocavity. However, to simplify the open quantum model, we make the approximation that only one plasmonic mode interacts with the QE(s).

We divide the Hamiltonian into two components to facilitate an easier discussion of the model, the system Hamiltonian ($\mathcal{H}_{sys}$) and the reservoir Hamiltonian ($\mathcal{H}_{res}$): $\mathcal{H} = \mathcal{H}_{sys}+\mathcal{H}_{res}$. First, the system Hamiltonian describes the plasmonic mode of the nanocavity ($\mathcal{H}_{cav}$), the QEs ($\mathcal{H}_{QEs}$), the interaction of QEs with the plasmonic mode ($\mathcal{H}_{int}$) and the driving pump field ($\mathcal{H}_{pump}$), and is given by:

$$\mathcal{H}_{sys} = \underbrace{\Delta_{cav} a^\dagger a}_{\mathcal{H}_{cav}} + \underbrace{\sum_j^N \frac{1}{2}\Delta_d \sigma_z^{(j)}}_{\mathcal{H}_{QEs}} + \underbrace{\sum_j^N g(\mathbf{r}^{(j)}) \left(a^\dagger \sigma_-^{(j)} + a\sigma_+^{(j)}\right)}_{\mathcal{H}_{int}} + \underbrace{i\sqrt{\kappa_{in}}\left(\alpha^* a - \alpha a^\dagger\right)}_{\mathcal{H}_{pump}} , \quad (4.1)$$

where N is the number of QEs placed in the nanocavity, $\Delta_{cav} = \omega_{cav} - \omega_p$ is the detuning of the cavity resonance (ω_{cav}) from the pump frequency (ω_p), $\left\{a, a^\dagger\right\}$ are the bosonic operators that create and annihilate the plasmonic excitations, $\Delta_d = \omega_{QE} - \omega_p$ is the detuning of each QE's resonant frequency (ω_{QE}) from the pump frequency (ω_p), and $\sigma_z^{(j)}$ is the Pauli z-operator describing the j-th two-level QE—see Appendix A14 for the derivation. The interaction of the plasmonic mode with the j-th QE is given by $\left(a^\dagger \sigma_-^{(j)} + a\sigma_+^{(j)}\right)$, with a coupling strength $g(\mathbf{r}^{(j)})$—which is dependent on the position $\mathbf{r}^{(j)}$ of each QE within the plasmonic nanocavity—that is given by:

$$g(\mathbf{r}^{(j)}) = \sqrt{\frac{\hbar\omega_{cav}}{2\varepsilon_0\varepsilon V}}\, \mathbf{d}^{(j)} \cdot \mathbf{u}(\mathbf{r}^{(j)}) , \quad (4.2)$$

where ε is the electric permittivity of the material hosting the QEs, $\mathbf{d}^{(j)}$ is the dipole mo-

ment of the j-th QE, V and $\mathbf{u}(\mathbf{r})$ are the mode volume and normalised electric field of the plasmonic mode respectively obtained from the QNM calculations. Note that the dependency of the coupling strength on the QE's location within the plasmonic nanocavity is via the normalised field of the plasmonic mode $\mathbf{u}(\mathbf{r})$, and the mode volume is therefore given by: $V = \frac{\int d\mathbf{r}|\mathbf{u}(\mathbf{r})|^2}{\mathrm{Max}[|\mathbf{u}(\mathbf{r})|^2]}$ (see Appendix A15 for further details). Finally, the last term of equation 4.1 describes a driving pump field, which is an external coherent monochromatic source exciting the system; $\sqrt{\kappa_{in}}$ is the rate that energy couples into the system and α is the amplitude of the coherent state, defined by the source's photon flux $c|\alpha|^2$ (for further details see Appendix A16).

While the system Hamiltonian suitably describes the excitation of the system and the interactions between the QEs and the plasmonic mode, it contains no description of any losses. Such systems have two loss channels: the decoherence of each 2-level QE, due to the linewidth of the excited state coming from its (ro-)vibrational energy states; and the radiative and Ohmic losses of the plasmonic environment, which significantly alter the quantum dynamics of QEs placed within plasmonic nanocavities. We represent these two loss channels with two separate reservoir Hamiltonians, as (see Appendix A14 for the derivation):

$$\begin{aligned}\mathcal{H}_{res} = &\sum_{j}^{N}\int_{0}^{\infty} d\omega_{vib}\ \sigma_z^{(j)}\kappa_{vib}(\omega_{vib})\left[b_{vib}^{\dagger}e^{i\omega_{vib}t} - b_{vib}e^{-i\omega_{vib}t}\right] \\ &- i\sum_{\lambda}\int_{0}^{\infty} d\omega\kappa_{res}(\omega)\left[b_{\lambda}(\omega)a^{\dagger}e^{i\Delta(\omega)t} - b_{\lambda}^{\dagger}(\omega)ae^{-i\Delta(\omega)t}\right]\ , \end{aligned} \tag{4.3}$$

where the first term describes the coupling of the QEs to a phonon bath reservoir with

phonon frequencies ω_{vib} and strength $\kappa_{vib}(\omega_{vib})$—where $\left\{b_{vib}, b_{vib}^{\dagger}\right\}$ are the phonon reservoir operators. The second term of equation 4.3 accounts for the coupling of the plasmonic mode to a background plasmon reservoir—with photon frequencies ω and coupling strength $\kappa_{res}(\omega)$—to account for the energy lost both radiatively and via Ohmic losses. Note that $\Delta(\omega) = \omega - \omega_p$ is the detuning of the frequency ω from the pump frequency (ω_p), and $\left\{b_{\lambda}(\omega), b_{\lambda}^{\dagger}(\omega)\right\}$ are the plasmon reservoir creation and annihilation operators.

Finally, the time evolution of this system is described by the density operator, ρ, via the Lindblad master equation:

$$\begin{aligned}\frac{d}{dt}\rho = &-i\left[\mathcal{H}_{sys}, \rho\right] + 2\kappa_{out} a\rho a^{\dagger} - \kappa_{out}\left(a^{\dagger}a\rho + \rho a^{\dagger}a\right) \\ &+ \sum_{j}^{N}\left[\kappa_{vib}\sigma_z^{(j)}\rho\sigma_z^{(j)} - \frac{\kappa_{vib}}{2}\left(\sigma_z^{(j)2}\rho + \rho\sigma_z^{(j)2}\right)\right],\end{aligned} \tag{4.4}$$

where κ_{out} is the imaginary part of the complex QNM eigenfrequency. To calculate the quantum dynamics of the system one typically must solve equation 4.4 numerically, which provides solutions for the time evolution of the states as well as the expectation value of any other operator of the system—via $\langle O\rangle = \mathrm{Tr}[O\rho]$.

In this chapter, the plasmonic nanocavity we consider is the SoM geometry, as shown in Figure 4.1A and B. This is formed of a spherical gold NP of 40 nm radius assembled 1 nm above a flat gold mirror, separated by a molecular monolayer with refractive index $n = 2.5$—which is consistent with recent experimental set-ups [57]. As we have previously discussed [72, 78], the symmetry of the system supports the spherical harmonic

nomenclature for the labelling of the modes: $i = (l, m)$, for a set of positive integers l and $-l \leq m \leq l$. The first order $(1, 0)$ mode of this plasmonic nanocavity is resonant at $\tilde{\omega}_{cav} = 338.88 - i9.8$ THz (i.e. $\sim$ 900 nm), with the normalised electric field mode profile $\mathbf{u}(\mathbf{r})$ shown on a slice through the centre of the cavity in Figure 4.1C—exhibiting a large central extrema, and a mode volume of Re$[V] = 60.01$ nm^3. For each QE, we considered a Cy5 molecule that has a dipole moment $d = 10.1$D and atomic linewidth $\kappa_{vib} = 25$meV [57].

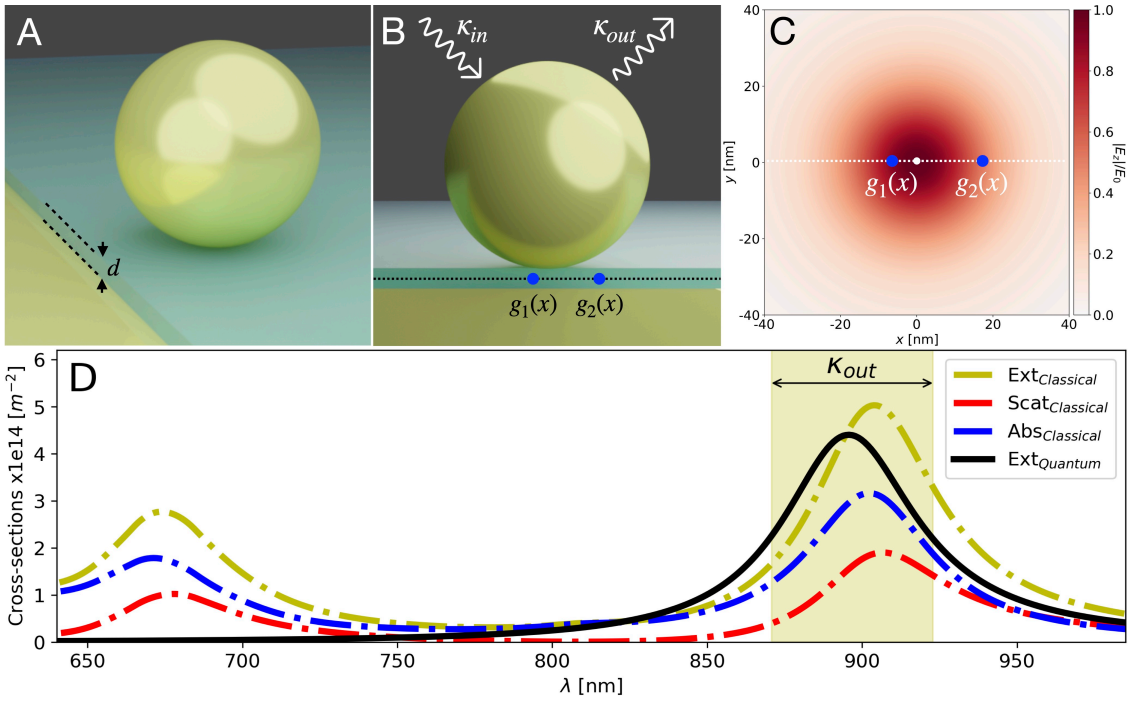

Figure 4.1: A. SoM geometry for a spherical gold NP assembled a distance d above a flat gold substrate, separated by a spacer of refractive index n. B. SoM schematic showing the coupling of energy in and out of the system with rates κ_{in} and κ_{out}, respectively, and shows two emitters placed at different locations. C. The normalised mode profile of the $(1, 0)$ mode on a plane through the centre of the cavity, with the white and blue dots respectfully indicating the centre of the cavity and the dependence of the coupling strength on the emitter positions. D. The comparison of the classical absorption, scattering and extinction cross-sections with the quantum extinction cross-section.

We also perform further classical EM calculations, where a plane wave is incident on the plasmonic nanocavity to obtain the absorption (σ_{abs}), scattering (σ_{scat}) and extinction (σ_{ext}) cross-sections—which are all shown in Figure 4.1D. Note that the $(1,0)$ plasmonic mode for this nanocavity is spectrally isolated from other plasmonic modes, and we can therefore safely assume that only one mode interacts with the QEs (as described above). Also note that the κ_{out} obtained from the QNM calculations (i.e. the imaginary part of the complex eigenfrequency, $\tilde{\omega}_{cav}$) corresponds to the full-width half-maximum of the extinction cross-section, as highlighted in Figure 4.1D.

4.2.1 STEADY-STATE EQUIVALENCY

Although the above information (obtained from classical QNM calculations) adequately describes the plasmonic environment and its coupling to QEs—providing values for the open quantum model parameters: Δ_{cav}, κ_{out}, $g(\mathbf{r}^{(j)})$—one also needs to quantify the rate with which energy from an external source couples into (κ_{in}) the specific nanocavity. To achieve this, we solve equation 4.4 analytically in steady state. We then take the solution to the classical limit, where it yields the same extinction cross-section obtained from the classical EM calculations for the plasmonic nanocavity, and therefore provides a direct link between the quantum and classical descriptions of the system.

We start by using a pump field, as shown in equation 4.1, to represent an external source incident on the system. The pump field originates by singling out an input field mode from the photonic reservoir and, under the mean-field approximation, replacing the

field operator $b_\lambda(\omega)$—from equation 4.3—with a complex number α that best describes the amplitude of the coherent input field state. As the reservoir describes the rest of the universe, it is a valid assumption that the reservoir remains unchanged due to the quantum statistics of the pump mode not significantly affecting the statistics of the reservoir. The mechanisms through which energy is transferred to/from the reservoir are schematically shown in Figure 4.1B—with the emitter arrangement on a plane through the centre of the cavity—characterising the rates at which energy is coupled into (κ_{in}) and lost (κ_{out}) from the system.

Classically, the extinction cross-section (σ_{ext}) is defined as the total power lost by the system (P_{out}) relative to the incident intensity (S) of the plane wave: $\sigma_{ext} = P_{out}/S$. When considering their quantum analogues, these become: $P_{out} = 2\kappa_{out}\hbar\omega\langle a^\dagger a\rangle$ and $S = c\omega|\alpha|^2$, noting that $\langle a^\dagger a\rangle = \frac{\kappa_{in}|\alpha|^2}{\kappa_{out}^2+\Delta_c^2}$ is proportional to both $\langle a\rangle$ and $\langle a^\dagger\rangle$ (see Appendix A16 for the full derivation). Hence, the quantum extinction cross-section in the steady state becomes:

$$\langle\sigma_{ext}\rangle = \frac{2\kappa_{in}\kappa_{out}}{c}\frac{1}{\kappa_{out}^2+\Delta_{cav}^2}\ , \tag{4.5}$$

which on resonance ($\Delta_{cav} = 0$), where $\langle\sigma_{ext}\rangle = \sigma_{ext}$, returns the in-coupling coefficient as:

$$\kappa_{in} = \frac{\kappa_{out}}{2}c_0\sigma_{ext}\ , \tag{4.6}$$

where c_0 is the speed of light constant, and σ_{ext} can be obtained numerically. The res-

onant quantum extinction cross-section ($\langle\sigma_{ext}\rangle$) is in good agreement with its classical counterpart (σ_{ext}), both shown in Figure 4.1D. Note that on resonance (~ 900 nm), the values of the quantum and classical extinction cross-sections match exactly. The differences away from the resonance are due to contributions from higher order modes to the classical extinction cross-section [137, 138] that are ignored quantum mechanically, and the fact that for the quantum description we are using a quantised QNM. By definition, QNMs have fixed frequencies which assumes that each QNM is an isolated resonance (with a certain linewidth) rather than a resonant response of a continuum of modes—as plasmons are.

With all the physical parameters of the system obtained, our open quantum model now fully describes the interaction between the SoM geometry and multiple QEs placed at any position within the plasmonic nanocavity. We would like to emphasise the flexibility of this driven formalism. For example, by setting the in-coupling constant κ_{in} to zero, the pumping field no longer drives the system. In this regime, the system is free to be initialised in any particular state, allowing the free decay dynamics of specific light-matter interactions to be probed. Our attention now turns to solving the master equation of equation 4.4 for the density matrix, ρ, and obtaining the population dynamics of the quantum states.

4.3 TWO-EMITTER DYNAMICS

Motivated by the current difficulties experienced throughout the field of plasmonics regarding the nanometre control of emitter placement within nanocavities, this section studies the population dynamics of the quantum states to reveal how the position-dependent coupling strength affects the light-matter interactions.

For simplicity, consider first the well studied case of a single emitter placed at the centre of the SoM cavity ($x_1 = 0$ nm) [139], with the pump laser turned off. Figure 4.2 shows the population dynamics using the state notation $|n, s_i\rangle$, where n and s_i are respectively the occupancies of the field and i^{th} emitter states—in this model, the emitter is either in the ground $|g\rangle$ or excited $|e\rangle$ state. With the field state initially excited and no pumping present, energy is passed between the field ($|1, g\rangle$) and emitter ($|0, e\rangle$) for several cycles before being lost from the system—either radiatively or through any combination of the non-radiative processes outlined above. The system eventually returns to the ground state ($|0, g\rangle$). These Rabi oscillations are made more clear in the upper inset, where the population dynamics are shown on a logarithmic scale, revealing that $g^2 > \kappa_{out}\kappa_{vib}$ and the system is therefore in the strong coupling regime. The lower inset makes the comparison of the logarithmic scale population dynamics to the case where the atomic linewidth is ignored ($\kappa_{vib} = 0$), highlighting the blurring effect the molecule's dephasing has on the Rabi oscillations.

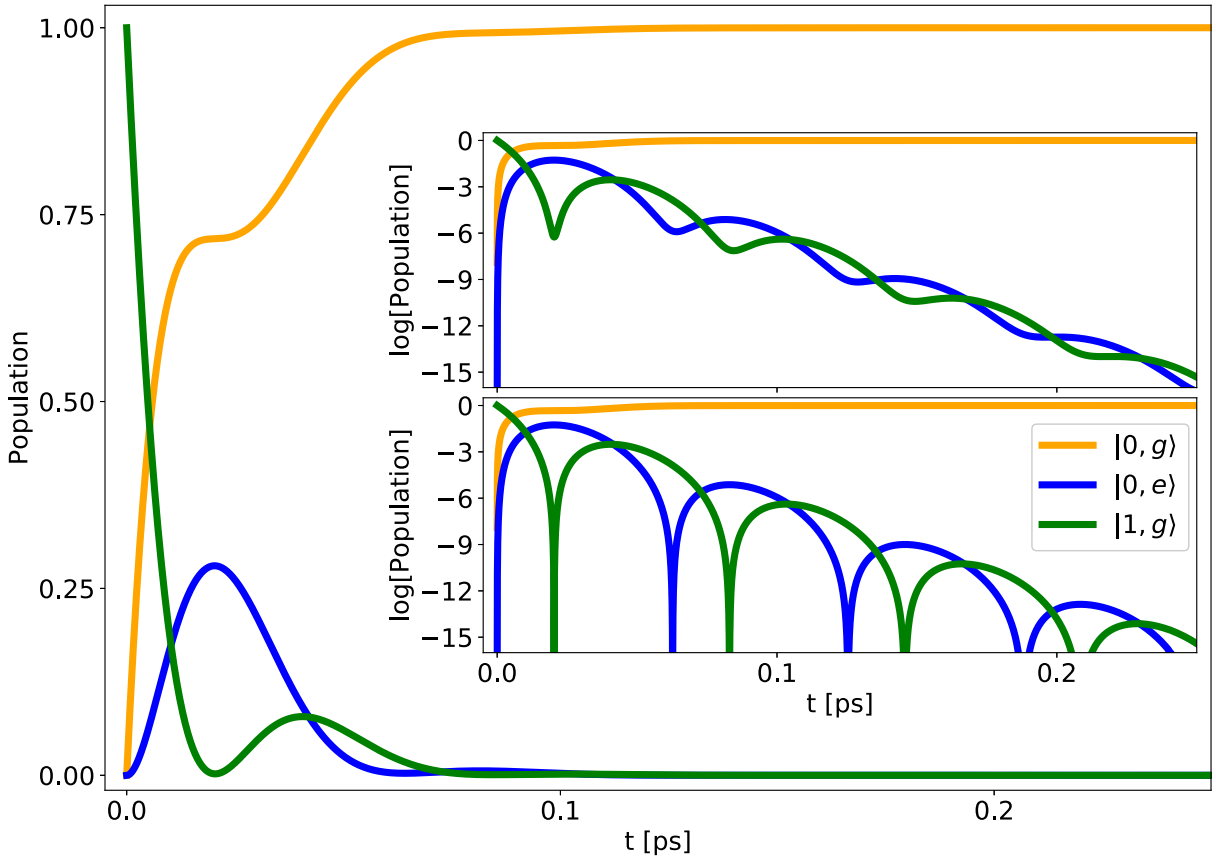

Figure 4.2: The population dynamics for the SoM geometry coupled to a single emitter at the centre of the cavity—initialised in the excited field state. The inset compares the population dynamics on a logarithmic scale to highlight the Rabi oscillations, with (upper) and without (lower) the atomic dephasing (κ_{vib}) included in the model.

Consider next the simplest two-emitter system, whereby both emitters are placed at the centre of the cavity. The state basis is extended to accommodate the additional emitter and—for a field state initialisation, now $|1, g, g\rangle$—the population dynamics are shown in Figure 4.3. Due to the shared position of the emitters, they interact with the plasmonic mode degenerately. The Rabi oscillations are again shown more clearly on the logarithmic scale of the insets, with (upper) and without (lower) the QE's dephasing included in the model.

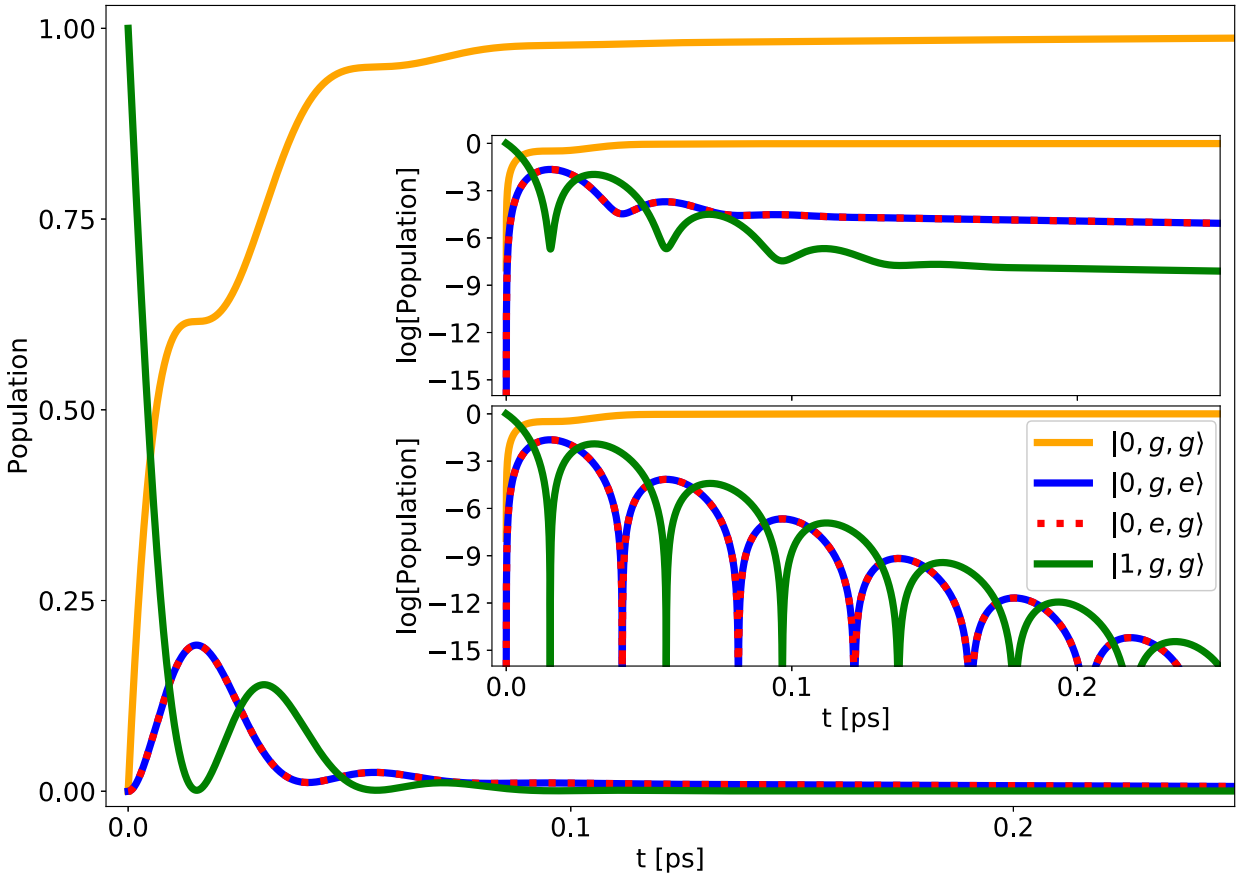

Figure 4.3: The population dynamics for the SoM geometry coupled to two emitters at the centre of the cavity—initialised in the excited field state. The inset compares the population dynamics on a logarithmic scale to highlight the Rabi oscillations, with (upper) and without (lower) the atomic dephasing (κ_{vib}) included in the model.

Relative to the single emitter case, the peak populations of the emitter states are reduced due to the same initial energy entering the system—the single photon with which the field state is initialised—being shared between the two emitters. In addition, the Rabi frequency is increased due to the $\sqrt{N} = \sqrt{2}$ enhancement to the collective coupling strength of the two emitters. However, the increased Rabi frequency is limited by the total decay rate of the system, which follows $\Omega^2_{Rabi} = 4g^2 - \kappa^2_{out}$ [140]. Although the system is further into the strong coupling regime than the single emitter case, it is worth noting that

the populations of the two emitter system decay faster; this is both due to the increased Rabi frequency—the interactions and energy exchanges happen on a shorter timescale—as well as the additional factor of κ_{vib} supplied by the second emitter, which increases the rate at which energy is lost from the system.

With this additional emitter placed in the nanocavity, our attention now turns to exploring the position-dependent interactions of the emitters with the plasmonic mode, as well as the interactions between the emitters. Due to the cylindrical symmetry of the cavity and the $(1, 0)$ mode, the variation of the emitter positions are considered along the x-direction—as indicated by the white dashed line in Figure 4.1C. The positioning of the two emitters within the cavity is explored in Figure 4.4, for symmetric (A-C) and asymmetric (D-G) arrangements. Figure 4.4A diagrammatically shows the symmetric displacement of the two emitters away from the centre of the cavity. Due to the symmetry of the mode, these emitters experience degenerate excited state populations for all positions $|x|$—as shown in Figure 4.4B. The data of $|x| = 0$ corresponds to both emitters at the centre of the cavity and the dynamics shown in Figure 4.3. As the emitters move away from the cavity centre, they get further from the mode extrema and experience a rapid reduction in the strength with which they couple to the plasmonic mode. Beyond $|x| = 6$ nm the coupling is so weak that the Rabi oscillations are lost, and the emitters are analogous to an over-damped harmonic oscillator. Another way of visualising this decline out of the strong coupling regime is through the collective coupling strength g_E—as shown in Figure 4.4C relative to the coupling of a single emitter at the centre of the cavity, g_0. Due to the dependence of the coupling strength on the mode profile, this changes with the position

of the emitters as: $\sqrt{u_1(x)^2 + u_2(x)^2}$, which becomes $\sqrt{2}u(x)$ for the symmetric placement of the emitters. With both emitters in the centre, the collective coupling strength receives a $\sqrt{2}$ enhancement; as $|x|$ increases, $u(x) \to 0$, and the coupling strength reduces to zero as the system returns to the empty cavity limit.

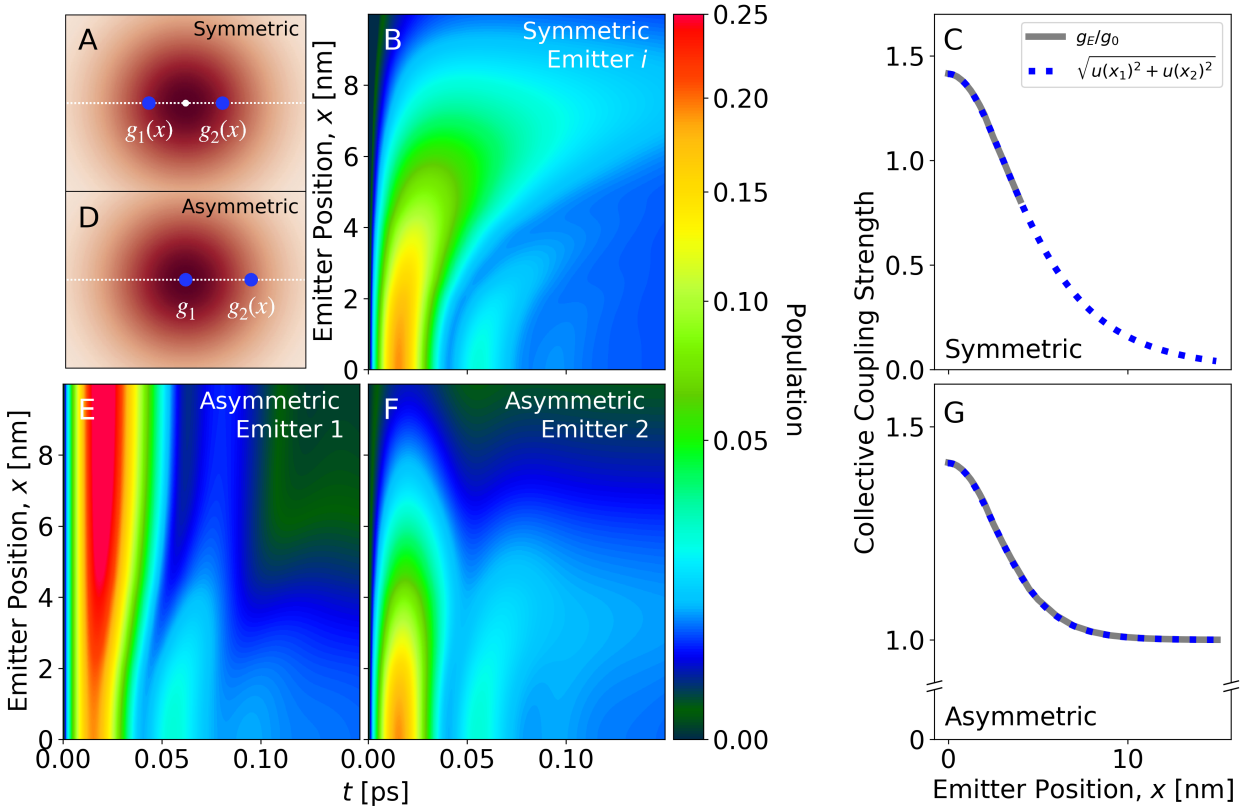

Figure 4.4: The excited emitter state population dynamics of the SoM geometry interacting with two emitters, for symmetric (A-C) and asymmetric (D-G) emitter arrangements—initialised in the excited field state. Schematics for the symmetric (A) and asymmetric (D) emitter placements, along the x-axis on a plane through the centre of the cavity. Population dynamics as a function of emitter positioning for the: (B) degenerate symmetric emitters; (E) central emitter and (F) displaced emitter for the asymmetric arrangement. Collective coupling strength as a function of emitter positioning for the symmetric (C) and asymmetric (G) arrangements.

If instead the emitters are moved asymmetrically, whereby one of the emitters remains at the centre of the cavity while the other moves along the x-axis—as shown in Figure 4.4D—the population dynamics of the central emitter and displaced emitter now differ, and are respectively shown in Figure 4.4E and F. Here the displaced emitter still experiences an increased Rabi period associated to the reduction in coupling strength, but its population decays more slowly with position due to the stronger coupling the central emitter maintains. Although the central emitter's Rabi frequency also reduces as the displaced emitter moves out of the cavity, its population increases as the system returns to a single emitter interaction. In Figure 4.4E this corresponds to the line where the displaced emitter is at $x = 10$ nm, which exhibits the same dynamics as seen for the single emitter system in Figure 4.2. Due to the central emitter (where $u_1(0) = 1$), the collective coupling strength reduces more slowly than for the symmetric case—as shown in Figure 4.4G. This instead follows $\sqrt{1 + u_2(x)^2}$, and reduces to unity once the displaced emitter is far enough away.

4.4 PUMPED DYNAMICS

Experimentally, one does not have the ability to directly observe the dynamics of emitter(s) placed within the nano-gap, let alone of a system initialised with an excited QE in a plasmonic nanocavity—as discussed in Section 4.3. Instead, the system is usually driven by a classical laser field and the scattered light is collected to deduce the plasmon-emitter

dynamics. We are able to simulate this scenario with our model through the direct connection of the experimentally accessible extinction cross-section with the field extinction rate, $\langle a \rangle$:

$$\langle \sigma_{ext} \rangle = -\frac{\sqrt{\kappa_{in}}(\alpha \langle a^\dagger \rangle + \alpha^* \langle a \rangle)}{c|\alpha|^2} \, . \tag{4.7}$$

In our case, since α (which defines the source's photon flux) is real, this reduces to $\langle \sigma_{ext} \rangle = -2\sqrt{\kappa_{in}}|\langle a \rangle|/c\alpha$ (see Appendix A16).

For this laser driven regime, we consider the vacuum state initialisation of the system that is pumped at a rate $\sqrt{\kappa_{in}}\alpha$—such that the average photon number in the system is $N = 10^{-6}$. Instead of the population dynamics, in this regime it is more applicable to consider the expectation value of the lowering operator, $\langle a \rangle$—which describes the rate at which energy is removed from the excited field state. This is obtained by first solving the master equation for the density matrix, and then taking the trace with the field operator: $\langle a \rangle = \mathsf{Tr}[a\rho]$.

Returning to a single emitter system, the $\langle a \rangle$ is shown in Figure 4.5A for an emitter at the centre of the cavity, with both the plasmon ($\Delta_p = \omega_p/\omega_{em}$) and cavity ($\Delta_{cav}$) resonances detuned relative to the pump field. This exhibits the signature characteristic of strong coupling: the anti-crossing between the plasmon-emitter resonances. The black and white dashed lines respectively show $\Delta_{cav} = \Delta_p$ and $\Delta_p = 0$—the two resonances which cross in a weakly coupled system, but instead form an avoided crossing here since our system is in the strong coupling regime. The hybridisation and coherent interactions

between an emitter and the field states in this strongly coupled regime prevents the two states from crossing [141].

Many experimental analyses of strongly coupled systems persist with a classical description of their emitters, which has been largely adopted in literature despite the significant phase of the QNMs being overlooked [142–144]. Wu et al. [91] has recently revealed that this phase can easily be incorporated through the consideration of a complex coupling strength, which accounts for the dispersive nature of a media and its complex mode volume. The complex frequencies of the hybridised states follow [3, 142]:

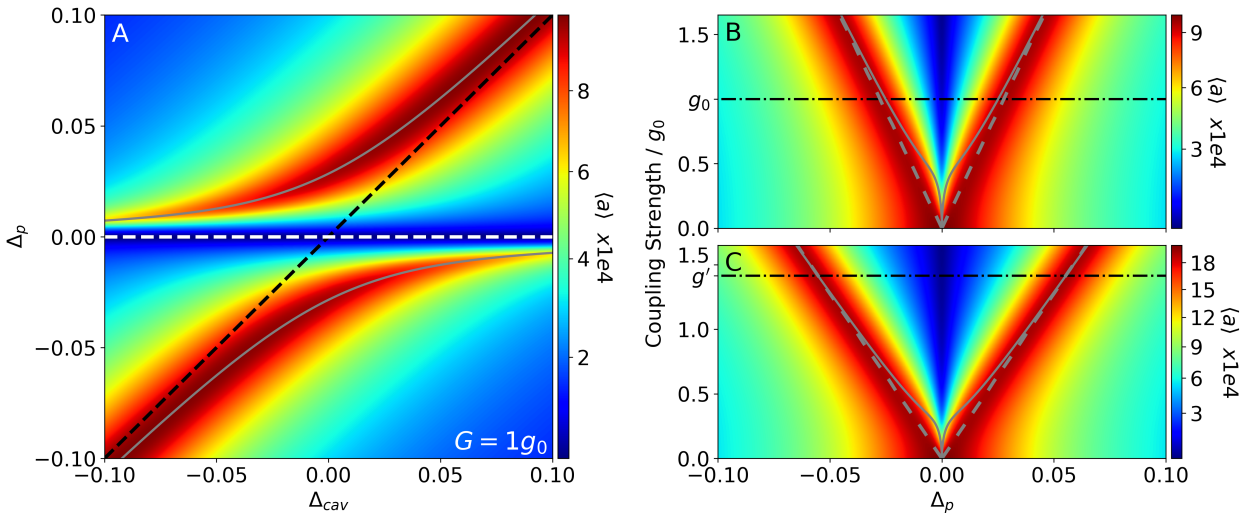

Figure 4.5: (A) The $\langle a \rangle$ of the driven single emitter SoM system as a function of both cavity ($\Delta_{cav} = \frac{\omega_{cav} - \omega_{em}}{\omega_{cav}}$) and plasmon ($\Delta_p = \omega_p / \omega_{em}$) detunings. The black and white dashed lines respectively show $\Delta_{cav} = \Delta_p$ and $\Delta_p = 0$. Rabi splitting in terms of $\langle a \rangle$, as a function of both plasmon detuning and coupling strength for (B) one and (C) two emitters at the centre of the cavity. Grey dashed lines trace the peaks of these split resonances. Solid grey lines follow $\omega_{\pm}$ [91]. $g_0 = 1$ and $g' = \sqrt{2}$ respectively mark the collective coupling strengths in these systems.

$$\tilde{\omega}_{\pm} = \frac{\tilde{\omega}_e + \tilde{\omega}_{cav}}{2} \pm \sqrt{g^2[1 - iR] + \left(\frac{\tilde{\omega}_e - \tilde{\omega}_{cav}}{2}\right)^2}, \tag{4.8}$$

where R = Im[V]/Re[V] is the ratio of the imaginary and real components of the mode volume [71], and the imaginary components of $\tilde{\omega}_e$ and $\tilde{\omega}_{cav}$ are respectively κ_{vib} and κ_{out}. For systems with a large quality factor, Q, the negligibly small Im[V] makes it apparent that classical descriptions may be sufficient. Note that equation 4.8 is derived from a Hermitian system, considering the dephasing components as the imaginary parts of the frequency. For low Q systems such as our plasmonic nanoantenna, the complex nature of the mode volume has the ability to significantly alter the observed dynamics. The $\omega_{\pm}$ solutions are plotted as the grey lines in Figure 4.5A, demonstrating the strong agreement with the results obtained from our non-Hermitian description of the light-matter interactions within these nanoantenna systems.

Taking a fixed line of $\Delta_{cav} = 0$ from this anti-crossing plot and instead varying the coupling strength, the characteristic Rabi splitting is respectively observed in Figure 4.5B and C for one and two emitters placed within the plasmonic nanocavity. For an empty cavity ($g = 0$), a singular resonance is observed which is attributed to the absorption and re-emission of the energy collected by the plasmonic mode. Increasing the coupling between the emitter(s) and the cavity quickly sees the hybridisation of the plasmon and emitter resonances, and the emergence of two split peaks. This arises due to the coupling strength exceeding the timescale over which energy is dissipated from the system—even

with the presence of the QE's dephasing—leading to the coherent exchange of energy between the field and emitter(s) [145]. For multiple emitters in the cavity—such as Figure 4.5C—the coupling strength scales with $\sqrt{N}$ which causes the field and emitters to hybridise even more intensely, resulting in an increased splitting of peaks. The $\omega_{\pm}$ solutions are again plotted here as solid grey lines, highlighting the swift hybridisation and splitting of the peaks.

Here we must address the observed splitting at low coupling strengths, despite the population dynamics of these one and two emitter configurations showing a relatively small number—or even no—Rabi oscillations. This stems from the strong coupling condition: $g^2 > \kappa_{out}\kappa_{vib}$, which should more accurately be interpreted as two separate conditions—$g > \kappa_{out}$ and $g > \kappa_{vib}$—to yield a more intuitive picture of the interactions occurring here. For a single emitter at the centre of the cavity we have: $g^2/\kappa_{out}\kappa_{vib} = 4.64$, placing the system well into the strong coupling regime. On the other hand, $g/\kappa_{out} = 0.48$, leading to a large radiative re-emission (and Ohmic dissipation) and limiting the number of Rabi oscillations observed for the single emitter; whereas $g/\kappa_{vib} = 9.74$, allowing the Rabi splitting to be clearly distinguished even for very small coupling strengths. This is corroborated through the Rabi splitting frequencies of Wu et al. [91], where κ_{out} and κ_{vib} are respectively used as the imaginary components of $\tilde{\omega}_{cav}$ and $\tilde{\omega}_{e}$—yielding the same split peaks for low coupling strengths.

4.5 SEMI-PERSISTENT ENTANGLEMENT

Our attention now turns to an exotic state preparation for the non-pumped two emitter system: specifically the initialisation of one emitter in the excited state, and the other in the ground state. Through the consideration of emitter placements within the nano-cavity, here we study the population dynamics of the states to reveal the intriguing properties they posses.

To most clearly demonstrate the unique dynamics presented by this preparation, we initially ignore the inherent atomic linewidths of the emitters (κ_{vib}), and consider both emitters placed at the centre of the cavity (see Figure 4.6A). In contrast to the field state initialised two emitter system in Figure 4.3 and Figure 4.4, here the primary energy exchange and Rabi oscillations are observed between the two emitters—with twice as much energy passed to the initially non-excited emitter than to the plasmonic mode. Due to the asymmetric initialisation, the emitters no longer interact with the field degenerately: they instead oscillate out of phase with each other as energy is passed between them. The key observation here is that the emitters exchange energy until they reach an equal, non-zero steady state value. This long lived state originates from the symmetric and anti-symmetric superpositions formed from the states of the two emitters:

$$|S\rangle = \frac{1}{\sqrt{2}}\left(|0,e,g\rangle + |0,g,e\rangle\right) \tag{4.9}$$

$$|A\rangle = \frac{1}{\sqrt{2}}\left(|0,e,g\rangle - |0,g,e\rangle\right) \ , \tag{4.10}$$

which respectively describe the super- and sub-radiant states, as shown in Figure 4.6A with black dot-dashed and dotted lines. Although the super-radiant state rapidly decays to zero, the sub-radiant state is driven into the steady state. This occurs due to the asymmetry of the state, with the interactions of the $|1, g, g\rangle$ state with the components of $|A\rangle$ ($|0, e, g\rangle$ and $|0, g, e\rangle$) perfectly cancelling out.

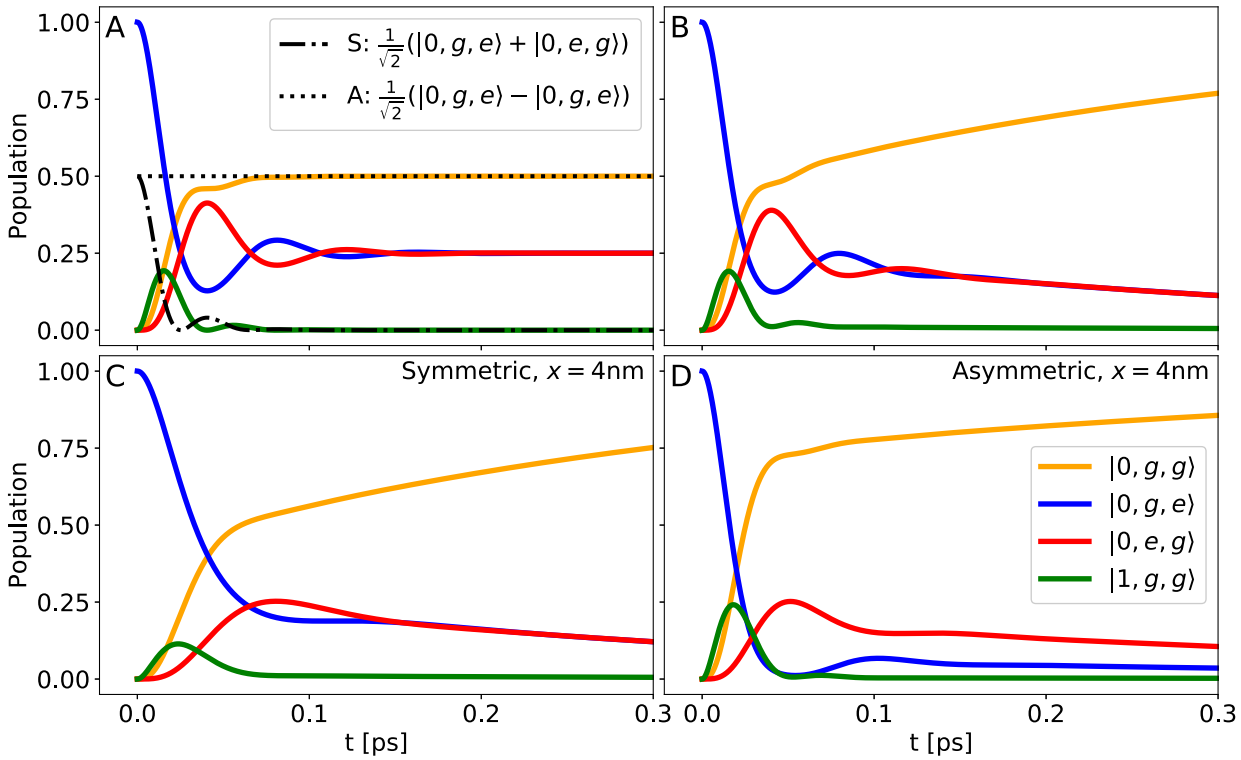

Figure 4.6: The population dynamics for the SoM geometry coupling to two emitters—initialised in one of the excited emitter states. S and A respectively describe the super- and sub-radiant superposition states. The dynamics for the emitters placed at the centre of the cavity—with (B) and without (A) the atomic linewidth (κ_{vib}) included in the model. The symmetric (C) and asymmetric (D) placement of the two emitters, at a distance of $x = |4|$ nm.

If the atomic linewidth of the emitters are reintroduced, the same dynamics are shown in Figure 4.6B; however, the QE dephasing stops the formation of the sub-radiant state in the steady state. Although these emitter states are still much longer lived than those of the field state initialised systems (Figure 4.3), the sub-radiant state decays and the system eventually returns to the ground state. This remains a good demonstration of how semi-persistent states may be long lived in these extreme but lossy systems.

For a more realistic arrangement of the emitters, Figure 4.6C and D respectively refer to the symmetric and asymmetric placement of the emitters at $x = |4|$ nm. Although the symmetric arrangement provides a weaker collective coupling strength than the asymmetric arrangement for the same emitter distances—as shown in Figure 4.4—the symmetry provides an equal coupling of the emitters, and therefore causes them to exchange energy with the field at the same rate. This therefore leads to the two emitters having oscillations of the same period that are perfectly out of phase, as in Figure 4.6A and B, that allows their populations to converge on this long lived state. In contrast, the more strongly yet unequally coupled asymmetric placement causes the emitters to exchange energy with the field at different rates. They therefore do not converge on this long lived state, expediting the decay of energy from the system—more so for the initially excited emitter that remains at the cavity centre (mode extrema). This is an interesting conclusion to draw: that the coherence between emitters—brought about through symmetry—can have a stronger influence than the coupling strength in determining the longevity of quanta within nanoantenna-based light-matter interactions.

4.6 MULTI-EMITTER DYNAMICS

For applicability to a wider audience within the plasmonic and photonic communities—where multi-emitter systems are often considered in order to reach the strong coupling regime and offset limitations in emitter placement—here we extend our analysis of emitter positioning and exotic state initialisations to an $N > 2$ emitter system. Here we choose $N = 8$, but keep the discussion generalised as it is applicable for any number of emitters. Here the position-dependent interactions between the N emitters and the plasmonic mode are explored, analogously to the symmetric and asymmetric placements of the two emitter system in Figure 4.4.

Consider the simplified case of all $N = 8$ emitters placed at the centre of the SoM cavity, whose population dynamics are shown in Figure 4.7 for a field state initialised system. Due to the degeneracies of the system, it can be described by using only three states: the vacuum state $|0, \vec{g}\rangle$, the excited field state $|1, \vec{g}\rangle$, and an N-fold degenerate state with any one of the N emitters excited $|0, \phi\rangle$. Here $|\vec{g}\rangle = \Pi_i^8 |g_i\rangle$ is a state in which all of the emitters are in their ground states, and $|\phi_j\rangle = |e_j\rangle \Pi_{i \neq j}^8 |g_i\rangle$ is the state where emitter j is excited whilst the rest remaining in their ground states; for this system, $|\phi_j\rangle$ is degenerate for all j and can therefore be written generally as $|\phi\rangle$. The collective interaction of the plasmonic mode with the N emitters (grey dashed line) follows $N|0, \phi\rangle$. In addition, the Rabi oscillations are also more clearly shown on the logarithmic scale of the insets, with (upper) and without (lower) the QE's dephasing included in the model.

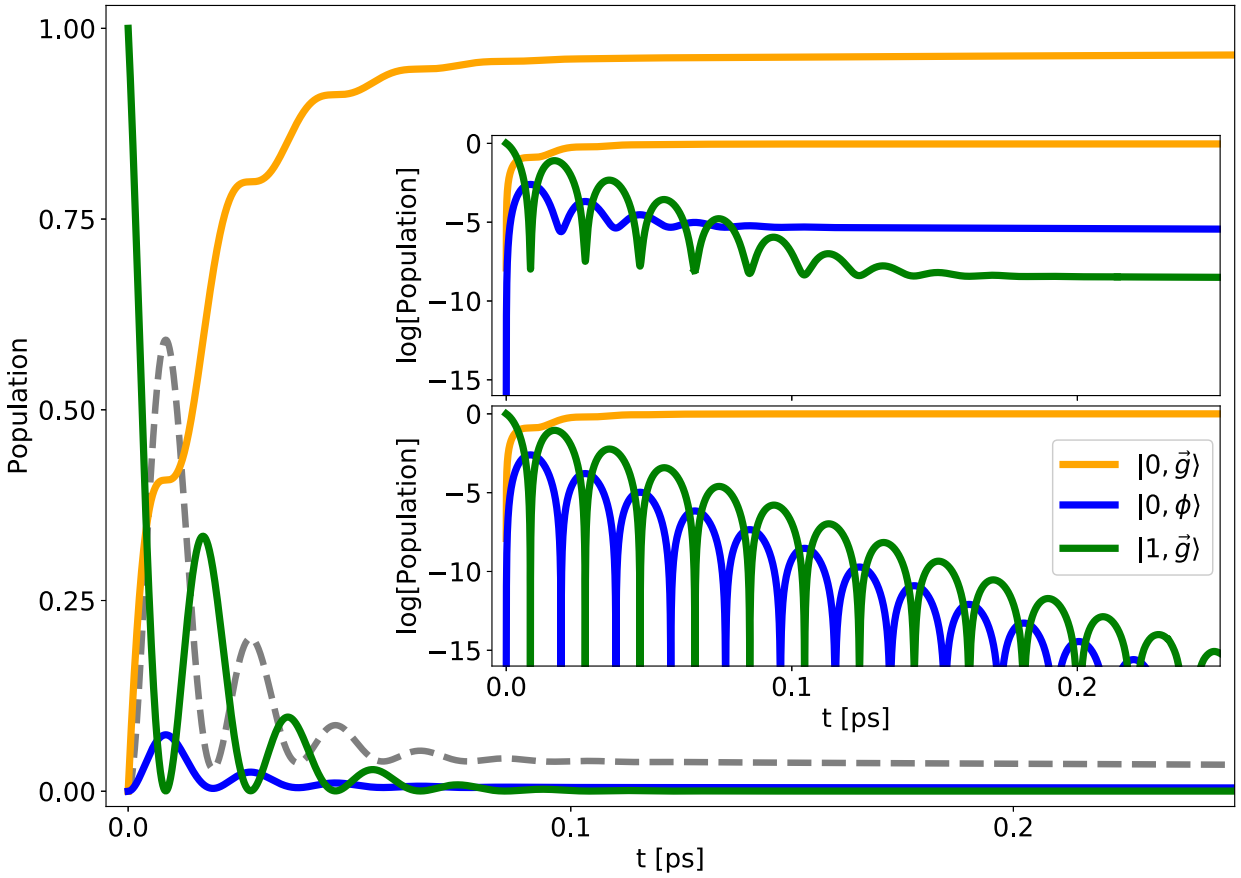

Figure 4.7: The population dynamics for the SoM geometry coupling to eight emitters at the centre of the cavity—initialised in the excited field state. The grey dashed line describes the interaction of the field state with the collective state of the excited emitters: $N|0,\phi\rangle$. The inset compares the population dynamics on a logarithmic scale to highlight the Rabi oscillations, with (upper) and without (lower) the atomic dephasing (κ_{vib}) included in the model.

The position-dependent interactions of these $N = 8$ emitters with the plasmonic mode of the SoM cavity are explored in Figure 4.8, for a symmetric ring (A-B) and encircled emitter (C-E) arrangements. The variation of emitter placements are first considered for the symmetric ring, as diagrammatically shown in Figure 4.8A. Due to the symmetry of the mode, the emitters on this ring retain degenerate excited state populations for all po-

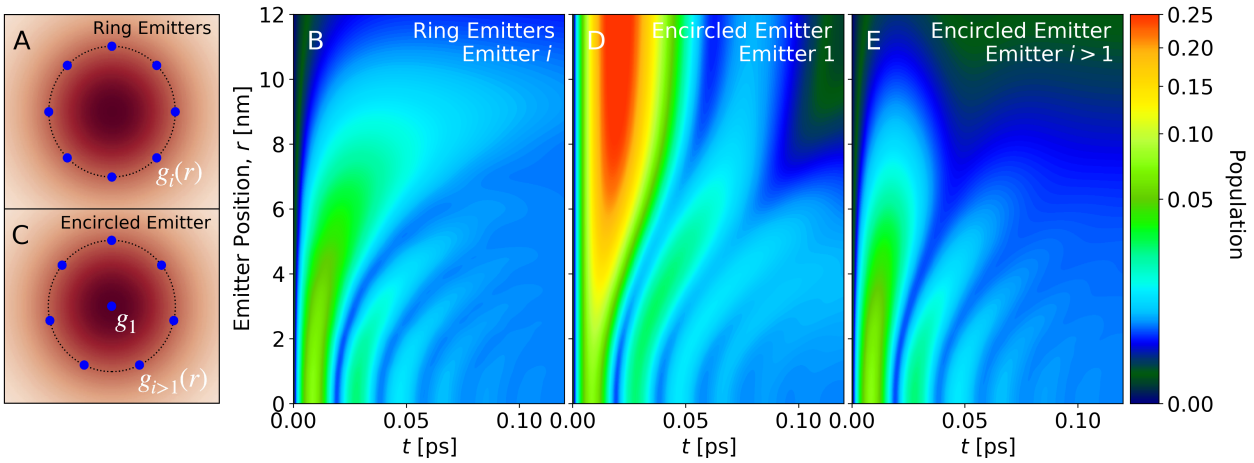

Figure 4.8: The excited emitter state population dynamics of the SoM geometry interacting with eight emitters, for ring (A-B) and encircled emitter (C-E) arrangements, initialised in the excited field state. Schematics for the ring (A) and encircled emitter (C) placements, at a radius r on a plane through the centre of the cavity. Population dynamics as a function of emitter positioning for the: (B) degenerate ring of emitters; (D) central emitter and (E) degenerate surrounding emitters of the encircled emitter arrangement.

sitions $|r|$—as shown in Figure 4.8B—with each emitter following the N-fold degenerate state of $|0, \phi\rangle$.

The data for $r = 0$ corresponds to the N emitters at the centre of the cavity, and the dynamics shown in Figure 4.7: this exhibits six clear exchanges of energy between the emitters and the field. Although the $\sqrt{N}$ enhancement leads to an extreme coupling strength and increased Rabi frequency, each emitter has a relatively low peak population due to the single quanta being shared across all eight QEs. As for the two emitter system of Figure 4.4, the coupling strength and Rabi frequency decrease as the emitters move away from the centre of the cavity; this continues until the collective coupling is so weak that the Rabi oscillations are lost.

We now consider an asymmetric arrangement of the emitters—as shown in Figure 4.8C—whereby one of the emitters remains at the centre of the cavity and the other $N-1$ emitters form an encircling ring at a radius r. The central and surrounding emitters now follow separate dynamics, where $|\phi_1\rangle$ of the central emitter is no longer degenerate with $|\phi_{j>1}\rangle$ of the other emitters on the ring—their population dynamics are respectively shown in Figure 4.8D and E. Analogously to the asymmetric displacement of the two emitter system, the surrounding emitters in this arrangement experience a reducing Rabi frequency and population as r increases, however, they do so at a slower rate due to the maintained strong coupling of the central, encircled emitter. This central emitter also experiences a reduced Rabi frequency, but its population rises with r as it approaches the single emitter case.

Similar phenomenon to the semi-persistent entangled states presented in Section 4.5 occur when there are more than two emitters in the system. As before, the system is initialised asymmetrically such that one of the emitters is excited and the remaining $N-1$ emitters are prepared in their ground states. The population dynamics are most clearly shown in Figure 4.9A, where the emitters are all placed at the centre of the cavity. This compares the population of the initialised emitter $|0,\phi_1\rangle$ (blue) with the collective population of the other $N-1$ emitters: $(N-1)|0,\phi_{j>1}\rangle$ (magenta). Due to the degeneracies of the $N-1$ non-initialised emitters—and the collective state this forms—this N emitter system exchanges energy in a very similar manner as the two emitter system of Figure 4.6. Here they exchange energy until they reach their steady-state values, revealing a significant fraction (over 80%) of the energy residing within a sub-radiant state—with the majoritively

held in the initially excited emitter—where the collective molecular excitation does not decay and entanglement persists. The energy exchange occurs with unequal populations due to the N emitters sharing the singular quanta; differing scales are therefore applied to each state to highlight the shared frequency with which the Rabi oscillations occur.

For clarity of the underlying dynamics, the inherent atomic linewidths of the emitters (κ_{vib}) are ignored in Figure 4.9A, but are included in Figure 4.9B for the same sys-

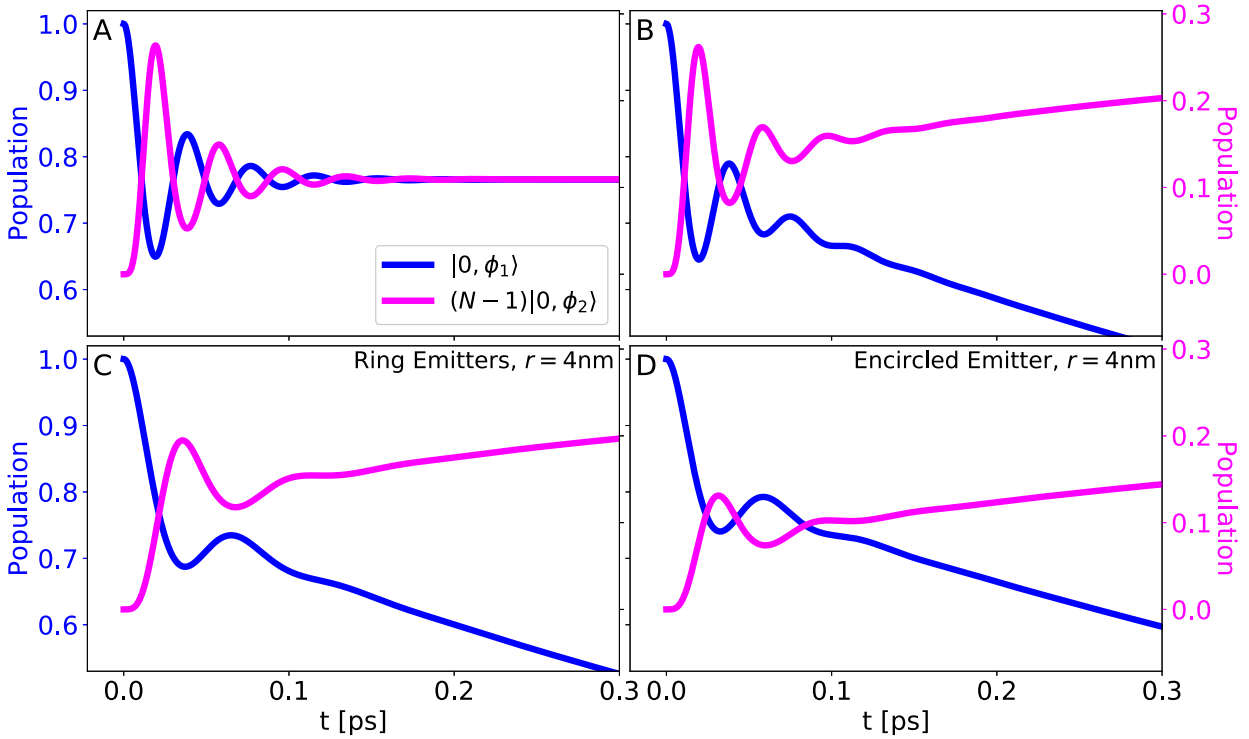

Figure 4.9: The population dynamics for the SoM geometry coupling to eight emitters—initialised in one of the excited emitter states (blue) and compared to the collective excited state of the other emitters (magenta). The dynamics for the emitters placed at the centre of the cavity—with (B) and without (A) the atomic linewidth (κ_{vib}) included in the model. The ring (C) and encircled emitter (D) arrangements, at a radius $r = 4$ nm on a plane through the centre of the cavity.

tem. Here the dephasing stops the formation of steady-state populations, with all states eventually decaying to the vacuum state. For the symmetric ring and encircled emitter arrangements of Figure 4.8A and C, their population dynamics for an emitter initialised system are respectively shown in Figure 4.9C and D—for a radius of $r = 4$ nm. For the symmetric ring of emitters, the coupling strength at this distance is significantly reduced—as apparent by the limited Rabi oscillations—but the coherent dynamics of the emitters helps maintain the longevity of the states. For the encircled emitter arrangement, the central emitter is initially excited which maintains the degeneracy for the surrounding $N - 1$ emitters. The stronger coupling supplied by the central emitter is insufficient to offset the effects of the emitters exchanging energy with the field at different rates. This reduces the populations of the excited emitter states, and more quickly reduces the system to the vacuum state.

These excited emitter states are, however, much longer lived than those of the field state initialised system, demonstrating semi-persistent states in extremely strong coupled systems where the energy exchanges happen over an even shorter timescale. This extension to multiple emitter systems offers insight into interpreting and simplifying multi-emitter light-matter interactions in plasmonic nanoantennas, as well as gaining intuition in the formation of exotic state preparations with nanoplasmonics.

Realisation of such an exotic state preparation is difficult to achieve (even with just two emitters) due to the emitter placement and, to the best of our knowledge, has not currently been attained in this kind of nanoantenna system. We propose this asymmet-

ric initialisation of emitter states can be achieved through pairing the emitter placement with the modal extrema. For example, the $(1,0)$ mode exhibits a central extrema at 900 nm for this geometry, whilst the $(2,0)$ mode is concentrically confined with an additional ring-extrema at 675 nm that exists away from the cavity centre [72, 78]. Placing resonant emitters (such as two different fluorescent molecules) at the respective anti-nodes of these two modes may offer control over their independent resonant and retardant excitations from separate pump fields. Such fabrications may have the ability to facilitate the production of these exotic states, and support long-lived light-matter quantum entanglement in room temperature plasmonic devices.

4.7 CONCLUSION

The potential of plasmonic nanoantennas to host QEs (such as fluorescent molecules, J-aggregates and quantum dots) has recently been identified, revealing the highly suitable environment for studying light-matter interactions at room temperature. One such nanoantenna that stands out for its enhancement and confinement capabilities is that of the SoM geometry—whose versatile cavity environment has the ability to host multiple emitters simultaneously. Here we quantise the QNMs of a lossy open quantum system to build a cavity QED description of the system. This allows strongly coupled interactions between emitters and the plasmonic environment to be modelled whilst addressing the coupling to external reservoir systems, in addition to laser driven excitations. This

is achieved in a fully consistent manner through the QNM infrastructure—which parameterises the system by directly linking the quantum variables to experimentally measurable quantities—enabling the return to the classical limit.

By analysing the dynamics of the light-matter interactions for single and multi-emitter systems, we reveal how the position-dependence of the emitters effects the collective coupling strengths and Rabi oscillations. Through a driven excitation regime, the Rabi splitting and anti-crossing are observed for a single emitter system—characteristic signatures of strong coupling. Finally, exotic state preparations are considered in multi-emitter systems, whereby specific emitter initialisations result in massively increased state longevity through the formation of semi-persistent entangled states. This study offers significant intuition into how emitter arrangements and preparations affect the interactions between emitters and the plasmonic environment—applicable in SERS [77] and controlled emitter [57] experiments.

5 CONCLUSION

Plasmonic nanocavities are a very promising platform for studying light-matter interactions. In recent years, through developments in nanofabrication techniques and the formation of pico-cavities, these nanocavities have realised the strong coupling of a single molecule in ambient conditions [4], and even the real-time tracking of chemical reactions across a single molecule [146]. The extreme photonic environment which has enabled these breakthroughs arises due to the unprecedented enhancement and sub-diffraction limit confinement within plasmonic nanocavities, which causes the plasmonic modes of each nanometallic component to intensely hybridise. The feats attained by these extreme plasmonic environments have gathered significant attention due to their potential to facilitate quantum devices that operate in ambient conditions. To aid in this goal, this thesis provides a comprehensive analysis of light-matter interactions of emitters placed within the cavities of plasmonic nanoantennas, from three very different perspectives—using a variety of theoretical methodologies and numerical modelling techniques.

The vast majority of experimental analyses of plasmonic nanocavities rely on exciting the system with a plane wave and measuring its emission to the far-field, heavily

overlooking the manner in which both these processes occur. Chapter 2 addresses the misconception that energy is coupled into a system just as efficiently as it is out-coupled, revealing that—in general—a nanocavity radiates energy much more efficiently than it receives it. The origin of this phenomena is identified through a Green's function based multipolar decomposition (Mie theory), and we unveil many of the intricacies with which energy is coupled into and out of nanocavities. This reveals the mode selectivity of plane wave sources, and how non–quasi-static effects are accentuated through the hybridisation process. From this deep understanding of nanocavity light facilitation, we outline the custom design of plasmonic systems that support tailored relative in- and out-coupling rates—from enhanced to retardant excitation regimes. By unveiling the inequitable emissive and excitational properties of plasmonic systems, we gain a deeper understanding of how nanocavities facilitate and control light-matter interactions, aiding in the fabrication of more efficient, strongly coupled, SERS-capable, single molecule plasmonic nanocavities that operate in ambient conditions [4, 18, 57].

Chapter 3 considers a more realistic form of the NPoM geometry through the analysis of several commonly occurring polyhedral NPs assembled on a mirror. Here a QNM approach is adopted to obtain the modal near-field charge distributions and complex eigenfrequencies supported by each polyhedron's unique facet orientations and assemblies on the mirror; through a NFFT technique, the corresponding far-field emission profiles are also obtained. These reveal the paramount importance of the exact facet morphology on the supported near-field resonances and a plethora of morphological-dependent intricacies on their ability to radiate from the system—as well as how neigh-

bouring facets, polyhedral symmetry and nanoscale facet alterations can fundamentally alter the emission patterns. Via the reconstruction of the modal responses, the total far-field emission can be probed for specific emitter frequencies and positions within the cavity—forming a direct link with experimental emission observations. This exposes just how extraordinarily strongly a nanocavity's radiative emission profile depends on the polyhedral morphology, transition frequency and emitter positioning. The analysis of polyhedral NPoM geometries from both the near- and far-field not only aids in the identification of polyhedra and their facet assemblies from experimental scattering measurements, but paves the way in determining the exact positioning of emitters within nanocavity geometries [57].

Finally, Chapter 4 considers the ability of the SoM geometry to host QEs from a quantum perspective, with the QNM infrastructure importantly connecting the quantum and classical variables to enable a model that is fully consistent in returning to the classical limit. Here the supported QNMs are quantised in order to access the quantum dynamics of the system within the strong coupling regime, whilst light-matter interactions are modelled through laser driven excitation regimes and the coupling to external reservoir systems. The position dependence of the collective coupling strength and Rabi oscillations are observed in multi-emitter systems—for a series of emitter arrangements—in addition to the Rabi splitting and anti-crossing when operating in a laser driven excitation regime. Finally, excited emitter longevity is explored through exotic state preparations, uncovering massive lifetime enhancements for emitter initialised systems—through the formation of semi-persistent entangled states. This is significant for applications in SERS

and prospective quantum computing experiments [4, 18, 57], offering routes for increased emitter lifetimes within systems that also offer efficient radiative emission.

5.1 FUTURE WORK

A future aim of the model presented in Chapter 2 is to develop the analytics such that they can be used to describe the modes of the dimer antenna and NPoM geometry. This is currently underway within the group, where the spherical NP formulation will be extended to describe the dimer antenna—retaining it's applicability to NPs of any radii. The aim is to then model a highly asymmetric dimer antenna that closely resembles the NPoM geometry. From there, the analytical decomposition of these geometries would allow their plasmonic responses to be broken down into their modal and constituent parts, offering insight into how energy is scattered and passed between the plasmonics elements. Specifically, this could unveil how and through what process the hybridisation between the modes of each plasmonic element produces a red shifting of the combined plasmonic response.

Understanding how this hybridisation process operates—especially on an analytical level—is tremendously beneficial in the design of tailored plasmonic nanoantenna systems. Instead of manually selecting the plasmonic components and predicting the amount of red-shifting that will occur during the hybridisation—as was required in Subsection 2.4.2 to obtain $\gamma_{exc} = \gamma_{rad}$—we would have access to an automated process that

is capable of yielding systems with extremised in- and out-coupling rates after the hybridisation. With a greater control over the exact excitational and emissive properties of plasmonic nanoantennas, it would become significantly easier to form plasmonic nanocavities that also have equal in- and out-coupling rates in at least one frequency region.

For systems where the γ_{exc} is smaller than the γ_{rad}, their emissive capabilities will be limited to the rate at which the system can receive energy. By fabricating plasmonics systems that increase the γ_{exc}, they would therefore also have access to increased rates of emission—up to the γ_{rad} defined by the geometry. Systems that have optimised the rates at which they collected and emitted energy have the ability to increase their Raman signals by remarkable amounts—governed by the ratio of the γ_{ext} to the γ_{rad}—even when compared to unoptimised plasmonic systems of a very similar size and emitter wavelength. The increased emissive capabilities would therefore directly aid in any experiment that collects the signals from SERS [4, 18, 57, 79–82].

The software used in Section 3.4—to obtain the far field emission patterns from the polyhedral nanoantenna systems—offers another route for developing this line of study. The way RETOP collects and processes the information from the numerical simulations means it can also be utilised to obtain the non-radiative response of these systems—especially the coupling to and launching of surface plasmon polaritons (SPPs) along the surface of the mirror. This is especially important when it comes to studying the radiative efficiency of the modes and how this changes with the geometry of the system [107]. In addition, the same α-coefficient treatment of Section 3.5 applies to the modal SPPs,

allowing the total SPP response of the system to be determined. This would have the same dependencies on both the position and frequency of the emitter placed within the cavity, and reveal the intricate nature with which SPPs are excited and emitted. The non-radiative nature of plasmonics modes is difficult to probe from the far-field and the modal decomposition is not currently accessible experimentally; as such, this form of analysis would be invaluable to experimentalists working with these systems.

Our collaborated work with Elliot et al. [107] took the analysis of these polyhedral nanoantenna formations in a different direction, focusing instead on the structural identification of these systems from their emissive response. By simulating many variations of each of these structures (in the form of a parametric sweep), a library was built detailing how the spacer thickness, spacer refractive index, NP diameter and facet size affect the supported plasmonic modes. Together these span a large parameter space and consider nearly every possible formation; however, the analysis currently does not encompass the imperfect structures that can arise during fabrication. One route for improving this would be to implement asymmetric distortions in the parameter sweep, as well as considering the varied effects of rounding.

This work could be extended further by combining this library of varied polyhedral systems with the analysis presented in Section 3.5. By incorporating the total emissive response of each of these systems—as a function of both emitter frequency and positioning—into the library of results, this would further aid in the experimental identification of the exact plasmonic geometry, as well as the specific emitter location within

the cavity. Being able to do so for any system that lies within the parameter space considered—defined by the geometrical variations and emitter placements—would be extremely useful for any experimentalist working with these systems.

A natural development to the work of Chapter 4 would be to apply the model to the more realistic geometries considered in Chapter 3. This would offer insight into how the differing plasmonic environments supported by these polyhedral systems affects their ability to interact with QEs. The added complexities of the varying facet morphologies may require extra care, but would make this research much more applicable and relevant to the experimentalists working with these systems—taking steps towards designing and controlling realistic systems for the facilitation of quantum computation. Depending on the specifics of the polyhedral system—and the frequency isolation of its supported modes—the model may need to be developed to considered multiple modes: in order for this to produce experimentally realisable results. This is especially important when considering the polyhedral systems, due to the spatial profiles of each mode within the cavity and the differing abilities with which they couple to QEs.

In relation to this, an additional development to this model—spurred by current limitations—would be to include the direct interaction between QEs placed within these nanocavities. Given the intense optical environments and extremely close proximity of the QEs, their ability to exchange energy directly may lead to noticeable alterations in the results presented in Chapter 4—for the spherical NP system—as well as when considering polyhedral NP systems. Specifically, one would expect the alterations to be most

apparent in the population dynamics—for both field and emitter initiated systems—with the extent of which to heavily depend on the emitters' proximity.

REFERENCES

[1] Y. Kaluzny, P. Goy, M. Gross, et al. Observation of Self-Induced Rabi Oscillations in Two-Level Atoms Excited Inside a Resonant Cavity: The Ringing Regime of Superradiance. *Phys. Rev. Lett.*, 51:1175–1178, 1983.

[2] R. J. Thompson, G. Rempe, and H. J. Kimble. Observation of normal-mode splitting for an atom in an optical cavity. *Phys. Rev. Lett.*, 68:1132–1135, 1992.

[3] P Torma and W L Barnes. Strong coupling between surface plasmon polaritons and emitters: a review. *Reports on Progress in Physics*, 78(1):013901, 2014.

[4] Rohit Chikkaraddy, Bart De Nijs, Felix Benz, et al. Single-molecule strong coupling at room temperature in plasmonic nanocavities. *Nature*, 535(7610):127–130, 2016.

[5] David Pines and David Bohm. A Collective Description of Electron Interactions: II. Collective vs Individual Particle Aspects of the Interactions. *Phys. Rev.*, 85:338–353, 1952.

[6] Hiroshi Sugimoto, Shiho Yashima, and Minoru Fujii. Hybridized Plasmonic Gap Mode of Gold Nanorod on Mirror Nanoantenna for Spectrally Tailored Fluorescence Enhancement. *ACS Photonics*, 5:3421–3427, 2018.

[7] Jeremy J. Baumberg, Javier Aizpurua, Maiken H. Mikkelsen, et al. Extreme nanophotonics from ultrathin metallic gaps. *Nature Materials*, 18(7):668–678, 2019.

[8] Gleb M. Akselrod, Christos Argyropoulos, Thang B. Hoang, et al. Probing the mechanisms of large Purcell enhancement in plasmonic nanoantennas. *Nature Photonics*, 8:835–840, 2014.

[9] Timothy J. Davis, Daniel E. Gomez, and Ann Roberts. Plasmonic circuits for manipulating optical information. *Nanophotonics*, 6(3):543–559, 2017.

[10] Nuttawut Kongsuwan, Angela Demetriadou, Rohit Chikkaraddy, et al. Suppressed Quenching and Strong-Coupling of Purcell-Enhanced Single-Molecule Emission in Plasmonic Nanocavities. *ACS Photonics*, pages 186–191, 2018.

[11] Víctor Pacheco-Pena, Miguel Beruete, Antonio I. Fernandez-Dominguez, et al. Description of Bow-Tie Nanoantennas Excited by Localized Emitters Using Conformal Transformation. *ACS Photonics*, 3:1223–1232, 2016.

[12] Brian J. Roxworthy, Abdul M. Bhuiya, Xin Yu, et al. Reconfigurable nanoantennas using electron-beam manipulation. *Nature Communications*, 5, 2014.

[13] Ivan S. Maksymov, Andrey E. Miroshnichenko, and Yuri S. Kivshar. Actively tunable bistable optical Yagi-Uda nanoantenna. *Optics Express*, 20:8929–8938, 2012.

[14] Yuanhua Sun, Haobin Zhang, Guangjun Wen, et al. Research progress in Yagi antennas. *Procedia Engineering*, 29:2116–2121, 2012.

[15] Shobhit K. Patel and Christos Argyropoulos. Plasmonic nanoantennas: Enhancing light-matter interactions at the nanoscale. *EPJ Applied Metamaterials*, 2, 2015.

[16] Zoran Jaksic, Marko Obradov, Slobodan Vukovic, et al. Plasmonic enhancement of light trapping in photodetectors. *Facta universitatis - series: Electronics and Energetics*, 27: 183–203, 2014.

[17] Vincenzo Giannini, Antonio I. Fernandez-Dominguez, Susannah C. Heck, et al. Plasmonic nanoantennas: Fundamentals and their use in controlling the radiative properties of na-

noemitters. *Chemical Reviews*, pages 3888–3912, 2011.

[18] Felix Benz, Mikolaj K. Schmidt, Alexander Dreismann, et al. Single-molecule optomechanics in “picocavities". *Science*, 354(6313):726–729, 2016.

[19] Felix Benz, Christos Tserkezis, Lars O. Herrmann, et al. Nanooptics of molecular-shunted plasmonic nanojunctions. *Nano Letters*, 15(1):669–674, 2015.

[20] Bart de Nijs, Richard W. Bowman, Lars O. Herrmann, et al. Unfolding the contents of sub-nm plasmonic gaps using normalising plasmon resonance spectroscopy. *Faraday Discuss.*, 178:185–193, 2015.

[21] Pascal Anger, Palash Bharadwaj, and Lukas Novotny. Enhancement and quenching of single-molecule fluorescence. *Physical Review Letters*, 96:113002, 2006.

[22] K. J. Savage, M. M. Hawkeye, R. Esteban, et al. Revealing the quantum regime in tunnelling plasmonics. *Nature*, 491:574–577, 2012.

[23] Alexandros Emboras, Jens Niegemann, Ping Ma, et al. Atomic Scale Plasmonic Switch. *Nano Letters*, 16(1):709–714, 2016.

[24] Daniel O. Sigle, Jan Mertens, Lars O. Herrmann, et al. Monitoring morphological changes in 2D monolayer semiconductors using atom-thick plasmonic nanocavities. *ACS Nano*, 9 (1):825–830, 2015.

[25] Shiho Yashima, Hiroshi Sugimoto, Hiroyuki Takashina, et al. Fluorescence enhancement and spectral shaping of silicon quantum dot monolayer by plasmonic gap resonances. *Journal of Physical Chemistry C*, 120:28795–28801, 2016.

[26] Hiroyuki Kishida and Maiken H. Mikkelsen. Ultrafast Lifetime and Bright Emission from Graphene Quantum Dots Using Plasmonic Nanogap Cavities. *Nano Letters*, 22:904–910, 2022.

[27] Jiani Huang, Andrew J. Traverso, Guoce Yang, et al. Real-Time Tunable Strong Coupling:

From Individual Nanocavities to Metasurfaces. *ACS Photonics*, 6:838–843, 2019.

[28] Thang B. Hoang, Gleb M. Akselrod, Christos Argyropoulos, et al. Ultrafast spontaneous emission source using plasmonic nanoantennas. *Nature Communications*, 6:7788, 2015.

[29] Gulis Zengin, Martin Wersäll, Sara Nilsson, et al. Realizing strong light-matter interactions between single-nanoparticle plasmons and molecular excitons at ambient conditions. *Physical Review Letters*, 114:157401, 2015.

[30] Thang B. Hoang, Gleb M. Akselrod, and Maiken H. Mikkelsen. Ultrafast Room-Temperature Single Photon Emission from Quantum Dots Coupled to Plasmonic Nanocavities. *Nano Letters*, 16:270–275, 2016.

[31] Jing Wang, Svetlana V. Boriskina, Hongyun Wang, et al. Illuminating Epidermal Growth Factor Receptor Densities on Filopodia through Plasmon Coupling. *ACS Nano*, 5(8):6619–6628, 2011.

[32] Vivian E. Ferry, Jeremy N. Munday, and Harry A. Atwater. Design Considerations for Plasmonic Photovoltaics. *Advanced Materials*, 22(43):4794–4808, 2010.

[33] David Conklin, Sanjini Nanayakkara, Tae-Hong Park, et al. Exploiting Plasmon-Induced Hot Electrons in Molecular Electronic Devices. *ACS Nano*, 7(5):4479–4486, 2013.

[34] Rejiya C.S., Jatish Kumar, Raji V., et al. Laser immunotherapy with gold nanorods causes selective killing of tumour cells. *Pharmacological Research*, 65(2):261–269, 2012.

[35] Che-Kuan Chu, Yi-Chou Tu, Yu-Wei Chang, et al. Cancer cell uptake behavior of Au nanoring and its localized surface plasmon resonance induced cell inactivation. *Nanotechnology*, 26(7):075102, 2015.

[36] M.R.K. Ali, Y. Wu, and M.A. El-Sayed. Gold-Nanoparticle-Assisted Plasmonic Photothermal Therapy Advances Toward Clinical Application. *J. Phys. Chem. C*, 123, 2019.

[37] A.B. Taylor and P. Zijlstra. Single-Molecule Plasmon Sensing: Current Status and Future

Prospects. *ACS Sensors*, 2, 2017.

[38] R.E. Armstrong, M. Horacek, and P. Zijlstra. Plasmonic Assemblies for Real-Time Single-Molecule Biosensing. *Small*, 16, 2020.

[39] C. Clavero. Plasmon-induced hot-electron generation at nanoparticle/metal-oxide interfaces for photovoltaic and photocatalytic devices. *Nature Photonics*, 8, 2014.

[40] Ben Yang, Gong Chen, Atif Ghafoor, et al. Sub-nanometre resolution in single-molecule photoluminescence imaging. *Nature Photonics*, 14(11):693–699, 2020.

[41] Yao Zhang, Qiu Shi Meng, Li Zhang, et al. Sub-nanometre control of the coherent interaction between a single molecule and a plasmonic nanocavity. *Nature Communications*, 8:15225, 2017.

[42] Cloudy Carnegie, Jack Griffiths, Bart de Nijs, et al. Room-Temperature Optical Picocavities below 1 nm^3 Accessing Single-Atom Geometries. *The Journal of Physical Chemistry Letters*, 9(24):7146–7151, 2018.

[43] Keita Tomita, Yasuhiro Kojima, and Fumihiko Kannari. Selective Coherent Anti-Stokes Raman Scattering Microscopy Employing Dual-Wavelength Nanofocused Ultrafast Plasmon Pulses. *Nano Letters*, 18(2):1366–1372, 2018.

[44] Wenjing Liu, Bumsu Lee, Carl H. Naylor, et al. Strong ExcitonPlasmon Coupling in MoS2 Coupled with Plasmonic Lattice. *Nano Letters*, 16(2):1262–1269, 2016.

[45] Angelos Xomalis, Xuezhi Zheng, Rohit Chikkaraddy, et al. Detecting mid-infrared light by molecular frequency upconversion in dual-wavelength nanoantennas. *Science*, 374(6572): 1268–1271, 2021.

[46] Wen Chen, Philippe Roelli, Huatian Hu, et al. Continuous-wave frequency upconversion with a molecular optomechanical nanocavity. *Science*, 374(6572):1264–1267, 2021.

[47] Derek A. Long. *The Raman effect: a unified treatment of the theory of Raman scattering by*

molecules. John Wiley & Sons, 2002.

[48] Lukas Novotny and Bert Hecht. *Principles of nano-optics*. Cambridge University Press, 2 edition, 2012.

[49] Jean Michel Gerard and Bruno Gayral. Strong Purcell effect for InAs quantum boxes in three-dimensional solid-state microcavities. *Journal of Lightwave Technology*, 17:2089–2095, 1999.

[50] P. B. Johnson and R. W. Christy. Optical constants of the noble metals. *Physical Review B*, 6(12):4370–4379, 1972.

[51] Lumerical Inc. https://www.lumerical.com/.

[52] COMSOL Multiphysics®v. 5.6. www.comsol.com. COMSOL AB, Stockholm, Sweden.

[53] Kane S. Yee and Jei S. Chen. The finite-difference time-domain (FDTD) and the finite-volume time-domain (FVTD) methods in solving Maxwell's equations. *IEEE Transactions on Antennas and Propagation*, 45:354–363, 1997.

[54] J. A. Porto, R. Carminati, and J. J. Greffet. Theory of electromagnetic field imaging and spectroscopy in scanning near-field optical microscopy. *Journal of Applied Physics*, 88(8): 4845–4850, 2000.

[55] Rémi Carminati, Manuel Nieto-Vesperinas, and Jean-Jacques Greffet. Reciprocity of evanescent electromagnetic waves. *Journal of the Optical Society of America A*, 15(3): 706–712, 1998.

[56] R. Ruppin. Decay of an excited molecule near a small metal sphere. *The Journal of Chemical Physics*, 76(4):1681–1684, 1982.

[57] Rohit Chikkaraddy, V. A. Turek, Nuttawut Kongsuwan, et al. Mapping Nanoscale Hotspots with Single-Molecule Emitters Assembled into Plasmonic Nanocavities Using DNA Origami. *Nano Letters*, 18(1):405–411, 2018.

[58] Craig F. Bohren. *Absorption and scattering of light by small particles*. John Wiley & Sons, 1983.

[59] Julius Adams Stratton. *Electromagnetic Theory*. John Wiley & Sons, 1941.

[60] Francis E. Low. *Classical Field Theory: Electromagnetism and Gravitation*. John Wiley & Sons, 1997.

[61] Wei Yan, Rémi Faggiani, and Philippe Lalanne. Rigorous modal analysis of plasmonic nanoresonators. *Physical Review B*, 97(20):205422, 2018.

[62] F. J.García De Abajo. Multiple scattering of radiation in clusters of dielectrics. *Physical Review B - Condensed Matter and Materials Physics*, 60(8):6086–6102, 1999.

[63] Milton Kerker, Dau-Sing Wang, and H Chew. Surface enhanced Raman scattering (SERS) by molecules adsorbed at spherical particles: errata. *Applied Optics*, 19(24):4159–4174, 1980.

[64] H. Chew. Transition rates of atoms near spherical surfaces. *The Journal of Chemical Physics*, 87(2):1355–1360, 1987.

[65] A. S. Bereza, A. V. Nemykin, S. V. Perminov, et al. Light scattering by dielectric bodies in the Born approximation. *Physical Review A*, 95(6):063839, 2017.

[66] Philip J. Wyatt. Scattering of electromagnetic plane waves from inhomogeneous spherically symmetric objects. *Physical Review*, 127(5):1837–1843, 1962.

[67] F. J. García de Abajo. Relativistic energy loss and induced photon emission in the interaction of a dielectric sphere with an external electron beam. *Physical Review B - Condensed Matter and Materials Physics*, 59(4):3095–3107, 1999.

[68] K Ohtaka and M Inoue. Light scattering from macroscopic spherical bodies. I. Integrated density of states of transverse electromagnetic fields. *Physical Review B*, 25(2):677–688, 1982.

[69] Cheng Zhang, Jean Paul Hugonin, Jean Jacques Greffet, et al. Surface Plasmon Polaritons Emission with Nanopatch Antennas: Enhancement by Means of Mode Hybridization. *ACS Photonics*, 6(11):2788–2796, 2019.

[70] H Chew, P. J. McNulty, and M Kerker. Model for Raman and fluorescent scattering by molecules embedded in small particles. *Physical Review A*, 13(1):396–404, 1976.

[71] Philippe Lalanne, Wei Yan, Kevin Vynck, et al. Light Interaction with Photonic and Plasmonic Resonances. *Laser and Photonics Reviews*, 12, 2018.

[72] Nuttawut Kongsuwan, Angela Demetriadou, Matthew Horton, et al. Plasmonic Nanocavity Modes: From Near-Field to Far-Field Radiation. *ACS Photonics*, 7(2):463–471, 2020.

[73] Chen To Tai and C. Yeh. *Dyadic Green's Functions in Electromagnetic Theory*. IEEE Press, 2 edition, 1972.

[74] Image from Wikipedia under Creative Commons licensing for reuse and modification. https://en.wikipedia.org/wiki/Spherical_harmonics/.

[75] Fabrizio Frezza, Fabio Mangini, and Nicola Tedeschi. Introduction to electromagnetic scattering: tutorial. *Journal of the Optical Society of America A*, 35(1):163–173, 2018.

[76] Antton Babaze, Ruben Esteban, Javier Aizpurua, et al. Second-Harmonic Generation from a Quantum Emitter Coupled to a Metallic Nanoantenna. *ACS Photonics*, 7(3):701–713, 2020.

[77] Felix Benz, Rohit Chikkaraddy, Andrew Salmon, et al. SERS of Individual Nanoparticles on a Mirror: Size Does Matter, but so Does Shape. *Journal of Physical Chemistry Letters*, 7 (12):2264–2269, 2016.

[78] Kalun Bedingfield, Eoin Elliott, Nuttawut Kongsuwan, et al. Morphology dependence of nanoparticle-on-mirror geometries: A quasinormal mode analysis. *EPJ Appl. Metamat.*, 9, 2022.

[79] Hiroshi Sugimoto, Tianhong Chen, Ren Wang, et al. Plasmon-Enhanced Emission Rate of Silicon Nanocrystals in Gold Nanorod Composites. *ACS Photonics*, 2(9):1298–1305, 2015.

[80] Denis G. Baranov, Martin Wersall, Jorge Cuadra, et al. Novel Nanostructures and Materials for Strong LightMatter Interactions. *ACS Photonics*, 5(1):24–42, 2018.

[81] Alec Rose, Thang B. Hoang, Felicia McGuire, et al. Control of Radiative Processes Using Tunable Plasmonic Nanopatch Antennas. *Nano Letters*, 14(8):4797–4802, 2014.

[82] Martin Wersall, Jorge Cuadra, Tomasz J. Antosiewicz, et al. Observation of Mode Splitting in Photoluminescence of Individual Plasmonic Nanoparticles Strongly Coupled to Molecular Excitons. *Nano Letters*, 17(1):551–558, 2017.

[83] Jan Mertens, Anna L. Eiden, Daniel O. Sigle, et al. Controlling Subnanometer Gaps in Plasmonic Dimers Using Graphene. *Nano Letters*, 13(11):5033–5038, 2013.

[84] C. Tserkezis, R. Esteban, D. O. Sigle, et al. Hybridization of plasmonic antenna and cavity modes: Extreme optics of nanoparticle-on-mirror nanogaps. *Phys. Rev. A*, 92:053811, 2015.

[85] Ji-Hyeok Huh, Jaewon Lee, and Seungwoo Lee. Comparative Study of Plasmonic Resonances between the Roundest and Randomly Faceted Au Nanoparticles-on-Mirror Cavities. *ACS Photonics*, 5:413–421, 2018.

[86] Kalun Bedingfield and Angela Demetriadou. On the excitation and radiative decay rates of plasmonic nanoantennas. *Nanophotonics*, 11:2271–2281, 2022.

[87] Anna Lombardi, Angela Demetriadou, Lee Weller, et al. Anomalous Spectral Shift of Near- and Far-Field Plasmonic Resonances in Nanogaps. *ACS Photonics*, 3(3):471–477, 2016.

[88] J. Mertens, A. Demetriadou, R. W. Bowman, et al. Tracking Optical Welding through Groove Modes in Plasmonic Nanocavities. *Nano Letters*, 16(9):5605–5611, 2016.

[89] Q. Bai, M. Perrin, C. Sauvan, et al. Efficient and intuitive method for the analysis of light scattering by a resonant nanostructure. *Opt. Express*, 21(22):27371–27382, 2013.

[90] Christophe Sauvan, Tong Wu, Rachid Zarouf, et al. Normalization, orthogonality, and completeness of quasinormal modes of open systems: the case of electromagnetism. *Opt. Express*, 30(5):6846–6885, 2022.

[91] Tong Wu, Massimo Gurioli, and Philippe Lalanne. Nanoscale Light Confinement: the Qs and Vs. *ACS Photonics*, 8(6):1522–1538, 2021.

[92] Philip Trøst Kristensen, Rong-Chun Ge, and Stephen Hughes. Normalization of quasinormal modes in leaky optical cavities and plasmonic resonators. *Phys. Rev. A*, 92:053810, 2015.

[93] C. Sauvan, J. P. Hugonin, I. S. Maksymov, et al. Theory of the spontaneous optical emission of nanosize photonic and plasmon resonators. *Physical Review Letters*, 110(23):237401, 2013.

[94] Philippe Lalanne. Light-in-complex-nanostructures/MAN: Versions 7.1 of QNMEig and QNMPole. *Zenodo*, 2020.

[95] R.K. Chang and A.J. Campillo. *Optical Processes in Microcavities*. World Scientific, 1996.

[96] Rong-Chun Ge and Stephen Hughes. Design of an efficient single photon source from a metallic nanorod dimer: a quasi-normal mode finite-difference time-domain approach. *Opt. Lett.*, 39(14):4235–4238, 2014.

[97] Philip Trøst Kristensen and Stephen Hughes. Modes and Mode Volumes of Leaky Optical Cavities and Plasmonic Nanoresonators. *ACS Photonics*, 1(1):2–10, 2014.

[98] David A. Powell. Resonant dynamics of arbitrarily shaped meta-atoms. *Phys. Rev. B*, 90: 075108, 2014.

[99] Xuezhi Zheng, Ventsislav K. Valev, Niels Verellen, et al. Implementation of the Natural Mode Analysis for Nanotopologies Using a Volumetric Method of Moments (V-MoM) Algorithm. *IEEE Photonics Journal*, 6(4):1–13, 2014.

[100] Ruey-Lin Chern, Chien C. Chang, and C. Chung Chang. Surface and bulk modes for peri-

odic structures of negative index materials. *Phys. Rev. B*, 74:155101, 2006.

[101] A. Taflove, A. Oskooi, and S.G Johnson. *Advances in FDTD computational electrodynamics: photonics and nanotechnology*. Artech house, 2013.

[102] Jorn Zimmerling, Lei Wei, Paul Urbach, et al. Efficient computation of the spontaneous decay rate of arbitrarily shaped 3D nanosized resonators: a Krylov model-order reduction approach. *Applied Physics A*, 122, 2016.

[103] Rongkuo Zhao, Yu Luo, A. I. Fernández-Domínguez, et al. Description of van der Waals Interactions Using Transformation Optics. *Phys. Rev. Lett.*, 111:033602, 2013.

[104] Aaswath Raman and Shanhui Fan. Photonic Band Structure of Dispersive Metamaterials Formulated as a Hermitian Eigenvalue Problem. *Phys. Rev. Lett.*, 104:087401, 2010.

[105] Jorn Zimmerling, Lei Wei, Paul Urbach, et al. A Lanczos model-order reduction technique to efficiently simulate electromagnetic wave propagation in dispersive media. *Journal of Computational Physics*, 315:348–362, 2016.

[106] Rose M. Joseph, Susan C. Hagness, and Allen Taflove. Direct time integration of Maxwell's equations in linear dispersive media with absorption for scattering and propagation of femtosecond electromagnetic pulses. *Opt. Lett.*, 16(18):1412–1414, 1991.

[107] Eoin Elliott, Kalun Bedingfield, Junyang Huang, et al. Fingerprinting the hidden facets of plasmonic nanocavities. *Accepted: ACS Photonics*, 2022.

[108] Jianji Yang, Jean-Paul Hugonin, and Philippe Lalanne. Light-in-complex-nanostructures/RETOP: Version 8.1. *Zenodo*, 2020.

[109] Jianji Yang, Jean-Paul Hugonin, and Philippe Lalanne. Near-to-Far Field Transformations for Radiative and Guided Waves. *ACS Photonics*, 3(3):395–402, 2016.

[110] Anders Pors and Sergey I. Bozhevolnyi. Quantum Emitters near Layered Plasmonic Nanostructures: Decay Rate Contributions. *ACS Photonics*, 2(2):228–236, 2015.

[111] A.E. Balanis. *Antenna Theory Analysis and Design*. John Wiley & Sons, 4 edition, 2016.

[112] K. Demarest, Z. Huang, and R. Plumb. An FDTD near- to far-zone transformation for scatterers buried in stratified grounds. *IEEE Transactions on Antennas and Propagation*, 44(8): 1150–1157, 1996.

[113] Rohit Chikkaraddy, Xuezhi Zheng, Felix Benz, et al. How Ultranarrow Gap Symmetries Control Plasmonic Nanocavity Modes: From Cubes to Spheres in the Nanoparticle-on-Mirror. *ACS Photonics*, 4(3):469–475, 2017.

[114] Syed Mubeen, Shunping Zhang, Namhoon Kim, et al. Plasmonic Properties of Gold Nanoparticles Separated from a Gold Mirror by an Ultrathin Oxide. *Nano Letters*, 12(4): 2088–2094, 2012.

[115] Tomasz J. Antosiewicz, S. Peter Apell, and Timur Shegai. PlasmonExciton Interactions in a CoreShell Geometry: From Enhanced Absorption to Strong Coupling. *ACS Photonics*, 1 (5):454–463, 2014.

[116] Judith Langer, Dorleta Jimenez de Aberasturi, Javier Aizpurua, et al. Present and Future of Surface-Enhanced Raman Scattering. *ACS Nano*, 14(1):28–117, 2020.

[117] Christophe Sauvan, Tong Wu, Rachid Zarouf, et al. Normalization, orthogonality, and completeness of quasinormal modes of open systems: the case of electromagnetism [Invited]. *Opt. Express*, 30(5):6846–6885, 2022.

[118] Sebastian Franke, Juanjuan Ren, and Stephen Hughes. Quantized quasinormal-mode theory of coupled lossy and amplifying resonators. *Phys. Rev. A*, 105:023702, 2022.

[119] Rui-Qi Li, D. Hernángomez-Pérez, F. J. García-Vidal, et al. Transformation Optics Approach to Plasmon-Exciton Strong Coupling in Nanocavities. *Phys. Rev. Lett.*, 117:107401, 2016.

[120] A. Cuartero-Gonzalez and A. I. Fernandez-Dominguez. Light-Forbidden Transitions in Plasmon-Emitter Interactions beyond the Weak Coupling Regime. *ACS Photonics*, 5(8):

3415–3420, 2018.

[121] Sebastian Franke, Juanjuan Ren, and Stephen Hughes. Impact of mode regularization for quasinormal mode perturbation theories. 2022.

[122] Alvaro Cuartero-González, Alejandro Manjavacas, and Antonio I Fernández-Domínguez. Distortion of the local density of states in a plasmonic cavity by a quantum emitter. *New Journal of Physics*, 23(7):073011, 2021.

[123] Chelsea Carlson, Robert Salzwedel, Malte Selig, et al. Strong coupling regime and hybrid quasinormal modes from a single plasmonic resonator coupled to a transition metal dichalcogenide monolayer. *Phys. Rev. B*, 104:125424, 2021.

[124] A. Cuartero-González and A. I. Fernández-Domínguez. Dipolar and quadrupolar excitons coupled to a nanoparticle-on-mirror cavity. *Phys. Rev. B*, 101:035403, 2020.

[125] Sebastian Franke, Stephen Hughes, Mohsen Kamandar Dezfouli, et al. Quantization of Quasinormal Modes for Open Cavities and Plasmonic Cavity Quantum Electrodynamics. *Phys. Rev. Lett.*, 122:213901, 2019.

[126] Johannes Feist, Antonio I. Fernandez-Dominguez, and Francisco J. Garcia-Vidal. Macroscopic QED for quantum nanophotonics: emitter-centered modes as a minimal basis for multiemitter problems. *Nanophotonics*, 10(1):477–489, 2021.

[127] Sebastian Franke, Juanjuan Ren, Marten Richter, et al. Fermi's Golden Rule for Spontaneous Emission in Absorptive and Amplifying Media. *Phys. Rev. Lett.*, 127:013602, 2021.

[128] Antonio I. Fernandez-Dominguez, Sergey I. Bozhevolnyi, and N. Asger Mortensen. Plasmon-Enhanced Generation of Nonclassical Light. *ACS Photonics*, 5(9):3447–3451, 2018.

[129] Tomá š Neuman, Ruben Esteban, Geza Giedke, et al. Quantum description of surface-enhanced resonant Raman scattering within a hybrid-optomechanical model. *Phys. Rev. A*,

100:043422, 2019.

[130] Mikolaj K. Schmidt, Ruben Esteban, Alejandro Gonzalez-Tudela, et al. Quantum Mechanical Description of Raman Scattering from Molecules in Plasmonic Cavities. *ACS Nano*, 10(6): 6291–6298, 2016.

[131] Rui-Qi Li, F. J. Garcia-Vidal, and A. I. Fernandez-Dominguez. Plasmon-Exciton Coupling in Symmetry-Broken Nanocavities. *ACS Photonics*, 5(1):177–185, 2018.

[132] A. Delga, J. Feist, J. Bravo-Abad, et al. Quantum Emitters Near a Metal Nanoparticle: Strong Coupling and Quenching. *Phys. Rev. Lett.*, 112:253601, 2014.

[133] C. Van Vlack, Philip Trøst Kristensen, and S. Hughes. Spontaneous emission spectra and quantum light-matter interactions from a strongly coupled quantum dot metal-nanoparticle system. *Phys. Rev. B*, 85:075303, 2012.

[134] T. Hümmer, F. J. García-Vidal, L. Martín-Moreno, et al. Weak and strong coupling regimes in plasmonic QED. *Phys. Rev. B*, 87:115419, 2013.

[135] Sebastian Wuestner, Andreas Pusch, Kosmas L. Tsakmakidis, et al. Gain and plasmon dynamics in active negative-index metamaterials. *Philosophical Transactions of the Royal Society A: Mathematical, Physical and Engineering Sciences*, 369(1950):3525–3550, 2011.

[136] Nuttawut Kongsuwan, Xiao Xiong, Ping Bai, et al. Quantum Plasmonic Immunoassay Sensing. *Nano Letters*, 19(9):5853–5861, 2019.

[137] Anna Lombardi, Angela Demetriadou, Lee Weller, et al. Anomalous Spectral Shift of Near- and Far-Field Plasmonic Resonances in Nanogaps. *ACS Photonics*, 3(3):471–477, 2016.

[138] P. Alonso-González, P. Albella, F. Neubrech, et al. Experimental Verification of the Spectral Shift between Near- and Far-Field Peak Intensities of Plasmonic Infrared Nanoantennas. *Phys. Rev. Lett.*, 110:203902, 2013.

[139] Gilbert Grynberg, Alain Aspect, Claude Fabre, et al. *Introduction to Quantum Optics: From*

the Semi-classical Approach to Quantized Light. Cambridge University Press, 2010.

[140] Rodney Loudon. The Quantum Theory of Light. *American Journal of Physics*, 42(11): 1041–1042, 1974.

[141] T.G. Eck. Level crossings and anticrossings. *Physica*, 33(1):157–162, 1967.

[142] Lucio Claudio Andreani, Giovanna Panzarini, and Jean-Michel Gérard. Strong-coupling regime for quantum boxes in pillar microcavities: Theory. *Phys. Rev. B*, 60:13276–13279, 1999.

[143] Kotni Santhosh, Ora Bitton, Lev Chuntonov, et al. Vacuum Rabi splitting in a plasmonic cavity at the single quantum emitter limit. *Nature Communications*, 7:11823, 2016.

[144] Kyung-Duck Park, Molly A. May, Haixu Lengand Jiarong Wang, et al. Tip-enhanced strong coupling spectroscopy, imaging, and control of a single quantum emitter. *Science Advances*, 5(7):eaav5931, 2019.

[145] Zhiguang Liu, Jiafang Li, Zhe Liu, et al. Fano resonance Rabi splitting of surface plasmons. *Scientific Reports*, 7(1), 2017.

[146] Chao-Yu Li, Sai Duan, Jun Yi, et al. Real-time detection of single-molecule reaction by plasmon-enhanced spectroscopy. *Science Advances*, 6(24):eaba6012, 2020.

APPENDICES

A1 SOLUTION TO THE HOMOGENEOUS SCALAR HELMHOLTZ EQUATION

The reduction of Maxwell's equations to a set of four differential equations—in the absence of a source ($\boldsymbol{J}, \rho = 0$)—leads to the general form of the homogeneous scalar Helmholtz equation [48]:

$$[\nabla^2 + k^2]\psi(\boldsymbol{r}) = 0 \; . \tag{A1}$$

By considering $\psi(\boldsymbol{r})$ as a separable function of the form [58]:

$$\psi(\boldsymbol{r}) = R(r)\Theta(\theta)\Phi(\phi) \; , \tag{A2}$$

in spherical coordinates the homogeneous scalar Helmholtz equation becomes:

$$\frac{\sin^2\theta}{R(r)}\partial_r\Big(r^2\partial_r R(r)\Big)+\frac{\sin\theta}{\Theta(\theta)}\partial_\theta\Big(\sin\theta\partial_\theta\Theta(\theta)\Big)+\frac{1}{\Phi(\phi)}\partial_\phi^2\Phi(\phi)+k^2r^2\sin^2\theta=0\ , \tag{A3}$$

where the gradient in spherical coordinates, $\nabla=\frac{\partial}{\partial r}\hat{\boldsymbol{r}}+\frac{1}{r}\frac{\partial}{\partial\theta}\hat{\boldsymbol{\theta}}+\frac{1}{r\sin\theta}\frac{\partial}{\partial\phi}\hat{\boldsymbol{\phi}}$, has been used—along with the following partial derivative notation: $\partial_x=\frac{\partial}{\partial x}$. Separating this into explicit dependencies on r, θ and ϕ yields three differential equations:

$$\frac{1}{\Phi(\phi)}\partial_\phi^2\Phi(\phi)=C_1 \tag{A4}$$

$$\frac{1}{\sin\theta\Theta(\theta)}\partial_\theta\Big(\sin\theta\partial_\theta\Theta(\theta)\Big)+\frac{C_1}{\sin^2\theta}=C_2 \tag{A5}$$

$$\frac{1}{R(r)}\partial_r\Big(r^2\partial_r R(r)\Big)+C_2+k^2r^2=0\ . \tag{A6}$$

By respectively setting the constants C_1 and C_2 to $-m^2$ and $-l(l+1)$, the three variables are separated and lead to independent differential equations that each only depend on a single variable (r, θ or ϕ):

$$\partial_\phi^2\Phi(\phi)+m^2\Phi(\phi)=0 \tag{A7}$$

$$\frac{1}{\sin\theta}\partial_\theta\Big(\sin\theta\partial_\theta\Theta(\theta)\Big)+\Big[l(l+1)-\frac{m^2}{\sin^2\theta}\Big]\Theta(\theta)=0 \tag{A8}$$

$$\partial_r\Big(r^2\partial_r R(r)\Big)+\big[k^2r^2-l(l+1)\big]R(r)=0\ . \tag{A9}$$

The constants introduced here depend on the angular, l, and magnetic, m, quantum numbers—where l is a positive integer, and m takes integer values in the range $-l\leq m\leq l$.

The independent solutions to these differential equations take the general forms:

$$\Phi(\phi) = A_m \, e^{im\phi} \tag{A10}$$

$$\Theta(\theta) = B_{l,m} \, P_l^m(\cos\theta) \tag{A11}$$

$$R(r) = C_l \, z_l(kr) \; , \tag{A12}$$

where $P_l^m(\cos\theta)$ are the associated Legendre polynomials, and $z_l(kr)$ are the spherical Bessel functions of either the first (j_l) or second (y_l) kind, or a linear combination of the two (spherical Hankel function). Therefore, the full solution to the homogeneous scalar Helmholtz equation—following the form of Eq. A2—becomes:

$$\psi(\boldsymbol{r}) = \sum_{l=0}^{\infty} \sum_{m=-l}^{l} A_{l,m} z_l(kr) Y_l^m(\Omega_r) \; , \tag{A13}$$

where $A_{l,m}$ is a scalar constant to be determined for the system in question, and $Y_l^m(\Omega_r)$ are the spherical Harmonics at the angular position of $\Omega_r = \{\theta_r, \phi_r\}$, given by

$$Y_l^m(\Omega_r) = \sum_{e,o} \sqrt{(2l+1)\frac{(l-m)!}{(l+m)!}} \, P_l^m(\cos\theta_r) \begin{cases} \cos m\phi \\ \\ \sin m\phi \end{cases} \; , \tag{A14}$$

where the summation accounts for both the even and odd ϕ-responses of the system.

A2 DERIVATION OF THE $C_{l,m}$ COEFFICIENT

The final step in evaluating the electric and magnetic fields is determining the coefficient $C_{l,m}$. To do this, the Ohm-Rayleigh method is applied (as outlined in Tai [73]) along with three overlap integrals between the VSH pairs. If, for example, one considers the overlap (orthogonality condition) between the $\boldsymbol{M}_{l,m}^{e,o}(k\boldsymbol{r})$ and $\boldsymbol{N}_{l,m}^{e,o}(k\boldsymbol{r})$ VSHs—defined as $I_{M\cdot N}$ for space saving—the explicit computation gives the following three-dimensional integral over all space:

$$I_{M\cdot N} = \int_0^{2\pi}\int_0^{\pi}\int_0^{\infty} \boldsymbol{M}_{l,m}^{e,o}(k\boldsymbol{r}) \cdot \boldsymbol{N}_{l,m}^{e,o}(k\boldsymbol{r}')r^2 \sin\theta dr d\theta d\phi \ . \tag{A15}$$

By expanding the dot product between the two VSHs, and explicitly considering the cross-terms between the even and odd components, we are left with:

$$I_{M\cdot N} = \int_0^{2\pi}\int_0^{\pi}\int_0^{\infty} \frac{m}{kr\sin\theta} z_l(kr)[krz_l(kr')]' P_l^m(\cos\theta)\partial_\theta P_l^m(\cos\theta)$$
$$\left[\begin{Bmatrix}-\sin m\phi \\ \cos m\phi\end{Bmatrix}\begin{Bmatrix}\cos m\phi \\ \sin m\phi\end{Bmatrix} - \begin{Bmatrix}\cos m\phi \\ \sin m\phi\end{Bmatrix}\begin{Bmatrix}-\sin m\phi \\ \cos m\phi\end{Bmatrix}\right] r^2\sin\theta dr d\theta d\phi \ , \tag{A16}$$

where we have considered a general spherical Bessel function, $z_l(kr)$, in place of either $j_l(kr)$ or $h_l^{(1)}(kr)$. Irrespective of the integrals, the ϕ-dependence renders this relation null and returns $I_{M\cdot N} = 0$—as required for orthogonal fields: recall that $\nabla \times \boldsymbol{N} = k\boldsymbol{M}$.

In addition to this VSH orthogonality condition, we have the self-orthogonality re-

lations for each VSH, as given by $I_{M\cdot M}$ and $I_{N\cdot N}$. In solving these integrals, the same general procedure is followed: the expansion of the dot product between the two VSHs, then the explicit consideration of even and odd cross-terms. Without the cancellation coming from the ϕ-dependence, additional steps must be taken to simplify these expressions. This requires a set of associated Legendre polynomial standard integrals and spherical Bessel function recurrence relations—as these also appear in later stages of the derivation, we present a summarised version here:

$$\int_0^{2\pi} [\sin m\phi \cos m\phi]\, d\phi = 0 \tag{A17}$$

$$\int_0^{2\pi} \sin^2 m\phi d\phi = \begin{cases} 0\ , & \text{when } m = 0 \\ \pi\ , & \text{when } m \neq 0, m \in Z \\ \pi - \frac{\sin 4m\pi}{4m}\ , & \text{when } m \neq 0 \end{cases} \tag{A18}$$

$$\int_0^{2\pi} \cos^2 m\phi d\phi = \begin{cases} \pi(1+\delta_0)\ , & \text{when } m \in Z \\ \pi + \frac{\sin 4m\pi}{4m}\ , & \text{when } m \neq 0 \end{cases} \tag{A19}$$

$$\int_0^{\pi} P_l^m(\cos\theta) P_{l'}^m(\cos\theta) \sin\theta d\theta = \begin{cases} 0\ , & \text{when } l \neq l' \\ \frac{2}{2l+1}\frac{(l+m)!}{(l-m)!}\ , & \text{when } l = l' \end{cases} \tag{A20}$$

$$\int_0^{\pi} \left[\frac{m^2}{\sin^2\theta} + \partial_\theta^2\right] P_l^m(\cos\theta) P_{l'}^m(\cos\theta) \sin\theta d\theta = \begin{cases} 0\ , & \text{when } l \neq l' \\ \frac{2l(l+1)}{2l+1}\frac{(l+m)!}{(l-m)!}\ , & \text{when } l = l' \end{cases} \tag{A21}$$

$$[xz_l(x)]' = \frac{x}{2l+1}\left[(l+1)z_{l-1}(x) - lz_{l+1}(x)\right] \tag{A22}$$

$$z_l(x) = \frac{x}{2l+1}\left[z_{l-1}(x) + z_{l+1}(x)\right] \tag{A23}$$

and $\int_0^\infty z_l(kr)z_l(kr')r^2dr = \int_0^\infty z_l(kr)z_l(k'r)r^2dr = \frac{\pi}{2}\frac{\delta(k-k')}{k^2}$, which is made possible by transferring the primed information from r to k—where $\delta_0 = \begin{cases} 1\,, & \text{when } m = 0 \\ 0\,, & \text{when } m \neq 0 \end{cases}$.

The self orthogonality integral of the $\boldsymbol{M}_{l,m}^{e,o}(k\boldsymbol{r})$ VSH—after expanding the dot product and simplifying the even and odd terms—becomes:

$$\begin{aligned} I_{M\cdot M} = &\int_0^\infty r^2 z_l(kr)z_l(kr')dr \int_0^{2\pi} \left\{1 - 2\sin m\phi\cos m\phi\right\} d\phi \\ &\times \int_0^\pi \left\{\frac{m^2}{\sin^2\theta}P_l^m(\cos\theta)P_{l'}^m(\cos\theta) + \partial_\theta P_l^m(\cos\theta)\partial_\theta P_{l'}^m(\cos\theta)\right\}\sin\theta d\theta\,, \end{aligned} \tag{A24}$$

which, when applying the above integrals, reduces to:

$$I_{M\cdot M} = (1+\delta_0)\pi^2\frac{l(l+1)}{2l+1}\frac{(l+m)!}{(l-m)!}\frac{\delta(k-k')}{k^2}\,. \tag{A25}$$

Similarly for the $\boldsymbol{N}_{l,m}^{e,o}(k\boldsymbol{r})$ VSH, but this requires an additional simplification of the radial terms:

$$I_{N\cdot N} = \frac{\pi(1+\delta_0)}{k^2}\frac{2l(l+1)}{2l+1}\frac{(l+m)!}{(l-m)!}\int_0^\infty \left[l(l+1)z_l(kr)z_l(kr') + [krz_l(kr)]'[krz_l(kr')]'\right]dr\,. \tag{A26}$$

From the recurrence relations of the spherical Bessel functions, which gives:

$$l(l+1)z_l(kr)z_l(kr')+[krz_l(kr)]'[krz_l(kr')]' = \frac{kk'r^2}{2l+1}\Big[(l+1)z_{l-1}(kr)z_{l-1}(k'r)+lz_{l+1}(kr)z_{l+1}(k'r)\Big] , \tag{A27}$$

and upon integrating, leads to the same solution for $I_{N\cdot N}$ as $I_{M\cdot M}$:

$$I_{N\cdot N} = I_{M\cdot M} = (1+\delta_0)\pi^2\frac{l(l+1)}{2l+1}\frac{(l+m)!}{(l-m)!}\frac{\delta(k-k')}{k^2} . \tag{A28}$$

From these expressions, along with $I_{M\cdot N} = 0$, the $C_{l,m}$ coefficient can be determined by using the Ohm-Rayleigh conditions [73]:

$$\nabla\times\Big[\overleftrightarrow{I}\delta(\boldsymbol{r}-\boldsymbol{r}')\Big] = \int_0^\infty d\kappa\sum_{l,m}\left[\boldsymbol{N}^{e,o}_{l,m}(\kappa)\otimes\boldsymbol{A}^{e,o}_{l,m}+\boldsymbol{M}^{e,o}_{l,m}(\kappa)\otimes\boldsymbol{B}^{e,o}_{l,m}\right] \tag{A29}$$

$$\overleftrightarrow{I}\delta(\boldsymbol{r}-\boldsymbol{r}') = \int_0^\infty dk\sum_{l,m}\frac{1}{k}\left[\boldsymbol{M}^{e,o}_{l,m}(\kappa)\otimes\boldsymbol{A}^{e,o}_{l,m}+\boldsymbol{N}^{e,o}_{l,m}(\kappa)\otimes\boldsymbol{B}^{e,o}_{l,m}\right] . \tag{A30}$$

Taking the dot product with the $\boldsymbol{M}^{e,o}_{l,m}(k\boldsymbol{r})$ VSH on the left gives:

$$\boldsymbol{M}^{e,o}_{l,m}(k\boldsymbol{r}')\cdot\overleftrightarrow{I}\delta(\boldsymbol{r}-\boldsymbol{r}') = \int_0^\infty dk\frac{1}{k}\big[\boldsymbol{M}^{e,o}_{l,m}(k\boldsymbol{r}')\cdot\boldsymbol{M}^{e,o}_{l,m}(\kappa)\otimes\boldsymbol{A}^{e,o}_{l,m} + \boldsymbol{M}^{e,o}_{l,m}(k\boldsymbol{r}')\cdot\boldsymbol{N}^{e,o}_{l,m}(\kappa)\otimes\boldsymbol{B}^{e,o}_{l,m}\big] , \tag{A31}$$

where the second term is zero due to the orthogonality of the VSHs. Integrating over all

space reduces this to:

$$\int_0^{2\pi}\int_0^{\pi}\int_0^{\infty} \boldsymbol{M}_{l,m}^{e,o}(k\boldsymbol{r}')\cdot\overleftrightarrow{I}\delta(\boldsymbol{r}-\boldsymbol{r}')r^2\sin\theta dr d\theta d\phi = (1+\delta_0)\frac{\pi^2}{k^3}\frac{l(l+1)}{2l+1}\frac{(l+m)!}{(l-m)!}\boldsymbol{A}_{l,m}^{e,o}\ . \tag{A32}$$

To simplify the left hand side, recall the relationship between the VSHs, $\boldsymbol{M}_{l,m}^{e,o}(k\boldsymbol{r}) = \frac{1}{k}\nabla\times\boldsymbol{N}_{l,m}^{e,o}(k\boldsymbol{r})$, as well the identity: $\nabla\times\boldsymbol{a}\cdot\overleftrightarrow{\boldsymbol{b}} = \boldsymbol{a}\cdot\nabla\times\overleftrightarrow{\boldsymbol{b}} + \nabla\cdot\left(\boldsymbol{a}\times\overleftrightarrow{\boldsymbol{b}}\right)$. Using these, the integrand becomes:

$$\begin{aligned}\frac{1}{k}\nabla\times\boldsymbol{N}_{l,m}^{e,o}(k\boldsymbol{r})\cdot\overleftrightarrow{I}\delta(\boldsymbol{r}-\boldsymbol{r}') = \frac{1}{k}\boldsymbol{N}_{l,m}^{e,o}(k\boldsymbol{r})\cdot\nabla\times\overleftrightarrow{I}\delta(\boldsymbol{r}-\boldsymbol{r}')\\ +\nabla\cdot\left(\frac{1}{k}\boldsymbol{N}_{l,m}^{e,o}(k\boldsymbol{r})\times\overleftrightarrow{I}\delta(\boldsymbol{r}-\boldsymbol{r}')\right)\ .\end{aligned} \tag{A33}$$

Upon applying dyadic Gauss theorem, $\int_V\nabla\cdot\overleftrightarrow{\boldsymbol{b}}dV = \oint_S\hat{\boldsymbol{n}}\cdot\overleftrightarrow{\boldsymbol{b}}dS$, the second term in the volume integral becomes a surface integral which evaluates to zero. The first term simply returns to $\boldsymbol{M}_{l,m}^{e,o}(k\boldsymbol{r}')$, and reduces this to:

$$\boldsymbol{M}_{l,m}^{e,o}(k\boldsymbol{r}') = (1+\delta_0)\frac{1}{k}\frac{\pi^2}{k^2}\frac{l(l+1)}{2l+1}\frac{(l+m)!}{(l-m)!}\boldsymbol{A}_{l,m}^{e,o}\ . \tag{A34}$$

Instead taking the dot product at the start with the $\boldsymbol{N}_{l,m}^{e,o}(k\boldsymbol{r})$ VSH, a similar expression is found that allows the determination of both $\boldsymbol{A}_{l,m}^{e,o}$ and $\boldsymbol{B}_{l,m}^{e,o}$:

$$\boldsymbol{A}_{l,m}^{e,o} = \boldsymbol{M}_{l,m}^{e,o}(k\boldsymbol{r}')\frac{k^3}{2\pi^2}(2-\delta_0)\frac{2l+1}{l(l+1)}\frac{(l-m)!}{(l+m)!} \tag{A35}$$

$$\boldsymbol{B}_{l,m}^{e,o} = \boldsymbol{N}_{l,m}^{e,o}(k\boldsymbol{r}')\ \frac{k^3}{2\pi^2}(2-\delta_0)\frac{2l+1}{l(l+1)}\frac{(l-m)!}{(l+m)!}\ , \tag{A36}$$

where the fact that $\frac{2}{1+\delta_0} = 2 - \delta_0$ has been used. These are indeed constants due to the singular dependence on $\mathbf{r}'$.

Returning to the definition of $\overleftrightarrow{I}\delta(\boldsymbol{r} - \boldsymbol{r}')$ of equation A30, this now becomes:

$$\overleftrightarrow{I}\delta(\boldsymbol{r} - \boldsymbol{r}') = \frac{1}{2\pi^2}\int_0^\infty \kappa^2 d\kappa \sum_{l,m}(2-\delta_0)\frac{2l+1}{l(l+1)}\frac{(l-m)!}{(l+m)!} \times \left[\boldsymbol{M}^{e,o}_{l,m}(\kappa)\otimes\boldsymbol{M}^{e,o}_{l,m}(k\boldsymbol{r}') + \boldsymbol{N}^{e,o}_{l,m}(\kappa)\otimes\boldsymbol{N}^{e,o}_{l,m}(k\boldsymbol{r}')\right] . \quad \text{(A37)}$$

With this and the wave equation in terms of the dyadic Green's function:

$$\nabla\times\nabla\times\overleftrightarrow{G}(\boldsymbol{r},\boldsymbol{r}') - k^2\overleftrightarrow{G}(\boldsymbol{r},\boldsymbol{r}') = \overleftrightarrow{I}\delta(\boldsymbol{r}-\boldsymbol{r}') , \quad \text{(A38)}$$

allows the dyadic Green's function to be determined:

$$\overleftrightarrow{G}(\boldsymbol{r},\boldsymbol{r}') = \sum_{l,m} C_{l,m}\left[\boldsymbol{M}^{e,o}_{l,m}(k\boldsymbol{r})\otimes\boldsymbol{M}^{e,o}_{l,m}(k\boldsymbol{r}') + \boldsymbol{N}^{e,o}_{l,m}(k\boldsymbol{r})\otimes\boldsymbol{N}^{e,o}_{l,m}(k\boldsymbol{r}')\right] , \quad \text{(A39)}$$

where $C_{l,m}$ is given by

$$C_{l,m} = \frac{ik}{4\pi}(2-\delta_0)\frac{2l+1}{l(l+1)}\frac{(l-m)!}{(l+m)!} . \quad \text{(A40)}$$

A3 SCATTERING AND ABSORPTION DUE TO AN ISOLATED NP EXCITED BY A DIPOLE SOURCE

In order to introduce the geometry into the model, a series boundary conditions must be applied to enforce a continuity of the tangential components of the fields across the surface of the NP. The electric and magnetic field conditions follow:

$$(\boldsymbol{E}_{inc} + \boldsymbol{E}_{scat} - \boldsymbol{E}_{int})\,|_{r=r_p} \times \hat{\boldsymbol{e}}_r = 0 \tag{A41}$$

$$(\boldsymbol{H}_{inc} + \boldsymbol{H}_{scat} - \boldsymbol{H}_{int})\,|_{r=r_p} \times \hat{\boldsymbol{e}}_r = 0\ , \tag{A42}$$

and are evaluated at the surface of the NP, where $r = r_p$. The θ-component of the electric boundary condition leads to:

$$\begin{aligned} B_l t_l^{(3)}\ \frac{1}{kr_p}\,\partial_\theta Y_l^m(\theta,\phi)\left[\mu_1[kr_p j_l(kr_p)]' + \mu_1 b_l[kr_p h_l^{(1)}(kr_p)]' - \mu_2 d_l \frac{1}{N}[Nkr_p j_l(Nkr_p)]'\right] \\ + A_l s_l^{(3)} \frac{1}{\sin\theta}\partial_\phi Y_l^m(\theta,\phi)\left[\mu_1 j_l(kr_p) + \mu_1 a_l h_l^{(1)}(kr_p) - \mu_2 c_l j_l(Nkr_p)\right] = 0\ , \end{aligned} \tag{A43}$$

and similarly for the ϕ-component:

$$\begin{aligned} B_l t_l^{(3)} \frac{1}{\sin\theta}\frac{1}{kr_p}\partial_\phi Y_l^m(\theta,\phi)\left[\mu_1[kr_p j_l(kr_p)]' + \mu_1 b_l[kr_p h_l^{(1)}(kr_p)]' - \mu_2 d_l \frac{1}{N}[Nkr_p j_l(Nkr_p)]'\right] \\ - A_l s_l^{(3)}\partial_\theta Y_l^m(\theta,\phi)\left[\mu_1 j_l(kr_p) + \mu_1 a_l h_l^{(1)}(kr_p) - \mu_2 c_l j_l(Nkr_p)\right] = 0\ . \end{aligned} \tag{A44}$$

These both lead to the same two equations which must independently equal zero for the above relations to hold true:

$$\mu_1 j_l(kr_p) + \mu_1 a_l h_l^{(1)}(kr_p) = \mu_2 c_l j_l(Nkr_p) \tag{A45}$$

$$\mu_1 N[kr_p j_l(kr_p)]' + \mu_1 b_l N[kr_p h_l^{(1)}(kr_p)]' = \mu_2 d_l [Nkr_p j_l(Nkr_p)]' \, . \tag{A46}$$

Similarly for the magnetic field, the θ and ϕ components lead to:

$$\begin{aligned} A_l s_l^{(3)} \frac{1}{kr_p} \partial_\theta Y_l^m(\theta,\phi) \left[[kr_p j_l(kr_p)]' + a_l [kr_p h_l^{(1)}(kr_p)]' - c_l [Nkr_p j_l(Nkr_p)]' \right] \\ + B_l t_l^{(3)} \frac{1}{\sin\theta} \partial_\phi Y_l^m(\theta,\phi) \left[j_l(kr_p) + b_l h_l^{(1)}(kr_p) - d_l N j_l(Nkr_p) \right] = 0 \end{aligned} \tag{A47}$$

$$\begin{aligned} A_l s_l^{(3)} \frac{1}{\sin\theta} \partial_\phi Y_l^m(\theta,\phi) \frac{1}{kr_p} \left[[kr_p j_l(kr_p)]' + a_l [kr_p h_l^{(1)}(kr_p)]' - c_l [Nkr_p j_l(Nkr_p)]' \right] \\ - B_l t_l^{(3)} \partial_\theta Y_l^m(\theta,\phi) \left[j_l(kr_p) + b_l h_l^{(1)}(kr_p) - d_l N j_l(Nkr_p) \right] = 0 \, , \end{aligned} \tag{A48}$$

which give the final two relations:

$$[kr_p j_l(kr_p)]' + a_l [kr_p h_l^{(1)}(kr_p)]' = c_l [Nkr_p j_l(Nkr_p)]' \tag{A49}$$

$$j_l(kr_p) + b_l h_l^{(1)}(kr_p) = d_l N j_l(Nkr_p) \, . \tag{A50}$$

From this set of four simultaneous equations—equations A45- A46 and A49- A50—the four l-dependent coefficients can be found which described how the incident energy from the dipole source interacts with the NP. The Mie scattering ($a_l,\ b_l$) and internal ($c_l,\ d_l$)

coefficients are finally given by [58, 73]:

$$a_l = \frac{\mu_2 j_l(Nkr_p)[kr_p j_l(kr_p)]' - \mu_1 j_l(kr_p)[Nkr_p j_l(Nkr_p)]'}{\mu_1 h_l^{(1)}(kr_p)[Nkr_p j_l(Nkr_p)]' - \mu_2 j_l(Nkr_p)[kr_p h_l^{(1)}(kr_p)]'} \tag{A51}$$

$$b_l = \frac{\mu_1 N^2 j_l(Nkr_p)[kr_p j_l(kr_p)]' - \mu_2 j_l(kr_p)[Nkr_p j_l(Nkr_p)]'}{\mu_2 h_l^{(1)}(kr_p)[Nkr_p j_l(Nkr_p)]' - \mu_1 N^2 j_l(Nkr_p)[kr_p h_l^{(1)}(kr_p)]'} \tag{A52}$$

$$c_l = \frac{\mu_1 j_l(kr_p)[kr_p h_l^{(1)}(kr_p)]' - \mu_1 h_l^{(1)}(kr_p)[kr_p j_l(kr_p)]'}{\mu_2 j_l(Nkr_p)[kr_p h_l^{(1)}(kr_p)]' - \mu_1 h_l^{(1)}(kr_p)[Nkr_p j_l(Nkr_p)]'} \tag{A53}$$

$$d_l = \frac{\mu_1 N j_l(kr_p)[kr_p h_l^{(1)}(kr_p)]' - \mu_1 N h_l^{(1)}(kr_p)[kr_p j_l(kr_p)]'}{\mu_1 N^2 j_l(Nkr_p)[kr_p h_l^{(1)}(kr_p)]' - \mu_2 h_l^{(1)}(kr_p)[Nkr_p j_l(Nkr_p)]'} \,. \tag{A54}$$

A4 INCIDENT ENERGY FROM A DIPOLE SOURCE

The incident energy contribution to the total energy is given by:

$$W_{inc} = \int \frac{1}{2}\text{Re}\left[E^{\theta}_{inc}H^{\phi *}_{inc} - E^{\phi}_{inc}H^{\theta *}_{inc}\right]\cdot\hat{\boldsymbol{n}}dA\ , \tag{A55}$$

where the field components are:

$$E^{\theta}_{inc} = C_{lm}\sum_{e,o}\left[s^{e,o}_{l,m}\boldsymbol{M}^{e,o\ (3)}_{l,m\ \theta}(k\boldsymbol{r}) + t^{e,o}_{l,m}\boldsymbol{N}^{e,o\ (3)}_{l,m\ \theta}(k\boldsymbol{r})\right] \tag{A56}$$

$$E^{\phi}_{inc} = C_{lm}\sum_{e,o}\left[s^{e,o}_{l,m}\boldsymbol{M}^{e,o\ (3)}_{l,m\ \phi}(k\boldsymbol{r}) + t^{e,o}_{l,m}\boldsymbol{N}^{e,o\ (3)}_{l,m\ \phi}(k\boldsymbol{r})\right] \tag{A57}$$

$$H^{\theta *}_{inc} = \frac{k}{i\omega\mu_1\mu_0}C^{*}_{lm}\sum_{e,o}\left[s^{e,o\ *}_{l,m}\boldsymbol{N}^{e,o\ (3)*}_{l,m\ \theta}(k\boldsymbol{r}) + t^{e,o\ *}_{l,m}\boldsymbol{M}^{e,o\ (3)*}_{l,m\ \theta}(k\boldsymbol{r})\right] \tag{A58}$$

$$H^{\phi *}_{inc} = \frac{k}{i\omega\mu_1\mu_0}C^{*}_{lm}\sum_{e,o}\left[s^{e,o\ *}_{l,m}\boldsymbol{N}^{e,o\ (3)*}_{l,m\ \phi}(k\boldsymbol{r}) + t^{e,o\ *}_{l,m}\boldsymbol{M}^{e,o\ (3)*}_{l,m\ \phi}(k\boldsymbol{r})\right]\ . \tag{A59}$$

Expanding the integrand, making sure to properly consider separate sets of even and odd components, this becomes:

$$\begin{aligned} E^{\theta}_{inc}H^{\phi *}_{inc} - E^{\phi}_{inc}H^{\theta *}_{inc} = \frac{k}{i\omega\mu_1\mu_0}|C_{l,m}|^2\Big\{ &\sum_{e,o}\left[s^{e,o}_{l,m}\boldsymbol{M}^{e,o\ (3)}_{l,m\ \theta}(k\boldsymbol{r}) + t^{e,o}_{l,m}\boldsymbol{N}^{e,o\ (3)}_{l,m\ \theta}(k\boldsymbol{r})\right] \\ &\sum_{e',o'}\left[s^{e',o'\ *}_{l,m}\boldsymbol{N}^{e',o'\ (3)*}_{l,m\ \phi}(k\boldsymbol{r}) + t^{e',o'\ *}_{l,m}\boldsymbol{M}^{e',o'\ (3)*}_{l,m\ \phi}(k\boldsymbol{r})\right] \\ -&\sum_{e,o}\left[s^{e,o}_{l,m}\boldsymbol{M}^{e,o\ (3)}_{l,m\ \phi}(k\boldsymbol{r}) + t^{e,o}_{l,m}\boldsymbol{N}^{e,o\ (3)}_{l,m\ \phi}(k\boldsymbol{r})\right] \\ &\sum_{e',o'}\left[s^{e',o'\ *}_{l,m}\boldsymbol{N}^{e',o'\ (3)*}_{l,m\ \theta}(k\boldsymbol{r}) + t^{e,'o'\ *}_{l,m}\boldsymbol{M}^{e',o'\ (3)*}_{l,m\ \theta}(k\boldsymbol{r})\right]\Big\}\ . \end{aligned} \tag{A60}$$

After carefully simplifying the expression, it takes the form:

$$E^{\theta}_{inc}H^{\phi*}_{inc} - E^{\phi}_{inc}H^{\theta*}_{inc} = \frac{1}{ir\omega\mu_1\mu_0}|C_{l,m}|^2 \times \sum_{e,o}\left[\left(\frac{mP^m_l(\cos\theta)}{\sin\theta}\right)^2 \begin{cases}\sin^2 m\phi \\ \cos^2 m\phi\end{cases} + \left(\partial_\theta P^m_l(\cos\theta)\right)^2 \begin{cases}\cos^2 m\phi \\ \sin^2 m\phi\end{cases}\right] \times \left[|s^{e,o}_{l,m}|^2 h^{(1)}_l(kr)[krh^{(1)*}_l(kr)]' - |t^{e,o}_{l,m}|^2 h^{(1)*}_l(kr)[krh^{(1)}_l(kr)]'\right] . \quad \text{(A61)}$$

Returning to the integral for the incident energy:

$$W_{inc} = \frac{1}{2}\text{Re}\left[\int_0^{2\pi}\int_0^{\pi}\left(E^{\theta}_{inc}H^{\phi*}_{inc} - E^{\phi}_{inc}H^{\theta*}_{inc}\right)r^2\sin\theta d\theta d\phi\right] , \quad \text{(A62)}$$

the standard integrals for the associated Legendre polynomials shown in Appendix A2 can be applied to reduce the incident energy to:

$$W_{inc} = -\frac{\pi r}{\omega\mu_1\mu_0}\frac{l(l+1)}{2l+1}\frac{(l+m)!}{(l-m)!}|C_{l,m}|^2 \times \sum_{e,o}\text{Re}\left[i|s^{e,o}_{l,m}|^2 h^{(1)}_l(kr)[krh^{(1)*}_l(kr)]' - i|t^{e,o}_{l,m}|^2 h^{(1)*}_l(kr)[krh^{(1)}_l(kr)]'\right] . \quad \text{(A63)}$$

To simplify the remaining complex terms and allow only the real parts to be selected, the radial dependent terms must receive some attention:

$$ih^{(1)}_l(kr)[krh^{(1)*}_l(kr)]' = kr(j_l y'_l - y_l j'_l) + i(j_l j_l + krj_l j'_l + y_l y_l + kry_l y'_l) \quad \text{(A64)}$$

$$ih^{(1)*}_l(kr)[krh^{(1)}_l(kr)]' = kr(j'_l y_l - j_l y'_l) + i(j_l j_l + krj_l j'_l + y_l y_l + kry_l y'_l) . \quad \text{(A65)}$$

Selecting only the real components, the incident decay rate becomes

$$W_{inc} = -\frac{\pi r}{\omega\mu_1\mu_0}\frac{l(l+1)}{2l+1}\frac{(l+m)!}{(l-m)!}|C_{l,m}|^2\sum_{e,o}\left[|s_{l,m}^{e,o}|^2 kr(j_l y_l' - y_l j_l') - |t_{l,m}^{e,o}|^2 kr(j_l' y_l - j_l y_l')\right] \ , \tag{A66}$$

and using the form of the Wronskian: $j_l(x)y_l'(x) - j_l'(x)y_l(x) = -\frac{1}{x^2}$, gives

$$W_{inc} = \frac{\pi}{k\omega\mu_1\mu_0}\frac{l(l+1)}{2l+1}\frac{(l+m)!}{(l-m)!}|C_{l,m}|^2\sum_{e,o}\left[|s_{l,m}^{e,o}|^2 + |t_{\mathbf{l}}^{e,o}|^2\right] \ . \tag{A67}$$

After substituting in the $C_{l,m} = \frac{ik}{4\pi}(2-\delta_0)\frac{2l+1}{l(l+1)}\frac{(l-m)!}{(l+m)!}$, the final expressing for the incident contribution to the total energy is given by:

$$W_{inc} = \frac{k}{16\pi\omega\mu_1\mu_0}(2-\delta_0)^2\frac{2l+1}{l(l+1)}\frac{(l-m)!}{(l+m)!}\sum_{e,o}\left[|s_{l,m}^{e,o}|^2 + |t_{l,m}^{e,o}|^2\right] \ , \tag{A68}$$

where $\delta_0 = 1$ when $m = 0$, and is zero otherwise.

A5 EXTINCTION ENERGY FROM A DIPOLE SOURCE

The extinction energy contribution to the total energy is given by:

$$W_{ext} = -\int \frac{1}{2}\mathrm{Re}\left[E^{\theta}_{inc}H^{\phi*}_{scat} - E^{\phi}_{inc}H^{\theta*}_{scat} + E^{\theta}_{scat}H^{\phi*}_{inc} - E^{\phi}_{scat}H^{\theta*}_{inc}\right]\cdot\hat{\boldsymbol{n}}dA\ , \tag{A69}$$

where the field components are:

$$E^{\theta,\phi}_{inc} = C_{lm}\sum_{e,o}\left[s^{e,o}_{l,m}\boldsymbol{M}^{e,o\ (3)}_{l,m\ \theta,\phi}(k\boldsymbol{r}) + t^{e,o}_{l,m}\boldsymbol{N}^{e,o\ (3)}_{l,m\ \theta,\phi}(k\boldsymbol{r})\right] \tag{A70}$$

$$E^{\theta,\phi}_{scat} = C_{lm}\sum_{e,o}\left[u^{e,o}_{l,m}\boldsymbol{M}^{e,o\ (3)}_{l,m\ \theta,\phi}(k\boldsymbol{r}) + v^{e,o}_{l,m}\boldsymbol{N}^{e,o\ (3)}_{l,m\ \theta,\phi}(k\boldsymbol{r})\right] \tag{A71}$$

$$H^{\theta*,\phi*}_{inc} = \frac{k}{i\omega\mu_1\mu_0}C^{*}_{lm}\sum_{e,o}\left[s^{e,o\ *}_{l,m}\boldsymbol{N}^{e,o\ (3)*}_{l,m\ \theta,\phi}(k\boldsymbol{r}) + t^{e,o\ *}_{l,m}\boldsymbol{M}^{e,o\ (3)*}_{l,m\ \theta,\phi}(k\boldsymbol{r})\right] \tag{A72}$$

$$H^{\theta*,\phi*}_{scat} = \frac{k}{i\omega\mu_1\mu_0}C^{*}_{lm}\sum_{e,o}\left[u^{e,o\ *}_{l,m}\boldsymbol{N}^{e,o\ (3)*}_{l,m\ \theta,\phi}(k\boldsymbol{r}) + v^{e,o\ *}_{l,m}\boldsymbol{M}^{e,o\ (3)*}_{l,m\ \theta,\phi}(k\boldsymbol{r})\right]\ . \tag{A73}$$

Expanding the integrand, making sure to properly consider separate sets of even and odd components, this becomes:

$$
\begin{aligned}
E^{\theta}_{inc}H^{\phi *}_{scat} - E^{\phi}_{inc}H^{\theta *}_{scat} + E^{\theta}_{scat}H^{\phi *}_{inc} - E^{\phi}_{scat}H^{\theta *}_{inc} = \frac{k}{i\omega\mu_1\mu_0}|C_{l,m}|^2 \Big\{ & \\
& \times \sum_{e,o} \left[s^{e,o}_{l,m} \boldsymbol{M}^{e,o\ (3)}_{l,m\ \theta}(k\boldsymbol{r}) + t^{e,o}_{l,m} \boldsymbol{N}^{e,o\ (3)}_{l,m\ \theta}(k\boldsymbol{r}) \right] \\
& \times \sum_{e',o'} \left[u^{e',o'\ *}_{l,m} \boldsymbol{N}^{e',o'\ (3)*}_{l,m\ \phi}(k\boldsymbol{r}) + v^{e',o'\ *}_{l,m} \boldsymbol{M}^{e',o'\ (3)*}_{l,m\ \phi}(k\boldsymbol{r}) \right] \\
& - \sum_{e,o} \left[s^{e,o}_{l,m} \boldsymbol{M}^{e,o\ (3)}_{l,m\ \phi}(k\boldsymbol{r}) + t^{e,o}_{l,m} \boldsymbol{N}^{e,o\ (3)}_{l,m\ \phi}(k\boldsymbol{r}) \right] \\
& \times \sum_{e',o'} \left[u^{e',o'\ *}_{l,m} \boldsymbol{N}^{e',o'\ (3)*}_{l,m\ \theta}(k\boldsymbol{r}) + v^{e',o'\ *}_{l,m} \boldsymbol{M}^{e',o'\ (3)*}_{l,m\ \theta}(k\boldsymbol{r}) \right] \\
& + \sum_{e,o} \left[u^{e,o}_{l,m} \boldsymbol{M}^{e,o\ (3)}_{l,m\ \theta}(k\boldsymbol{r}) + v^{e,o}_{l,m} \boldsymbol{N}^{e,o\ (3)}_{l,m\ \theta}(k\boldsymbol{r}) \right] \\
& \times \sum_{e',o'} \left[s^{e',o'\ *}_{l,m} \boldsymbol{N}^{e',o'\ (3)*}_{l,m\ \phi}(k\boldsymbol{r}) + t^{e',o'\ *}_{l,m} \boldsymbol{M}^{e',o'\ (3)*}_{l,m\ \phi}(k\boldsymbol{r}) \right] \\
& - \sum_{e,o} \left[u^{e,o}_{l,m} \boldsymbol{M}^{e,o\ (3)}_{l,m\ \phi}(k\boldsymbol{r}) + v^{e,o}_{l,m} \boldsymbol{N}^{e,o\ (3)}_{l,m\ \phi}(k\boldsymbol{r}) \right] \\
& \times \sum_{e',o'} \left[s^{e',o'\ *}_{l,m} \boldsymbol{N}^{e',o'\ (3)*}_{l,m\ \theta}(k\boldsymbol{r}) + t^{e',o'\ *}_{l,m} \boldsymbol{M}^{e',o'\ (3)*}_{l,m\ \theta}(k\boldsymbol{r}) \right] \Big\} .
\end{aligned}
\tag{A74}
$$

After carefully simplifying the expression, it takes the form:

$$E^{\theta}_{inc}H^{\phi *}_{scat} - E^{\phi}_{inc}H^{\theta *}_{scat} + E^{\theta}_{scat}H^{\phi *}_{inc} - E^{\phi}_{scat}H^{\theta *}_{inc} = \frac{1}{ir\omega\mu_1\mu_0}|C_{l,m}|^2 \sum_{e,o}$$
$$\times \left[\left(\frac{mP^m_l(\cos\theta)}{\sin\theta} \right)^2 \begin{cases} \sin^2 m\phi \\ \cos^2 m\phi \end{cases} + \left(\partial_\theta P^m_l(\cos\theta)\right)^2 \begin{cases} \cos^2 m\phi \\ \sin^2 m\phi \end{cases} \right] \tag{A75}$$
$$\times \Big\{ \left[s^{e,o}_{l,m} u^{e,o\,*}_{l,m} + u^{e,o}_{l,m} s^{e,o\,*}_{l,m} \right] h^{(1)}_l(kr)[krh^{(1)*}_l(kr)]'$$
$$- \left[t^{e,o}_{l,m} v^{e,o\,*}_{l,m} + v^{e,o}_{l,m} t^{e,o\,*}_{l,m} \right] h^{(1)*}_l(kr)[krh^{(1)}_l(kr)]' \Big\} .$$

Returning to the integral for the extinction energy:

$$W_{ext} = -\frac{1}{2}\mathrm{Re}\left[\int_0^{2\pi} \int_0^{\pi} \left(E^{\theta}_{inc}H^{\phi *}_{scat} - E^{\phi}_{inc}H^{\theta *}_{scat} + E^{\theta}_{scat}H^{\phi *}_{inc} - E^{\phi}_{scat}H^{\theta *}_{inc} \right) r^2 \sin\theta d\theta d\phi \right] , \tag{A76}$$

the standard integrals for the associated Legendre polynomials shown in Appendix A2 can be applied to reduce the incident energy to:

$$W_{ext} = \frac{\pi r}{\omega\mu_1\mu_0} \frac{l(l+1)}{2l+1} \frac{(l+m)!}{(l-m)!} |C_{l,m}|^2 \sum_{e,o} \mathrm{Re}\Big[\left[s^{e,o}_{l,m} u^{e,o\,*}_{l,m} + u^{e,o}_{l,m} s^{e,o\,*}_{l,m} \right] i h^{(1)}_l(kr)[krh^{(1)*}_l(kr)]'$$
$$- \left[t^{e,o}_{l,m} v^{e,o\,*}_{l,m} + v^{e,o}_{l,m} t^{e,o\,*}_{l,m} \right] i h^{(1)*}_l(kr)[krh^{(1)}_l(kr)]' \Big] . \tag{A77}$$

Here the radial components take an identical form to those of the incident energy, and

can therefore be replaced by the same expressions. The extinction energy becomes:

$$W_{ext} = \frac{\pi r}{\omega\mu_1\mu_0}\frac{l(l+1)}{2l+1}\frac{(l+m)!}{(l-m)!}|C_{l,m}|^2\sum_{e,o}\Big\{\left[s_{l,m}^{e,o}u_{l,m}^{e,o\,*}+u_{l,m}^{e,o}s_{l,m}^{e,o\,*}\right]kr(j_l y_l'-y_l j_l') - \left[t_{l,m}^{e,o}v_{l,m}^{e,o\,*}+v_{l,m}^{e,o}t_{l,m}^{e,o\,*}\right]kr(j_l' y_l - j_l y_l')\Big\}, \quad \text{(A78)}$$

and using the form of the Wronskian: $j_l(x)y_l'(x) - j_l'(x)y_l(x) = -\frac{1}{x^2}$, this gives:

$$W_{ext} = -\frac{\pi}{k\omega\mu_1\mu_0}\frac{l(l+1)}{2l+1}\frac{(l+m)!}{(l-m)!}|C_{l,m}|^2\sum_{e,o}\left[s_{l,m}^{e,o}u_{l,m}^{e,o\,*}+u_{l,m}^{e,o}s_{l,m}^{e,o\,*}+t_{l,m}^{e,o}v_{l,m}^{e,o\,*}+v_{l,m}^{e,o}t_{l,m}^{e,o\,*}\right]. \quad \text{(A79)}$$

After substituting in the $C_{l,m} = \frac{ik}{4\pi}(2-\delta_0)\frac{2l+1}{l(l+1)}\frac{(l-m)!}{(l+m)!}$, the final expressing for the extinction contribution to the total energy is given by:

$$W_{ext} = -\frac{k}{16\pi\omega\mu_1\mu_0}(2-\delta_0)^2\frac{2l+1}{l(l+1)}\frac{(l-m)!}{(l+m)!} \times\sum_{e,o}\left[s_{l,m}^{e,o}u_{l,m}^{e,o\,*}+u_{l,m}^{e,o}s_{l,m}^{e,o\,*}+t_{l,m}^{e,o}v_{l,m}^{e,o\,*}+v_{l,m}^{e,o}t_{l,m}^{e,o\,*}\right], \quad \text{(A80)}$$

where $\delta_0 = 1$ when $m = 0$, and is zero otherwise.

A6 MODAL DECOMPOSITION FOR THE NON-RADIATIVE DECAY RATE

The non-radiative decay rate can be determined using a similar method as above. The energy from a dipole source that is not radiated to the far-field is dissipated through Ohmic losses in the metal, and leads to the heating of the NP. The power dissipated within the lossy medium is given by:

$$P_{abs}(r) = \frac{1}{2}\mathsf{Re}\left[\boldsymbol{E}_{int} \cdot \boldsymbol{J}^*\right] \tag{A81}$$

$$= \frac{1}{2}\omega\mathsf{Im}\left[\varepsilon_{Au}(\omega)\right]\left|\boldsymbol{E}_{int}\right|^2 . \tag{A82}$$

The total energy absorbed by the NP is found by integrating the fields over the volume of the lossy medium:

$$W_{abs} = \int_V P_{abs}(r)dV \tag{A83}$$

$$= \frac{1}{2}\omega\mathsf{Im}\left[\varepsilon_{Au}(\omega)\right]\int_0^{r_p}\int_0^{\pi}\int_0^{2\pi}\left|\boldsymbol{E}_{int}\right|^2 r^2\sin\theta dr d\theta d\phi . \tag{A84}$$

Only the field inside the NP are required here, therefore the internal electric field is given by:

$$\boldsymbol{E}_{int}(\boldsymbol{r}) = C_{l,m}\sum_{e,o}\left[n_{l,m}^{e,o}\boldsymbol{M}_{l,m}^{e,o\ (1)}(Nk\boldsymbol{r}) + w_{l,m}^{e,o}\boldsymbol{N}_{l,m}^{e,o\ (1)}(Nk\boldsymbol{r})\right] , \tag{A85}$$

where the following notation has been introduced:

$$n_{l,m} = c_l \left(\boldsymbol{M}^{(3)}_{l,m}(k\boldsymbol{r}') \cdot \boldsymbol{p}(\boldsymbol{r}') \right) \tag{A86}$$

$$w_{l,m} = d_l \left(\boldsymbol{N}^{(3)}_{l,m}(k\boldsymbol{r}') \cdot \boldsymbol{p}(\boldsymbol{r}') \right) \ , \tag{A87}$$

which therefore leads to:

$$\begin{aligned} |\boldsymbol{E}_{int}(\boldsymbol{r})|^2 = |C_{l,m}|^2 \sum_{e,o} \left[n^{e,o}_{l,m} \boldsymbol{M}^{e,o\ (1)}_{l,m}(Nk\boldsymbol{r}) + w^{e,o}_{l,m} \boldsymbol{N}^{e,o\ (1)}_{l,m}(Nk\boldsymbol{r}) \right] \\ \times \sum_{e',o'} \left[n^{e',o'\ *}_{l,m} \boldsymbol{M}^{e',o'\ (1)*}_{l,m}(Nk\boldsymbol{r}) + w^{e',o'\ *}_{l,m} \boldsymbol{N}^{e',o'\ (1)*}_{l,m}(Nk\boldsymbol{r}) \right] \ . \end{aligned} \tag{A88}$$

Expanding out the brackets quickly becomes complicated due to the r, θ and ϕ components of the four VSH terms, which is followed by their cross-multiplication. Placing this back in the integral and using standard integrals to solve the ϕ-integral, this becomes:

$$\begin{aligned} W_{abs} = \frac{1}{2}\omega \mathsf{Im}\left[\varepsilon_{Au}(\omega)\right] |C_{l,m}|^2 \pi \sum_{e,o} \Bigg[|n^{e,o}_{l,m}|^2 \int_0^{r_p} r^2 |j_l(Nkr)|^2 dr \\ \times \int_0^{\pi} \sin\theta \left\{ \frac{m^2}{\sin^2\theta} \left(P^m_l(\cos\theta)\right)^2 + \left(\partial_\theta P^m_l(\cos\theta)\right)^2 \right\} d\theta \\ + |w^{e,o}_{l,m}|^2 \frac{1}{N^2k^2} \Bigg(l^2(l^2+1) \int_0^{r_p} |j_l(Nkr)|^2 dr \int_0^{\pi} \sin\theta \left(P^m_l(\cos\theta)\right)^2 d\theta \\ + \int_0^{r_p} |[Nkr j_l(Nkr)]'|^2 dr \int_0^{\pi} \sin\theta \left\{ \frac{m^2}{\sin^2\theta} \left(P^m_l(\cos\theta)\right)^2 + \left(\partial_\theta P^m_l(\cos\theta)\right)^2 \right\} d\theta \Bigg) \Bigg] \ . \end{aligned} \tag{A89}$$

The standard integrals for the associated Legendre polynomials shown in Appendix A2 can be applied to reduce the absorption energy to:

$$W_{abs} = \frac{\omega k^2}{16\pi}\frac{2l+1}{l(l+1)}\frac{(l-m)!}{(l+m)!}(2-\delta_0)^2 \mathrm{Im}\left[\varepsilon_{Au}(\omega)\right]\sum_{e,o}\left[|n_{l,m}^{e,o}|^2\int_0^{r_p} r^2|j_l(Nkr)|^2 dr \right.$$
$$\left. + |w_{l,m}^{e,o}|^2\frac{1}{N^2k^2}\int_0^{r_p}\left(l(l+1)|j_l(Nkr)|^2 + |[Nkrj_l(Nkr)]'|^2\right)dr\right], \quad \text{(A90)}$$

where $C_{l,m} = \frac{ik}{4\pi}(2-\delta_0)\frac{2l+1}{l(l+1)}\frac{(l-m)!}{(l+m)!}$ has been substituted in. Unfortunately, these radial integrals do not appear to be solvable analytically, and therefore must be solved using numerical integration techniques. The total non-radiative decay rate is then given by normalising this absorption energy by the incident energy from the dipole:

$$\gamma_{nrad} = \frac{W_{abs}}{W_{inc}}\,. \quad \text{(A91)}$$

A7 EXCITATION RATE SOLVER COMPARISON

To highlight the variance and sensitivity of the in- and out-coupling rates on the meshing type and electric permittivity fitting, Appendix Figure A1 compares the γ_{exc} found analytically with two numerical methods: FDTD [51], which used a quadrilateral base meshing; and COMSOL [52], which uses tetrahedral base meshing.

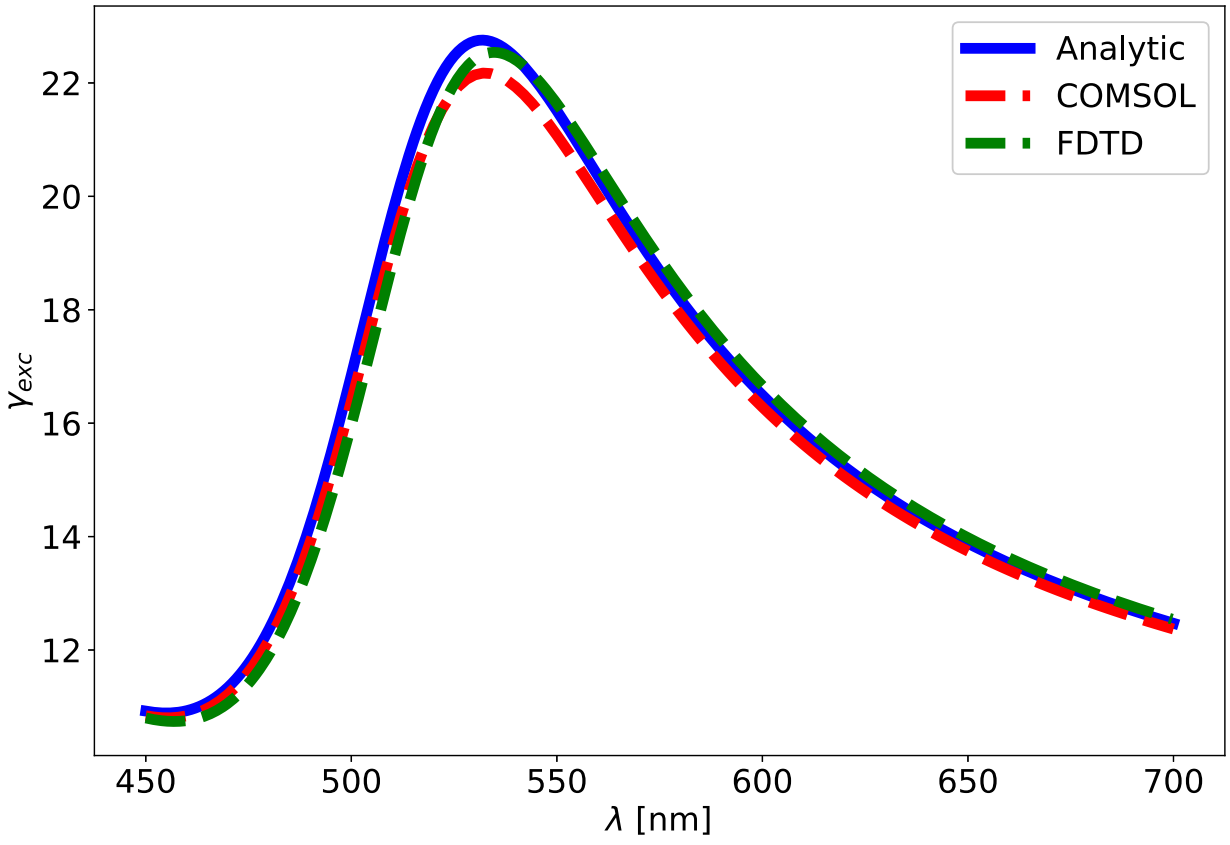

Figure A1: The γ_{exc} for an isolated NP of diameter 60 nm. The analytical modal decomposition (blue, full lines) is plotted together with numerical calculations for comparison: COMSOL (red, dashed lines) and FDTD (green, dashed lines).

A8 SELECTIVE NATURE OF PLANE WAVE EXCITATIONS

For a plane wave excitation with a particular polarisation, section 2.2.5 has revealed how this restricts the supported value of m. In addition to the $|E_x|$ field decomposition for an z-incident x-polarised plane wave shown in Figure 2.8, here Appendix Figure A2 and A3 respectively show the corresponding $|E_y|$ and $|E_z|$ decomposed field components.

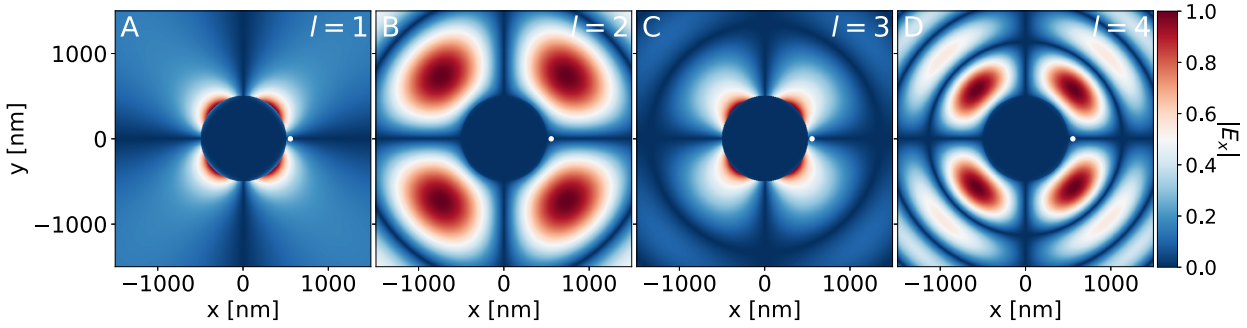

Figure A2: The total $|E_y|$ fields of a 1 μm diameter NP excited by an x-polarised plane wave. This is obtained from the modal decomposition for modes: (A) $l = 1$, (B) $l = 2$, (C) $l = 3$, (D) $l = 4$. The white dot indicates the position of the molecule excited in γ_{exc}.

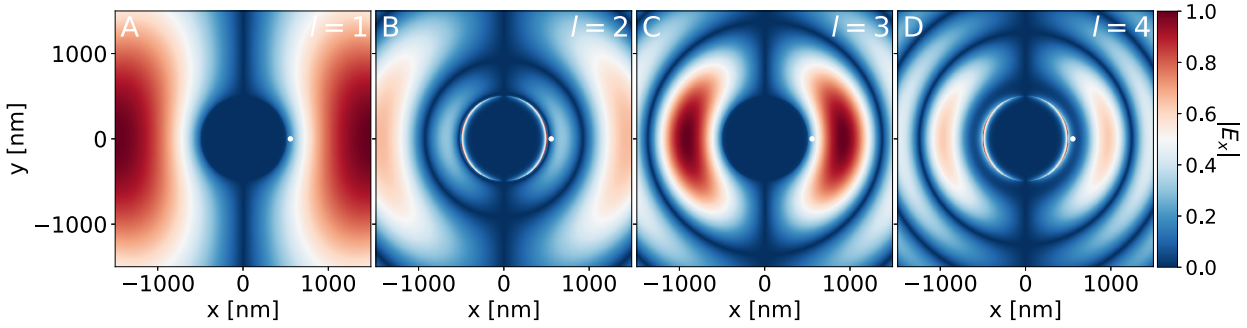

Figure A3: The total $|E_z|$ fields of a 1 μm diameter NP excited by an x-polarised plane wave. This is obtained from the modal decomposition for modes: (A) $l = 1$, (B) $l = 2$, (C) $l = 3$, (D) $l = 4$. The white dot indicates the position of the molecule excited in γ_{exc}.

In comparison to Figure 2.10, Appendix Figure A4 shows how the same three NP sizes couple to the dipole source. They are each able to efficiently scatter via the $l = 1$ mode, and although the smaller two NPs appear to be able to scatter for the $l = 2$ and

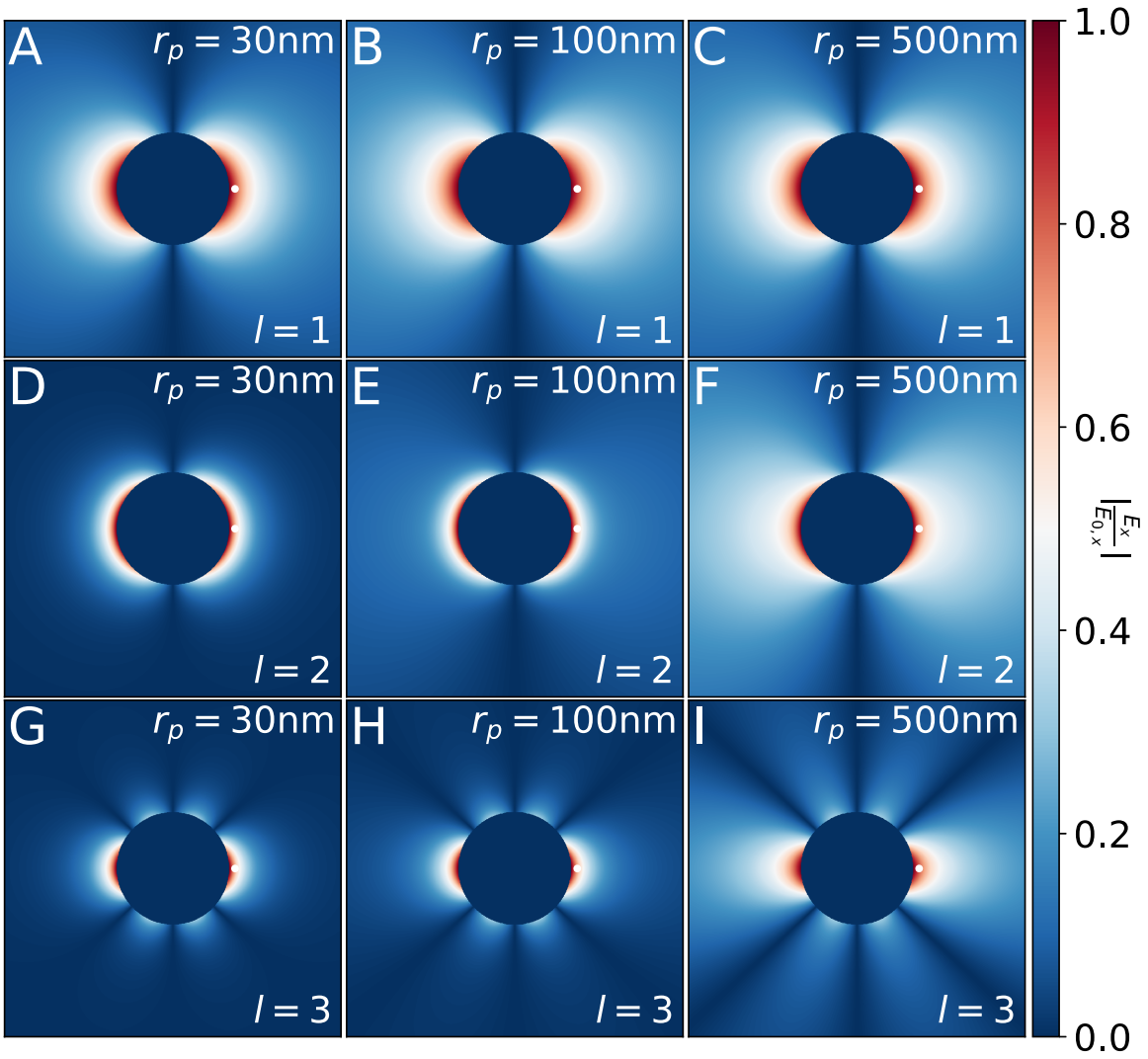

Figure A4: The modal contribution to the normalised electric field intensity around an isolated NP due to a close proximity x-polarised dipole source. (A-C) $l = 1$ mode. (D-F) $l = 2$ mode. (G-I) $l = 3$ mode. (A,D,G) $r_p = 30$ nm. (B,E,h) $r_p = 100$ nm. (C,F,I) $r_p = 500$ nm. The white dot indicates the position of the molecule which is the source when determining the γ_{rad}.

$l = 3$ modes, they do so much less efficiently. This is demonstrated by the much shorter exponential decay of the fields away from the surface of the NPs.

A9 NORMAL AND IN-PLANE EXCITATIONS

Relative to the mirror, Appendix Figure A5 compares the rates at which in-plane and normal plane wave incidences couple energy into the NPoM geometry. This reveals the distinct set of modes that each excite, with the red-shifting of the nanocavity causing them to appear in different spectral regimes, and they therefore do not interfere.

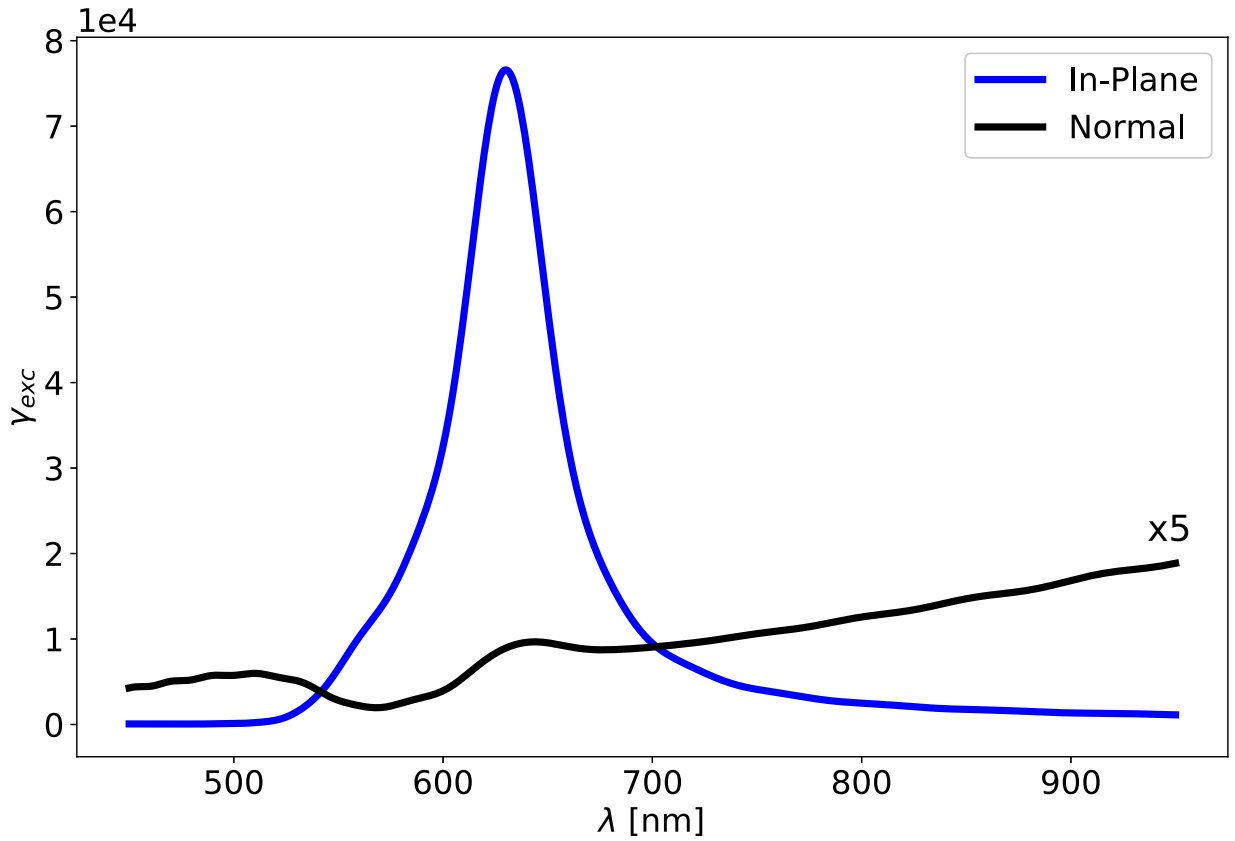

Figure A5: Numerical comparison of the γ_{exc} of the NPoM geometry—consisting of a 60 nm NP assembled $d = 1$ nm above an infinite flat substrate—for two differing plane wave incidences relative to the mirror: an in-plane (blue) and normal (black) plane wave excitation.

A10 NANOANTENNA EMITTER POSITIONING

The placement of an emitter in a nanocavity has a strong effect on how it interacts with the near-field plasmonic environment; to highlight that the origin of the in- and out-coupling differences is valid for all positions within the nanocavities, Appendix Figure A6 and A7 compare the γ_{exc} and γ_{rad} for differing positions of the dipole source within the cavity of the quasi-static symmetric dimer and NPoM antennas, respectively. Five emitter positions

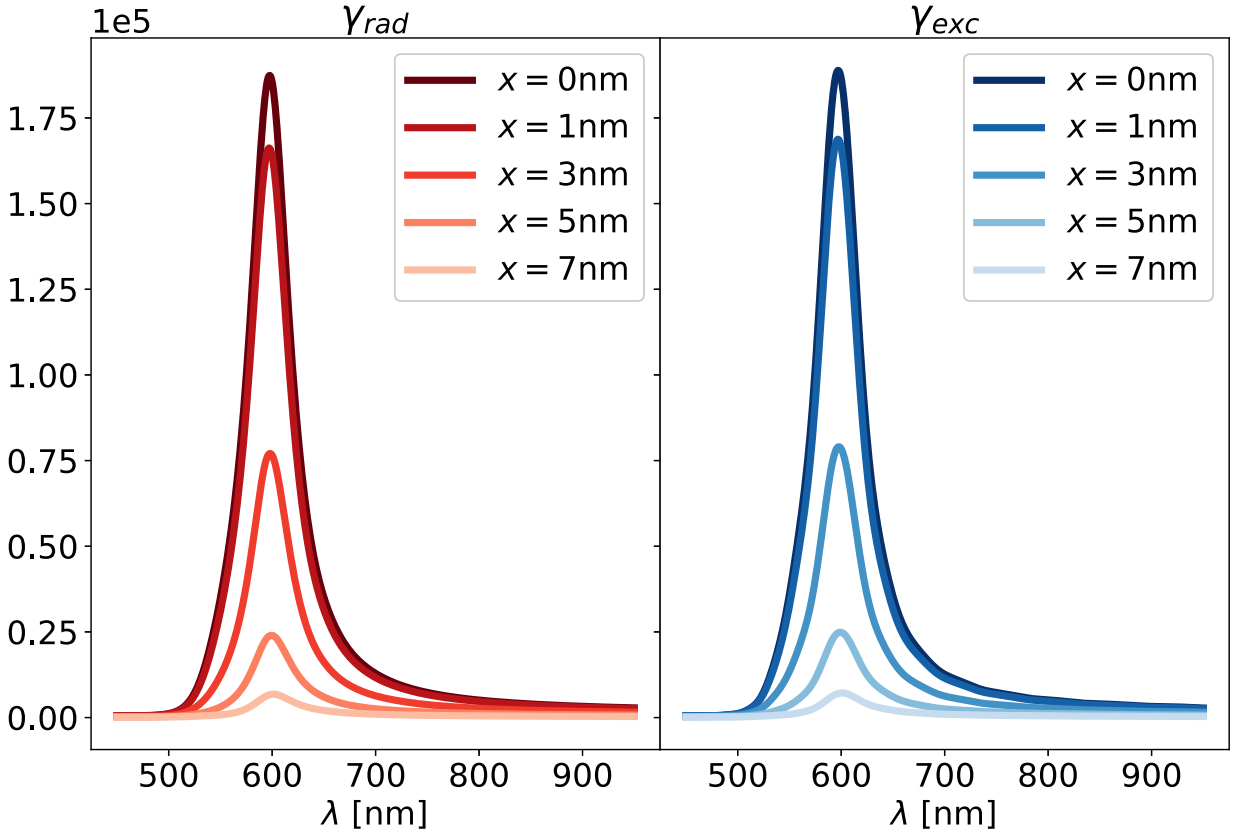

Figure A6: Numerical comparison of the γ_{rad} and γ_{exc} of the symmetric quasi-static dimer antenna of $2r_{p,1} = 2r_{p,1} = 60$ nm, for a series of emitter positions along the x-axis: $x = 0$ nm to $x = 7$ nm.

are considered along the x-axis, ranging from 0-7 nm. For both nanoantennas systems, the γ_{exc} and γ_{rad} reduce as the emitter is moved away from the centre of the cavity—as expected due to the lower confinement and enhancement of the field. Due to the singular $l = 1$ mode that appears in the hybridisation of the dimer cavity, the in- and out-coupling rates remain equal, and do so for all positions within the cavity. The NPoM system exhibits this characteristic unequal coupling rates, which it retains as the emitter is moved away from the centre—with the relative amplitude of the γ_{exc} and γ_{rad} remaining constant, in addition to the resonant frequencies and relative line widths.

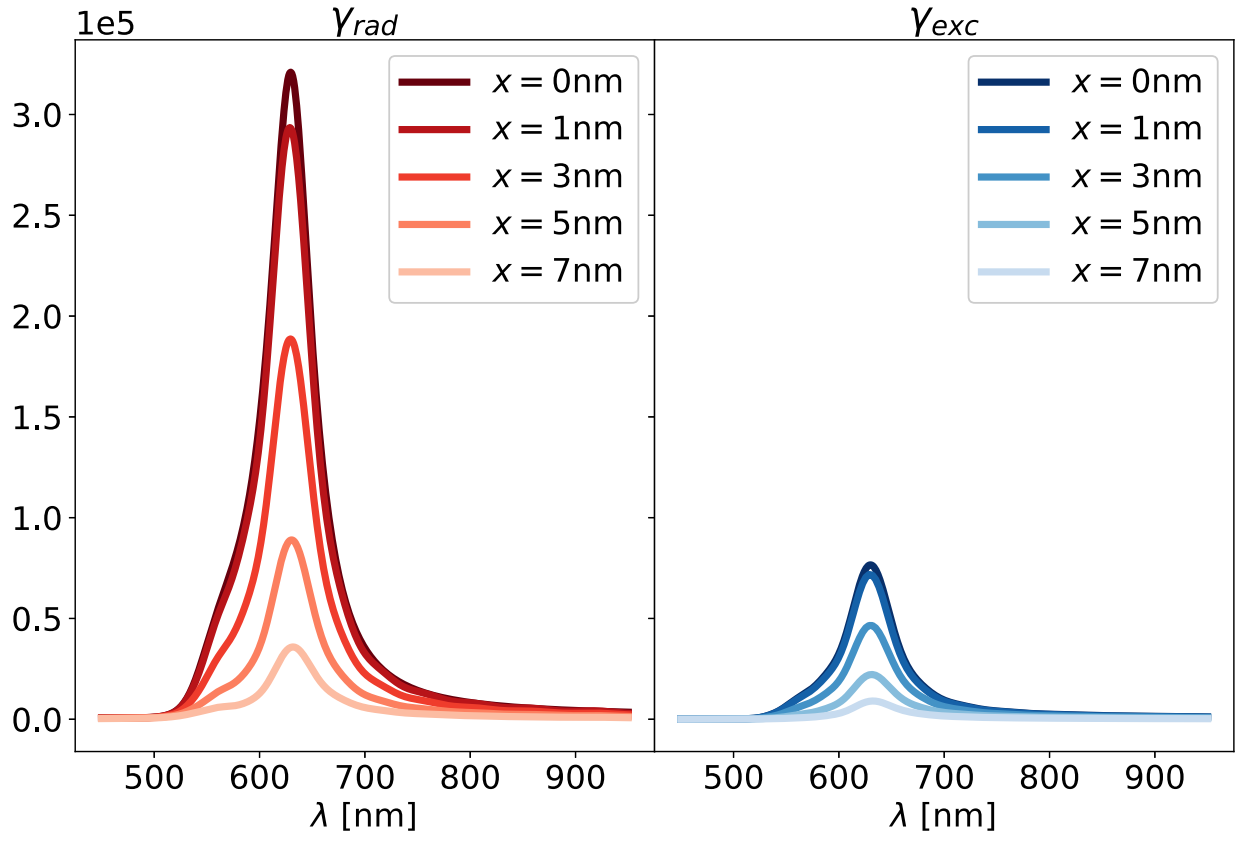

Figure A7: Numerical comparison of the γ_{rad} and γ_{exc} of the NPoM geometry of a $2r_p = 60$ nm gold NP assembled $d = 1$ nm above a gold substrate, for a series of emitter positions along the x-axis: $x = 0$ nm to $x = 7$ nm.

A11 EDGE ROUNDING

This section is dedicated to unveiling some of the subtleties involving the edge rounding in these polyhedral nanoantenna systems, and the strong impact this can have on the QNMs in both the near- and far-fields. One mode that is particularly sensitive to the rounding of the edges is the second $(2, 2)$ mode of the RhoM-Sq22 geometry—whose anti-nodes align with the facet edges. Appendix Figure A8 compares the near-field charge

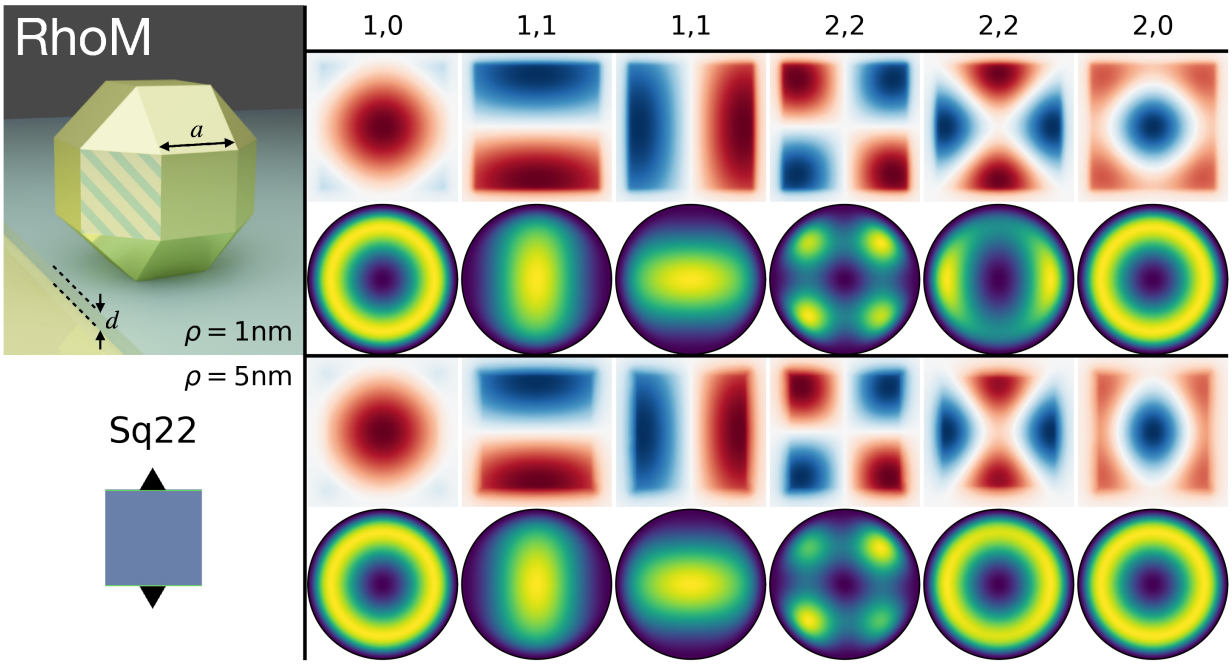

Figure A8: QNMs of the RhoM geometry assembled on its Sq22 facet for a characteristic edge length a and spacer thickness d, and edge rounding of (rows 1 and 2) $\rho = 1$ nm and (rows 3 and 4) $\rho = 5$ nm. Rows 1 and 3 are the normalised QNM electric near-fields (Re[$E_{z,lm}$]) on the xy-plane through the centre of the cavity. Rows 2 and 4 are the normalised time averaged far-field Poynting flux $\langle S_{lm} \rangle$. The modes from left to right are: $(1, 0)$, $(1, 1)$, $(1, 1)$, $(2, 2)$, $(2, 2)$, $(2, 0)$.

distributions and far-field emission profiles for this facet with edge rounding of (top) $\rho = 1$ nm and (bottom) $\rho = 5$ nm. As the rounding is increased, the effective elongation of the facet is more pronounced for the second $(2, 2)$ mode and the $(2, 0)$ mode—whilst leaving the other modes largely unchanged. In the near-field, the $(2, 0)$ mode is visibly stretched along the elongation axis, and the lost central node of the $(2, 2)$ mode becomes more significantly non-zero. In the far-field this non-zero centre field leads to the $(2, 2)$ mode emitting just like an $m = 0$ mode.

The second $(2, 2)$ mode—with the edge align anti-nodes—of the CoM-Sq geometry is also strongly effected by the rounding of the edges. Due to the proportionally large rounding of the CoM geometry ($\rho = 1$ nm compared to $a = 8$ nm), this mode is significantly distorted. Appendix Figure A9 compares these far-field emission profiles with those for a proportionally smaller edge rounding: $\rho = 1$ nm and $a = 20$ nm. This yields a significantly more clear $(2, 2)$ mode, where all four lobes are easily discernible.

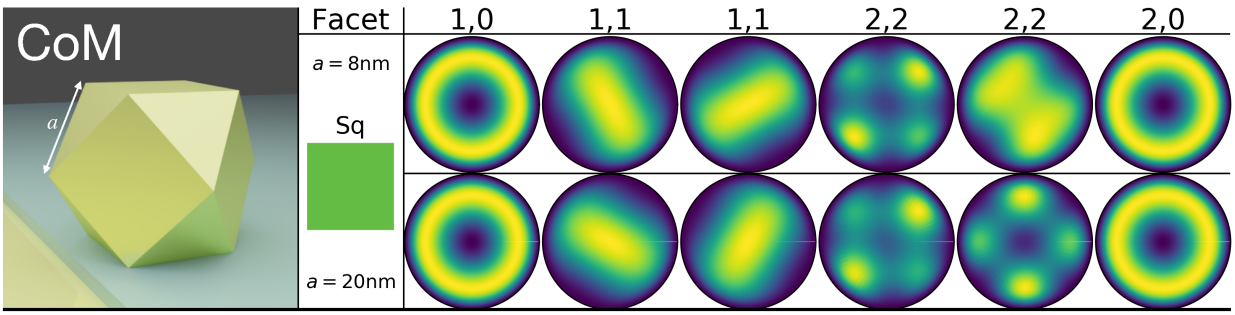

Figure A9: Far-field emission for the QNMs of the CoM geometry assembled on its square facet, for a characteristic edge length a and spacer thickness d. The colour corresponds to the normalised time averaged far-field Poynting flux $\langle S_{lm} \rangle$, for edge roundings of (top row) $\rho = 1$ nm and (bottom row) $\rho = 5$ nm. The modes from left to right are: $(1, 0)$, $(1, 1)$, $(1, 1)$, $(2, 2)$, $(2, 2)$, $(2, 0)$.

A12 POLYHEDRAL NANOANTENNA COUPLING COEFFICIENTS

To complete the emitter transition frequencies selected with each facet assembly in Figure 3.7, here Appendix Figure A10 shows the α-coefficients for these same systems calculated for the reversed emitter frequencies. The same paths are considered, and the modal response of each system still in general follows the intensities of the corresponding near-field charge distributions.

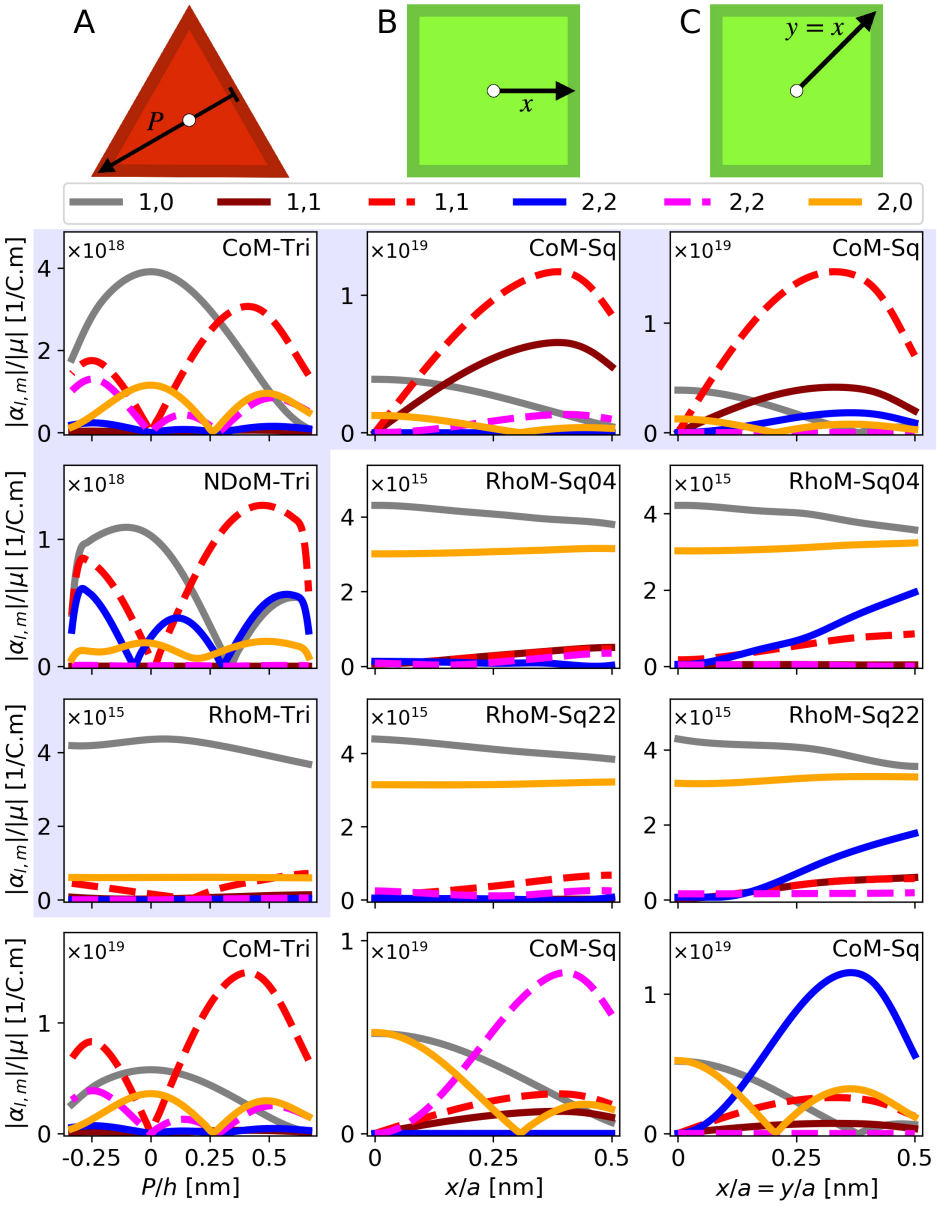

Figure A10: α-coefficients of the polyhedral NPoM geometries, for a series of emitter positions within the nanocavities. Column A - The triangular facets of the polyhedral systems, following a path from the facet edge to the opposing corner, through the centre of the facet—normalised to the height of the triangular facet ($h = \sqrt{3}a/2$). Column B - The square facets of the polyhedral systems, following a path along the x-axis from the centre of the facet. Column C - The square facets of the polyhedral systems, following a path along the diagonal from the centre of the facet. White and blue backgrounds respectively correspond to emitter transition wavelengths of $\lambda_{em} = 775$ nm and $\lambda_{em} = 900$ nm.

A13 NDOM EMISSION PROFILE

For the confirmation of the NDoM results with a molecule place closed to the centre of the cavity, Appendix Figure A11 compares the theoretically calculated total far-field emission profile with the equivalent experimental observations.

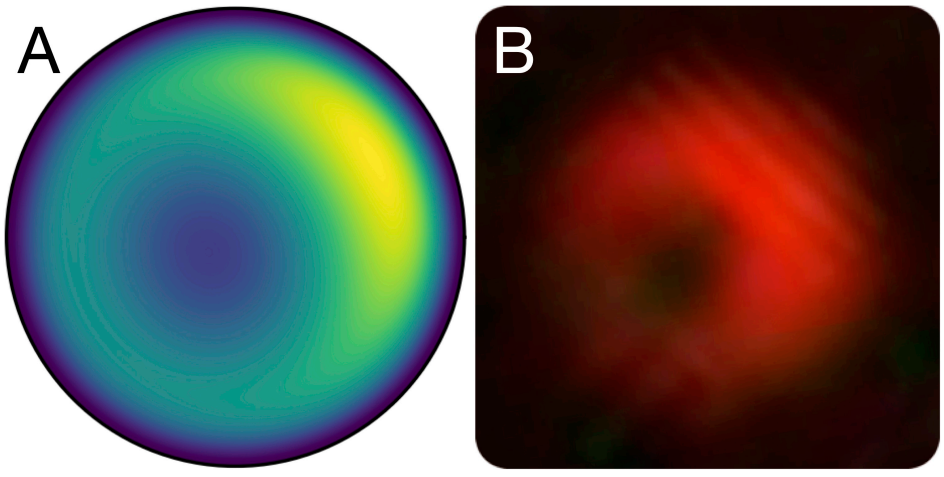

Figure A11: Total far-field emission profiles of the NDoM geometry for an emitter placed close to the centre of the cavity. (A) Numerical emission profile reconstructed from modal emission profiles and α-coefficients. (B) Experimentally observed far-field emission.

A14 DRIVEN CAVITY QED

Consider a cavity QED model of a QNM coupled to a two level system. For the point of explanation and to concise the notation introduced here, it is most suitable to detail the analytics for the case of a single emitter. Note that this may easily be generalised to describe any number of emitters. In the Schrödinger picture, the Hamiltonian that describes the driven open system and reservoirs follows the time-dependent Schrödinger equation (TDSE), $i\partial_t|\psi\rangle = \mathcal{H}|\psi\rangle$, where $\mathcal{H}$ is given by:

$$\begin{aligned}\mathcal{H} = {} & a^\dagger a\omega_{cav} + \frac{1}{2}\sigma_z\omega_e + g(\mathbf{r})\left(a^\dagger + a\right)(\sigma_+ + \sigma_-) \\ & + \sum_\lambda \int_0^\infty d\omega b_\lambda^\dagger(\omega) b_\lambda(\omega)\omega + \int_0^\infty d\omega_{vib}\; b_{vib}^\dagger(\omega_{vib}) b_{vib}(\omega_{vib})\omega_{vib} \\ & + \int_0^\infty d\omega_{vib}\; \sigma_z \kappa_{vib}(\omega_{vib})\left(b_{vib}^\dagger + b_{vib}\right) \\ & -i\sum_\lambda \int_0^\infty d\omega\; \kappa(\omega)\big(b_\lambda(\omega) - b_\lambda^\dagger(\omega)\big)\left(a^\dagger + a\right)\;,\end{aligned} \tag{A92}$$

where $a|n\rangle = \sqrt{n}\;|n-1\rangle$ and $a^\dagger|n\rangle = \sqrt{n-1}\;|n\rangle$. The terms respectively describe the energy associated to: the plasmonic mode of frequency ω_{cav}, the emitter of frequency ω_e, the coupling between the plasmonic mode and the emitter with strength $g(\boldsymbol{r})$, the photonic background reservoir of frequency ω, the phononic background reservoir of frequency ω_{vib}, the coupling between the emitter and a phonon reservoir with a strength $\kappa_{vib}(\omega_{vib})$, and the coupling of the plasmonic mode to the reservoir (emission from the system) with

strength $\kappa(\omega)$. It is useful to group together the non-interacting terms, and call this $\mathcal{H}_0$,

$$\mathcal{H}_0 = a^\dagger a\omega_{cav} + \frac{1}{2}\sigma_z\omega_e + \sum_\lambda \int_0^\infty d\omega b_\lambda^\dagger(\omega) b_\lambda(\omega)\omega + \int_0^\infty d\omega_{vib}\; b_{vib}^\dagger(\omega_{vib}) b_{vib}(\omega_{vib})\omega_{vib}\;. \tag{A93}$$

To simplify the Hamiltonian, consider moving to the interaction picture where the operators evolve under $\mathcal{H}_0 O = e^{i\mathcal{H}_0 t} O_S e^{-i\mathcal{H}_0 t}$, and the time dependence due to $\mathcal{H}_0$ is removed from the state such that $|\psi\rangle \longrightarrow |\tilde{\psi}\rangle = e^{i\mathcal{H}_0 t}|\psi_S\rangle$. Substituting $|\psi_S\rangle = e^{-i\mathcal{H}_0 t}|\tilde{\psi}\rangle$ into the TDSE:

$$i\partial_t|\psi\rangle = \mathcal{H}|\psi\rangle\;, \tag{A94}$$

we find that the Schrödinger equation in the interaction picture, upon differentiating $e^{-i\mathcal{H}_0 t}$, rearranges to:

$$i\partial_t|\tilde{\psi}\rangle = e^{i\mathcal{H}_0 t}\mathcal{H}_{int}e^{-i\mathcal{H}_0 t}|\tilde{\psi}\rangle\;, \tag{A95}$$

where $\mathcal{H}_{int} = \mathcal{H} - \mathcal{H}_0$:

$$\mathcal{H}_{int} = g(\mathbf{r})\left(a^\dagger + a\right)(\sigma_+ + \sigma_-) + \int_0^\infty d\omega_{vib}\;\sigma_z\kappa_{vib}(\omega_{vib})\left(b_{vib}^\dagger + b_{vib}\right) - i\sum_\lambda \int_0^\infty d\omega\;\kappa(\omega)\big(b_\lambda(\omega) - b_\lambda^\dagger(\omega)\big)\left(a^\dagger + a\right)\;. \tag{A96}$$

To evaluate $e^{i\mathcal{H}_0 t}\mathcal{H}_{int}e^{-i\mathcal{H}_0 t}$ we must use the unity transformation, under which we find:

$$e^{i\mathcal{H}_0 t}a^\dagger e^{-i\mathcal{H}_0 t} = a^\dagger e^{i\omega_{cav}t} \tag{A97}$$

$$e^{i\mathcal{H}_0 t}\sigma_+ e^{-i\mathcal{H}_0 t} = \sigma_+ e^{i\omega_e t} \tag{A98}$$

$$e^{i\mathcal{H}_0 t}b^\dagger_{\lambda'}(\omega')e^{-i\mathcal{H}_0 t} = b^\dagger_{\lambda'}(\omega')e^{i\omega' t} \tag{A99}$$

$$e^{i\mathcal{H}_0 t}b^\dagger_{vib}(\omega_{vib})e^{-i\mathcal{H}_0 t} = b^\dagger_{vib}(\omega_{vib})e^{i\omega_{vib}t}\ , \tag{A100}$$

while σ_z, $a^\dagger a$, $b^\dagger_\lambda b_\lambda$, and $b^\dagger_{vib}b_{vib}$ are unchanged since each commute with $\mathcal{H}_0$. Using these relations, we find the interaction picture Hamiltonian is:

$$\begin{aligned} e^{i\mathcal{H}_0 t}\mathcal{H}_{int}e^{-i\mathcal{H}_0 t} &= g(\mathbf{r})\left[a^\dagger\sigma_- e^{i(\omega_{cav}-\omega_e)t} + a^\dagger\sigma_+ e^{i(\omega_{cav}+\omega_e)t} + h.c.\right] \\ &+ \int_0^\infty d\omega_{vib}\kappa_{vib}(\omega_{vib})\sigma_z\left[b^\dagger_{vib}(\omega_{vib})e^{i\omega_{vib}t} + b_{vib}(\omega_{vib})e^{-i\omega_{vib}t}\right] \\ &+ \sum_\lambda\int_0^\infty d\omega\kappa(\omega)\left[ib^\dagger_\lambda(\omega)ae^{i(\omega-\omega_{cav})t} + ib^\dagger_\lambda(\omega)a^\dagger e^{i(\omega+\omega_{cav})t} + h.c.\right]\ . \end{aligned} \tag{A101}$$

We make the rotating wave approximation by removing the rapid oscillating terms, $\propto e^{\pm i(\omega_{cav}+\omega_e)t}$, which time average to zero. We therefore simplify $\mathcal{H}_{int}$ to:

$$\begin{aligned} \mathcal{H}_{int} &\simeq g(\mathbf{r})\left[a^\dagger\sigma_- e^{i(\omega_{cav}-\omega_e)t} + a\sigma_+ e^{-i(\omega_{cav}-\omega_e)t}\right] \\ &+ \int_0^\infty d\omega_{vib}\kappa_{vib}(\omega_{vib})\sigma_z\left[b^\dagger_{vib}(\omega_{vib})e^{i\omega_{vib}t} + b_{vib}(\omega_{vib})e^{-i\omega_{vib}t}\right] \\ &- i\sum_\lambda\int_0^\infty d\omega\kappa(\omega)\left[b_\lambda(\omega)a^\dagger e^{i(\omega_{cav}-\omega)t} - b^\dagger_\lambda(\omega)ae^{-i(\omega_{cav}-\omega)t}\right]\ . \end{aligned} \tag{A102}$$

We assume that each mode of the reservoir (which contains the state of the incoming and out-going far-field) is initially in its vacuum state, with the exception of a pump mode at frequency ω_p which we single out from the reservoir.

$$\begin{aligned}\mathcal{H}_{int} &= g(\mathbf{r})\left[a^\dagger\sigma_- e^{i(\omega_{cav}-\omega_e)t} + a\sigma_+ e^{-i(\omega_{cav}-\omega_e)t}\right] \\ &+ \int_0^\infty d\omega_{vib}\kappa_{vib}(\omega_{vib})\sigma_z\left[b^\dagger_{vib}(\omega_{vib})e^{i\omega_{vib}t} + b_{vib}(\omega_{vib})e^{-i\omega_{vib}t}\right] \\ &- i\sum_\lambda\int_0^\infty d\omega\kappa(\omega)\left[b_\lambda(\omega)a^\dagger e^{i(\omega_{cav}-\omega)t} - b^\dagger_\lambda(\omega)ae^{-i(\omega_{cav}-\omega)t}\right] \\ &- i\kappa(\omega_p)\left[b(\omega_p)a^\dagger e^{i(\omega_{cav}-\omega_p)t} - b^\dagger(\omega_p)ae^{-i(\omega_{cav}-\omega_p)t}\right] .\end{aligned} \tag{A103}$$

We transform to the frame co-rotation with the pump field with the unitary operator $U = e^{i\mathcal{H}_0' t}$, where

$$\mathcal{H}_0 = \Delta_{cav}a^\dagger a + \frac{1}{2}\Delta_d\sigma_z , \tag{A104}$$

with $\Delta_{cav} = \omega_{cav} - \omega_p$ and $\Delta_d = \omega_e - \omega_p$. These are the detunings of the cavity (ω_{cav}) and dipole (ω_e), respectively. This transforms $a^\dagger$ and σ_+ as

$$e^{-i\mathcal{H}_0' t}a^\dagger e^{i\mathcal{H}_0' t} = a^\dagger e^{-i(\omega_{cav}-\omega_p)t} \tag{A105}$$

$$e^{-i\mathcal{H}_0' t}\sigma_+ e^{i\mathcal{H}_0' t} = \sigma_+ e^{-i(\omega_e-\omega_p)t} , \tag{A106}$$

and their hermitian conjugates accordingly. All other operators are unchanged. Under

this unitary transformation, the Schrödinger equation becomes:

$$i\partial_t|\psi'\rangle = \left[\mathcal{H}_0' + e^{-i\mathcal{H}_0' t}\tilde{\mathcal{H}}_{int}e^{i\mathcal{H}_0' t}\right]|\psi'\rangle \tag{A107}$$

$$= \mathcal{H}|\psi'\rangle \ . \tag{A108}$$

The final Hamiltonian is given by substituting equations A105 and A106 into A108, such that:

$$\begin{aligned}\mathcal{H} = {} & \Delta_{cav}a^\dagger a + \frac{1}{2}\Delta_d\sigma_z + g(\mathbf{r})\left(a^\dagger\sigma_- + a\sigma_+\right) + i\kappa(\omega_p)\left(b^\dagger(\omega_p)a - b(\omega_p)a^\dagger\right) \\ & + \int_0^\infty d\omega_{vib}\ \sigma_z\kappa_{vib}(\omega_{vib})\left[b_{vib}^\dagger e^{i\omega_{vib}t} - b_{vib}e^{-i\omega_{vib}t}\right] \\ & - i\sum_\lambda\int_0^\infty d\omega\kappa(\omega)\left[b_\lambda(\omega)a^\dagger e^{i\Delta(\omega)t} - b_\lambda^\dagger(\omega)ae^{-i\Delta(\omega)t}\right] \ ,\end{aligned} \tag{A109}$$

where $\Delta = \omega - \omega_p$ is the detuning relative to the photon reservoir (ω). Note that here the prime notation has been dropped.

In singling out the input field mode from the last term of $\mathcal{H}$ the mean field approximation is taken, which assumes the pump mode is in a highly excited coherent state. The field operator $b_\lambda(\omega)$ can therefore be replaced with a complex number α—the amplitude of the coherent state that best describes the mean value of the input field. In addition, we assume that the reservoir remains unchanged as the quantum statistics of the pump mode do not significantly affect the statistics of the reservoir. The reservoir can, however, have an important effect on the pump field—in the form of noise—but these are not considered under the mean field approximation.

The Hamiltonian (A109) for the driven, open quantum system can be split into system and reservoir components: $\mathcal{H} = \mathcal{H}_{sys} + \mathcal{H}_{res}$:

$$\mathcal{H}_{sys} = \Delta_{cav} a^\dagger a + \frac{1}{2}\Delta_d \sigma_z + g(\mathbf{r})\left(a^\dagger \sigma_- + a\sigma_+\right) + i\sqrt{\kappa_{in}}\left(\alpha^* a - \alpha a^\dagger\right) \tag{A110}$$

$$\mathcal{H}_{res} = \int_0^\infty d\omega_{vib}\ \sigma_z \kappa_{vib}(\omega_{vib})\left[b_{vib}^\dagger e^{i\omega_{vib}t} - b_{vib} e^{-i\omega_{vib}t}\right] - i\sum_\lambda \int_0^\infty d\omega \kappa(\omega)\left[b_\lambda(\omega) a^\dagger e^{i\Delta(\omega)t} - b_\lambda^\dagger(\omega) a e^{-i\Delta(\omega)t}\right] . \tag{A111}$$

Here $\sqrt{\kappa_{in}}\left(\alpha^* a - \alpha a^\dagger\right)$ describes the driving term which pumps energy into the system, with in-coupling constant $\sqrt{\kappa_{in}} = \kappa(\omega_p)$. The driving pump field is therefore an incoming monochromatic plane wave, with a photon flux of $c|\alpha|^2$.

This can easily be generalised for any number of emitters N:

$$\mathcal{H}_{sys} = \Delta_{cav} a^\dagger a + \sum_j^N \left[\frac{1}{2}\Delta_d \sigma_z^{(j)} + g(\mathbf{r}^{(j)})\left(a^\dagger \sigma_-^{(j)} + a\sigma_+^{(j)}\right)\right] + i\sqrt{\kappa_{in}}\left(\alpha^* a - \alpha a^\dagger\right) \tag{A112}$$

$$\mathcal{H}_{res} = \sum_j^N \int_0^\infty d\omega_{vib}\ \sigma_z^{(j)} \kappa_{vib}(\omega_{vib})\left[b_{vib}^\dagger e^{i\omega_{vib}t} - b_{vib} e^{-i\omega_{vib}t}\right] - i\sum_\lambda \int_0^\infty d\omega \kappa(\omega)\left[b_\lambda(\omega) a^\dagger e^{i\Delta(\omega)t} - b_\lambda^\dagger(\omega) a e^{-i\Delta(\omega)t}\right] . \tag{A113}$$

With the Hamiltonian for this model complete, the Born-Markov approximation can be made for the reservoirs, allowing the time evolution of this system to be described by

the density operator, ρ, via the Lindblad master equation:

$$\frac{d}{dt}\rho = -i\left[\mathcal{H}_{sys}, \rho\right] + 2\kappa_{out} a\rho a^{\dagger} - \kappa_{out}\left(a^{\dagger}a\rho + \rho a^{\dagger}a\right) + \sum_{j}^{N}\left[\kappa_{vib}\sigma_{z}^{(j)}\rho\sigma_{z}^{(j)} - \frac{\kappa_{vib}}{2}\left(\sigma_{z}^{(j)2}\rho + \rho\sigma_{z}^{(j)2}\right)\right] . \tag{A114}$$

For the parameters entering the Hamiltonian and master equation, the photonic and phononic decay rates may be obtained, along with the coupling strength and pump field coefficient—as described in the main text. These are respectively given by: $\kappa_{out} = 1.23 \times 10^{14}$ rad/s, $\kappa_{vib} = 6.05 \times 10^{12}$ rad/s, $g = 5.89 \times 10^{13}$ rad/s, with the pump field coefficient following $\alpha = \kappa_{out}\sqrt{\langle N\rangle}/(2\sqrt{\kappa_{in}})$, and is chosen such that the average photon number in the system under the pump field regime is $\langle N\rangle = 10^{-6}$.

A15 MODE VOLUME

In order to introduce an emitter into the quantum mechanical description of the nanoplasmonic system, the coupling strength $g(\boldsymbol{r})$ between the emitter and the set of plasmonic modes is required. This is related to the quantised electric field $\boldsymbol{E}$ by:

$$\hat{\mathbf{d}} \cdot \mathbf{E}_n = g_n(\mathbf{r})(a_n^\dagger + a_n)(\sigma_+ + \sigma_-) \ , \tag{A115}$$

which, for a dipole operator $\hat{\mathbf{d}} = \mathbf{d}\left(|g\rangle\langle e| + |e\rangle\langle g|\right)$ and field operator given by equation A118 below, becomes:

$$g_n(\mathbf{r}) = \sqrt{\frac{\hbar\omega_n}{2\varepsilon_0\varepsilon(\mathbf{r})}}\frac{1}{\mathcal{N}_n}\mathbf{d} \cdot \mathbf{u}_n(\mathbf{r}) \ , \tag{A116}$$

when keeping only the resonant terms in $\hat{\mathbf{d}} \cdot \mathbf{E}_n$. Here $\boldsymbol{d}$ is the dipole moment of the emitter, and $\mathcal{N}_n$ is the electric field normalisation term that needs to be determined for each mode—specified by the index n. This normalisation ensures that the field mode—with frequency ω—has a vacuum energy of $\hbar\omega$.

The quantised, transverse fields for a general set of normal modes are given by:

$$\mathbf{A}_n(\mathbf{r},t) = \sqrt{\frac{\hbar}{2\varepsilon_0\varepsilon(\mathbf{r})\omega_n}}\frac{1}{\mathcal{N}_n}\left[\mathbf{u}_n^*(\mathbf{r})\hat{a}_n^\dagger e^{-i\omega_n t} + \text{h.c.}\right] \tag{A117}$$

$$\mathbf{E}_n(\mathbf{r},t) = \sqrt{\frac{\hbar\omega_n}{2\varepsilon_0\varepsilon(\mathbf{r})}}\frac{1}{\mathcal{N}_n}\left[i\mathbf{u}_n^*(\mathbf{r})\hat{a}_n^\dagger e^{-i\omega_n t} + \text{h.c.}\right] \tag{A118}$$

$$\mathbf{B}_n(\mathbf{r},t) = \sqrt{\frac{\hbar}{2\varepsilon_0\varepsilon(\mathbf{r})\omega_n}}\frac{1}{\mathcal{N}_n}\left[\nabla\times\mathbf{u}_n^*(\mathbf{r})\hat{a}_n^\dagger e^{-i\omega_n t} + \text{h.c.}\right]\ , \tag{A119}$$

where $\mathbf{E}_n(\mathbf{r},t) = -\dot{\mathbf{A}}_n(\mathbf{r},t)$ and $\mathbf{B}_n(\mathbf{r},t) = \nabla\times\mathbf{A}_n(\mathbf{r},t)$, which are also related to $\mathbf{D}_n(\mathbf{r},t) = \varepsilon_0\varepsilon(\mathbf{r})\mathbf{E}_n(\mathbf{r},t)$ and $\mathbf{B}_n(\mathbf{r},t) = \mu_0\mu(\mathbf{r})\mathbf{H}_n(\mathbf{r},t)$. The orthonormal modes, $\mathbf{u}_n$, are defined such that $\int \mathbf{u}_n\mathbf{u}_m^* d\mathbf{r} = \delta_{nm}$. The energy of the field is described by the Hamiltonian:

$$\mathcal{H} = \frac{1}{2}\int d\mathbf{r}\left[\varepsilon_0\varepsilon(\mathbf{r})|\mathbf{E}(\mathbf{r})|^2 + \frac{1}{\mu_0\mu(\mathbf{r})}|\mathbf{B}(\mathbf{r})|^2\right]\ , \tag{A120}$$

where the mode normalisation condition therefore arises as $\langle 0_n|\mathcal{H}|0_n\rangle = \frac{1}{2}\hbar\omega_n$, where $|0_n\rangle$ is the vacuum state for mode n.

Expanding the Hamiltonian in terms of these quantised electric and magnetic fields of equations A118 and A119 gives:

$$\begin{aligned}\mathcal{H} = \frac{\hbar\omega_n}{4}\mathcal{N}_n^{-2}\int d\mathbf{r}\Big\{&\Big[|\mathbf{u}_n(\mathbf{r})|^2\left(\hat{a}_n^\dagger\hat{a}_n + \hat{a}_n\hat{a}_n^\dagger\right) - \mathbf{u}_n^{*,2}(\mathbf{r})\hat{a}_n^\dagger\hat{a}_n^\dagger e^{-2i\omega_n t} - \mathbf{u}_n^2(\mathbf{r})\hat{a}_n^2 e^{2i\omega_n t}\Big]\\ +\frac{1}{\varepsilon_0\varepsilon(\mathbf{r})\mu_0\mu(\mathbf{r})\omega_n^2}&\Big[|\nabla\times\mathbf{u}_n(\mathbf{r})|^2\left(\hat{a}_n^\dagger\hat{a}_n + \hat{a}_n\hat{a}_n^\dagger\right) + (\nabla\times\mathbf{u}_n^*(\mathbf{r}))^2\hat{a}_n^\dagger\hat{a}_n^\dagger e^{-2i\omega_n t}\\ &+(\nabla\times\mathbf{u}_n(\mathbf{r}))^2\hat{a}_n\hat{a}_n e^{2i\omega_n t}\Big]\Big\}\ .\end{aligned} \tag{A121}$$

With this, the vacuum energy becomes:

$$\langle 0|\mathcal{H}|0\rangle = \frac{\hbar\omega_n}{4}\mathcal{N}_n^{-2}\int d\mathbf{r}\Big\{|\mathbf{u}_n(\mathbf{r})|^2 + \frac{1}{\varepsilon_0\varepsilon(\mathbf{r})\mu_0\mu(\mathbf{r})\omega_n^2}|\nabla\times\mathbf{u}_n(\mathbf{r})|^2\Big\}\,, \tag{A122}$$

as $\langle 0|(\hat{a}_n^\dagger\hat{a}_n + \hat{a}_n\hat{a}_n^\dagger)|0\rangle = 1$, and $\langle 0|\hat{a}_n^\dagger\hat{a}_n^\dagger|0\rangle = \langle 0|\hat{a}_n\hat{a}_n|0\rangle = 0$. The second term can be rewritten using the following identity for the vector potential: $\int d\mathbf{r}\,|\nabla\times\mathbf{A}|^2 = -\int d\mathbf{r}\mathbf{A}^*\cdot\nabla^2\mathbf{A}$, where the Helmholtz equation then gives: $\nabla^2\mathbf{A} = -\mu(\mathbf{r})\varepsilon(\mathbf{r})k^2\mathbf{A}$. Applying this to the mode $\mathbf{u}_n$, the vacuum energy becomes:

$$\langle 0|\mathcal{H}|0\rangle = \frac{\hbar\omega_n}{4}\mathcal{N}_n^{-2}\int d\mathbf{r}\Big\{|\mathbf{u}_n(\mathbf{r})|^2 + \frac{1}{\varepsilon_0\mu_0\omega_n^2}k^2|\mathbf{u}_n(\mathbf{r})|^2\Big\}\,. \tag{A123}$$

Finally, using $k_n^2 = \varepsilon_0\mu_0\omega_n^2$ reveals the equal contribution from the electric and magnetic fields, and gives the vacuum energy of:

$$\langle 0|\mathcal{H}|0\rangle = \frac{\hbar\omega_n}{2}\mathcal{N}_n^{-2}\int d\mathbf{r}|\mathbf{u}_n(\mathbf{r})|^2\,. \tag{A124}$$

Returning to the vacuum condition ($\langle 0_n|\mathcal{H}|0_n\rangle = \frac{1}{2}\hbar\omega_n$), the modes must be normalised such that: $\mathcal{N}_n^{-2}\int d\mathbf{r}|\mathbf{u}_n(\mathbf{r})|^2 = 1$.

For the usual mode volume normalisation that field operators are defined by, the substitution of $\mathcal{N}_n = \sqrt{V_n}$ finally gives:

$$V_n = \int d\mathbf{r}|\mathbf{u}_n(\mathbf{r})|^2\,. \tag{A125}$$

This corresponds to the simplest expression for the mode volume, but any definition may be chosen provided that the mode, $\mathbf{u}_n$, is re-scaled to the mode volume's normalisation. For a mode volume normalised by the maximum energy in the system:

$$V_n = \frac{\int d\mathbf{r}|\mathbf{u}_n(\mathbf{r})|^2}{\mathrm{Max}[|\mathbf{u}_n(\mathbf{r})|^2]} \ , \tag{A126}$$

the mode must be re-scaled such that:

$$\mathbf{u}_n(\mathbf{r}) = \frac{\sqrt{\varepsilon(\mathbf{r})}\mathbf{E}_n(\mathbf{r})}{\sqrt{\mathrm{Max}[\varepsilon(\mathbf{r})|\mathbf{E}_n(\mathbf{r})|^2]}} \ . \tag{A127}$$

For systems where the atomic components are embedded within a uniform dielectric media, the electric permittivities become real and position independent. In this regime, the re-scaled mode definition simplifies to:

$$\mathbf{u}_n(\mathbf{r}) = \frac{\mathbf{E}_n(\mathbf{r})}{\sqrt{\mathrm{Max}[|\mathbf{E}_n(\mathbf{r})|^2]}} \ . \tag{A128}$$

Note that this re-scaling of the mode function is required in order to be consistent with the mode volume definition—this is different to a general field normalisation, whereby the fields, mode functions and mode volume would all be normalised by a factor of $\sqrt{\mathrm{QN}}$, where $\mathrm{QN} = \int d\mathbf{r}|\mathbf{u}_n(\mathbf{r})|^2$.

Finally, we wish to note the connection here with the terms in the Hamiltonian—and therefore master equation—of Appendix A14. The first term of $\mathcal{H}_{sys}$ in equation A113 originates from a direct simplification of equation A121, whilst the term describing the

strength with which the emitter(s) and plasmonic mode are coupled is obtained through equations A115 and A116.

A16 IN-COUPLING CONSTANT

The final parameter required for the driven Hamiltonian is the rate at which the field pumps energy into the system, κ_{in}, which is connected to the system's ability to gather incident energy, σ_{ext}. Starting classically, the extinction cross-section is defined by:

$$\sigma_{ext} = \frac{P_{out}}{S} \ , \tag{A129}$$

where P_{out} is the total power lost by the system, and S is the intensity of the plane wave excitation. By considering the quantum analogues, an expression for $\langle \sigma_{ext} \rangle$ (in the steady state) is obtained below, in terms of κ_{in} and κ_{out}.

To do this, the Lindblad master equation is used to consider the rate of change of photon number in the cavity

$$\frac{d}{dt}\langle a^\dagger a \rangle = \mathsf{Tr}[\dot{\rho} a^\dagger a] \tag{A130}$$

$$= -i\mathsf{Tr}[[\mathcal{H}_{sys}, \rho]\, a^\dagger a] + 2\kappa_{out}\mathsf{Tr}[a\rho a^\dagger a^\dagger a - \frac{1}{2}a^\dagger a \rho a^\dagger a - \frac{1}{2}\rho a^\dagger a a^\dagger a] \ . \tag{A131}$$

The second term becomes: $2\kappa_{out}\mathsf{Tr}[\rho a^\dagger a^\dagger a a - \rho a^\dagger a a^\dagger a] = 2\kappa_{out}\mathsf{Tr}[\rho a^\dagger (a a^\dagger - 1) a - \rho a^\dagger a a^\dagger a] = -2\kappa_{out}\mathsf{Tr}[\rho a^\dagger a] = -2\kappa_{out}\langle a^\dagger a \rangle$, whereas the first expands to

$$-i\mathsf{Tr}[[\mathcal{H}_{sys}, \rho]\, a^\dagger a] = -ig(\mathbf{r})\langle a^\dagger \sigma_- \rangle + ig(\mathbf{r})\langle a \sigma_+ \rangle - \sqrt{\kappa_{in}}\alpha\langle a^\dagger \rangle - \sqrt{\kappa_{in}}\alpha^*\langle a \rangle \ . \tag{A132}$$

In the steady state, this becomes:

$$\frac{d}{dt}\langle a^\dagger a\rangle = 0 = -ig(\mathbf{r})\langle a^\dagger \sigma_-\rangle + ig(\mathbf{r})\langle a\sigma_+\rangle - \sqrt{\kappa_{in}}(\alpha^*\langle a\rangle + \alpha\langle a^\dagger\rangle) - 2\kappa_{out}\langle a^\dagger a\rangle \ , \quad \text{(A133)}$$

where $-2\kappa_{out}\langle a^\dagger a\rangle$ is the rate at which photons are lost (through absorption and emission), and $-\sqrt{\kappa_{in}}(\alpha^*\langle a\rangle + \alpha\langle a^\dagger\rangle)$ is the rate at which they are excited by the driving field. In addition, $\langle a\rangle$ is required:

$$\frac{d}{dt}\langle a\rangle = \mathsf{Tr}[\dot{\rho}a] \quad \text{(A134)}$$

$$= -i\mathsf{Tr}[[\mathcal{H}_{sys},\rho]\,a] + 2\kappa_{out}\mathsf{Tr}[a\rho a^\dagger a - \frac{1}{2}a^\dagger a\rho a - \frac{1}{2}\rho a^\dagger a a] \ . \quad \text{(A135)}$$

Using $aa^\dagger = a^\dagger a + 1$ along with the cyclic nature of the trace, the second term becomes: $2\kappa_{out}\mathsf{Tr}[\rho a^\dagger a a - \frac{1}{2}\rho(a^\dagger a+1)a - \frac{1}{2}\rho a^\dagger a a] = -\kappa_{out}\mathsf{Tr}[\rho a] = -\kappa_{out}\langle a\rangle$, whereas the first expands to

$$-i\mathsf{Tr}[[\mathcal{H}_{sys},\rho]\,a] = -i\mathsf{Tr}\left[\Delta_c\rho a + g(\mathbf{r})\rho\sigma_- - i\sqrt{\kappa_{in}}\alpha\right] \ , \quad \text{(A136)}$$

where we have used $[a,b] = ab - ba$. In the steady state, this becomes:

$$\frac{d}{dt}\langle a\rangle = 0 = -\left(\kappa_{out} + i\Delta_c\right)\langle a\rangle - ig(\mathbf{r})\langle\sigma_-\rangle - \sqrt{\kappa_{in}}\alpha \ . \quad \text{(A137)}$$

The in-coupling coefficient and extinction cross-sections are determined for the nanoantenna with an empty cavity; here this is achieved by taking the empty cavity limit

where the coupling strength between the emitter(s) and cavity is set to zero ($g = 0$). These steady state expressions for $\langle a \rangle$ and $\langle a^\dagger a \rangle$ therefore reduce to:

$$\frac{d}{dt}\langle a \rangle = 0 = -\left(\kappa_{out} + i\Delta_c\right)\langle a \rangle - \sqrt{\kappa_{in}}\alpha \tag{A138}$$

$$\frac{d}{dt}\langle a^\dagger a \rangle = 0 = -\sqrt{\kappa_{in}}(\alpha\langle a^\dagger \rangle + \alpha^*\langle a \rangle) - 2\kappa_{out}\langle a^\dagger a \rangle \ . \tag{A139}$$

These may now be solved for:

$$\langle a \rangle = -\frac{\sqrt{\kappa_{in}}\alpha}{\kappa_{out} + i\Delta_c}\frac{\kappa_{out} - i\Delta_c}{\kappa_{out} - i\Delta_c} \tag{A140}$$

$$= -\frac{\sqrt{\kappa_{in}}\alpha\left(\kappa_{out} - i\Delta_c\right)}{\kappa_{out}^2 + \Delta_c^2} \tag{A141}$$

$$\langle a^\dagger \rangle = -\frac{\sqrt{\kappa_{in}}\alpha^*\left(\kappa_{out} + i\Delta_c\right)}{\kappa_{out}^2 + \Delta_c^2} \tag{A142}$$

$$2\kappa_{out}\langle a^\dagger a \rangle = \frac{\kappa_{in}|\alpha|^2\left(\kappa_{out} + i\Delta_c\right)}{\kappa_{out}^2 + \Delta_c^2} + \frac{\kappa_{in}|\alpha|^2\left(\kappa_{out} - i\Delta_c\right)}{\kappa_{out}^2 + \Delta_c^2} \ , \tag{A143}$$

and therefore:

$$\langle a^\dagger a \rangle = \frac{\kappa_{in}|\alpha|^2}{\kappa_{out}^2 + \Delta_c^2} \ . \tag{A144}$$

The power lost from the cavity is $P = 2\kappa_{out}\hbar\omega\langle a^\dagger a \rangle = \frac{2\kappa_{in}\kappa_{out}|\alpha|^2}{\kappa_{out}^2+\Delta_c^2}\hbar\omega$. Since $c|\alpha|^2$ is the flux of the plane wave excitation, its intensity is $S = c\hbar\omega|\alpha|^2$. Recalling equation A129, the steady state expectation value of the quantum extinction cross-section is therefore

given by:

$$\langle \sigma_{ext} \rangle = \frac{2\kappa_{in}\kappa_{out}}{c} \frac{1}{\kappa_{out}^2 + \Delta_c^2} \ . \tag{A145}$$

Recalling the legitimate definition of the classical in-coupling coefficient: $\kappa_{in} = \frac{\kappa_{out}}{2} c \sigma_{ext}$, the quantum expectation value of the extinction cross-section becomes:

$$\langle \sigma_{ext} \rangle = \sigma_{ext} \frac{\kappa_{out}^2}{\kappa_{out}^2 + \Delta_c^2} \ , \tag{A146}$$

which on resonance ($\Delta_c = 0$), returns: $\langle \sigma_{ext} \rangle = \sigma_{ext}$.